TECHNISCHE UNIVERSITÄT WIEN

D I S S E R T A T I O N

Mixed Finite Element Methods For Nonlinear Continuum Mechanics And Shells

ausgeführt zum Zwecke der Erlangung des akademischen Grades
eines Doktors der Technik unter der Leitung von

Prof. Dr. Joachim Schöberl

E101 – Institut für Analysis und Scientific Computing, TU Wien

eingereicht an der Technischen Universität Wien
Fakultät für Mathematik und Geoinformation

von

Dipl. Ing. Michael Neunteufel

Matrikelnummer: 01241601
Dr.-Schober-Straße 85
1130 Wien

Diese Dissertation haben begutachtet:

1. **Prof. Joachim Schöberl**
   Institut für Analysis und Scientific Computing, TU Wien

2. **Prof. Antonio Gil**
   Zienkiewicz Centre for Computational Engineering, College of Engineering, Swansea University

3. **Prof. Max Wardetzky**
   Institute for Numerical and Applied Mathematics, University of Göttingen

4. **Prof. Astrid Pechstein**
   Institute of Technical Mechanics, Johannes Kepler University Linz

Wien, am 11. Februar 2021

Kurzfassung

In dieser Arbeit werden gemischte Formulierungen für nichtlineare Probleme in der Kontinuumsmechanik und Schalentheorie vorgestellt und besprochen.

Während Standardmethoden in der Kontinuumsmechanik, wo das Verschiebungsfeld als Unbekannte angesetzt wird, oftmals den Nachteil von nicht robusten Formulierungen mit sich bringt, können Kombinationen von Funktionenräumen mit schwächerer Regularität sogenannte "Locking" Phänomene verhindern. Gemischte Zweifeld-Methoden, die zusätzlich noch den Spannungstensor als Unbekannte verwenden, werden in der linearisierten Elastizitätstheorie bereits häufiger verwendetet. Diese können jedoch nicht sofort auf nichtlineare Materialien verallgemeinert werden, da sie im Allgemeinen nicht invertierbar sind. Zusätzlich setzen geometrische Nichtlinearitäten die Multiplikation von Ableitungen voraus, welche bei Räumen mit geringer Regularität nicht wohldefiniert sind. Dadurch motiviert werden sogenannte Dreifeld-Formulierungen vorgestellt, wo ein "Lifting" von distributionellen Ableitungen auf eine quadratisch integrierbare Funktion verwendet wird. Dieser Ansatz wird auch für (fast) inkompressible Materialien speziell behandelt.

Für (nichtlineare) Koiter-Schalen ist ein zweimal schwach differenzierbares Verschiebungsfeld notwendig, da ein Differenzialoperator vierter Ordnung involviert ist. Die Konstruktion von solchen global differenzierbaren finiten Elementen hat sich als äußerst schwierig erwiesen. Stattdessen führen wir ein zusätzliches Spannungsfeld ein um Verschiebungen in den Sobolevraum erster Ordnung und damit einfacheren Elementen zu ermöglichen. Wir zeigen, dass sich diese Methode im Falle kleiner Verzerrungen bei Platten zu der Hellan–Herrmann–Johnson Methode vereinfacht. Weiters werden Erweiterungen zu nichtlinearen Naghdi Schalen präsentiert.

Bei dünnen Schalen tritt bei gekrümmten Elementen sogenanntes Membranlocking auf. Wir präsentieren eine Interpolationsmethode beruhend auf den etwas weniger bekannten Regge finiten Elementen um ein solches Locking auf Dreiecksgittern zu verhindern. Dieser Ansatz kann mithilfe von finiten Elementen für den topologischen Dualraum als gemischtes Variationsproblem angesetzt werden. Wir diskutieren Zusammenhänge zwischen der vorgestellten Methode und bereits existierenden Elementen.

Abstract

In this work mixed formulations for nonlinear problems in continuum mechanics and shells are presented and discussed.

While standard methods in continuum mechanics, where the displacement field is used as unknown, often suffer from non-robust formulations, a combination of function spaces with lower regularity assumptions may circumvent so-called "locking" phenomena. Mixed two-field methods, where the stress tensor is considered as additional unknown, are already used quite often in linear elasticity. These approaches, however, can mostly not directly be generalized to nonlinear materials, as they are in general not invertable. Additionally, geometric nonlinearities require multiplication of derivatives, which are not well-defined for spaces with low regularities. With this motivation so-called three-field formulations are proposed, where a lifting of distributional derivatives to square-integrable functions is accomplished. This approach is further extended to (nearly) incompressible materials.

For (nonlinear) Koiter shells a twice weakly differentiable displacement field is required, as a fourth-order differential operator is involved. The construction of such globally differentiable finite elements has turned out to be extremely challenging. Instead, we introduce an additional stress field to enable displacements to be in a first order Sobolev space and thus more simple finite elements are available. We show that this method simplifies to the Hellan–Herrmann–Johnson method in the small strain regime for plates. Further, extensions to nonlinear Naghdi shells are presented.

For thin shell structures so-called membrane locking occurs for curved elements. We present an interpolation procedure based on the less common Regge finite elements to prevent this locking behavior for triangulations. This approach can be accomplished with finite elements for the topological dual space as mixed variational problem. We discuss connections between the presented methods and existing elements.

Acknowledgement

First of all, I want to use this opportunity to thank Prof. Joachim Schöberl for supervising and supporting my work throughout my bachelor, master, and doctoral studies since more than five years now. With his knowledge, motivation, and far-reaching interests I had the opportunity to get in touch with several fields of research widening my knowledge. I am very grateful for the countless time-intensive discussions during the last years.

Secondly, I wish to thank Prof. Antonio Gil, Prof. Max Wardetzky, and Prof. Astrid Pechstein for reading and reviewing this thesis.

I want to thank my colleagues in the working group. I enjoined the discussions on and off topics during lunch and coffee breaks and especially the weekly together lunch cooking, which I'm really missing since the start of the Corona pandemics.

Special thanks are extended to Christoph Wintersteiger and Stefan Portisch for answering several mostly organizational questions and Matthias Hochsteger and Christopher Lackner for supporting me overcoming countless bugs and strange behaviors in programming codes. Moreover, I want to thank my former office mate and friend Tobias Danczul for proofreading this thesis and his generous help.

I would like to express my thanks to my parents and my brother for supporting me throughout the whole study and providing me a pleasant environment, especially since the home-office marathons started in 2020.

Vienna, February, 2021   Michael Neunteufel

Eidesstattliche Erklärung

Ich erkläre an Eides statt, dass ich die vorliegende Dissertation selbstständig und ohne fremde Hilfe verfasst, andere als die angegebenen Quellen und Hilfsmittel nicht benutzt bzw. die wörtlich oder sinngemäß entnommenen Stellen als solche kenntlich gemacht habe.

Wien, am 11. Februar 2021

_____
Michael Neunteufel

Contents

1. Introduction

Nonlinear elasticity is an active and huge topic of research including theory and applications in industry. Even in the subtopics of continuum mechanics and shells the literature is enormous and research interest did not decrease especially since the beginning of finite elements decades ago.

The most direct approach to solve problems arising in elasticity numerically is to use Lagrangian finite elements for the vector valued displacement field u as unknown.

Under the assumption of small deformations and isotropic materials the linear problem of continuum mechanics reads in strong form: Find $u \in [H^1(\Omega)]^d$ fulfilling given boundary conditions and

$$-\operatorname{div}(2\hat{\mu}\,\boldsymbol{\epsilon}(u) + \hat{\lambda}\operatorname{div}(u)\boldsymbol{I}) = f \text{ in } \Omega, \tag{1.0.1}$$

and the nonlinear problem: Find $u \in [H^1(\Omega)]^d$ fulfilling given boundary conditions and

$$-\operatorname{div}(\boldsymbol{P}(u)) = f \text{ in } \Omega. \tag{1.0.2}$$

Here, $\Omega \subset \mathbb{R}^d$, $d = 2, 3$, is a bounded domain, $\hat{\mu}$ and $\hat{\lambda}$ the Lamé parameters, f an external force, $\boldsymbol{\epsilon}(\cdot)$ denotes the symmetric part of the gradient, and $\boldsymbol{P}$ the first Piola–Kirchhoff stress tensor.

In the linear case one easily obtains with Korn's inequality [96] $c_k\|u\|^2_{H^1} \leq \|u\|^2_{L^2} + \|\boldsymbol{\epsilon}(u)\|^2_{L^2}$ that the coercivity constant deteriorates for anisotropic domains as then $c_k \to 0$. Further, nearly incompressible materials are characterized by the parameter $\hat{\lambda} \gg 1$. Thus, the standard method is neither robust in the parameter $\hat{\lambda}$ nor for deteriorating aspect ratio. Mixed methods, where additional fields with less regularity assumptions are used, overcome the aforementioned problems. E.g., by introducing the pressure $p = \hat{\lambda}\operatorname{div}(u)$ a regularized Stokes problem with penalty is obtained

$$\int_\Omega 2\hat{\mu}\boldsymbol{\epsilon}(u) : \boldsymbol{\epsilon}(\delta u)\,dx + \int_\Omega p\operatorname{div}(\delta u)\,dx = \int_\Omega f \cdot \delta u\,dx \quad \text{for all } \delta u, \tag{1.0.3a}$$

$$\int_\Omega \operatorname{div}(u)\delta p\,dx \quad - \int_\Omega \frac{1}{\hat{\lambda}}p\,\delta p\,dx \quad = 0 \qquad \text{for all } \delta p, \tag{1.0.3b}$$

which is well-defined for the limit $\hat{\lambda} \to \infty$, if a stable pairing for (u, p) is considered.

For a robust formulation with respect to anisotropic domains the *tangential-displacement and normal-normal-stress continuous* (TDNNS) method introduces the stress tensor $\boldsymbol{\sigma} = \mathbb{C}\boldsymbol{\epsilon}(u)$, with $\boldsymbol{\sigma} \in H(\operatorname{div}\operatorname{div}, \Omega) = \{\boldsymbol{\sigma} \in [L^2(\Omega)]^{d \times d}_{\text{sym}} \mid \operatorname{div}(\operatorname{div}(\boldsymbol{\sigma})) \in H^{-1}(\Omega)\}$, and assumes the displacement u to be in the weaker $H(\operatorname{curl})$ space. As proven in [171, 172, 174], the

formulation

$$\int_\Omega \mathbb{C}^{-1}\boldsymbol{\sigma} : \delta\boldsymbol{\sigma}\, dx + \langle \mathrm{div}(\delta\boldsymbol{\sigma}), u\rangle = 0 \qquad \text{for all } \delta\boldsymbol{\sigma} \in H(\mathrm{div\, div}, \Omega), \quad (1.0.4a)$$

$$\langle \mathrm{div}(\boldsymbol{\sigma}), \delta u\rangle \qquad\qquad = -\int_\Omega f \cdot \delta u\, dx \quad \text{for all } \delta u \in H(\mathrm{curl}, \Omega), \qquad (1.0.4b)$$

where $\langle \cdot, \cdot \rangle$ denotes the duality pairing $H(\mathrm{curl})^* \times H(\mathrm{curl})$, is robust in the aspect ratio and, by adding a stabilization term, also in the incompressible limit [211]. Constructing stable mixed formulation for nonlinear elasticity has gained interest in the last 30 years and is an ongoing topic of research [209, 205, 130, 176, 189, 187, 55, 237, 43, 223, 203, 204, 6, 22, 208, 204, 128]. An extension of the TDNNS method to nonlinear materials is not straight forward as the material law cannot be inverted in general and the geometric nonlinearity requires multiplication of the deformation gradient $\boldsymbol{F} = \boldsymbol{I} + \nabla u$. As only the curl of $u \in H(\mathrm{curl})$ is square-integrable its gradient is a distribution, which cannot be directly multiplied. Thus, we propose three approaches based on the Hu–Washizu principle where the distributional deformation gradient or Cauchy–Green strain tensor is lifted to an additional square-integrable strain field and the stress acts as the corresponding Lagrange multiplier, e.g.,

$$\mathcal{L}(u, \boldsymbol{F}, \boldsymbol{P}) = \int_\Omega \Psi(\boldsymbol{F})\, dx - \langle \boldsymbol{F} - \boldsymbol{I} - \nabla u, \boldsymbol{P}\rangle, \qquad (1.0.5)$$

with $\Psi(\cdot)$ denoting a hyperelastic energy potential. For the additional strain fields so-called Regge elements [190, 78, 85, 147] are used entailing more beneficial properties than standard discontinuous elements. Therefore, we propose novel basis functions for Regge quadrilaterals, hexahedra, and prism elements.

The (nearly) incompressible case in the nonlinear setting is characterized by $\det(\boldsymbol{F}) = \det(\boldsymbol{I} + \nabla u) = 1$, i.e., the volume is preserved during deformation. We show how the distributional determinant for displacement fields discretized with Nédélec elements can be lifted to a regular field.

For thin-walled structures a dimension reduction yields the equation of shells, where the energy splits additively into a membrane, bending, and shearing part

$$t\, E_{\mathrm{mem}}(u) + t^3 E_{\mathrm{bend}}(u, \beta) + t\, E_{\mathrm{shear}}(u, \beta) = f(u). \qquad (1.0.6)$$

Here, t denotes the thickness parameter, u the displacement of the shell, and β a rotation field for Naghdi shells. By assuming the Kirchhoff–Love hypothesis the shearing energy is zero and expressing β in terms of u leads to a fourth order differential operator in the bending term. For plates the linearized bending energy then reduces to the biharmonic problem

$$E_{\mathrm{bend}}^{\mathrm{lin}}(w) = \frac{1}{2}\|\nabla^2 w\|_{L^2}^2. \qquad (1.0.7)$$

For a primal method the vertical deflection w requires H^2-conforming finite elements, i.e., finite elements which are globally differentiable. The construction of such (high-order)

elements is tedious. The *Hellan–Herrmann–Johnson* (HHJ) method [114, 116, 127, 91] introduces the linearized moment tensor $\boldsymbol{\sigma} := \nabla^2 w$ as additional unknown leading to the mixed saddle-point problem

$$\int_\Omega \boldsymbol{\sigma} : \delta\boldsymbol{\sigma} \, dx \; + \langle \operatorname{div}(\delta\boldsymbol{\sigma}), \nabla w \rangle = 0 \qquad \text{for all } \delta\boldsymbol{\sigma} \in H(\operatorname{div}\operatorname{div}, \Omega), \quad (1.0.8\text{a})$$

$$\langle \operatorname{div}(\boldsymbol{\sigma}), \nabla \delta w \rangle \qquad\qquad = -\int_\Omega f \cdot \delta w \, dx \quad \text{for all } \delta w \in H^1(\Omega), \qquad (1.0.8\text{b})$$

where the same duality pairing as in (1.0.4) is used. Thus, the regularity requirement of w reduces to be in H^1 enabling the usage of standard Lagrangian elements. We extend the HHJ method to nonlinear Koiter shells by using the moment tensor $\boldsymbol{\sigma} \in H(\operatorname{div}\operatorname{div})$, which is the energetic conjugate to the difference of the curvature tensors between the initial and deformed configuration. By adding additional shearing parameters $\gamma \in H(\operatorname{curl})$ the method is generalized to nonlinear Naghdi shells in terms of a hierarchical model [98]. It turns out that this approach extends the TDNNS method for Reissner–Mindlin plates [173] to nonlinear shells.

When dividing (1.0.6) by t^3 and assuming that the shell problem is in the bending dominated regime [71, 72], i.e., $f = t^3 \hat{f}$ with $\hat{f} = \mathcal{O}(1)$, the limit case of vanishing thickness $t \to 0$ enforces zero membrane and shear energy, $E_{\text{mem}}(u) = E_{\text{shear}}(u, \beta) = 0$. Due to the lack of finite element approximations to represent pure bending modes without inducing parasitic membrane and shearing modes, the numerical solution tends to be trivially zero and so-called locking occurs. The phenomenon of shear locking is mathematically well understood and several methods based on the problem intrinsic tangential continuity of the rotational field have been proposed [8, 31, 65, 173, 241, 170, 123, 151, 170, 119, 35, 125, 224, 210]. Membrane locking, however, is more involved as it appears only for curved shell elements [217, 218, 47, 135, 72, 11, 75, 76, 139, 181]. We propose adding the Regge interpolation operator into the membrane energy term,

$$\|\mathcal{I}_h^{\mathcal{R}} \boldsymbol{E}_{\overline{\tau}}(u)\|_{\boldsymbol{M}}^2, \qquad (1.0.9)$$

where $\boldsymbol{E}_{\overline{\tau}}(u)$ denotes the Green strain tensor on the surface and $\boldsymbol{M}$ the material tensor, alleviates membrane locking without introducing spurious zero-energy modes. Further, we present a connection to the *mixed interpolation of tensorial components* (MITC) elements [34, 35, 135] by proposing a tying point procedure to perform the interpolation, where no explicit construction of Regge elements is needed. Therefore, the method can easily be incorporated into existing shell elements.

1.1. Outline of this thesis

This thesis focuses on two major topics of nonlinear elasticity, namely continuum mechanics (Chapters 2, 4, and 6) and shells (Chapter 7 and 8). The therein involved Sobolev and finite element spaces are discussed in detail in Chapter 3 and 5, respectively. The structure of this work is given as follows:

- Chapter 2 is devoted to the derivation of equation of nonlinear elasticity. We assume a minimization problem induced by a hyperelastic energy potential and compute the

first variation to conclude the corresponding Euler–Lagrange equation in weak and strong form. Then, under the small strain assumption, the equation of linear elasticity is derived.

- In Chapter 3 a variational framework is briefly presented including standard and less common Sobolev spaces, important inequalities, and abstract existence and uniqueness results for linear variational formulations.

- The standard primal formulation of linear elasticity and several mixed formulations are discussed in terms of applicability and robustness properties in Chapter 4. Methods based on the Hellinger–Reissner principle involving the stress tensor as additional unknown and Hu–Washizu three field formulations, where, additionally to displacement and stress fields, also the strain tensor is used, are compared. We focus on robustness with respect to the incompressible limit and deteriorating aspect ratio of domains.

- Chapter 5 is dedicated to summarize the ingredients to construct high-order finite elements including: Standard H^1 Lagrangian (nodal) and discontinuous L^2 elements, Nédélec and Raviart–Thomas/Brezzi–Douglas–Marini elements developed for discretizing the Sobolev spaces $H(\mathrm{curl})$ and $H(\mathrm{div})$ in a conforming way, as well as matrix valued Hellan–Herrmann–Johnson and Regge elements related to the function spaces $H(\mathrm{div\,div})$ and $H(\mathrm{curl\,curl})$, respectively. Further, novel hierarchical and arbitrary order Regge elements for quadrilaterals, hexahedra, and prisms are proposed. The principle of functionals is used to construct finite elements for the topological dual spaces to define interpolation operators or to use them directly in variational formulations. Transformation rules for the resulting dual finite elements are presented to achieve geometry-free discretizations.

- Three different approaches to generalize the TDNNS method from linear to nonlinear elasticity based on lifting of distributions to more regular functions by means of a Hu–Washizu formulation are proposed in Chapter 6. The case of (nearly) incompressible materials is treated by a lifting procedure of the distributional determinant of the deformation gradient. We prove that all nonlinear approaches are consistent and the corresponding linearizations are uniquely solvable. Numerical results are presented to confirm the performance of these methods.

- In Chapter 7 the equation of nonlinear shells is derived from full 3D elasticity by a "geometrically exact" approach including shear deformable Naghdi and shear rigidity Koiter shells, which get linearized and reduced to plates and beams. The problem of computing the shape operator on discretized non-smooth manifolds and finite elements on surfaces are discussed. Then, a formulation for nonlinear Koiter shells circumventing the usually required C^1-continuity of elements based on the Hellan–Herrmann–Johnson method and an extension to nonlinear Naghdi shells by introducing additional rotational unknowns discretized by Nédélec elements is proposed. The relation to existing methods for linear plates is discussed and numerically verified. Further, several numerical examples are presented.

- We conclude with Chapter 8 where the locking behavior of shells induced by the small thickness parameter t is discussed. After an overview of shear locking in the context of Reissner–Mindlin plates is given, we focus on the phenomenon of membrane locking. To reduce and alleviate this unintended behavior we insert the Regge interpolation operator into the membrane energy term weakening the implicitly given kernel constraints. We discuss a tying point interpolation procedure revealing a connection to the MITC shell elements. Several numerical examples are presented to validate the performance of the method.

Some of the presented results have been published in the works [164, 165, 163]. In this thesis, however, we generalize and discuss these results and add several additional comments.

Implementations

For all numerical examples the open source finite element software Netgen and NGSolve[1], see [196, 197], were used. The novel Regge elements are implemented in NGSolve and therefore directly available.

Notation

When integrating over a volume, boundary, or co-dimensional 2 boundaries (edges in 3D and vertices in 2D) the notations dx, ds, $d\lambda$ are used. Further notations, which will be used throughout this work, are listed below:

$a \preceq b$	$a \leq c\,b$ with $c > 0$ independent of mesh-size h
$a \succeq b$	$b \preceq a$
$a \sim b$	$a \preceq b$ and $a \succeq b$
$\boldsymbol{I}$	identity matrix
$\boldsymbol{A} : \boldsymbol{B} = \sum_{i,j=1}^{d} \boldsymbol{A}_{ij}\boldsymbol{B}_{ij}$	Frobenius scalar product
$\mathrm{sym}(\boldsymbol{A}) = \frac{1}{2}(\boldsymbol{A} + \boldsymbol{A}^{\top})$	symmetric part of matrix
$\mathrm{skw}(\boldsymbol{A}) = \frac{1}{2}(\boldsymbol{A} - \boldsymbol{A}^{\top})$	skew-symmetric part of matrix
$\mathrm{tr}(\boldsymbol{A}) = \sum_{i=1}^{d} \boldsymbol{A}_{ii}$	trace of matrix
$\mathrm{dev}(\boldsymbol{A}) = \boldsymbol{A} - \frac{\mathrm{tr}(\boldsymbol{A})}{d}\boldsymbol{I}$	deviatoric part of matrix
$u \times v$	cross product of vectors in three dimensions
$u \otimes v = uv^{\top}$	dyadic product (tensor product)
$u \odot v = \mathrm{sym}(u \otimes v)$	symmetric dyadic product
$u \cdot v = \sum_{i=1}^{d} u_i v_i$	Euclidean scalar product
$\nabla a = \left(\frac{\partial a}{\partial x_1}, \ldots, \frac{\partial a}{\partial x_d}\right),\ \nabla u = \left(\frac{\partial u_i}{\partial x_j}\right)_{i,j=1}^{d}$	gradient of scalar and vector valued function
$\mathrm{GL}(d)$	set of regular matrices of dimension d
$\mathrm{SO}(d)$	special orthogonal group of dimension d
$\mathbb{M}_{+}(d)$	set of $d \times d$ matrices with positive determinant
$\mathbb{S}_{>}(d)$	set of positive definite $d \times d$ matrices

---

[1]https://ngsolve.org/

$\hat{E}$	Young modulus
$\hat{\nu}$	Poisson ratio
$\hat{\mu}, \hat{\lambda}$	Lamé parameters
$\mathbb{S}^d$	unit sphere in $d+1$ dimensions
$\|\cdot\|_2$	Euclidean norm
$\|\cdot\|_F$	Frobenius norm
$\mathrm{div}(u) = \sum_{i=1}^d \frac{\partial u_i}{\partial x_i}$, $\mathrm{div}(\boldsymbol{A}) = \begin{pmatrix} \sum_{i=1}^d \frac{\partial \boldsymbol{A}_{1i}}{\partial x_i} \\ \vdots \\ \sum_{i=1}^d \frac{\partial \boldsymbol{A}_{di}}{\partial x_i} \end{pmatrix}$	divergence of vector and matrix valued function
$\boldsymbol{P}_n = n \otimes n$	normal projection
$u_n = u \cdot n$	normal component of vector
$u_t = u - (u \cdot n)n = (\boldsymbol{I} - \boldsymbol{P}_n)u$	tangential component of vector
$\boldsymbol{A}_{nn} = n^\top \boldsymbol{A} n$	normal-normal component of matrix
$\boldsymbol{A}_{nt} = (\boldsymbol{I} - \boldsymbol{P}_n)\boldsymbol{A}n$	normal-tangential component of matrix
$\boldsymbol{A}_{tt} = (\boldsymbol{I} - \boldsymbol{P}_n)\boldsymbol{A}(\boldsymbol{I} - \boldsymbol{P}_n)$	tangential-tangential component of matrix

2. Elasticity

This section is devoted to the introduction of the equations of elasticity. We focus on hyperelastic materials and refer to the literature for a comprehensive introduction into (nonlinear) elasticity and continuum mechanics [87, 117, 154, 236, 58, 56, 142].

2.1. Strain tensors

Let $\Omega \subset \mathbb{R}^d$ be an open and bounded domain in $d = 2, 3$ dimensions and let the boundary $\partial\Omega$ be sufficiently smooth. Then $\overline{\Omega}$ describes the reference configuration of a body, also called undeformed configuration. The boundary is split into a Dirichlet and Neumann part Γ_D and Γ_N, respectively, with $\Gamma_D \cap \Gamma_N = \emptyset$ and $\overline{\Gamma_D} \cup \overline{\Gamma_N} = \partial\Omega$. Further, we assume that the measure of Γ_D is not zero, i.e., $|\Gamma_D| \neq 0$.

Applying external forces to the body leads to *deformation* represented by the function

$$\Phi : \overline{\Omega} \to \mathbb{R}^d$$
$$x \mapsto \Phi(x), \tag{2.1.1}$$

which can be split additively into the identity function and the *displacement* u

$$\Phi = \mathrm{id} + u. \tag{2.1.2}$$

Next, we introduce the *deformation gradient*

$$\boldsymbol{F} := \boldsymbol{I} + \nabla u = \nabla\Phi, \tag{2.1.3}$$

where $\boldsymbol{I}$ denotes the identity matrix. A deformation is called *permissible* if the *deformation determinant* $J := \det(\boldsymbol{F})$ is greater than zero, $J > 0$, which entails that the material is non-interpenetrable, i.e., the orientation is preserved and volume elements with positive measure have also positive measure after the deformation.

To measure the quadratic change of lengths of the deformation the *Cauchy–Green strain tensor* is introduced as

$$\boldsymbol{C} := \boldsymbol{F}^\top \boldsymbol{F}. \tag{2.1.4}$$

It is also called *metric tensor* in the context of differential geometry and shells, see Section 7.2. There holds for $\Phi \in C^2(\Omega, \mathbb{R}^d)$ with Taylor's theorem

$$\frac{\|\Phi(x + \Delta x) - \Phi(x)\|^2}{\|\Delta x\|^2} = \frac{\Delta x^\top \boldsymbol{C} \Delta x}{\|\Delta x\|^2} + \mathcal{O}(\|\Delta x\|), \qquad \text{for } \|\Delta x\| \to 0. \tag{2.1.5}$$

If $\boldsymbol{C} = \boldsymbol{I}$, then the body gets not deformed, however, it could be rotated or translated. The following theorem states that these motions are exactly the kernel of $\boldsymbol{C} - \boldsymbol{I}$, so-called *rigid body motions*.

> **2.1 Theorem.** *Let Ω be a connected domain and $\Phi \in C^1(\Omega, \mathbb{R}^d)$. Then a deformation is a rigid body motion if and only if*
>
> $$\Phi(x) = a + \boldsymbol{Q}x, \tag{2.1.6}$$
>
> *where $a \in \mathbb{R}^d$ and $\boldsymbol{Q} \in \mathrm{SO}(d)$.*

Proof. See e.g., [87, Theorem 1.8-1]. □

This motivates the definition of the *Green strain tensor*

$$\boldsymbol{E} := \frac{1}{2}\left(\boldsymbol{C} - \boldsymbol{I}\right) \tag{2.1.7}$$

measuring the real strains induced by the deformation Φ. Inserting (2.1.3)–(2.1.4) yields the representation

$$\boldsymbol{E} = \frac{1}{2}\left(\nabla u^\top \nabla u + \nabla u^\top + \nabla u\right). \tag{2.1.8}$$

Assuming $\nabla u = \mathcal{O}(\varepsilon)$ with $1 \gg \varepsilon > 0$ small and neglecting all higher order terms gives the linearized strain tensor

$$\boldsymbol{\epsilon}(u) := \frac{1}{2}\left(\nabla u^\top + \nabla u\right) = \mathrm{sym}(\nabla u) \tag{2.1.9}$$

used in linearized elasticity.

2.2. Hyperelastic materials

We consider *hyperelastic constitutive relations*, i.e., the deformation energy is given by a potential $\Psi : \Omega \times \mathbb{R}^{d \times d} \to \mathbb{R}$

$$E_{\mathrm{def}} = \int_\Omega \Psi(x, \boldsymbol{F}(u(x))) \, dx. \tag{2.2.1}$$

For more general elastic materials and a derivation based on conservation laws we refer to the literature. Further, for ease of presentation we assume that the potential is *homogeneous*, i.e.,

$$\Psi(x, \cdot) = \Psi(\cdot). \tag{2.2.2}$$

Given Dirichlet data u_D on Γ_D, a static body load f, and traction forces g on Γ_N we can define the following minimization problem

$$\mathcal{W}(u) := \int_\Omega \Psi(\boldsymbol{F}(u)) - f \cdot u \, dx - \int_{\Gamma_N} g \cdot u \, ds \to \min!. \tag{2.2.3}$$

We seek for a function u (the function space will be specified later) in the set of admissible displacements given by

$$V := \{u : \Omega \to \mathbb{R}^d \,|\, u = u_D \text{ on } \Gamma_D, \, \det(\boldsymbol{F}(u)) > 0\}. \tag{2.2.4}$$
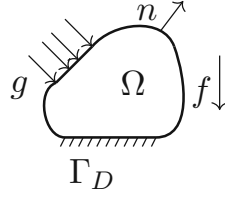
Figure 2.1.: Initial configuration of a body Ω with Dirichlet boundary Γ_D, external forces f and g, and outer normal vector n.

Note, that the constraint $\det(\boldsymbol{F}(u)) > 0$ is often given implicitly in the material law or is neglected in the small deformation case.

To compute the weak formulation of (2.2.3) we take the first variation in direction δu, well-known as the *principle of virtual works*, yielding

$$\partial_u \mathcal{W}(u)(\delta u) = \int_\Omega \frac{\partial \Psi}{\partial \boldsymbol{F}} : \nabla \delta u - f \cdot \delta u \, dx - \int_{\Gamma_N} g \cdot \delta u \, ds \stackrel{!}{=} 0 \qquad (2.2.5)$$

for all admissible test functions δu, i.e., $\delta u \in V_0$, where

$$V_0 := \{\delta u : \Omega \to \mathbb{R}^d \,|\, \delta u = 0 \text{ on } \Gamma_D\}. \qquad (2.2.6)$$

By defining the *first Piola–Kirchhoff stress tensor*

$$\boldsymbol{P} := \frac{\partial \Psi}{\partial \boldsymbol{F}} \qquad (2.2.7)$$

and integration by parts in (2.2.5), we obtain the Euler–Lagrange equation of (2.2.3)

$$\begin{cases} -\mathrm{div}(\boldsymbol{P}) = f & \text{in } \Omega, \\ u = u_D & \text{on } \Gamma_D, \\ \boldsymbol{P}n = g & \text{on } \Gamma_N, \end{cases} \qquad (2.2.8)$$

where n denotes the outer normal vector of Ω, cf. Figure 2.1.

Definition 2.1. We call a hyperelastic potential

- *objective* (*frame-indifferent*), if for all $\boldsymbol{F} \in \mathbb{M}_+(d)$ and $\boldsymbol{Q} \in \mathrm{SO}(d)$

$$\Psi(\boldsymbol{Q}\boldsymbol{F}) = \Psi(\boldsymbol{F}). \qquad (2.2.9)$$

- *isotropic*, if for all $\boldsymbol{F} \in \mathbb{M}_+(d)$ and $\boldsymbol{Q} \in \mathrm{SO}(d)$

$$\Psi(\boldsymbol{F}\boldsymbol{Q}) = \Psi(\boldsymbol{F}). \qquad (2.2.10)$$

For an isotropic material as e.g., steel there are no preferred directions. A crucial consequence of objectivity is that the energy potential only depends on the Cauchy–Green strain tensor.

> **2.2 Theorem.** *A potential $\Psi : \mathbb{R}^{d \times d} \to \mathbb{R}$ is frame-indifferent if and only if it is a function of the Cauchy–Green strain tensor $\boldsymbol{C} = \boldsymbol{F}^\top \boldsymbol{F}$, i.e.,*
>
> $$\Psi(\boldsymbol{F}) = \hat{\Psi}(\boldsymbol{C}). \tag{2.2.11}$$

Proof. See e.g., [58, Chapter VI, Theorem 1.6]. $\qquad\square$

Assuming a frame-indifferent and isotropic potential yields that it is a function of the invariants of the Cauchy–Green strain tensor.

> **2.3 Theorem (Rivlin–Ericksen).** *An energy potential $\Psi : \mathbb{R}^{d \times d} \to \mathbb{R}$ is frame-indifferent and isotropic if and only if there exists a function $\overline{\Psi} : \mathbb{S}_>(d) \to \mathbb{R}$ depending only on the invariants of the characteristic polynomial $\det(\lambda \boldsymbol{I} - \boldsymbol{C}) = \lambda^3 - I_1(\boldsymbol{C})\lambda^2 - I_2(\boldsymbol{C})\lambda - I_3(\boldsymbol{C})$ such that*
>
> $$\Psi(\boldsymbol{F}) = \overline{\Psi}(I_1(\boldsymbol{C}), I_2(\boldsymbol{C}), I_3(\boldsymbol{C})), \tag{2.2.12}$$
>
> *where, with $\mathrm{tr}(\boldsymbol{C})$ and $\det(\boldsymbol{C})$ denoting the trace and determinant of $\boldsymbol{C}$,*
>
> $$I_1(\boldsymbol{C}) = \mathrm{tr}(\boldsymbol{C}), \qquad I_2(\boldsymbol{C}) = \frac{1}{2}\left(\mathrm{tr}(\boldsymbol{C})^2 - \mathrm{tr}(\boldsymbol{C}^2)\right), \qquad I_3(\boldsymbol{C}) = \det(\boldsymbol{C}). \tag{2.2.13}$$

Proof. See e.g., [195]. $\qquad\square$

Throughout this thesis we will consider frame-indifferent potentials and write Ψ independently of arguments $\boldsymbol{F}$, $\boldsymbol{C}$, and $\boldsymbol{E}$.

Using Theorem 2.2, the weak form (2.2.5) can be rewritten as: Find u admissible such that for all $\delta u \in V_0$

$$\int_\Omega 2 \frac{\partial \Psi}{\partial \boldsymbol{C}}(\boldsymbol{C}(u)) : \mathrm{sym}(\boldsymbol{F}\nabla \delta u)\, dx = \int_\Omega f \cdot \delta u\, dx + \int_{\Gamma_N} g \cdot \delta u\, ds, \tag{2.2.14}$$

where we utilized that $\partial_u \boldsymbol{C}(u)(\delta u) = 2\,\mathrm{sym}(\boldsymbol{F}\nabla \delta u)$.

Defining the *second Piola–Kirchhoff stress tensor*

$$\boldsymbol{\Sigma} := 2 \frac{\partial \Psi}{\partial \boldsymbol{C}} \tag{2.2.15}$$

and exploiting the symmetry of $\boldsymbol{\Sigma}$ gives

$$\int_\Omega \boldsymbol{F}\boldsymbol{\Sigma} : \nabla \delta u\, dx = \int_\Omega f \cdot \delta u\, dx + \int_{\Gamma_N} g \cdot \delta u\, ds. \tag{2.2.16}$$

Consequently, we obtain the relation

$$\boldsymbol{P} = \boldsymbol{F}\boldsymbol{\Sigma}. \tag{2.2.17}$$

Note that in contrast to $\boldsymbol{\Sigma}$, $\boldsymbol{P}$ is not symmetric. For the sake of completeness, the (symmetric) *Cauchy stress tensor* $\boldsymbol{\sigma}$ acting on the deformed configuration of the body is introduced by

$$\boldsymbol{\sigma} = \frac{1}{J}\boldsymbol{P}\boldsymbol{F}^\top = \frac{1}{J}\frac{\partial \Psi}{\partial \boldsymbol{F}}\boldsymbol{F}^\top. \tag{2.2.18}$$

The *St. Venant–Kirchhoff* material law

$$\Psi_{\mathrm{VK}}(\boldsymbol{E}) = \hat{\mu}\|\boldsymbol{E}\|_F^2 + \frac{\hat{\lambda}}{2}\mathrm{tr}(\boldsymbol{E})^2 \tag{2.2.19}$$

is widely used to model nonlinear behavior in a moderate deformation regime. It may happen for large deformations, however, that elements get compressed heavily and are even pressed through others. The material law of *Neo–Hooke*

$$\Psi_{\mathrm{NH}}(\boldsymbol{C}) = \frac{\hat{\mu}}{2}\left(\mathrm{tr}(\boldsymbol{C}-\boldsymbol{I}) - \log(\det(\boldsymbol{C}))\right) + \frac{\hat{\lambda}}{8}(\log(\det(\boldsymbol{C})))^2 \tag{2.2.20}$$

prevents this non-physical behavior as there holds

$$\Psi_{\mathrm{NH}}(\boldsymbol{C}) \to \infty \quad \text{for } \det(\boldsymbol{C}) = (\det(\boldsymbol{F}))^2 \to 0 \text{ or } \det(\boldsymbol{C}) \to \infty, \tag{2.2.21}$$

i.e., infinite energy is needed to completely compress or stretch the material. We remark that, especially in the (nearly) incompressible regime, a slightly different material law of Neo–Hooke is also used, namely

$$\tilde{\Psi}_{\mathrm{NH}}(\boldsymbol{C}) = \frac{\hat{\mu}}{2}\left(\mathrm{tr}(\boldsymbol{C}-\boldsymbol{I}) - \log(\det(\boldsymbol{C}))\right) + \frac{\hat{\lambda}}{2}(\sqrt{\det(\boldsymbol{C})} - 1)^2. \tag{2.2.22}$$

The two material constants $\hat{\mu} > 0$ and $\hat{\lambda} > 0$ used above are the so-called Lamé parameters. Two more physically interpretable constants are the Young's modulus $\hat{E} > 0$, representing the stiffness of a solid material, and the Poisson's ratio $0 \leq \hat{\nu} < 1/2$. The latter describes the amount of expansion or contraction in the perpendicular direction to the force compressing or stretching the material. To convert these parameters the following formulae are used

$$\hat{\nu} = \frac{\hat{\lambda}}{2(\hat{\lambda} + \hat{\mu})}, \qquad\qquad \hat{E} = \frac{\hat{\mu}(3\hat{\lambda} + 2\hat{\mu})}{\hat{\lambda} + \hat{\mu}}, \tag{2.2.23a}$$

$$\hat{\lambda} = \frac{\hat{E}\hat{\nu}}{(1+\hat{\nu})(1-2\hat{\nu})}, \qquad\qquad \hat{\mu} = \frac{\hat{E}}{2(1+\hat{\nu})}. \tag{2.2.23b}$$

Note, that in the limit $\hat{\nu} \to \frac{1}{2}$, or equivalently $\hat{\lambda} \to \infty$, the material is called incompressible necessitating special (numerical) treatment.

2.3. Theoretical results of nonlinear elasticity

The question of existence and uniqueness of this (highly nonlinear) equations is delicate [142, 87]. From physical examples it is known that we cannot expect uniqueness. Considering e.g., a rubber strip where both ends are fixed and neglecting gravity the identity
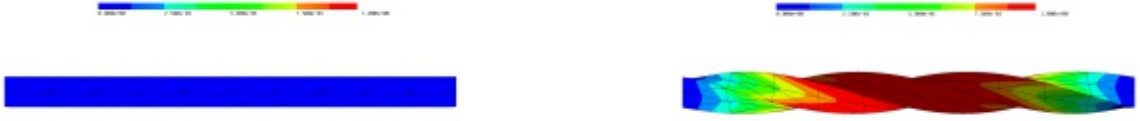
Figure 2.2.: Two solutions of rubber strip clamped on left and right boundary.

is a trivial solution for the displacement. When twisting one of the ends by 2π ($360°$) we obtain a different solution to the same boundary conditions, see Figure 2.2. In this manner we can even produce infinitely many solutions by twisting. Other examples are given e.g., by buckling or snap through problems, where for one external force two different solutions exist (one before and one after the snap through).

For existence one approach exploits, if possible, the polyconvex structure of the energy potential Ψ in its invariants $I_i(\boldsymbol{C})$, compare (2.2.13), proving the existence of minimizers [29]. The material law of St. Venant–Kirchhoff is not polyconvex, but the Neo–Hooke material law falls in this category. A large class of Ogden-type materials fulfills this assumption. Another ansatz uses the implicit function theorem obtaining a unique solution for small data. Therefore, however, strong regularity assumptions have to be made [87].

Only little rigorous mathematical numerical analysis for finite elasticity has been accomplished so far. E.g., in [70] a priori error estimates for finite element discretizations in nonlinear elasticity are discussed for polyconvex materials under the assumption of sufficiently small right-hand sides.

2.4. Linearized elasticity

Under the assumption of small deformations all three stress tensors (2.2.7), (2.2.15), and (2.2.18) reduce to one, which we denote by $\boldsymbol{\sigma}$. Assuming a quadratic potential $\Psi(\cdot)$ we deduce a linear stress-strain relation by $\boldsymbol{\sigma} = \mathbb{C}\boldsymbol{\epsilon}$, where $\mathbb{C}$ denotes the fourth order elasticity tensor. For an isotropic and frame-indifferent material the stress-strain relation is of the form

$$\begin{pmatrix} \boldsymbol{\sigma}_{11} \\ \boldsymbol{\sigma}_{22} \\ \boldsymbol{\sigma}_{33} \\ \boldsymbol{\sigma}_{12} \\ \boldsymbol{\sigma}_{13} \\ \boldsymbol{\sigma}_{23} \end{pmatrix} = \frac{\hat{E}}{(1+\hat{\nu})(1-2\hat{\nu})} \begin{pmatrix} 1-\hat{\nu} & \hat{\nu} & \hat{\nu} & & & \\ \hat{\nu} & 1-\hat{\nu} & \hat{\nu} & & 0 & \\ \hat{\nu} & \hat{\nu} & 1-\hat{\nu} & & & \\ & & & 1-2\hat{\nu} & & \\ & & & & 1-2\hat{\nu} & \\ & 0 & & & & 1-2\hat{\nu} \end{pmatrix} \begin{pmatrix} \boldsymbol{\epsilon}_{11} \\ \boldsymbol{\epsilon}_{22} \\ \boldsymbol{\epsilon}_{33} \\ \boldsymbol{\epsilon}_{12} \\ \boldsymbol{\epsilon}_{13} \\ \boldsymbol{\epsilon}_{23} \end{pmatrix}.$$

$$(2.4.1)$$

For $\hat{\nu} \neq \frac{1}{2}$ relation (2.4.1) can be inverted, $\boldsymbol{\epsilon} = \mathbb{C}^{-1}\boldsymbol{\sigma}$,

$$\begin{pmatrix} \epsilon_{11} \\ \epsilon_{22} \\ \epsilon_{33} \\ \epsilon_{12} \\ \epsilon_{13} \\ \epsilon_{23} \end{pmatrix} = \frac{1}{\hat{E}} \begin{pmatrix} 1 & -\hat{\nu} & -\hat{\nu} & & & \\ -\hat{\nu} & 1 & -\hat{\nu} & & & \\ -\hat{\nu} & -\hat{\nu} & 1 & & & \\ & & & 1+\hat{\nu} & & \\ & & & & 1+\hat{\nu} & \\ & & & & & 1+\hat{\nu} \end{pmatrix} \begin{pmatrix} \sigma_{11} \\ \sigma_{22} \\ \sigma_{33} \\ \sigma_{12} \\ \sigma_{13} \\ \sigma_{23} \end{pmatrix} \tag{2.4.2}$$

and $\mathbb{C}^{-1}$ is called the *compliance tensor*. The strong form of (2.2.8) becomes in the linearized case

$$\begin{cases} -\mathrm{div}(\boldsymbol{\sigma}) = f & \text{in } \Omega, \\ u = u_D & \text{on } \Gamma_D, \\ \boldsymbol{\sigma}n = g & \text{on } \Gamma_N, \end{cases} \tag{2.4.3}$$

and the variational problem (inserting the stress-strain relation) reads: Find $u \in V$ such that for all $\delta u \in V_0$

$$\int_\Omega \mathbb{C}\boldsymbol{\epsilon}(u) : \boldsymbol{\epsilon}(\delta u)\, dx = \int_\Omega f \cdot \delta u\, dx + \int_{\Gamma_N} g \cdot \delta u\, ds. \tag{2.4.4}$$

The material laws of St. Venant–Kirchhoff and Neo–Hooke reduce to the linear material law of Hooke

$$\Psi_{\mathrm{H}}(\boldsymbol{\epsilon}) := \hat{\mu}\|\boldsymbol{\epsilon}\|_F^2 + \frac{\hat{\lambda}}{2}(\mathrm{tr}(\boldsymbol{\epsilon}))^2 \tag{2.4.5}$$

and we obtain the problem: Find u admissible such that for all admissible test functions δu

$$\int_\Omega 2\hat{\mu}\,\boldsymbol{\epsilon}(u) : \boldsymbol{\epsilon}(\delta u) + \hat{\lambda}\,\mathrm{div}(u)\mathrm{div}(\delta u)\, dx = \int_\Omega f \cdot \delta u\, dx + \int_{\Gamma_N} g \cdot \delta u\, ds. \tag{2.4.6}$$

The unique solvability of (2.4.4) is proven in Chapter 4. Note that (2.4.4) and (2.4.6) coincide for $\mathbb{C}$ defined as in (2.4.1). Further, relation (2.4.2) can be written compactly as

$$\boldsymbol{\epsilon} = \frac{1}{\hat{E}}\left((1+\hat{\nu})\boldsymbol{\sigma} - \hat{\nu}\,\mathrm{tr}(\boldsymbol{\sigma})\boldsymbol{I}\right) = \frac{1}{\hat{E}}\left((1+\hat{\nu})\mathrm{dev}(\boldsymbol{\sigma}) + \frac{1-2\hat{\nu}}{2}\mathrm{tr}(\boldsymbol{\sigma})\boldsymbol{I}\right), \tag{2.4.7}$$

where $\mathrm{dev}(\boldsymbol{A})$ denotes the deviatoric part of a matrix. Here, the case $\hat{\nu} = 0.5$ is well-defined leading to the identity $\boldsymbol{\epsilon} = \frac{1+\hat{\nu}}{\hat{E}}\mathrm{dev}(\boldsymbol{\sigma})$, which is unique up to the trace of $\boldsymbol{\sigma}$.

3. Variational framework

In this chapter we introduce and discuss essential properties of Sobolev and function spaces used in this thesis and summarize important inequalities, existence, and uniqueness results for coercive and saddle-point problems.

Therefore, let $\Omega \subset \mathbb{R}^d$, $d = 2, 3$ be an open *Lipschitz domain*, i.e., the boundary $\partial\Omega$ can be described by a finite number of Lipschitz continuous functions. Further, we assume that the boundary is either smooth, $\partial\Omega \in C^\infty$, or piece-wise smooth, i.e., there exists a finite partition $\Gamma_i \in C^\infty$, $i = 1, \ldots, n$, with $\partial\Omega = \bigcup_i \overline{\Gamma}_i$ and $\Gamma_i \cap \Gamma_j = \emptyset$ for $i \neq j$. For a Lipschitz domain there exists an (almost everywhere) defined outer normal vector $n : \partial\Omega \to \mathbb{S}^{d-1}$.

The set of k-times differentiable scalar-, vector-, and matrix-valued functions is denoted by $C^k(\Omega)$, $[C^k(\Omega)]^d$, and $[C^k(\Omega)]^{d \times d}$, respectively. With $\mathcal{D}(\Omega) := C_0^\infty(\Omega)$ the set of all smooth test functions with compact support is denoted and with $\mathcal{D}'(\Omega) := (C_0^\infty(\Omega))'$ the set of all distributions.

3.1. Function spaces

The gradient of a scalar function $u \in C^1(\Omega)$ and vector field $v \in [C^1(\Omega)]^d$ is defined as

$$\nabla u := \left(\frac{\partial u}{\partial x_1}, \ldots, \frac{\partial u}{\partial x_d} \right), \qquad \nabla v = \left(\frac{\partial v_i}{\partial x_j} \right)_{i,j=1}^d. \tag{3.1.1}$$

For a vector field $v \in [C^1(\Omega)]^d$ and a matrix valued function $\boldsymbol{A} \in [C^1(\Omega)]^{d \times d}$ the divergence is given by

$$\mathrm{div}(v) := \sum_{i=1}^d \frac{\partial v_i}{\partial x_i}, \qquad \mathrm{div}(\boldsymbol{A}) := \begin{pmatrix} \sum_{j=1}^d \frac{\partial \boldsymbol{A}_{1j}}{\partial x_j} \\ \vdots \\ \sum_{j=1}^d \frac{\partial \boldsymbol{A}_{dj}}{\partial x_j} \end{pmatrix}. \tag{3.1.2}$$

In two spatial dimensions two different curl-operators exist, namely

$$\mathrm{Curl}(u) := \begin{pmatrix} \frac{\partial u}{\partial x_2} \\ -\frac{\partial u}{\partial x_1} \end{pmatrix}, \qquad \mathrm{curl}(v) := \frac{\partial v_2}{\partial x_1} - \frac{\partial v_1}{\partial x_2}, \tag{3.1.3}$$

whereas in three dimension we use both notations for

$$\mathrm{curl}(v) := \nabla \times v = \left(\frac{\partial v_3}{\partial x_2} - \frac{\partial v_2}{\partial x_3}, \frac{\partial v_1}{\partial x_3} - \frac{\partial v_3}{\partial x_1}, \frac{\partial v_2}{\partial x_1} - \frac{\partial v_1}{\partial x_2} \right)^\top \tag{3.1.4}$$

and for matrix valued functions the curl is taken row-wise.

14

3.1.1. Scalar and vector valued spaces

We define for $u, v : \Omega \to \mathbb{R}^d$ the L^2-scalar product and norm by

$$\langle u, v \rangle_{L^2(\Omega)} := \int_\Omega u \cdot v \, dx, \qquad \qquad \|u\|^2_{L^2(\Omega)} := \langle u, u \rangle_{L^2(\Omega)} \qquad (3.1.5)$$

and call u square-integrable if it has finite L^2-norm, $\|u\|_{L^2(\Omega)} < \infty$. If the domain Ω is obvious it will be neglected for a more compact notation. We define the following Sobolev spaces

$$L^2(\Omega) := \{u : \Omega \to \mathbb{R} \,|\, \|u\|_{L^2} < \infty\}, \qquad (3.1.6a)$$

$$L^2_0(\Omega) := \{u \in L^2(\Omega) \,|\, \int_\Omega u \, dx = 0\}, \qquad (3.1.6b)$$

$$H^1(\Omega) := \{u \in L^2(\Omega) \,|\, \nabla u \in [L^2(\Omega)]^d\}, \qquad (3.1.6c)$$

$$H^k(\Omega) := \{u \in L^2(\Omega) \,|\, \nabla u \in [H^{k-1}(\Omega)]^d\}, \qquad (3.1.6d)$$

$$H(\mathrm{div}, \Omega) := \{u \in [L^2(\Omega)]^d \,|\, \mathrm{div}(u) \in L^2(\Omega)\}, \qquad (3.1.6e)$$

$$H(\mathrm{curl}, \Omega) := \{u \in [L^2(\Omega)]^d \,|\, \mathrm{curl}(u) \in [L^2(\Omega)]^{d^\star}\}, \qquad (3.1.6f)$$

with $d^\star := 2d - 3$ and the differential operators are understood in weak sense. E.g., the weak gradient $v = \nabla u \in [L^2(\Omega)]^d$ of $u \in H^1(\Omega)$ is defined by the relation

$$\int_\Omega v \cdot \Psi \, dx = - \int_\Omega u \, \mathrm{div}(\Psi) \, dx \qquad (3.1.7)$$

for all smooth test functions $\Psi \in [\mathcal{D}(\Omega)]^d$.

The corresponding (semi-) norms to the function spaces (3.1.6) are given by

$$\|u\|^2_{H^1} := \|u\|^2_{L^2} + \|\nabla u\|^2_{L^2}, \qquad (3.1.8a)$$

$$\|u\|^2_{H^k} := \|u\|^2_{L^2} + \|\nabla u\|^2_{H^{k-1}(\Omega)}, \qquad (3.1.8b)$$

$$|u|_{H^k} := \|\nabla^k u\|_{L^2}, \qquad (3.1.8c)$$

$$\|u\|^2_{H(\mathrm{div})} := \|u\|^2_{L^2} + \|\mathrm{div}(u)\|^2_{L^2}, \qquad (3.1.8d)$$

$$\|u\|^2_{H(\mathrm{curl})} := \|u\|^2_{L^2} + \|\mathrm{curl}(u)\|^2_{L^2}. \qquad (3.1.8e)$$

For Lipschitz-domains the function spaces can be defined equivalently [2] by

$$H^1(\Omega) = \overline{C^\infty(\overline{\Omega})}^{\|\cdot\|_{H^1}}, \; H(\mathrm{curl}, \Omega) = \overline{C^\infty(\overline{\Omega})}^{\|\cdot\|_{H(\mathrm{curl})}}, \; H(\mathrm{div}, \Omega) = \overline{C^\infty(\overline{\Omega})}^{\|\cdot\|_{H(\mathrm{div})}}, \quad (3.1.9)$$

where $C^\infty(\overline{\Omega})$ denotes the set of infinitely differentiable functions up to the boundary and $\overline{C^\infty(\overline{\Omega})}^{\|\cdot\|_V}$ denotes the closure with respect to the norm $\|\cdot\|_V$.

Further, we define the trace space of $H^1(\Omega)$ for $\Gamma \subset \partial\Omega$ by

$$H^{\frac{1}{2}}(\Gamma) := \overline{C^\infty(\overline{\Gamma})}^{\|\cdot\|_{H^{\frac{1}{2}}(\Gamma)}}, \quad \|u\|^2_{H^{\frac{1}{2}}(\Gamma)} := \|u\|^2_{L^2(\Gamma)} + \int_\Gamma \int_\Gamma \frac{|u(x) - u(y)|^2}{|x - y|^d} \, ds(x) \, ds(y) \tag{3.1.10}$$

and its dual space $H^{-\frac{1}{2}}(\Gamma) := H^{\frac{1}{2}}(\Gamma)^*$.

In the following we summarize essential properties of the Sobolev spaces, which can be found in several textbooks, e.g., [53, 58]. For the spaces $H^1(\Omega)$, $H(\text{div}, \Omega)$, and $H(\text{curl}, \Omega)$ there exist well-defined trace operators. Let n denote the outer normal vector of $\partial\Omega$. Then, the normal and tangential component of a vector valued function u is given by $u_n := u \cdot n$ and $u_t := u - (u \cdot n)n$, respectively.

3.1 Theorem (Traces). *Let $u \in H^1(\Omega)$, n be the outer normal vector on $\partial\Omega$ and t the tangential vector on $\partial\Omega$ for two dimensions. Then there exists a linear and bounded operator*

$$\text{tr}_\Gamma : H^1(\Omega) \to H^{\frac{1}{2}}(\Gamma), \quad \|\text{tr}_\Gamma(u)\|_{H^{\frac{1}{2}}(\Gamma)} \preceq \|u\|_{H^1} \quad \forall u \in H^1(\Omega) \qquad (3.1.11)$$

such that $(\text{tr}_\Gamma(u))(x) = u(x) \ \forall x \in \Gamma$ for $u \in C^1(\overline{\Omega})$.
Let $u \in H(\text{div}, \Omega)$. Then there exists a linear and bounded operator

$$\text{tr}_{n,\Gamma} : H(\text{div}, \Omega) \to H^{-\frac{1}{2}}(\Gamma), \|\text{tr}_{n,\Gamma}(u)\|_{H^{-\frac{1}{2}}} \preceq \|u\|_{H(\text{div})} \quad \forall u \in H(\text{div}, \Omega) \quad (3.1.12)$$

such that $(\text{tr}_{n,\Gamma}(u))(x) = u(x) \cdot n(x) \ \forall x \in \Gamma$ for $u \in [C^1(\overline{\Omega})]^d$.
Let $u \in H(\text{curl}, \Omega)$. Then there exists a linear and bounded operator

$$\text{tr}_{t,\Gamma} : H(\text{curl}, \Omega) \to [H^{-\frac{1}{2}}(\Gamma)]^{d^\star}, \|\text{tr}_{t,\Gamma}(u)\|_{H^{-\frac{1}{2}}} \preceq \|u\|_{H(\text{curl})} \forall u \in H(\text{curl}, \Omega) \ (3.1.13)$$

such that $(\text{tr}_{t,\Gamma}(u))(x) = u(x) \cdot t(x)$ if $d = 2$ and $(\text{tr}_{t,\Gamma}(u))(x) = u(x) \times n(x)$ if $d = 3$ $\forall x \in \Gamma$ for $u \in [C^1(\overline{\Omega})]^d$.

Therefore, the following spaces with zero traces on $\Gamma \subset \partial\Omega$ can be defined by

$$H^1_\Gamma(\Omega) := \{u \in H^1(\Omega) \,|\, \text{tr}_\Gamma(u) = 0\}, \qquad (3.1.14a)$$
$$H_\Gamma(\text{div}, \Omega) := \{u \in H(\text{div}, \Omega) \,|\, \text{tr}_{n,\Gamma}(u) = 0\}, \qquad (3.1.14b)$$
$$H_\Gamma(\text{curl}, \Omega) := \{u \in H(\text{curl}, \Omega) \,|\, \text{tr}_{t,\Gamma}(u) = 0\}. \qquad (3.1.14c)$$

For $\Gamma = \partial\Omega$ we will use the notations $H^1_0(\Omega)$, $H_0(\text{div}, \Omega)$, and $H_0(\text{curl}, \Omega)$.

Additionally to $H^{-\frac{1}{2}}(\Gamma)$ we will use the dual spaces $H^{-1}(\Omega) := H^1_0(\Omega)^*$, $H(\text{div}, \Omega)^*$, and $H(\text{curl}, \Omega)^*$. The corresponding norms are defined as follows: For a Hilbert space V and its topological dual space V^* the dual norm for $f \in V^*$ is given by

$$\|f\|_{V^*} := \sup_{\substack{u \in V \\ u \neq 0}} \frac{\langle f, u\rangle_{V^* \times V}}{\|v\|_V}, \qquad\qquad \langle f, u\rangle_{V^* \times V} := f(u). \qquad (3.1.15)$$

The dual space of $H_0(\text{curl})$ and $H_0(\text{div})$ is given by $H^{-1}(\text{div})$ [171, Lemma 1] and $H^{-1}(\text{curl})$ [143, Lemma 1],

$$H_0(\text{curl})^* = H^{-1}(\text{div}) := \{u \in [H^{-1}(\Omega)]^d \,|\, \text{div}(u) \in H^{-1}(\Omega)\}, \qquad (3.1.16)$$
$$H_0(\text{div})^* = H^{-1}(\text{curl}) := \{u \in [H^{-1}(\Omega)]^d \,|\, \text{curl}(u) \in [H^{-1}(\Omega)]^{d^\star}\}, \qquad (3.1.17)$$

where the differential operators are understood in the sense of distributions.

Having well-defined traces at hand enables integration by parts:

3.2 Theorem (Green's formulae). *There holds for all $u \in H^1(\Omega)$ and $v \in H(\mathrm{div}, \Omega)$*

$$\int_\Omega \nabla u \cdot v \, dx = -\int_\Omega u \, \mathrm{div}(v) \, dx + \langle \mathrm{tr}_{n,\partial\Omega}(v), \mathrm{tr}_{\partial\Omega}(u) \rangle_{H^{-\frac{1}{2}} \times H^{\frac{1}{2}}} \qquad (3.1.18)$$

and for all $u \in H(\mathrm{curl}, \Omega)$ and $v \in [H^1(\Omega)]^{d^\star}$

$$\int_\Omega \mathrm{curl}(u) \cdot v \, dx = \int_\Omega u \cdot \mathrm{Curl}(v) \, dx - \langle \mathrm{tr}_{t,\partial\Omega}(u), \mathrm{tr}_{\partial\Omega}(v) \rangle_{H^{-\frac{1}{2}} \times H^{\frac{1}{2}}}. \qquad (3.1.19)$$

As we will construct finite element spaces element-wise the question arises which interface conditions have to be fulfilled such that we obtain a global function in the above spaces.

3.3 Theorem (Interface conditions). *Let $\mathcal{T} = \{T_1, \ldots, T_n\}$ be a non-overlapping domain decomposition of Ω, i.e., $T_i \cap T_j = \emptyset$ for $i \neq j$ and $\overline{\Omega} = \bigcup_i \overline{T_i}$. Define $\Gamma_{ij} := \overline{T_i} \cap \overline{T_j}$ the common interface of two neighboring sub-domains $T_i, T_j \in \mathcal{T}$. Let u, v, ξ be defined piece-wise for each T_i such that $u_i = u|_{T_i} \in H^1(T_i)$, $v_i = v|_{T_i} \in H(\mathrm{div}, T_i)$, and $\xi_i = \xi|_{T_i} \in H(\mathrm{curl}, T_i)$, respectively. If for all $i, j \in \{1, \ldots, n\}$*

- $\mathrm{tr}_{\Gamma_{ij}}(u_i) = \mathrm{tr}_{\Gamma_{ij}}(u_j)$ *then $u \in H^1(\Omega)$ and $(\nabla u)|_{T_i} = \nabla u_i$.*

- $\mathrm{tr}_{n,\Gamma_{ij}}(v_i) = \mathrm{tr}_{n,\Gamma_{ij}}(v_j)$ *then $v \in H(\mathrm{div}, \Omega)$ and $\mathrm{div}(v)|_{T_i} = \mathrm{div}(v_i)$.*

- $\mathrm{tr}_{t,\Gamma_{ij}}(\xi_i) = \mathrm{tr}_{t,\Gamma_{ij}}(\xi_j)$ *then $\xi \in H(\mathrm{curl}, \Omega)$ and $\mathrm{curl}(\xi)|_{T_i} = \mathrm{curl}(\xi_i)$.*

3.1.2. Matrix valued spaces

To introduce (less common) matrix valued function spaces we start with the set of all symmetric and skew-symmetric matrices in L^2 denoted by $[L^2(\Omega)]^{d \times d}_{\mathrm{sym}}$ and $[L^2(\Omega)]^{d \times d}_{\mathrm{skw}}$, respectively. Next, we define the following matrix valued function spaces

$$H^{\mathrm{sym}}(\mathrm{div}, \Omega) := \{\boldsymbol{\sigma} \in [L^2(\Omega)]^{d \times d}_{\mathrm{sym}} \,|\, \mathrm{div}(\boldsymbol{\sigma}) \in [L^2(\Omega)]^d\}, \qquad (3.1.20)$$

$$H(\mathrm{div\,div}, \Omega) := \{\boldsymbol{\sigma} \in [L^2(\Omega)]^{d \times d}_{\mathrm{sym}} \,|\, \mathrm{div}(\mathrm{div}(\boldsymbol{\sigma})) \in H^{-1}(\Omega)\}, \qquad (3.1.21)$$

$$H(\mathrm{curl\,curl}, \Omega) := \{\boldsymbol{\sigma} \in [L^2(\Omega)]^{d \times d}_{\mathrm{sym}} \,|\, \mathrm{curl}(\mathrm{curl}(\boldsymbol{\sigma})^\top) \in [H^{-1}(\Omega)]^{d^\star \times d^\star}\}, \qquad (3.1.22)$$

with the norms

$$\|\boldsymbol{\sigma}\|^2_{H^{\mathrm{sym}}(\mathrm{div})} := \|\boldsymbol{\sigma}\|^2_{L^2} + \|\mathrm{div}(\boldsymbol{\sigma})\|^2_{L^2}, \qquad (3.1.23)$$

$$\|\boldsymbol{\sigma}\|^2_{H(\mathrm{div\,div})} := \|\boldsymbol{\sigma}\|^2_{L^2} + \|\mathrm{div}(\mathrm{div}(\boldsymbol{\sigma}))\|^2_{H^{-1}}, \qquad (3.1.24)$$

$$\|\boldsymbol{\sigma}\|^2_{H(\mathrm{curl\,curl})} := \|\boldsymbol{\sigma}\|^2_{L^2} + \|\mathrm{curl}(\mathrm{curl}(\boldsymbol{\sigma})^\top)\|^2_{H^{-1}}. \qquad (3.1.25)$$

Note that $\mathrm{curl}(\mathrm{curl}(\boldsymbol{\sigma})^\top)$ is the incompatibility operator also denoted by $\mathrm{Inc}(\boldsymbol{\sigma}) := \mathrm{curl}^\top \mathrm{curl}(\boldsymbol{\sigma}) := \mathrm{curl}(\mathrm{curl}(\boldsymbol{\sigma})^\top)$.

An equivalent characterization of the spaces $H(\mathrm{div}\,\mathrm{div})$ and $H(\mathrm{curl}\,\mathrm{curl})$ are given by [211],

$$H(\mathrm{div}\,\mathrm{div},\Omega) = \{\boldsymbol{\sigma} \in [L^2(\Omega)]_{\mathrm{sym}}^{d\times d} \,|\, \mathrm{div}(\boldsymbol{\sigma}) \in H(\mathrm{curl})^*\}, \tag{3.1.26a}$$

$$H(\mathrm{curl}\,\mathrm{curl},\Omega) = \{\boldsymbol{\sigma} \in [L^2(\Omega)]_{\mathrm{sym}}^{d\times d} \,|\, \mathrm{curl}(\boldsymbol{\sigma})^\top \in [H(\mathrm{div})^*]^{d^\star}\}. \tag{3.1.26b}$$

Other definitions of $H(\mathrm{div}\,\mathrm{div})$ **and** $H(\mathrm{curl}\,\mathrm{curl})$**:** A different definition of the space $H(\mathrm{div}\,\mathrm{div})$ was given in [182] in the context of densely defined operators for solving the biharmonic plate equation

$$H(\mathrm{div}\,\mathrm{div},\Omega;Q^*)_{\mathrm{sym}} := \{\boldsymbol{\sigma} \in [L^2(\Omega)]_{\mathrm{sym}}^{d\times d} \,|\, \text{ the functional } F : u \mapsto \int_\Omega \nabla^2 u : \boldsymbol{\sigma}\,dx,\ u \in W,$$
$$\text{is bounded in the } Q\text{-norm}\}, \tag{3.1.27}$$

where with $\Gamma_1, \Gamma_2 \subset \partial\Omega$

$$W := \{u \in H^2(\Omega) \,|\, u = 0, \frac{\partial u}{\partial n} = 0 \text{ on } \Gamma_1,\ u = 0 \text{ on } \Gamma_2\},$$
$$Q := \{u \in H^1(\Omega) \,|\, u = 0 \text{ on } \Gamma_1 \cup \Gamma_2\}, \quad \|\cdot\|_Q := \|\cdot\|_{H^1},$$

together with the norm

$$\|\boldsymbol{\sigma}\|_{\mathrm{divdiv};Q^*}^2 := \|\boldsymbol{\sigma}\|_{L^2}^2 + \|\mathrm{div}(\mathrm{div}(\boldsymbol{\sigma}))\|_{Q^*}^2.$$

Equality of definitions (3.1.21) and (3.1.27) holds if $\Gamma_1 = \partial\Omega$ and thus $Q = H_0^1(\Omega)$. In [80, 81] (3.1.21) and (3.1.22) are denoted by $H^{-1}(\mathrm{div}\,\mathrm{div})$ and $H^{-1}(\mathrm{curl}\,\mathrm{curl})$. Therein the authors define the spaces

$$H(\mathrm{div}\,\mathrm{div},\Omega;L^2) := \{\boldsymbol{\sigma} \in [L^2(\Omega)]_{\mathrm{sym}}^{d\times d} \,|\, \mathrm{div}(\mathrm{div}(\boldsymbol{\sigma})) \in L^2(\Omega)\}, \tag{3.1.28}$$

$$H(\mathrm{curl}\,\mathrm{curl},\Omega;L^2) := \{\boldsymbol{\sigma} \in [L^2(\Omega)]_{\mathrm{sym}}^{d\times d} \,|\, \mathrm{curl}(\mathrm{curl}(\boldsymbol{\sigma})^\top) \in [L^2(\Omega)]^{d^\star\times d^\star}\}, \tag{3.1.29}$$

where more regularity is required.

Traces, Green's formulae and interface conditions: Note, that the divergence and curl operator are taken row-wise for matrix valued functions. As before, trace operators, Green's identities, and interface conditions can be specified and thus, spaces with zero traces can be defined analogously. The space $H^{\mathrm{sym}}(\mathrm{div})$ requires the square-integrability of the divergence and thus, has a well-defined (vector-valued) normal trace. The other two spaces are more involved. We only note that for $H(\mathrm{div}\,\mathrm{div})$ and $H(\mathrm{curl}\,\mathrm{curl})$ the normal-normal $\boldsymbol{\sigma}_{nn} := n^\top\boldsymbol{\sigma}n$, and tangential-tangential, $\boldsymbol{\sigma}_{tt} := (\boldsymbol{I} - \boldsymbol{P}_n)\boldsymbol{\sigma}(\boldsymbol{I} - \boldsymbol{P}_n)$ with the normal projection $\boldsymbol{P}_n := n \otimes n$, traces, respectively, are well-defined. Further, the interface conditions are a bit more complicated. For more details we refer to [211, 174]. The results for $H(\mathrm{curl}\,\mathrm{curl})$ are topic of further research.

Thus, we can define spaces with zero traces

$$H_{\Gamma_N}(\mathrm{div}\,\mathrm{div}) := \{\boldsymbol{\sigma} \in [L^2(\Omega)]_{\mathrm{sym}}^{d\times d} \,|\, \mathrm{div}(\mathrm{div}(\boldsymbol{\sigma})) \in H_{\Gamma_D}^{-1}(\Omega),\ \mathrm{tr}_{nn,\Gamma_N}(\boldsymbol{\sigma}) = 0\}, \tag{3.1.30a}$$

$$H_{\Gamma_N}(\mathrm{curl}\,\mathrm{curl}) := \{\boldsymbol{\sigma} \in [L^2(\Omega)]_{\mathrm{sym}}^{d\times d} \,|\, \mathrm{curl}(\mathrm{curl}(\boldsymbol{\sigma})^\top) \in [H_{\Gamma_D}^{-1}(\Omega)]^{d^\star\times d^\star},\ \mathrm{tr}_{tt,\Gamma_N}(\boldsymbol{\sigma}) = 0\}. \tag{3.1.30b}$$

For the sake of completeness of matrix-valued function spaces in the spirit of $H(\operatorname{div}\operatorname{div})$ and $H(\operatorname{curl}\operatorname{curl})$ we give also the definition of the space $H(\operatorname{curl}\operatorname{div})$, used e.g., for the incompressible Stokes equations as stress space in combination with $H(\operatorname{div})$-conforming velocity fields, with corresponding norm

$$H(\operatorname{curl}\operatorname{div},\Omega) := \{\boldsymbol{\sigma} \in [L^2(\Omega)]^{d\times d} \,|\, \operatorname{curl}(\operatorname{div}(\boldsymbol{\sigma})) \in [H^{-1}(\Omega)]^{d^\star}\}$$
$$= \{\boldsymbol{\sigma} \in [L^2(\Omega)]^{d\times d} \,|\, \operatorname{div}(\boldsymbol{\sigma}) \in H(\operatorname{div},\Omega)^*\},$$
$$\|\boldsymbol{\sigma}\|^2_{H(\operatorname{curl}\operatorname{div})} := \|\boldsymbol{\sigma}\|^2_{L^2} + \|\operatorname{curl}(\operatorname{div}(\boldsymbol{\sigma}))\|^2_{H^{-1}}.$$

Note that the normal-tangential trace, $\boldsymbol{\sigma}_{nt} := (\boldsymbol{I} - \boldsymbol{P}_n)\boldsymbol{\sigma}n$, is well-defined, we refer for more details to [143, 108].

3.2. Inequalities

We state some useful inequalities, which can be found in the literature. Friedrichs' inequality asserts that the full norm can be controlled by its corresponding semi-norm if all traces vanish on a non-trivial part on the boundary.

3.4 Lemma (Friedrichs' inequality). *Let Ω be a connected and bounded Lipschitz domain and assume that $\Gamma_D \subset \partial\Omega$ has positive measure. For $k \in \mathbb{N}$ there exists a constant $c_F > 0$ such that for all $u \in H^k_{\Gamma_D}(\Omega)$*

$$\|u\|_{H^k} \le c_F |u|_{H^k}, \tag{3.2.1}$$

and c_F depends only on Ω, Γ_D and k.

Poincarè's inequality can be used to control the H^1-norm by its semi-norm and the mean value if no boundary conditions are prescribed.

3.5 Lemma (Poincarè's inequality). *Let Ω be a connected and bounded Lipschitz domain. There exists a constant $c_P > 0$ depending only on Ω such that for all $u \in H^1(\Omega)$*

$$\|u\|^2_{H^1} \le c_P^2 \left(|u|^2_{H^1} + \left(\int_\Omega u\,dx \right)^2 \right). \tag{3.2.2}$$

Surprisingly, the full gradient of a vector valued function can be bounded by its symmetric part, cf. [96], at the cost of possibly large constants for anisotropic domains.

3.6 Lemma (Korn's inequality). *Let Ω be a connected and bounded Lipschitz domain. Then there exists a constant $\hat{c}_K > 0$ such that*

$$\hat{c}_K^2 \|u\|^2_{H^1} \le \|u\|^2_{L^2} + \|\boldsymbol{\epsilon}(u)\|^2_{L^2} \tag{3.2.3}$$

for all $u \in [H^1(\Omega)]^d$ and $\hat{c}_K$ depends only on Ω. Assume further that $\Gamma_D \subset \partial\Omega$ has

positive measure. Then there exists a constant $c_K > 0$ such that

$$c_K^2 \|u\|_{H^1}^2 \leq \|\epsilon(u)\|_{L^2}^2 \tag{3.2.4}$$

for all $u \in [H_{\Gamma_D}^1(\Omega)]^d$. The constants $\hat{c}_K$ and c_K tend to zero for deteriorating aspect ratio.

3.3. Existence and uniqueness for variational problems

For linear variational problems frameworks (depending on the problem structure) for proving existence and uniqueness have been developed, which can be found in several finite element textbooks e.g., [53, 58]. Let therefore $(V, \|\cdot\|_V)$ and $(Q, \|\cdot\|_Q)$ be two Hilbert spaces equipped with their natural norms.

Definition 3.1. A bilinear form $a : V \times Q \to \mathbb{R}$ is called

1. *continuous* (or *bounded*) if there exists $\alpha > 0$ such that for all $u \in V$ and $p \in Q$

$$|a(u, p)| \leq \alpha \|u\|_V \|p\|_Q,$$

2. *coercive* (or *elliptic*) if $V = Q$ and there exists $\beta > 0$ such that for all $u \in V$

$$a(u, u) \geq \beta \|u\|_V^2$$

3. *non-negative* if $V = Q$ and for all $u \in V$

$$a(u, u) \geq 0$$

The existence and uniqueness for elliptic problems of the form: Find $u \in V$ such that for all $\delta u \in V$

$$a(u, \delta u) = f(\delta u) \tag{3.3.1}$$

follows directly by Lax–Milgram.

3.7 Theorem (Lax–Milgram). *Let $a(\cdot, \cdot) : V \times V \to \mathbb{R}$ be a continuous and elliptic bilinear form. Then, for all $f \in V^*$ there exists a unique solution $u \in V$ of* (3.3.1) *and there holds the stability estimate (with β as in Definition 3.1)*

$$\|u\|_V \leq \frac{1}{\beta} \|f\|_{V^*}. \tag{3.3.2}$$

Indefinite saddle-point problems, arising e.g., for minimization problems under constrains, are of the following form: Find $(u, p) \in V \times Q$ such that for all $(\delta u, \delta p) \in V \times Q$

$$a(u, \delta u) + b(\delta u, p) = f(\delta u), \tag{3.3.3a}$$
$$b(u, \delta p) \qquad\qquad = g(\delta p). \tag{3.3.3b}$$

Equation (3.3.3b) enforces a constraint on u, which can be incorporated as a penalty formulation yielding the structure ($t > 0$ large)

$$a(u, \delta u) + b(\delta u, p) = f(\delta u), \tag{3.3.4a}$$

$$b(u, \delta p) - \frac{1}{t}c(p, \delta p) = g(\delta p). \tag{3.3.4b}$$

To prove existence and uniqueness of those type of saddle-point problems the following theorems are used involving the famous Ladyzhenskaya–Babuška–Brezzi (LBB) condition [141, 24, 61].

3.8 Theorem (Brezzi). *Assume that $a(\cdot, \cdot) : V \times V \to \mathbb{R}$ and $b(\cdot, \cdot) : V \times Q \to \mathbb{R}$ are continuous bilinear forms, i.e.,*

$$|a(u, v)| \leq \alpha_2 \|u\|_V \|v\|_V \quad \forall u, v \in V, \tag{3.3.5}$$

$$|b(u, q)| \leq \beta_2 \|u\|_V \|q\|_Q \quad \forall u \in V, \forall q \in Q. \tag{3.3.6}$$

Assume there holds coercivity of $a(\cdot, \cdot)$ on the kernel, i.e.,

$$a(u, u) \geq \alpha_1 \|u\|_V^2 \quad \forall u \in V_0, \tag{3.3.7}$$

$$V_0 := \{u \in V \mid b(u, q) = 0 \quad \forall q \in Q\} \tag{3.3.8}$$

and there holds the LBB condition

$$\sup_{u \in V} \frac{b(u, q)}{\|u\|_V} \geq \beta_1 \|q\|_Q \quad \forall q \in Q. \tag{3.3.9}$$

Then, the mixed problem (3.3.3) is uniquely solvable. The solution fulfills the stability estimate

$$\|u\|_V + \|q\|_Q \leq c \left(\|f\|_{V^*} + \|g\|_{Q^*} \right) \tag{3.3.10}$$

with the constant c depending on $\alpha_1, \alpha_2, \beta_1$, and β_2.

3.9 Theorem (extended Brezzi). *Assume all requirements of Theorem 3.8 are fulfilled. Further, let $c(\cdot, \cdot)$ be a continuous and non-negative bilinear form and $a(\cdot, \cdot)$ non-negative. Then, for $t \geq 1$, the mixed problem (3.3.4) has a unique solution, fulfilling the following stability estimate independent of t*

$$\|u\|_V + \|q\|_Q \leq c \left(\|f\|_{V^*} + \|g\|_{Q^*} \right), \qquad c \neq c(t). \tag{3.3.11}$$

---

4. Standard and mixed methods for linear elasticity

In this section we give an overview of (mixed) formulations of linear elasticity. For the ease of presentation we assume homogeneous Dirichlet boundary condition $u = 0$ on the whole boundary $\Gamma_D = \partial\Omega$ throughout the section. Note, that the case of inhomogeneous Dirichlet data and mixed boundary conditions can easily be adopted.

4.1. Standard primal setting

In the primal setting of (2.4.4) the Sobolev space $[H_0^1(\Omega)]^d$ is used for the displacement u and the following bilinear form and right-hand side are defined

$$a(u, \delta u) := \int_\Omega 2\hat{\mu}\,\boldsymbol{\epsilon}(u) : \boldsymbol{\epsilon}(\delta u) + \hat{\lambda}\,\mathrm{div}(u)\mathrm{div}(\delta u)\,dx = \int_\Omega \mathbb{C}\boldsymbol{\epsilon}(u) : \boldsymbol{\epsilon}(\delta u)\,dx, \qquad (4.1.1a)$$

$$f(\delta u) := \int_\Omega f \cdot \delta u\,dx. \qquad (4.1.1b)$$

To prove coercivity of (4.1.1a) we use Korn's inequality to control the whole gradient by its symmetric part. Note that the constant c_K^2 tends to zero for anisotropic domains. We obtain coercivity and continuity of the bilinear form and continuity of the right-hand side

$$|a(u, \delta u)| \leq (2\hat{\mu} + \hat{\lambda})\|u\|_{H^1}\|\delta u\|_{H^1}, \qquad (4.1.2a)$$

$$a(u, u) \geq 2\hat{\mu}\,c_K\|u\|_{H^1}^2, \qquad (4.1.2b)$$

$$|f(\delta u)| \leq \|f\|_{H^{-1}}\|\delta u\|_{H^1}. \qquad (4.1.2c)$$

Thus, with Lax–Milgram, Theorem 3.7, we obtain a unique solution. However, the problem is ill-conditioned for $\hat{\lambda} \to \infty$ or $c_K \to 0$ as these parameters are involved in the continuity and coercivity constants.

To obtain a robust formulations for nearly incompressible materials like rubber we can introduce the pressure

$$p := \hat{\lambda}\,\mathrm{div}(u) \qquad (4.1.3)$$

as additional unknown leading the following saddle point problem:

4.1 Problem. *Find $(u, p) \in [H_0^1(\Omega)]^d \times L_0^2(\Omega)$ such that for all $(\delta u, \delta p) \in [H_0^1(\Omega)]^d \times$*

$L_0^2(\Omega)$

$$\int_\Omega 2\hat{\mu}\,\boldsymbol{\epsilon}(u) : \boldsymbol{\epsilon}(\delta u)\,dx + \int_\Omega \operatorname{div}(\delta u)p\,dx = \int_\Omega f \cdot \delta u\,dx, \qquad (4.1.4\text{a})$$

$$\int_\Omega \operatorname{div}(u)\delta p\,dx \qquad -\frac{1}{\hat{\lambda}}\int_\Omega p\,\delta p\,dx \quad = 0. \qquad (4.1.4\text{b})$$

Due to the (extended) Brezzi Theorem 3.9 the solution of (4.1.4) is robust in $\hat{\lambda}$, for $\hat{\lambda} \geq 1$. Now, also the limit case $\hat{\lambda} \to \infty$ is well-defined leading to a Stokes type problem. Thus, one has to use Stokes stable finite elements for discretization. Note, that we have to use $L_0^2(\Omega)$ for the pressure space as Dirichlet data are prescribed on the whole boundary. If $|\overline{\Gamma_D}| < |\partial\Omega|$ the space $L^2(\Omega)$ has to be used instead.

4.2. Hellinger–Reissner mixed methods

The concept of including the stresses additionally to displacements goes back to [115, 180, 192]. Using more variables enables to shift regularity assumptions between the involved spaces. The resulting saddle-point problems are more complicated to analyze but more robust methods can be constructed.

4.2.1. Primal mixed method

Assuming a regular elasticity tensor $\mathbb{C}$ one may invert the stress-strain relation $\boldsymbol{\sigma} = \mathbb{C}\boldsymbol{\epsilon}$, i.e.,

$$\boldsymbol{\sigma} = \mathbb{C}\boldsymbol{\epsilon} = 2\hat{\mu}\boldsymbol{\epsilon}(u) + \hat{\lambda}\operatorname{tr}(\boldsymbol{\epsilon})\boldsymbol{I}, \quad \boldsymbol{\epsilon}(u) = \mathbb{C}^{-1}\boldsymbol{\sigma} = \frac{1}{2\hat{\mu}}\operatorname{dev}(\boldsymbol{\sigma}) + \frac{1}{d(d\,\hat{\lambda} + 2\hat{\mu})}\operatorname{tr}(\boldsymbol{\sigma})\boldsymbol{I}, \quad (4.2.1)$$

with $\operatorname{dev}(\boldsymbol{\sigma}) := \boldsymbol{\sigma} - \frac{\operatorname{tr}(\boldsymbol{\sigma})}{d}\boldsymbol{I}$ the deviatoric part of a matrix. Using (4.2.1) as an additional equation with $\boldsymbol{\sigma}$ as new unknown yields:

4.2 Problem. *Find $(\boldsymbol{\sigma}, u) \in V \times Q$ such that for all $(\delta\boldsymbol{\sigma}, \delta u) \in V \times Q$*

$$\int_\Omega \mathbb{C}^{-1}\boldsymbol{\sigma} : \delta\boldsymbol{\sigma}\,dx - \int_\Omega \boldsymbol{\epsilon}(u) : \delta\boldsymbol{\sigma}\,dx = 0, \qquad (4.2.2\text{a})$$

$$-\int_\Omega \boldsymbol{\sigma} : \boldsymbol{\epsilon}(\delta u)\,dx \qquad\qquad = -\int_\Omega f \cdot \delta u\,dx. \qquad (4.2.2\text{b})$$

Choosing $V := [L^2(\Omega)]_{\mathrm{sym}}^{d \times d}$ and $Q := [H_0^1(\Omega)]^d$ leads a well-defined problem.

Proof. Defining

$$a : V \times V \to \mathbb{R}, \qquad a(\boldsymbol{\sigma}, \delta\boldsymbol{\sigma}) := \int_\Omega \mathbb{C}^{-1}\boldsymbol{\sigma} : \delta\boldsymbol{\sigma}\,dx,$$

$$b : V \times Q \to \mathbb{R}, \qquad b(\boldsymbol{\sigma}, \delta u) := \int_\Omega \boldsymbol{\epsilon}(\delta u) : \boldsymbol{\sigma}\,dx,$$

the continuity of $b(\cdot, \cdot)$ as well as coercivity and continuity of $a(\cdot, \cdot)$ are obvious. The LBB condition follows immediately by choosing for given $u \in H_0^1(\Omega)$ $\boldsymbol{\sigma} := \boldsymbol{\epsilon}(u) \in [L^2(\Omega)]_{\text{sym}}^{d \times d}$, yielding

$$\sup_{\boldsymbol{\sigma} \in [L^2(\Omega)]_{\text{sym}}^{d \times d}} \frac{b(\boldsymbol{\sigma}, u)}{\|\boldsymbol{\sigma}\|_{L^2}} \geq \|\boldsymbol{\epsilon}(u)\|_{L^2} \geq c_K \|u\|_{H^1}.$$

Thus, Theorem 3.8 can be applied. $\qquad\square$

Due to Korn's inequality we expect problems for $c_K \to 0$. To obtain a robust formulation for $\hat{\lambda} \to \infty$ the pressure p as in (4.1.4) can be introduced.

4.2.2. Dual mixed method

Integration by parts in (4.2.2) gives the variational equation:

4.3 Problem. *Find $(\boldsymbol{\sigma}, u) \in V \times Q$ such that for all $(\delta\boldsymbol{\sigma}, \delta u) \in V \times Q$*

$$\int_\Omega \mathbb{C}^{-1} \boldsymbol{\sigma} : \delta\boldsymbol{\sigma} \, dx + \int_\Omega u \cdot \text{div}(\delta\boldsymbol{\sigma}) \, dx = 0, \qquad (4.2.3\text{a})$$

$$\int_\Omega \text{div}(\boldsymbol{\sigma}) \cdot \delta u \, dx \qquad\qquad = -\int_\Omega f \cdot \delta u \, dx. \qquad (4.2.3\text{b})$$

This time $V := H^{\text{sym}}(\text{div}, \Omega)$ and $Q := [L^2(\Omega)]^d$ can be chosen, see e.g., [58]. Thus, the displacement u is discontinuous, whereas $\boldsymbol{\sigma}$ has a well-defined divergence operator. Note, that in the case of pure Dirichlet boundary conditions the stress space has to be adapted to $\tilde{H}^{\text{sym}}(\text{div}, \Omega) := \{\boldsymbol{\sigma} \in H^{\text{sym}}(\text{div}, \Omega) \,|\, \text{tr}(\boldsymbol{\sigma}) = 0\}$ as by taking the trace of the first equation in (4.2.1) we have

$$\int_\Omega \text{tr}(\boldsymbol{\sigma}) \, dx = (2\hat{\mu} + d\hat{\lambda}) \int_\Omega \text{tr}(\boldsymbol{\epsilon}) \, dx = (2\hat{\mu} + d\hat{\lambda}) \int_\Omega \text{div}(u) \, dx = (2\hat{\mu} + d\hat{\lambda}) \int_{\partial\Omega} u_n \, ds = 0.$$

One can prove [14] that on the kernel $V_0 = \{\boldsymbol{\sigma} \in H^{\text{sym}}(\text{div}, \Omega) \,|\, \int_\Omega \text{div}(\boldsymbol{\sigma}) \cdot u \, dx = 0 \quad \forall u \in [L^2(\Omega)]^d\}$ the bilinear form $a(\cdot, \cdot)$ is coercive independently of $\hat{\lambda}$ enabling a robust method for $\hat{\lambda} \to \infty$. For the (non-trivial) construction of conforming finite elements for $H^{\text{sym}}(\text{div}, \Omega)$ fulfilling the discrete kernel coercivity for Problem 4.3 we refer to [9, 3, 20], where quite high polynomial orders have to be used.

4.2.3. Dual mixed method with weak symmetry

Due to the difficulty of constructing finite elements for Problem 4.3 the symmetry of $H^{\text{sym}}(\text{div}, \Omega)$ can be broken and reinforced in weak sense [13, 215, 15] leading to:

4.4 Problem. *Find $(\boldsymbol{\sigma}, u, \boldsymbol{\omega}) \in [H(\text{div}, \Omega)]^d \times [L^2(\Omega)]^d \times [L^2(\Omega)]_{\text{skw}}^{d \times d}$ such that for all*

$$(\delta\boldsymbol{\sigma}, \delta u, \delta\boldsymbol{\omega}) \in [H(\mathrm{div}, \Omega)]^d \times [L^2(\Omega)]^d \times [L^2(\Omega)]^{d\times d}_{\mathrm{skw}}$$

$$\int_\Omega \mathbb{C}^{-1}\boldsymbol{\sigma} : \delta\boldsymbol{\sigma}\, dx + \int_\Omega u \cdot \mathrm{div}(\delta\boldsymbol{\sigma})\, dx + \int_\Omega \boldsymbol{\omega} : \delta\boldsymbol{\sigma}\, dx = 0, \tag{4.2.4a}$$

$$\int_\Omega \mathrm{div}(\boldsymbol{\sigma}) \cdot \delta u\, dx = -\int_\Omega f \cdot \delta u\, dx, \tag{4.2.4b}$$

$$\int_\Omega \boldsymbol{\sigma} : \delta\boldsymbol{\omega}\, dx = 0. \tag{4.2.4c}$$

Existence and uniqueness follows directly as the problem is equivalent to (4.2.3). In this setting comparably simple elements can be constructed as e.g., the PEERS (plane elasticity element with reduced symmetry) element [13].

4.3. TDNNS mixed method

Depending on how the term $\int_\Omega \mathrm{div}(\boldsymbol{\sigma}) \cdot u\, dx$ is interpreted, different regularity assumptions have to be made. In (4.2.3) the term is interpreted as L^2-inner product, whereas in (4.2.2) in the sense of the duality pairing $\langle \mathrm{div}(\boldsymbol{\sigma}), u\rangle_{H^{-1}\times H^1}$. A third approach is to use the duality pairing $\langle \mathrm{div}(\boldsymbol{\sigma}), u\rangle_{H(\mathrm{curl})^*\times H(\mathrm{curl})}$. Consequently, $\boldsymbol{\sigma}$ lies in the function space $H(\mathrm{div\,div}, \Omega) =: V$, compare (3.1.26a), and u in $H_0(\mathrm{curl}, \Omega) =: Q$ and the tangential-displacement normal-normal-stress continuous method in terms of Sobolev spaces reads:

4.5 Problem. *Find $(\boldsymbol{\sigma}, u) \in V \times Q$ such that for all $(\delta\boldsymbol{\sigma}, \delta u) \in V \times Q$*

$$\int_\Omega \mathbb{C}^{-1}\boldsymbol{\sigma} : \delta\boldsymbol{\sigma}\, dx + \langle \mathrm{div}(\delta\boldsymbol{\sigma}), u\rangle_{H(\mathrm{curl})^*\times H(\mathrm{curl})} = 0, \tag{4.3.1a}$$

$$\langle \mathrm{div}(\boldsymbol{\sigma}), \delta u\rangle_{H(\mathrm{curl})^*\times H(\mathrm{curl})} = -\int_\Omega f \cdot \delta u\, dx. \tag{4.3.1b}$$

For a proof that the problem is well-posed we refer to [171, 174]. As therein Korn's inequality is not used the formulation is robust with respect to large aspect ratios [172]. Further, by adding a consistent stabilization term the method is also robust in the incompressible limit $\hat{\lambda} \to \infty$ [211].

4.4. Hu–Washizu principle

Instead of using the stress $\boldsymbol{\sigma}$ and displacement u as independent fields leading to a two-field saddle-point problem, the Hu–Washizu principle [230] uses further the strain $\boldsymbol{\epsilon}$ as additional unknown yielding the following three-field formulation:

4.6 Problem. *Find $(\boldsymbol{\epsilon}, u, \boldsymbol{\sigma}) \in [L^2(\Omega)]^{d\times d}_{\mathrm{sym}} \times [H^1_0(\Omega)]^d \times [L^2(\Omega)]^{d\times d}_{\mathrm{sym}}$ such that for all*

$$(\delta\boldsymbol{\epsilon}, \delta u, \delta\boldsymbol{\sigma}) \in [L^2(\Omega)]^{d\times d}_{\mathrm{sym}} \times [H^1_0(\Omega)]^d \times [L^2(\Omega)]^{d\times d}_{\mathrm{sym}}$$

$$\int_\Omega \mathbb{C}\boldsymbol{\epsilon} : \delta\boldsymbol{\epsilon}\,dx \qquad\qquad -\int_\Omega \boldsymbol{\sigma} : \delta\boldsymbol{\epsilon}\,dx \qquad = 0, \qquad\qquad (4.4.1a)$$

$$-\int_\Omega \boldsymbol{\sigma} : \mathrm{sym}(\nabla\delta u)\,dx = -\int_\Omega f\cdot\delta u\,dx, \quad (4.4.1b)$$

$$\int_\Omega \boldsymbol{\epsilon} : \delta\boldsymbol{\sigma}\,dx \ -\int_\Omega \mathrm{sym}(\nabla u) : \delta\boldsymbol{\sigma}\,dx \qquad\qquad = 0. \qquad\qquad (4.4.1c)$$

Choosing $V := [L^2(\Omega)]^{d\times d}_{\mathrm{sym}} \times [H^1_0(\Omega)]^d$ and $Q := [L^2(\Omega)]^{d\times d}_{\mathrm{sym}}$ one can easily prove that the requirements of Brezzi's Theorem 3.8 are fulfilled, see e.g., [58].

Again, it is possible to shift regularity between u and $\boldsymbol{\sigma}$ such that $(u, \boldsymbol{\sigma}) \in [L^2(\Omega)]^d \times H^{\mathrm{sym}}(\mathrm{div}, \Omega)$ and $(u, \boldsymbol{\sigma}) \in H_0(\mathrm{curl}, \Omega) \times H(\mathrm{div\,div}, \Omega)$ are also stable pairings, compare also the first limitation principle in [219].

Different three-field formulations using an additional *enhanced strain* have been proposed in the literature, see e.g., [210, 129] for more details. Therein, the strain is assumed to decompose additivly into a compatible part, associated with the displacement field, and an enhanced part. These methods were proven to be stable and efficient by various patch tests and benchmark problems. In [185] also rigorous stability and convergence proofs were provided. The equivalence of some classes of EAS and Hellinger–Reissner elements has been proven in [48]. By assuming that the discrete stress space is perpendicular to the enhanced strain space, the stresses can be eliminated a priori yielding a system involving only the displacement and the enhanced strain fields.

One main difference between the Hellinger–Reissner methods and the Hu–Washizu principle is the inversion of the material law represented by the fourth order tensor $\mathbb{C}$. This will play an essential role for the nonlinear case as the involved materials cannot be inverted in general. Further, the additional strain field provides more flexibility for constructing stable methods.

5. Finite elements

This chapter is devoted to give an overview of H^1, L^2, $H(\mathrm{curl})$, $H(\mathrm{div})$, and $H(\mathrm{div\,div})$ elements and facet spaces. For the Regge elements used to discretize the function space $H(\mathrm{curl\,curl})$ we present a novel hierarchical, arbitrary order basis for triangles, quadrilaterals, tetrahedra, hexahedra, and prisms. Further, given the degrees of freedom (dofs) and the basis functions the implementation of projections into the finite element spaces by discretizing the dual spaces is discussed. Finally, the (linear) TDNNS method is briefly introduced in terms of finite elements as preparation for Chapter 6.

We start by giving basic definitions and notations regarding triangulations and the reference element.

5.1. Basics and notations

Let $\Omega \subset \mathbb{R}^d$, $d = 2, 3$, be a domain with Lipschitz boundary and $\mathcal{T}_h = \{T\}$ a triangulation consisting of piece-wise (possibly polynomial curved) triangles and quadrilaterals in two space dimensions and tetrahedra, prisms, or hexahedra in three dimensions.

Definition 5.1 (Regular triangulation). We call a triangulation $\mathcal{T}_h$ of Ω *regular* if

1. the elements are non-overlapping $T^\circ \cap \tilde{T}^\circ = \emptyset$, $T \neq \tilde{T} \in \mathcal{T}_h$, where T° denotes the interior of T,

2. the domain Ω is covered by the elements $\overline{\Omega} = \bigcup_{T \in \mathcal{T}_h} \overline{T}$,

3. the intersection of two elements is either empty, or a common face, edge, or vertex of both.

The subscript h indicates that discretized objects are considered. For a more regular mesh, see Definition 5.3, h directly corresponds to the size of the elements of $\mathcal{T}_h$.

The set of all vertices of the triangulation of $\mathcal{T}_h$ is given by $\mathcal{V}_h$. With $\mathcal{F}_h$ the set of all facets, edges and faces in two and three dimensions, respectively, is denoted and in three dimensions the set of all edges is given by $\mathcal{E}_h$. Analogously, we can define these sets for a single element $T \in \mathcal{T}_h$ with the notation $\mathcal{V}_h(T)$, $\mathcal{F}_h(T)$, and $\mathcal{E}_h(T)$. Further, on each boundary ∂T we define the outer normal vector n.

The set of all piece-wise polynomials on the triangulation $\mathcal{T}_h$ up to degree k is defined by $\mathcal{P}^k(\mathcal{T}_h) = \prod_{T \in \mathcal{T}_h} \mathcal{P}^k(T)$ and the polynomials living only on the skeleton are denoted by $\mathcal{P}^k(\mathcal{F}_h)$ and $\mathcal{P}^k(\mathcal{E}_h)$.

Definition 5.2. For a facet $F \in \mathcal{F}_h$ with corresponding neighboring elements T_1, T_2 we define the global facet normal w.l.o.g. by $n_F := n_{T_1} = -n_{T_2}$. For a piece-wise smooth
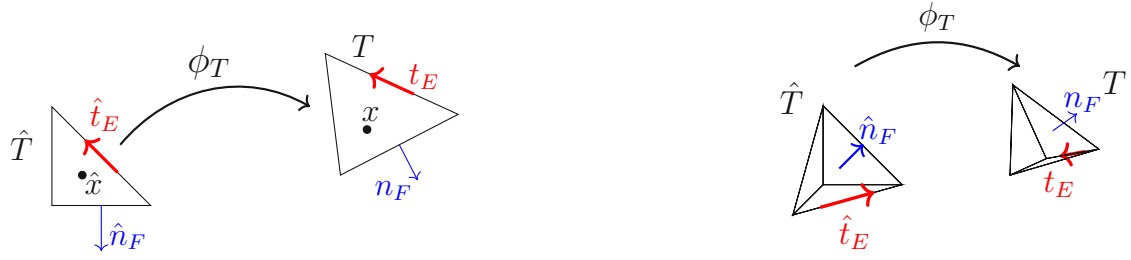
Figure 5.1.: Mapping from reference to physical triangle and tetrahedron with corresponding normal and tangential vectors.

scalar or vector valued function $u : T_1 \cup T_2 \to \mathbb{R}^d$ the *jump*, and for a vector valued function u the normal and tangential jump are defined by

$$[\![u]\!]_F := u|_{T_1} - u|_{T_2}, \quad [\![u_n]\!]_F := u_{n_{T_1}}|_{T_1} + u_{n_{T_2}}|_{T_2}, \quad [\![u_t]\!]_F := [\![u - u_n n]\!]_F. \tag{5.1.1}$$

For a boundary facet $F \subset \partial T \cap \partial \Omega$ the jumps are given by

$$[\![u]\!]_F := u|_T, \quad [\![u_n]\!]_F := u_{n_T}, \quad [\![u_t]\!]_F := [\![u - u_n n]\!]_F. \tag{5.1.2}$$

For the ease of presentation we will neglect the subscript F if no misunderstandings are possible.

For finite element methods it is a common strategy to define the elements, more precisely their basis functions, on a reference element and map them onto so-called physical elements in such a manner that globally a valid (finite element) function is achieved. In the following we will denote the reference element by $\hat{T}$ and for a (possibly curved) physical element T a one-to-one transformation function

$$\begin{aligned} \Phi_T : \hat{T} &\to T \\ \hat{x} &\mapsto \Phi_T(\hat{x}) = x. \end{aligned} \tag{5.1.3}$$

The *Jacobian* and *Hessian* of the transformation Φ_T are given by

$$\boldsymbol{G}_T := \nabla \Phi_T, \qquad\qquad \boldsymbol{H}_{T,i} := \nabla^2 \Phi_{T,i}, \quad i = 1, \ldots, d. \tag{5.1.4}$$

Further, we define the *Jacobi determinant* $J_T := \det(\boldsymbol{G}_T)$, measuring the volume deformation, as well as $J_F := \|\mathrm{cof}(\boldsymbol{G}_T)\hat{n}_F\|_2 = J_T\|\boldsymbol{G}_T^{-\top}\hat{n}_F\|_2$ and $J_E := \|\boldsymbol{G}_T\hat{t}_E\|_2$, where $\hat{n}_F$ and $\hat{t}_E$ are the corresponding facet outer normal vector and normalized tangential edge vector of the reference element. The transformation of these vectors is given by, compare Figure 5.1,

$$n_F \circ \Phi_T = \frac{J_T}{J_F}\boldsymbol{G}_T^{-\top}\hat{n}_F, \qquad\qquad t_E \circ \Phi_T = \frac{1}{J_E}\boldsymbol{G}_T\hat{t}_E. \tag{5.1.5}$$

The local mesh size can be defined by

$$h \circ \Phi_T := \|\boldsymbol{G}_T\|, \qquad\qquad h_T := \max_{x \in T} h(x). \qquad\qquad (5.1.6)$$

Depending on the shape of the elements a family of triangulations fulfills different regularity assumptions.

Definition 5.3. A family of regular triangulations $(\mathcal{T}_h)_{h>0}$ is called

- *shape-regular*, if there exists $c_1, c_2 > 0$ independent of h_T such that the condition number of $\boldsymbol{G}_T$ is bounded: $c_1 \leq \|\boldsymbol{G}_T\|\|\boldsymbol{G}_T^{-1}\| \leq c_2$ for all $T \in \mathcal{T}_h$.

- *quasi-uniform*, if there exist $c_1, c_2 > 0$ independent of h such that for all $T \in \mathcal{T}_h$: $c_1 h \leq h_T \leq c_2 h$.

- *uniform*, if there exists a $h > 0$ such that for all $x \in \Omega : h(x) = h$.

For a shape-regular triangulation the elements do not degenerate for $h \to 0$, i.e., the angles are strictly bounded away from 0 and 180 degrees. In a quasi-uniform triangulation the elements have nearly the same size, whereas for a uniform mesh all elements are of the same size. Throughout this thesis we will assume shape-regular triangulations, although in most cases they will be quasi-uniform.

For a shape-regular triangulation there holds $|J_T| \approx h_T^d$ and thus, the element and facet mesh size can also be defined as

$$h_T := |J_T|^{\frac{1}{d}}, \qquad\qquad h_F := \frac{|J_{T_1}| + |J_{T_2}|}{|J_F|} \quad \text{for } F = T_1 \cap T_2. \qquad (5.1.7)$$

Having a regular triangulation at hand we can give the definition of a finite element [86] and a finite element space.

Definition 5.4 (Finite element). The triplet $(T, V, \mathcal{N})$ is called a *finite element* if

1. the element domain $T \subset \mathbb{R}^d$ is a bounded and closed set with non-empty interior and piece-wise smooth boundary,

2. the space of *shape functions* V is finite dimensional,

3. the set of *degrees of freedom* (dofs) $\mathcal{N} = \{N_1, \ldots, N_k\}$ is a basis for V^*, the dual space of V.

Definition 5.5 (Finite element space). Let $\mathcal{T}_h = \{T\}$ be a regular triangulation of $\Omega \subset \mathbb{R}^d$ and each T is equipped with a finite element $(T, V(T), \mathcal{N}(T))$. We call the space of shape functions, where the dofs shared between elements coincide,

$$V_h := \{u \in \prod_{T \in \mathcal{T}_h} V(T) \,|\, N(u|_{T_i}) = N(u|_{T_j}) \quad \forall N \in \mathcal{N}(T_i) \cap \mathcal{N}(T_j)\} \qquad (5.1.8)$$

a *finite element space*.

5.2. Construction of (high-order) finite elements

We discuss the construction of (high-order) H^1-, L^2-, $H(\mathrm{div})$-, and $H(\mathrm{curl})$-conforming finite elements, hybridization spaces, and further of the matrix valued $H(\mathrm{div\,div})$ (Hellan–Herrmann–Johnson) and $H(\mathrm{curl\,curl})$ (Regge) elements including (homogeneous) essential boundary conditions on $\Gamma_D \subset \partial\Omega$. For all elements the corresponding spaces and dofs are given for triangles and tetrahedral except the $H(\mathrm{curl\,curl})$ elements, where a (new) basis is explicitly constructed for triangles, quadrilaterals, tetrahedra, hexahedra, and prisms.

We note, that it is possible to construct all elements with variable polynomial order, e.g., different orders for edges, faces and inner dofs. For the ease of presentation, however, we will consider only elements with uniform order. Further, for the construction of global elements the orientation of edges and faces is essential. We will not focus on this problem by assuming that the orientations always fit and refer to [239] and therein references.

First, we give a brief overview of orthogonal polynomials.

5.2.1. Orthogonal polynomials

To construct hierarchical high-order finite element basis orthogonal polynomials play a crucial rule. Besides the fast evaluation due to their three-term recursions and numerical stability they lead to sparser matrices. For more details about orthogonal polynomials and their application in (high-order) finite elements we refer to [1, 5, 44] and references therein. We define the *Legendre polynomials* via Rodrigues' formula

$$l_n : [-1,1] \to \mathbb{R}, \qquad\qquad l_n(x) := \frac{1}{2^n n!} \frac{d^n}{dx^n} \left(x^2 - 1\right)^n \tag{5.2.1}$$

fulfilling the orthogonality property

$$\int_{-1}^{1} l_i(x) l_j(x)\, dx = \frac{2}{2i+1} \delta_{ij}, \tag{5.2.2}$$

where δ_{ij} denotes the *Kronecker delta*. The *integrated Legendre polynomials* are given for $x \in [-1,1]$ by

$$L_n : [-1,1] \to \mathbb{R}, \qquad\qquad L_n(x) := \int_{-1}^{x} l_{n-1}(s)\, ds, \quad n \geq 2, \tag{5.2.3}$$

satisfying

$$\int_{-1}^{1} L_i'(x) L_j'(x)\, dx = 0, \quad i \neq j, \qquad \int_{-1}^{1} L_i(x) L_j(x)\, dx = 0, \quad |i-j| > 2. \tag{5.2.4}$$

Further, the *scaled Legendre polynomials* and *scaled integrated Legendre polynomials* are defined by

$$l_n^S(x,y) := y^n l_n\left(\frac{x}{y}\right), \qquad x \in [-y,y],\, y \in (0,1], \tag{5.2.5}$$

$$L_n^S(x,y) := y^n L_n\left(\frac{x}{y}\right), \qquad x \in [-y,y],\, y \in (0,1], \quad n \geq 2 \tag{5.2.6}$$

and for $\alpha, \beta > -1$ the *(scaled) Jacobi polynomials* $P_n^{(\alpha,\beta)} : [-1, 1] \to \mathbb{R}$ by

$$P_n^{(\alpha,\beta)}(x) := \frac{(-1)^n}{2^n n!} \frac{1}{\omega(x)} \frac{d^n}{dx^n} \left(\omega(x) \left(1 - x^2\right)^n \right), \qquad \omega(x) := (1-x)^\alpha (1-x)^\beta, \quad (5.2.7)$$

$$P_n^{(\alpha,\beta),S}(x,y) := P_n^{(\alpha,\beta)} \left(\frac{x}{y} \right) y^n, \qquad x \in [-y, y], \, y \in (0, 1], \quad (5.2.8)$$

satisfying

$$\int_{-1}^{1} \omega(x) P_i^{(\alpha,\beta)}(x) P_j^{(\alpha,\beta)}(x) \, dx = \frac{2^{\alpha+\beta+1}}{2i + \alpha + \beta + 1} \frac{\Gamma(i + \alpha + 1)\Gamma(i + \beta + 1)}{n! \Gamma(i + \alpha + \beta + 1)} \delta_{ij}, \quad (5.2.9)$$

where $\Gamma(\cdot)$ denotes the *Gamma function*. With $P_n^{(0,0)}(x) = l_n(x)$ the Legendre polynomials can be recovered. Note, that all these orthogonal polynomials can be efficiently evaluated in terms of a three-term recursion, see [239].

The construction of an L^2-orthogonal basis of order k on a triangle is based on the *Dubiner basis* [95]

$$\varphi_{i,j}^D : [-1, 1] \times [0, 1] \to \mathbb{R}, \qquad \varphi_{i,j}^D(x,y) := l_i^S(x, 1 - y) P_j^{(2i+1,0)}(2y - 1), \qquad i + j \le k. \quad (5.2.10)$$

Therefore, with the *Duffy transformation* from the quadrilateral $[-1, 1]^2$ to the reference triangle

$$D : [-1, 1]^2 \to \hat{T}$$
$$(\xi, \eta) \mapsto (x, y) := \left(\frac{1}{4}(1 + \xi)(1 - \eta), \frac{1}{2}(1 + \eta) \right), \quad (5.2.11a)$$
$$D^{-1} : \hat{T} \to [-1, 1]^2$$
$$(x, y) \mapsto (\xi, \eta) = \left(\frac{\lambda_2 - \lambda_1}{1 - \lambda_3}, 2\lambda_3 - 1 \right) = \left(\frac{\lambda_2 - \lambda_1}{\lambda_1 + \lambda_2}, 1 - 2(\lambda_1 + \lambda_2) \right), \quad (5.2.11b)$$

where $\lambda_1 := 1 - x - y$, $\lambda_2 := x$, and $\lambda_3 := y$ denote the barycentric coordinates of $\hat{T}$, compare Figure 5.8, we obtain that $\varphi_{i,j}^D(\lambda_2 - \lambda_1, \lambda_3)$, $i + j \le k$, build a basis of polynomial order k on the reference triangle $\hat{T}$.

Also in three dimensions the corresponding Dubiner basis combined with the Duffy transformation from the hexahedron $[-1, 1]^3$ to the reference tetrahedron $\hat{T}$

$$D : [-1, 1]^3 \to \hat{T}$$
$$(x, y, z) = \left(\frac{1}{8}(1 + \xi)(1 - \eta)(1 - \zeta), \frac{1}{4}(1 + \eta)(1 - \zeta), \frac{1}{2}(1 + \zeta) \right)$$
$$D^{-1} : \hat{T} \to [-1, 1]^3$$
$$(\xi, \eta, \zeta) = \left(\frac{\lambda_2 - \lambda_1}{\lambda_2 + \lambda_1}, \frac{\lambda_3 - (\lambda_1 + \lambda_2)}{\lambda_1 + \lambda_2 + \lambda_3}, 2\lambda_4 - 1 \right),$$

Figure 5.2.: Lowest order H^1- and L^2-conforming finite elements for triangle and tetrahedron.

where $\lambda_1 := 1 - x - y - z$, $\lambda_2 := x$, $\lambda_3 := y$, and $\lambda_4 := z$ denote the barycentric coordinates of $\hat{T}$, cf. Figure 5.11, lead to the following polynomial basis of $\hat{T}$

$$\varphi_{i,j,n}^{D,3} : [0,1]^3 \to \mathbb{R}, \; \varphi_{i,j,n}^{D,3}(\lambda_1,\lambda_2,\lambda_3) := l_i^S(\lambda_2 - \lambda_1, \lambda_1 + \lambda_2) P_j^{2i+1,S}(\lambda_3 - \lambda_1 - \lambda_2, \lambda_3 + \lambda_1 + \lambda_2)$$
$$\times P_n^{2i+2j+2}(1 - 2(\lambda_1 + \lambda_2 + \lambda_3)), \qquad i + j + n \leq k. \tag{5.2.12}$$

If we restrict the Dubiner basis $\varphi^{D,3}$ to edges or faces the Legendre or 2D Dubiner polynomials are recovered, which is useful to construct elements leading to valid lower dimensional elements when restricted to faces or edges. Also the restriction of the 2D Dubiner basis to edges leads to Legendre polynomials.

5.2.2. Finite element space for L^2 and H^1

The Lagrangian finite elements use piece-wise (smooth) polynomials which are globally continuous to obtain a H^1-conforming finite element space, see Theorem 3.3, whereas discontinuous piece-wise polynomials are sufficient to discretize L^2

$$\begin{aligned} U_h^k &:= \mathcal{P}^k(\mathcal{T}_h) \cap C(\Omega), \\ U_{h,0}^k &:= \{u \in U_h^k \,|\, u = 0 \text{ on } \Gamma_D\} \end{aligned} \tag{5.2.13}$$

$$Q_h^k := \mathcal{P}^k(\mathcal{T}_h),. \tag{5.2.14}$$

For a (high-order) construction of these finite elements we refer e.g., to [239, 58, 240]. The dofs can be specified as follows in three dimensions:

5.1 Theorem. *Let $\mathcal{T}_h$ be a triangulation of $\Omega \subset \mathbb{R}^3$ consisting of tetrahedra and $k > 0$. If for a function $u \in U_h^k$ holds*

$$u(V) = 0, \qquad \text{for all } V \in \mathcal{V}_h, \tag{5.2.15a}$$

$$\int_E u\, q\, d\lambda = 0 \qquad \text{for all } q \in \mathcal{P}^{k-2}(E) \text{ for all } E \in \mathcal{E}_h, \tag{5.2.15b}$$

$$\int_F u\, q\, ds = 0 \qquad \text{for all } q \in \mathcal{P}^{k-3}(F) \text{ for all } F \in \mathcal{F}_h, \tag{5.2.15c}$$

$$\int_T u\, q\, dx = 0 \qquad \text{for all } q \in \mathcal{P}^{k-4}(T) \text{ for all } T \in \mathcal{T}_h, \tag{5.2.15d}$$

Figure 5.3.: Lowest order RT and BDM elements for triangle and tetrahedron.

> *then $u \equiv 0$. If for a function $u \in Q_h^k$ with $k \geq 0$ holds*
>
> $$\int_T u\,q\,dx = 0 \qquad \text{for all } q \in \mathcal{P}^k(\mathcal{T}_h), \tag{5.2.16}$$
>
> *then $u \equiv 0$.*

In two dimensions for a triangulation consisting of triangles the dofs (5.2.15a)–(5.2.15c) are used for $u \in U_h^k$, where $\mathcal{E}_h$ and $\mathcal{F}_h$ are replaced with $\mathcal{F}_h$ and $\mathcal{T}_h$, respectively, compare Figure 5.2.

5.2.3. Finite element space for $H(\mathrm{div})$

To construct $H(\mathrm{div})$-conforming elements we notice that normal jumps have to be zero, see interface condition Theorem 3.3. Two different families have been proposed. The Raviart–Thomas (RT) elements [184] consisting of polynomials of order k and special polynomials of order $k + 1$ such that the range of the divergence operator is $\mathcal{P}^k(\mathcal{T}_h)$

$$
\begin{aligned}
RT^k &:= \{u = a + bx \,|\, a \in [\mathcal{P}^k(\mathcal{T}_h)]^d, b \in \mathcal{P}^{k,*}(\mathcal{T}_h), [\![u_n]\!]_F = 0 \,\forall F \in \mathcal{F}_h\}, \\
RT_0^k &:= \{u \in RT^k \,|\, u_n = 0 \text{ on } \Gamma_D\},
\end{aligned} \tag{5.2.17}
$$

where $\mathcal{P}^{k,*} := \{p \in \mathcal{P}^k \,|\, p = \sum_{i=1}^m \alpha_i x_1^{k_{i1}} \cdots x_d^{k_{id}}, \sum_{l=1}^d k_{il} = k, \forall i \in \{1, \ldots, m\}\}$ denotes the set of homogeneous polynomials of degree k. The class of Brezzi–Douglas–Marini (BDM) elements [63] uses the full polynomial space, see also Figure 5.3,

$$
\begin{aligned}
BDM^k &:= \{u \in [\mathcal{P}^k(\mathcal{T}_h)]^d \,|\, [\![u_n]\!]_F = 0 \,\forall F \in \mathcal{F}_h\}, \\
BDM_0^k &:= \{u \in BDM^k \,|\, u_n = 0 \text{ on } \Gamma_D\}.
\end{aligned} \tag{5.2.18}
$$

Note the relations for all $k \geq 1$

$$
\begin{aligned}
\mathrm{div}(RT^{k-1}) &= \mathrm{div}(BDM^k), \\
RT^{k-1} &\subsetneq BDM^k \subsetneq RT^k \subsetneq BDM^{k+1},
\end{aligned}
$$

i.e., the RT elements of order k approximate the divergence as good as BDM elements of order $k + 1$ with less shape functions. Using the BDM elements, however, gives beneficial L^2 approximations of a function. For more details of the properties and construction of $H(\mathrm{div})$-conforming elements we refer to [53, 239, 145].

The dofs of RT and BDM elements can be characterized by the following result.

5.2 Theorem. *Let $\mathcal{T}_h$ be a triangulation consisting of triangles or tetrahedra and $k \geq 0$. If for a function $u \in RT^k$ holds*

$$\int_F u_n \, q \, ds = 0 \qquad \text{for all } q \in \mathcal{P}^k(F) \text{ for all } F \in \mathcal{F}_h, \tag{5.2.19a}$$

$$\int_T u \cdot q \, dx = 0 \qquad \text{for all } q \in [\mathcal{P}^{k-1}(T)]^d \text{ for all } T \in \mathcal{T}_h. \tag{5.2.19b}$$

Then $u \equiv 0$. If for a function $u \in BDM^k$ with $k > 0$ holds (5.2.19a) and

$$\int_T u \cdot q \, dx = 0 \qquad \text{for all } q \in \mathcal{N}_I^{k-2}(T) \text{ for all } T \in \mathcal{T}_h, \tag{5.2.20}$$

where $\mathcal{N}_I$ is the Nédélec space of first kind defined in (5.2.25), then $u \equiv 0$.

When transforming an $H(\mathrm{div})$-conforming finite element from the reference to a physical element the continuity of its normal component has to be preserved. Therefore, the so-called *Piola transformation* is used.

5.3 Theorem (Piola transformation). *Let $\Phi : \hat{T} \to T$ be a diffeomorphic mapping from the reference element $\hat{T}$ to the physical element T. Let $\hat{\sigma} \in H(\mathrm{div}, \hat{T})$. Then, the Piola transformation defined by*

$$\sigma := P_\Phi[\hat{\sigma}] := (J^{-1} \boldsymbol{G} \hat{\sigma}) \circ \Phi^{-1}, \tag{5.2.21}$$

with $\boldsymbol{G}$ the gradient of Φ, $\boldsymbol{G} := \nabla \Phi$, and $J := \det(\boldsymbol{G})$ has the following properties:

1. σ is in the space $H(\mathrm{div}, T)$ with

$$\mathrm{div}_x(\sigma) = (J^{-1} \mathrm{div}_{\hat{x}}(\hat{\sigma})) \circ \Phi^{-1}. \tag{5.2.22}$$

2. Let furthermore $\hat{F}$ be a facet of the reference element and $F = \Phi(\hat{F})$. Then

$$\int_F \sigma \cdot n_F \, ds = \int_{\hat{F}} \hat{\sigma} \cdot n_{\hat{F}} \, d\hat{s}. \tag{5.2.23}$$

5.2.4. Finite element space for $H(\mathrm{curl})$

Similar to $H(\mathrm{div})$-conforming elements Theorem 3.3 states that the tangential jumps have to be zero for $H(\mathrm{curl})$-conforming elements. Again, two types of families exist called Nédélec elements of first and second kind [161, 162]. In two dimensions the Nédélec elements can be achieved by rotating the RT and BDM elements by 90 degrees, compare Figures 5.3 and 5.4. The local polynomial space for Nédélec elements of first kind is given by

$$\mathcal{N}_I^k(T) := [\mathcal{P}^k(T)]^d \oplus \{q \in [\mathcal{P}^{k+1,*}(T)]^d \,|\, x \cdot q = 0\} \tag{5.2.24}$$

Figure 5.4.: Lowest order Nédélec elements of first and second kind for triangle and tetrahedron.

and the finite element spaces in three dimensions by

$$\mathcal{N}_I^k := \{u \in \prod_{T \in \mathcal{T}_h} \mathcal{N}_I^k(T) \,|\, u_t \text{ continuous}\}, \tag{5.2.25}$$

$$\mathcal{N}_{I,0}^k := \{u \in \mathcal{N}_I^k \,|\, u_t = 0 \text{ on } \Gamma_D\},$$

$$\mathcal{N}_{II}^k := \{u \in [\mathcal{P}^k(\mathcal{T}_h)]^3 \,|\, u_t \text{ continuous}\},$$

$$\mathcal{N}_{II,0}^k := \{u \in \mathcal{N}_{II}^k \,|\, u_t = 0 \text{ on } \Gamma_D\}. \tag{5.2.26}$$

For the construction and properties of $H(\mathrm{curl})$-conforming elements we refer to [157, 239, 198]. The Nédélec elements are constructed such that the trace of a three-dimensional element results in a valid 2D Nédélec element, see Figure 5.4. Thus, we state the dofs only for three spatial dimensions. Note that the orthogonal space of a vector $u \in \mathbb{R}^d$ is defined as

$$u^\perp := \{u\}^\perp := \{v \in \mathbb{R}^d \,|\, v \cdot u = 0\}. \tag{5.2.27}$$

Further, we denote with $[\mathcal{P}^k(F)]^3 \cap n_F^\perp$ the space of tangential vector fields on the facet, i.e., the space $[\mathcal{P}^k(T_{\mathrm{trig}})]^2$ on a triangle is mapped onto the facet.

5.4 Theorem. *Let $\mathcal{T}_h$ be a triangulation consisting of tetrahedra and $k \geq 0$. If for a function $u \in \mathcal{N}_I^k$ holds*

$$\int_E u \cdot t_E \, q \, d\lambda = 0 \qquad \text{for all } q \in \mathcal{P}^k(E) \text{ for all } E \in \mathcal{E}_h, \tag{5.2.28a}$$

$$\int_F u_t \cdot q \, ds = 0 \qquad \text{for all } q \in [\mathcal{P}^{k-1}(F)]^3 \cap n_F^\perp \text{ for all } F \in \mathcal{F}_h, \tag{5.2.28b}$$

$$\int_T u \cdot q \, dx = 0 \qquad \text{for all } q \in [\mathcal{P}^{k-2}(T)]^3 \text{ for all } T \in \mathcal{T}_h, \tag{5.2.28c}$$

where t_E denotes the tangential vector of the edge E, then $u \equiv 0$. If for a function $u \in \mathcal{N}_{II}^k$ with $k > 0$ (5.2.28a) holds and

$$\int_F u_t \cdot q \, ds = 0 \qquad \text{for all } q \in RT^{k-2}(F) \text{ for all } F \in \mathcal{F}_h, \tag{5.2.29a}$$

$$\int_T u \cdot q \, dx = 0 \qquad \text{for all } q \in RT^{k-3}(T) \text{ for all } T \in \mathcal{T}_h, \tag{5.2.29b}$$

> *where $RT(F)$ and $RT(T)$ denote the two-dimensional Raviart–Thomas space (5.2.17) mapped onto the face and the 3D RT space on the element T, then $u \equiv 0$.*

To preserve the tangential continuity during transformation the so-called *covariant transformation* is used.

5.5 Theorem (Covariant transformation). *Let $\Phi : \hat{T} \to T$ be a diffeomorphic mapping from the reference element $\hat{T}$ to a physical element T. Let $\hat{u} \in H(\text{curl}, \hat{T})$. Then, the covariant transformation defined by*

$$u := \boldsymbol{G}^{-\top} \hat{u} \circ \Phi^{-1}, \tag{5.2.30}$$

where $\boldsymbol{G}$ denotes the gradient of Φ and $J = \det(\boldsymbol{G})$, has the following properties:

1. *Let $T \subset \mathbb{R}^3$. Then u is in $H(\text{curl}, T)$ with*

   $$\text{curl}_x(u) = P_\Phi[\text{curl}_{\hat{x}}(\hat{u})] = (J^{-1}\boldsymbol{G}\,\text{curl}_{\hat{x}}(\hat{u})) \circ \Phi^{-1}, \tag{5.2.31}$$

   where $P_\Phi[\cdot]$ denotes the Piola transformation (5.2.21).

2. *Let $T \subset \mathbb{R}^2$. Then u is in $H(\text{curl}, T)$ with*

   $$\text{curl}_x(u) = (J^{-1}\text{curl}_{\hat{x}}(\hat{u})) \circ \Phi^{-1}. \tag{5.2.32}$$

3. *Let furthermore $\hat{E}$ be an edge with tangential vector $t_{\hat{E}}$ of the reference element and $E = \Phi(\hat{E})$. Then*

   $$\int_E u \cdot t_E \, ds = \int_{\hat{E}} \hat{u} \cdot t_{\hat{E}} \, d\hat{s}. \tag{5.2.33}$$

Due to the factor $J^{-1}\boldsymbol{G}$ the following identity holds in three spatial dimensions for $u \in V_h$, V_h the Nédélec space of first or second kind, and W_h the RT or BDM space of appropriate polynomial orders

$$\text{div}(\text{curl}(u)) = \text{div}(P_\Phi[\text{curl}(\hat{u})]) = \frac{1}{J}\text{div}(\text{curl}(\hat{u})) \circ \Phi^{-1} = 0, \tag{5.2.34}$$

i.e., the exact sequence from the continuous level is inherited by the discrete one if the $H(\text{div})$- and $H(\text{curl})$-conforming elements are chosen. This is reflected in the *de Rham complex* in three dimensions:

$$
\begin{array}{ccccccc}
H^1 & \xrightarrow{\nabla} & H(\text{curl}) & \xrightarrow{\text{curl}} & H(\text{div}) & \xrightarrow{\text{div}} & L^2 \\
\cup & & \cup & & \cup & & \cup \\
U_h & \xrightarrow{\nabla} & V_h & \xrightarrow{\text{curl}} & W_h & \xrightarrow{\text{div}} & Q_h
\end{array}
$$
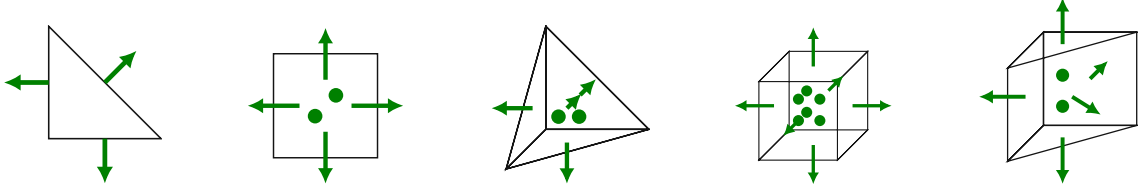
Figure 5.5.: Lowest order $H(\mathrm{div\,div})$ elements for triangles, quadrilaterals, tetrahedra, hexahedra, and prisms.

5.2.5. Finite element space for $H(\mathrm{div\,div})$, Hellan–Herrmann–Johnson elements

Normal-normal continuous elements for solving fourth order plate problems are used as part of the Hellan–Herrmann–Johnson (HHJ) method [114, 116, 127, 91]. In the context of mixed problems for elasticity the function space $H(\mathrm{div\,div})$ (3.1.21) has been closer investigated and the same finite element space for triangles and tetrahedra has been used in [211, 171].

For two-dimensional domains, triangular and quadrilateral elements have been introduced, while for three-dimensional meshes tetrahedral, hexahedral and prismatic elements have been developed so far, see [171, 172, 155].

For triangles and tetrahedral elements the space is given by

$$
\begin{aligned}
\Sigma_h^k &:= \{\boldsymbol{\sigma} \in [\mathcal{P}^k(\mathcal{T}_h)]_{\mathrm{sym}}^{d\times d} \,|\, [\![\boldsymbol{\sigma}_{nn}]\!]_F = 0 \,\forall F \in \mathcal{F}_h\}, \\
\Sigma_{h,0}^k &:= \{\boldsymbol{\sigma} \in \Sigma_h^k \,|\, \boldsymbol{\sigma}_{nn} = 0 \text{ on } \Gamma_D\},
\end{aligned}
\tag{5.2.35}
$$

see also Figure 5.5.

To preserve the normal-normal continuity during the mapping from the reference to the physical element the Piola transformation 5.2.21 is used twice, once from the left and right

$$
\boldsymbol{\sigma} \circ \Phi = \frac{1}{J^2} \boldsymbol{G} \hat{\boldsymbol{\sigma}} \boldsymbol{G}^\top.
\tag{5.2.36}
$$

The dofs are given by:

5.6 Theorem. *Let $\mathcal{T}_h$ a triangulation consisting of triangles or tetrahedra and $k \geq 0$. If for a function $\boldsymbol{\sigma} \in \Sigma_h^k$ holds*

$$
\int_F \boldsymbol{\sigma}_{nn} q \, ds = 0 \qquad \text{for all } q \in \mathcal{P}^k(F) \text{ for all } F \in \mathcal{F}_h,
\tag{5.2.37a}
$$

$$
\int_T \boldsymbol{\sigma} : \boldsymbol{q} \, dx = 0 \qquad \text{for all } \boldsymbol{q} \in [\mathcal{P}^{k-1}(\mathcal{T}_h)]_{\mathrm{sym}}^{d\times d},
\tag{5.2.37b}
$$

then $\boldsymbol{\sigma} \equiv 0$.

Other $H(\mathrm{div\,div})$ finite elements In [80, 81] an L^2-$H(\mathrm{div\,div})$ conforming finite element space of (3.1.28) has been defined in two and three dimensions where besides the normal-normal components also e.g., in 2D the vertices and $\partial_t(t^\top \boldsymbol{\sigma} n) + n^\top \mathrm{div}(\boldsymbol{\sigma})$ are degrees of freedom.
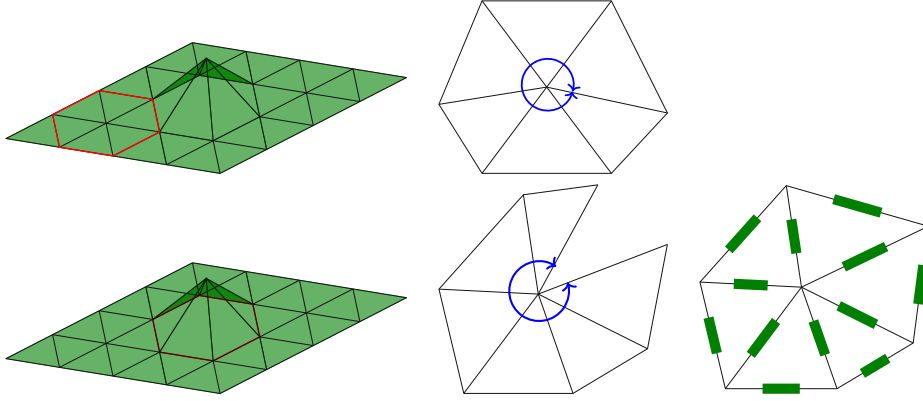
Figure 5.6.: Left: A non-flat surface consisting of piece-wise flat triangles. A flat and non-flat vertex patch is considered. Middle: Flattening both vertex patches preserving the angles leads that for the flat one the angles sum up to $\alpha = 2\pi$, whereas for the other holds $\alpha < 2\pi$ – an angle deficit. Right: By assigning a length to each edge a metric tensor is defined and is equivalent to the concept of angle deficits.

For the arising $H(\operatorname{div}\operatorname{div})$ functions in [182] a Helmholtz decomposition is used such that e.g., the fourth order plate problem splits into three second-order problems and thus, no explicit finite elements for $H(\operatorname{div}\operatorname{div})$ are directly needed.

5.2.6. Finite element space for $H(\operatorname{curl}\operatorname{curl})$, Regge elements

A geometric discretization of the Einstein field equations by the usage of a piece-wise constant metric was derived by Tullio Regge in [190]. In theoretical and numerical physics so-called Regge calculus got established and was applied e.g., in fields of relativity and quantum mechanics. In [234] a comprehensive overview of the development of Regge calculus over the last fifty years was given.

It was observed that Regge's approach of angle deficits is equivalent to specify lengths at all edges of a mesh [78, 77], analogously to the concept of Whitney-forms [233], see Figure 5.6, giving Regge calculus an analytical perspective. In the context of *finite element exterior calculus* (FEEC) [18, 16] a finite element structure has been developed [84, 85]. The resulting Regge finite elements have been extended to arbitrary polynomial order on triangles and tetrahedra in [147].

In this section we present a different hierarchical arbitrary order basis for triangular and tetrahedral Regge elements and a new (minimal) basis to construct Regge elements for quadrilateral, hexahedral, and prisms (see Figure 5.7).

The finite element space for triangles in 2D and tetrahedra in three dimensions is given by

$$
\begin{aligned}
\mathcal{R}_h^k &:= \{\boldsymbol{\sigma} \in [\mathcal{P}^k(\mathcal{T}_h)]_{\mathrm{sym}}^{d \times d} \,|\, \boldsymbol{\sigma}_{tt} \text{ continuous}\}, \\
\mathcal{R}_{h,0}^k &:= \{\boldsymbol{\sigma} \in \mathcal{R}_h^k \,|\, \boldsymbol{\sigma}_{tt} = 0 \text{ on } \Gamma_D\},
\end{aligned}
\tag{5.2.38}
$$
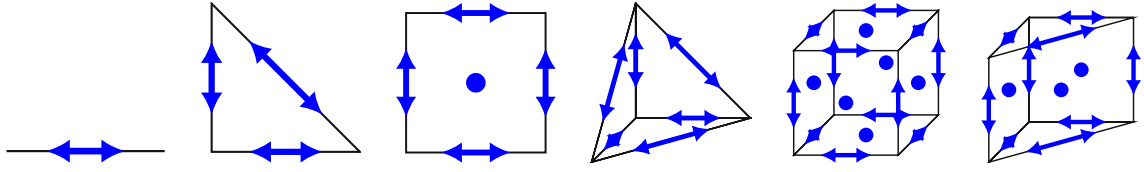
Figure 5.7.: Lowest order Regge elements for segments, triangles, quadrilaterals, tetrahedra, hexahedra, and prisms. Every two-sided arrow $\leftrightarrow$ corresponds to one degree of freedom.

where $\boldsymbol{\sigma}_{tt} := (\boldsymbol{I} - \boldsymbol{P}_n)\boldsymbol{\sigma}(\boldsymbol{I} - \boldsymbol{P}_n)$, $\boldsymbol{P}_n = n \otimes n$, and will be adapted for the other elements. Note, that the interface condition is given by the tangential-tangential continuity. Therefore, the Regge elements get transformed doubled covariantly, compare Theorem 5.5,

$$\boldsymbol{\sigma} \circ \Phi := \boldsymbol{G}^{-\top}\hat{\boldsymbol{\sigma}}\boldsymbol{G}^{-1}. \tag{5.2.39}$$

Triangular elements: Every edge $E = [e_1, e_2]$ of a triangle can be parameterized by

$$\xi_E = \frac{\lambda_{e_2} - \lambda_{e_1}}{\lambda_{e_1} + \lambda_{e_2}} \in [-1, 1]$$

and the outer normal vector is given by $n_E = -\nabla\lambda_{e_3} = \nabla(\lambda_{e_1} + \lambda_{e_2})$, see Figure 5.8.
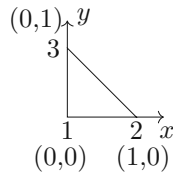
$$\lambda_1 = 1 - x - y,$$
$$\lambda_2 = x,$$
$$\lambda_3 = y,$$

Figure 5.8.: Reference triangle.

We define functionals, the dofs, on the reference triangle $\hat{T}$ with the local space $[\mathcal{P}^k(\hat{T})]^{2\times 2}_{\mathrm{sym}}$. Therefore, let $\{q_{\hat{E},n}\}$ and $\{\boldsymbol{q}_{\hat{T},n}\}$ denote a polynomial basis of $\mathcal{P}^k(\hat{E}_i)$ on the edge $\hat{E}_i$, $i = 1, 2, 3$, and $[\mathcal{P}^{k-1}(\hat{T})]^{2\times 2}_{\mathrm{sym}}$ on $\hat{T}$, respectively. Then the functionals read

$$\Psi_{\hat{E}_i,n} : \boldsymbol{\sigma} \mapsto \int_{\hat{E}_i} \boldsymbol{\sigma} : q_{\hat{E},n}t_{\hat{E}} \otimes t_{\hat{E}}\, ds, \tag{5.2.40a}$$

$$\Psi_{\hat{T},n} : \boldsymbol{\sigma} \mapsto \int_{\hat{T}} \boldsymbol{\sigma} : \boldsymbol{q}_{\hat{T},n}\, dx. \tag{5.2.40b}$$

Note that $t_{\hat{E}} \otimes t_{\hat{E}}$ is single-valued, i.e., does not depend on the orientation of $t_{\hat{E}}$.

On triangular elements the dofs are associated with the edges (5.2.40a), analogously to $H(\mathrm{curl})$-conforming elements, and inner bubbles (5.2.40b) for higher polynomial degree.

We now give an explicit basis for the corresponding shape functions $\{\boldsymbol{\varphi}_i\}$ to (5.2.40a)–(5.2.40b).

5.7 Theorem. *For the reference triangle $\hat{T}$ and $k \geq 0$ the following shape functions build a basis of $[\mathcal{P}^k(\hat{T})]^{2\times 2}_{\text{sym}}$:*

Edge functions: $i \in \{1, 2, 3\}$ $E_i = [e_1, e_2]$

Lowest order edge functions:

$$\boldsymbol{\varphi}_{E_i,0} := -\nabla\lambda_{e_1} \odot \nabla\lambda_{e_2}, \tag{5.2.41}$$

High order edge functions: for $n = 1, \ldots, k$

$$\boldsymbol{\varphi}_{E_i,n} := -l_n^S(\lambda_{e_2} - \lambda_{e_1}, \lambda_{e_1} + \lambda_{e_2})\nabla\lambda_{e_1} \odot \nabla\lambda_{e_2}, \tag{5.2.42}$$

Inner functions: *for $n + m \leq k - 1$*

$$\boldsymbol{\varphi}_{T^1,n,m} := \varphi_{n,m}^D(\lambda_1 - \lambda_2, \lambda_3)\lambda_1(\nabla\lambda_2 \odot \nabla\lambda_3), \tag{5.2.43a}$$

$$\boldsymbol{\varphi}_{T^2,n,m} := \varphi_{n,m}^D(\lambda_1 - \lambda_2, \lambda_3)\lambda_2(\nabla\lambda_3 \odot \nabla\lambda_1), \tag{5.2.43b}$$

$$\boldsymbol{\varphi}_{T^3,n,m} := \varphi_{n,m}^D(\lambda_1 - \lambda_2, \lambda_3)\lambda_3(\nabla\lambda_1 \odot \nabla\lambda_2). \tag{5.2.43c}$$

Proof. The space $[\mathcal{P}^k(\hat{T})]^{2\times 2}_{\text{sym}}$ has a dimension of $\frac{3}{2}(k+1)(k+2)$. The lowest order edge shape functions are linearly independent as $(\boldsymbol{\varphi}_{E_i,0})_{t_{E_j} t_{E_j}} = \delta_{ij}$, where E_i and t_{E_i} denotes the i-th edge and corresponding tangent vector. Due to the use of the scaled Legendre polynomials the higher order edge functions are also linearly independent. Further, there holds $(\boldsymbol{\varphi}_{T^i,n,m})_{t_{E_j} t_{E_j}} = 0$ for $i, j = 1, 2, 3$ and thus, the inner shapes are independent of the edge basis. The claim now follows together with the independence of $\lambda_i(\nabla\lambda_j \odot \nabla\lambda_k)$ for $i \neq j \neq k$ and counting all shape functions. $\qquad\square$

The symbol $\odot$ denotes the symmetric dyadic product of two vectors $a \odot b := \text{sym}(a \otimes b)$. In the lowest order case, $k = 0$, the basis functions are explicitly given by

$$\boldsymbol{\varphi}_{E_1,0} = \begin{pmatrix} 1 & \frac{1}{2} \\ \frac{1}{2} & 0 \end{pmatrix}, \quad \boldsymbol{\varphi}_{E_2,0} = \begin{pmatrix} 0 & \frac{1}{2} \\ \frac{1}{2} & 1 \end{pmatrix}, \quad \boldsymbol{\varphi}_{E_3,0} = \begin{pmatrix} 0 & -\frac{1}{2} \\ -\frac{1}{2} & 0 \end{pmatrix}. \tag{5.2.44}$$

Segments: In one dimension on the reference segment the Regge elements coincide with L^2-conforming discontinuous finite elements.

$$\overline{}$$
$$1 \qquad 2 \qquad\qquad\qquad\qquad \lambda_1 = (1-x)$$
$$\lambda_2 = x$$

Figure 5.9.: Reference segment.

Thus, a basis of polynomial order k is given by the Legendre polynomials, see Figure 5.9,

$$\boldsymbol{\varphi}_i = l_i(\lambda_2 - \lambda_1), \quad i = 0, \ldots, k. \tag{5.2.45}$$

Quadrilateral: An edge $E = [e_1, e_2]$ of the quadrilateral pointing from e_1 to e_2, cf. Figure 5.10 can be parameterized by

$$\xi_E = \sigma_{e_2} - \sigma_{e_1} \in [-1, 1].$$

The corresponding tangent vector, outer normal vector, and *edge extension parameter*, which is one on E and zero on the opposite edge, are given by

$$\tau_E = \frac{1}{2}\nabla(\sigma_{e_2} - \sigma_{e_1}), \quad n_E = \nabla(\lambda_{e_1} + \lambda_{e_2}), \quad \lambda_E = \lambda_{e_1} + \lambda_{e_2} \in [0,1].$$
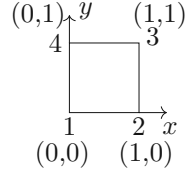
$$\begin{aligned}
\lambda_1 &= (1-x)(1-y), & \sigma_1 &= (1-x) + (1-y), \\
\lambda_2 &= x(1-y), & \sigma_2 &= x + (1-y), \\
\lambda_3 &= xy, & \sigma_3 &= x + y, \\
\lambda_4 &= (1-x)y, & \sigma_4 &= (1-x) + y,
\end{aligned}$$

Figure 5.10.: Reference quadrilateral.

We propose a minimal basis for quadrilateral $H(\operatorname{curl}\operatorname{curl})$ elements such that for an element of order k the polynomial space $[\mathcal{P}^k(\hat{T})]_{\mathrm{sym}}^{2\times2}$ is included. The trace of a quadrilateral element should lead to a valid 1D segment element. This motivates to define the local space on the reference quadrilateral $\hat{T}$ by the following tensor product ansatz

$$V(\hat{T}) := \begin{pmatrix} \mathcal{P}^k(\hat{I}_x)\mathcal{P}^{k+1}(\hat{I}_y^{H^1}) & \mathcal{P}^k(\hat{I}_x)\mathcal{P}^k(\hat{I}_y) \\ \mathrm{sym} & \mathcal{P}^{k+1}(\hat{I}_x^{H^1})\mathcal{P}^k(\hat{I}_y) \end{pmatrix}, \tag{5.2.46}$$

where $\hat{I}_x$ and $\hat{I}_y$ denote the reference segment in x- and y-direction. 1D H^1-conforming elements are denoted by $\hat{I}^{H^1}$, whereas the others correspond to L^2-conforming ones. This yields in the lowest order case $k = 0$ five shape functions, four on the edges and one inner bubble, cf. Figure 5.7,

$$\boldsymbol{\varphi}_{E_1,0} = (1-y)\begin{pmatrix}1&0\\0&0\end{pmatrix}, \quad \boldsymbol{\varphi}_{E_2,0} = y\begin{pmatrix}1&0\\0&0\end{pmatrix}, \quad \boldsymbol{\varphi}_{E_3,0} = (1-x)\begin{pmatrix}0&0\\0&1\end{pmatrix},$$
$$\boldsymbol{\varphi}_{E_4,0} = x\begin{pmatrix}0&0\\0&1\end{pmatrix}, \quad \boldsymbol{\varphi}_{T^1,0,0} = \begin{pmatrix}0&\frac{1}{2}\\\frac{1}{2}&0\end{pmatrix}. \tag{5.2.47}$$

Note, that the corresponding functionals as in (5.2.40) can easily be specified. For the ease of presentation, we specify the dofs only for triangles and tetrahedra explicitly.

5.8 Theorem. *For the reference quadrilateral $\hat{T}$ and $k \geq 0$ the following shape functions build a basis of $V(\hat{T})$:*
Edge functions: *$i \in \{1,2,3,4\}$ $E_i = [e_1, e_2]$*
Lowest order edge functions:

$$\boldsymbol{\varphi}_{E_i,0} := \lambda_{E_i}\,\nabla\tau_{E_i} \odot \nabla\tau_{E_i}, \tag{5.2.48}$$

High order edge functions: for $n = 1, \dots, k$

$$\boldsymbol{\varphi}_{E_i,n} := l_n(\xi_{E_i})\lambda_{E_i}\,\nabla\tau_{E_i} \odot \nabla\tau_{E_i}, \tag{5.2.49}$$

Inner functions: $\xi := 0.5(\sigma_{e_2} - \sigma_{e_1})$, $\eta := 0.5(\sigma_{e_4} - \sigma_{e_1})$, *for* $n, m \leq k - 1$,

$$\boldsymbol{\varphi}_{T^1,n,m} := l_{n+1}(\xi)l_{m+1}(\eta)(\nabla\xi \odot \nabla\eta), \tag{5.2.50a}$$

$$\boldsymbol{\varphi}_{T^2,n,m} := l_n(\xi)l_{m+1}(\eta)(1 - \xi^2)(\nabla\xi \odot \nabla\xi), \tag{5.2.50b}$$

$$\boldsymbol{\varphi}_{T^3,n,m} := l_{n+1}(\xi)l_m(\eta)(1 - \eta^2)(\nabla\eta \odot \nabla\eta). \tag{5.2.50c}$$

Proof. As $\lambda_{e_1} + \lambda_{e_2}$ is one at the edge and zero at the opposite one the edge functions (5.2.48)–(5.2.49) are linearly independent. The first class of inner shapes (5.2.50a) span the off-diagonal entry of the matrix valued function, whereas the others are acting on the diagonal. By noting that $1 - \xi^2 = x(1 - x)$ and $1 - \eta^2 = y(1 - y)$ we deduce that the other two types of inner bubbles are independent of the edge functions and by counting the shape functions $4(k + 1) + (k + 1)^2 + 2k(k + 1) = 2(k + 2)(k + 1) + (k + 1)^2 = \dim V_h(\hat{T})$ the claim follows. $\square$

Tetrahedron: The edges can be parameterized as for triangles and for a face $F = [f_1, f_2, f_3]$ the outer normal vector is given by $n_F = -\nabla\lambda_o = \nabla\lambda_F$ with $\lambda_F = \lambda_{f_1} + \lambda_{f_2} + \lambda_{f_3}$ and λ_o the opposite baricentric coordinate, compare Figure 5.11.
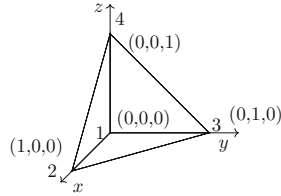
$$\lambda_1 = 1 - x - y - z$$
$$\lambda_2 = x$$
$$\lambda_3 = y$$
$$\lambda_4 = z$$

Figure 5.11.: Reference tetrahedron.

On the reference tetrahedron $\hat{T}$ with the local space $[\mathcal{P}^k(\hat{T})]^{3\times3}_{\text{sym}}$ we define $\{q_{\hat{E},n}\}$, $\{\boldsymbol{q}_{\hat{F},n}\}$, and $\{\boldsymbol{q}_{\hat{T},n}\}$ as the polynomial basis of $\mathcal{P}^k(\hat{E}_i)$ on the edge $\hat{E}_j$, $i = 1, \ldots, 6$, $[\mathcal{P}^{k-1}(\hat{F}_i)]^{3\times3}_{\text{sym}} \cap \hat{n}^{\perp}_F$ on the faces $\hat{F}_i$, $i = 1, \ldots, 4$, and $[\mathcal{P}^{k-1}(\hat{T})]^{3\times3}_{\text{sym}}$ on $\hat{T}$, respectively. Here, $[\mathcal{P}^{k-1}(\hat{F}_i)]^{3\times3}_{\text{sym}} \cap \hat{n}^{\perp}_F$ is understood as a basis $[\mathcal{P}^{k-1}(\hat{T}_{\text{trig}})]^{2\times2}_{\text{sym}}$ mapped onto the face $\hat{F}_i$. Additionally to the edge and inner dofs (5.2.40a)–(5.2.40b) facet dofs are used to fully prescribe the finite element

$$\Psi_{\hat{E}_i,n} : \boldsymbol{\sigma} \mapsto \int_{\hat{E}_i} \boldsymbol{\sigma} : q_{\hat{E},n} t_{\hat{E}} \otimes t_{\hat{E}} \, d\lambda, \tag{5.2.51a}$$

$$\Psi_{\hat{F}_i,n} : \boldsymbol{\sigma} \mapsto \int_{\hat{F}_i} \boldsymbol{\sigma} : \boldsymbol{q}_{\hat{F},n} \, ds, \tag{5.2.51b}$$

$$\Psi_{\hat{T},n} : \boldsymbol{\sigma} \mapsto \int_{\hat{T}} \boldsymbol{\sigma} : \boldsymbol{q}_{\hat{T},n} \, dx. \tag{5.2.51c}$$

If we restrict the tetrahedron $H(\text{curl curl})$ onto a facet it should coincide with a triangular element mapped onto the surface. Thus, the basis is given as follows:

5.9 Theorem. *For the reference tetrahedron $\hat{T}$ and $k \geq 0$ the following shape functions build a basis of $[\mathcal{P}^k(\hat{T})]^{3\times3}_{\text{sym}}$:*

Edge functions: $i \in \{1, \dots, 6\}$ $E_i = [e_1, e_2]$
Lowest order edge functions:

$$\boldsymbol{\varphi}_{E_i,0} := -\nabla\lambda_{e_1} \odot \nabla\lambda_{e_2}, \tag{5.2.52}$$

High order edge functions: for $n = 1, \dots, k$

$$\boldsymbol{\varphi}_{E_{ij},n} := -l_n^S(\lambda_{e_2} - \lambda_{e_1}, \lambda_{e_2} + \lambda_{e_1})\nabla\lambda_{e_1} \odot \nabla\lambda_{e_2}. \tag{5.2.53}$$

Facet functions: $i = 1, \dots, 4$ $F_i = [f_1, f_2, f_3]$, *for* $n + m \le k - 1$

$$\boldsymbol{\varphi}_{F_i^1,n,m} := \varphi_{n,m}^D(\lambda_{f_1} - \lambda_{f_2}, \lambda_{f_3})\lambda_{f_1}(\nabla\lambda_{f_2} \odot \nabla\lambda_{f_3}), \tag{5.2.54a}$$

$$\boldsymbol{\varphi}_{F_i^2,n,m} := \varphi_{n,m}^D(\lambda_{f_1} - \lambda_{f_2}, \lambda_{f_3})\lambda_{f_2}(\nabla\lambda_{f_3} \odot \nabla\lambda_{f_1}), \tag{5.2.54b}$$

$$\boldsymbol{\varphi}_{F_i^3,n,m} := \varphi_{n,m}^D(\lambda_{f_1} - \lambda_{f_2}, \lambda_{f_3})\lambda_{f_3}(\nabla\lambda_{f_1} \odot \nabla\lambda_{f_2}). \tag{5.2.54c}$$

Inner functions: *for* $n + m + o \le k - 2$

$$\boldsymbol{\varphi}_{T^1,n,m,o} := \varphi_{n,m,o}^{D,3}(\lambda_1, \lambda_2, \lambda_3)\lambda_1\lambda_2(\lambda_3 \odot \lambda_4), \tag{5.2.55a}$$

$$\boldsymbol{\varphi}_{T^2,n,m,o} := \varphi_{n,m,o}^{D,3}(\lambda_1, \lambda_2, \lambda_3)\lambda_2\lambda_3(\lambda_4 \odot \lambda_1), \tag{5.2.55b}$$

$$\boldsymbol{\varphi}_{T^3,n,m,o} := \varphi_{n,m,o}^{D,3}(\lambda_1, \lambda_2, \lambda_3)\lambda_3\lambda_4(\lambda_1 \odot \lambda_2), \tag{5.2.55c}$$

$$\boldsymbol{\varphi}_{T^4,n,m,o} := \varphi_{n,m,o}^{D,3}(\lambda_1, \lambda_2, \lambda_3)\lambda_4\lambda_1(\lambda_2 \odot \lambda_3), \tag{5.2.55d}$$

$$\boldsymbol{\varphi}_{T^5,n,m,o} := \varphi_{n,m,o}^{D,3}(\lambda_1, \lambda_2, \lambda_3)\lambda_1\lambda_3(\lambda_2 \odot \lambda_4), \tag{5.2.55e}$$

$$\boldsymbol{\varphi}_{T^6,n,m,o} := \varphi_{n,m,o}^{D,3}(\lambda_1, \lambda_2, \lambda_3)\lambda_2\lambda_4(\lambda_1 \odot \lambda_3). \tag{5.2.55f}$$

Proof. As the Regge triangle basis is recycled for the edge and face shape functions we immediately obtain that these are linearly independent. By construction the inner functions are independent of the edge and face basis. Therefore, the claim follows by counting the dimensions: $6(k+1) + 6k(k+1) + (k-1)k(k+2) = (k+1)(k+2)(k+3) = \dim V(\hat{T})$. $\square$

Hexahedral: Similar to the quadrilaterals the edge $E = [e_1, e_2]$ and face $F = [f_1, f_2, f_3, f_4]$ can be parameterized by, see Figure 5.12,

$$\xi_E = \sigma_{e_2} - \sigma_{e_1} \in [-1, 1], \quad (\xi_F, \eta_F) = (\sigma_{f_1} - \sigma_{f_2}, \sigma_{f_1} - \sigma_{f_4}) \in [-1, 1] \times [-1, 1]$$

and the edge extension parameter, which is zero on all parallel edges, *face extension parameter*, which is zero on the opposite face, and face normal vector are given by

$$\lambda_E = \lambda_{e_1} + \lambda_{e_2}, \quad \lambda_F = \lambda_{f_1} + \lambda_{f_2} + \lambda_{f_3} + \lambda_{f_4}, \quad n_F = -\nabla\lambda_F.$$
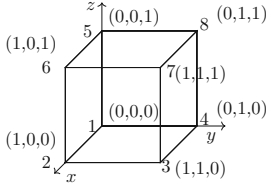
Figure 5.12.: Reference hexahedron.

$$\lambda_1 = (1-x)(1-y)(1-z), \quad \sigma_1 = (1-x)+(1-y)+(1-z)$$
$$\lambda_2 = x(1-y)(1-z), \quad \sigma_2 = x+(1-y)+(1-z)$$
$$\lambda_3 = xy(1-z), \quad \sigma_3 = x+y+(1-z)$$
$$\lambda_4 = (1-x)y(1-z), \quad \sigma_4 = (1-x)+y+(1-z)$$
$$\lambda_5 = (1-x)(1-y)z, \quad \sigma_5 = (1-x)+(1-y)+z$$
$$\lambda_6 = x(1-y)z, \quad \sigma_6 = x+(1-y)+z$$
$$\lambda_7 = xyz, \quad \sigma_7 = x+y+z$$
$$\lambda_8 = (1-x)yz, \quad \sigma_8 = (1-x)+y+z$$

For the construction of hexahedral elements we use a tensor product ansatz as for quadrilateral elements

$$V(\hat{T}) := \tag{5.2.56}$$

$$\begin{pmatrix} \mathcal{P}^k(\hat{I}_x)\mathcal{P}^{k+1}(\hat{I}_y^{H^1})\mathcal{P}^{k+1}(\hat{I}_z^{H^1}) & \mathcal{P}^k(\hat{I}_x)\mathcal{P}^k(\hat{I}_y)\mathcal{P}^{k+1}(\hat{I}_z^{H^1}) & \mathcal{P}^k(\hat{I}_x)\mathcal{P}^{k+1}(\hat{I}_y^{H^1})\mathcal{P}^k(\hat{I}_z) \\ & \mathcal{P}^{k+1}(\hat{I}_x^{H^1})\mathcal{P}^k(\hat{I}_y)\mathcal{P}^{k+1}(\hat{I}_z^{H^1}) & \mathcal{P}^{k+1}(\hat{I}_x^{H^1})\mathcal{P}^k(\hat{I}_y)\mathcal{P}^k(\hat{I}_z) \\ \text{sym} & & \mathcal{P}^{k+1}(\hat{I}_x^{H^1})\mathcal{P}^{k+1}(\hat{I}_y^{H^1})\mathcal{P}^k(\hat{I}_z) \end{pmatrix}.$$

The shape functions are chosen such that the restriction on a face delivers a valid $H(\text{curl curl})$ quadrilateral element.

5.10 Theorem. *For the reference hexahedron $\hat{T}$ and $k \geq 0$ the following shape functions build a basis of $V(\hat{T})$:*
_Edge functions__:_ $i \in \{1, \dots, 12\}$ $E_i = [e_1, e_2]$
Lowest order edge functions:

$$\boldsymbol{\varphi}_{E_i,0} := \lambda_{E_i} \nabla\tau_{E_i} \odot \nabla\tau_{E_i}, \tag{5.2.57}$$

High order edge functions: for $n = 1, \dots, k$

$$\boldsymbol{\varphi}_{E_i,n} := l_n(\xi_{E_i})\lambda_{E_i} \nabla\tau_{E_i} \odot \nabla\tau_{E_i}, \tag{5.2.58}$$

_Face functions__:_ $i \in \{1, \dots, 6\}$ $F_i = [f_1, f_2, f_3, f_4]$, _for $n, m \leq k - 1$,_

$$\boldsymbol{\varphi}_{F_i^1,n,m} := 0.25\,\lambda_{F_i}\,l_{n+1}(\xi_{F_i})l_{m+1}(\eta_{F_i})(\nabla\xi_{F_i} \odot \nabla\eta_{F_i}), \tag{5.2.59a}$$

$$\boldsymbol{\varphi}_{F_i^2,n,m} := 0.25\,\lambda_{F_i}\,l_n(\xi_{F_i})l_{m+1}(\eta_{F_i})(1 - \xi_{F_i}^2)(\nabla\xi_{F_i} \odot \nabla\xi_{F_i}), \tag{5.2.59b}$$

$$\boldsymbol{\varphi}_{F_i^3,n,m} := 0.25\,\lambda_{F_i}\,l_{n+1}(\xi_{F_i})l_m(\eta_{F_i})(1 - \eta_{F_i}^2)(\nabla\eta_{F_i} \odot \nabla\eta_{F_i}). \tag{5.2.59c}$$

Inner functions: $\xi := \sigma_{e_2} - \sigma_{e_1}$, $\eta := \sigma_{e_4} - \sigma_{e_1}$, $\zeta := \sigma_{e_5} - \sigma_{e_1}$, *for* $m, n, o \leq k$,

$$\boldsymbol{\varphi}_{T^1,m,n,o} := l_{m-1}(\xi)l_n(\eta)l_o(\zeta)(1-\xi^2)(\nabla\eta \odot \nabla\zeta), \tag{5.2.60a}$$

$$\boldsymbol{\varphi}_{T^2,m,n,o} := l_m(\xi)l_{n-1}(\eta)l_o(\zeta)(1-\eta^2)(\nabla\xi \odot \nabla\zeta), \tag{5.2.60b}$$

$$\boldsymbol{\varphi}_{T^3,m,n,o} := l_m(\xi)l_n(\eta)l_{o-1}(\zeta)(1-\zeta^2)(\nabla\xi \odot \nabla\eta), \tag{5.2.60c}$$

$$\boldsymbol{\varphi}_{T^4,m,n,o} := l_m(\xi)l_{n-1}(\eta)l_{o-1}(\zeta)(1-\eta^2)(1-\zeta^2)(\nabla\xi \odot \nabla\xi), \tag{5.2.60d}$$

$$\boldsymbol{\varphi}_{T^5,m,n,o} := l_{m-1}(\xi)l_n(\eta)l_{o-1}(\zeta)(1-\xi^2)(1-\zeta^2)(\nabla\eta \odot \nabla\eta), \tag{5.2.60e}$$

$$\boldsymbol{\varphi}_{T^6,m,n,o} := l_{m-1}(\xi)l_{n-1}(\eta)l_o(\zeta)(1-\xi^2)(1-\eta^2)(\nabla\zeta \odot \nabla\zeta). \tag{5.2.60f}$$

Proof. As the quadrilateral basis is used for the faces the independence of edge and face shape functions follows immediately. The inner shapes are constructed such that the are linearly independent of edge and face basis. Thus, by counting the shape functions $12(k+1) + 6((k+1)^2 + 2k(k+1)) + 3(k(k+1)^2 + k^2(k+1)) = 3(k+2)^2(k+1) + 3(k+1)^2(k+2) = \dim V(\hat{T})$ we conclude the proof. $\qquad\square$

Prism: The two triangular and three quadrilateral faces can be parametrized as done before, defining e.g., σ_i accordingly. The normal vector of a triangular $F = [f_1, f_2, f_3]$ and quadrilateral $F = [f_1, f_2, f_3, f_4]$ face is given by

$$n_F = -\nabla\mu_{f_1}, \qquad \lambda_F = \lambda_{f_1} + \lambda_{f_2} + \lambda_{f_3} + \lambda_{f_4}, \quad n_F = \frac{1}{2}\nabla\lambda_F.$$
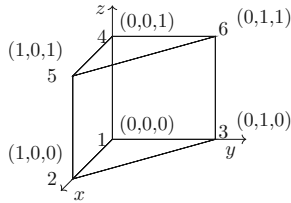
$$\begin{aligned} \lambda_1 &= 1 - x - y, & \mu_1 &= 1 - z \\ \lambda_2 &= x, & \mu_2 &= 1 - z \\ \lambda_3 &= y, & \mu_3 &= 1 - z \\ \lambda_4 &= 1 - x - y, & \mu_4 &= z \\ \lambda_5 &= x, & \mu_5 &= z \\ \lambda_6 &= y, & \mu_6 &= z \end{aligned}$$

Figure 5.13.: Reference prism.

The prismatic reference element is a bit more involved than the tetrahedron or hexahedral element due to the "mixture" of triangle and quadrilateral faces and the resulting different handling between x, y and z direction. The prismatic element can be represented by a tensor product of the 2D reference triangle in the x, y plane and a segment in z-direction $\hat{T} = \hat{T}_{\text{trig},x,y} \times \hat{I}_z$. Note that some segments correspond to 1D H^1-conforming elements (denoted by $\hat{I}_z^{H^1}$), whereas others to L^2-conforming ones. The local polynomial space is given by

$$V(\hat{T}) := \begin{pmatrix} \mathcal{P}^k(\hat{T}_{\text{trig},x,y})\mathcal{P}^{k+1}(\hat{I}_z^{H^1}) & \mathcal{P}^k(\hat{T}_{\text{trig},x,y})\mathcal{P}^{k+1}(\hat{I}_z^{H^1}) & (\mathcal{N}_I^k(\hat{T}_{\text{trig},x,y}))_x\mathcal{P}^k(\hat{I}_z) \\ & \mathcal{P}^k(\hat{T}_{\text{trig},x,y})\mathcal{P}^{k+1}(\hat{I}_z^{H^1}) & (\mathcal{N}_I^k(\hat{T}_{\text{trig},x,y}))_y\mathcal{P}^k(\hat{I}_z) \\ \text{sym} & & \mathcal{P}^{k+1}(\hat{T}_{\text{trig},x,y})\mathcal{P}^k(\hat{I}_z) \end{pmatrix}, \tag{5.2.61}$$

where the two-dimensional Nédélec space of first kind in the x, y component $\mathcal{N}_I^k(\hat{T}_{\text{trig},x,y})$, i.e, on $\hat{T}_{\text{trig},x,y}$ of the tensor product, appears in the last column in the first two rows. The upper-left 2×2 submatrix of $V(\hat{T})$ is constructed by the product of the Regge triangle and segment, $V(\hat{T}_{\text{trig},x,y}) \times V(\hat{I}_z)$, the lower-right component by a product of H^1-conforming triangle element with a Regge (or equivalently L^2-conforming) segment element, and the z-x and z-y components (and due to symmetry also the x-z and y-z components) by a product of a Nédélec triangular element of first kind with a L^2-conforming segment.

The shape functions have to be constructed such that the restriction on a triangle or quadrilateral face delivers a valid $H(\operatorname{curl}\operatorname{curl})$ triangle or quadrilateral element, respectively. E.g., in the lowest order case we obtain twelve shape functions, nine for the edges and three for the quadrilateral faces, which is the correct number for obtaining valid traces. Motivated by this and the tensor-product ansatz the basis is given by (the Nédélec triangular basis for the inner bubbles is taken from [239]):

5.11 Theorem. *For the reference prism $\hat{T}$ and $k \geq 0$ the following shape functions build a basis of $V(\hat{T})$:*

Edge functions:

Lowest order edge functions: *Horizontal edges:* $i \in \{1, \ldots, 6\}$ $E_i = [e_1, e_2]$

$$\boldsymbol{\varphi}_{E_i^H, 0} := -\mu_{e_1} \nabla\lambda_{e_1} \odot \nabla\lambda_{e_2}, \qquad (5.2.62)$$

Vertical edges: $i \in \{1, \ldots, 3\}$ $E_i = [e_1, e_2]$

$$\boldsymbol{\varphi}_{E_i^V} := \lambda_{e_1} \nabla\mu_{e_1} \otimes \nabla\mu_{e_1}, \qquad (5.2.63)$$

High order edge functions: *for $n = 1, \ldots, k$*

Horizontal edges: $i \in \{1, \ldots, 6\}$ $E_i = [e_1, e_2]$

$$\boldsymbol{\varphi}_{E_i^H, n} := -l_n(\sigma_{e_2} - \sigma_{e_1})\mu_{e_1} \nabla\lambda_{e_1} \odot \nabla\lambda_{e_2}, \qquad (5.2.64)$$

Vertical edges: $i \in \{1, \ldots, 3\}$ $E_i = [e_1, e_2]$

$$\boldsymbol{\varphi}_{E_i^V} := l_n(\mu_{e_2} - \mu_{e_1})\lambda_{e_1} \nabla\mu_{e_1} \otimes \nabla\mu_{e_1}, \qquad (5.2.65)$$

Face functions:

Triangular face, $i \in \{1, 2\}$ $F_i = [f_1, f_2, f_3]$ *for $n + m \leq k - 1$*

$$\boldsymbol{\varphi}_{F_i^1, n, m} := \mu_{e_1} \varphi_{n,m}^D(\lambda_{f_2} - \lambda_{f_1}, \lambda_{f_3})\lambda_{f_1}(\nabla\lambda_{f_2} \otimes \nabla\lambda_{f_3}), \qquad (5.2.66\text{a})$$

$$\boldsymbol{\varphi}_{F_i^2, n, m} := \mu_{e_1} \varphi_{n,m}^D(\lambda_{f_2} - \lambda_{f_1}, \lambda_{f_3})\lambda_{f_2}(\nabla\lambda_{f_3} \otimes \nabla\lambda_{f_1}), \qquad (5.2.66\text{b})$$

$$\boldsymbol{\varphi}_{F_i^3, n, m} := \mu_{e_1} \varphi_{n,m}^D(\lambda_{f_2} - \lambda_{f_1}, \lambda_{f_3})\lambda_{f_3}(\nabla\lambda_{f_1} \otimes \nabla\lambda_{f_2}), \qquad (5.2.66\text{c})$$

Quadrilateral face, $i \in \{1, 2, 3\}$ $F_i = [f_1, f_2, f_3, f_4]$ with horizontal edge $[f_1, f_2^*]$, $f_2^* = \begin{cases} f_2 & \text{if } \mu_{f_1} = \mu_{f_2} \\ f_4 & \text{else} \end{cases}$, $w := 0.5(\lambda_{f_1} \nabla\lambda_{f_2^*} - \lambda_{f_2^*} \nabla\lambda_{f_1})$, $\xi := \lambda_{f^{\max}} - \lambda_{f_1}$, $\zeta := \mu_{f^{\max}} - \mu_{f_1}$

---

for $n, m \leq k$

$$\boldsymbol{\varphi}_{F_i^1, n, m} := l_n(\xi) l_m(\zeta) w \odot \nabla \mu_{e_1}, \tag{5.2.67a}$$

$$\boldsymbol{\varphi}_{F_i^2, n, m} := \lambda_{f^{\max}} \lambda_{f_1} \, l_{n-1}(\xi) l_m(\zeta) (\nabla \mu_{e_1} \odot \nabla \mu_{e_1}), \tag{5.2.67b}$$

$$\boldsymbol{\varphi}_{F_i^3, n, m} := \mu_{f^{\max}} \mu_{f_1} \, l_n(\xi) l_{m-1}(\zeta) (\nabla \lambda_{f^{\max}} \odot \nabla \lambda_{f_1}), \tag{5.2.67c}$$

Inner functions: $\zeta := \mu_4 - \mu_1$, $n, m, o \geq 0$

$n + m \leq k - 1, o \leq k - 1:$

$$\boldsymbol{\varphi}_{T^1, n, m, o} := \varphi_{n,m}^D(\lambda_2 - \lambda_1, \lambda_3) l_o(\zeta) \mu_1 \mu_4 \lambda_1 \nabla \lambda_2 \odot \nabla \lambda_3, \tag{5.2.68a}$$

$$\boldsymbol{\varphi}_{T^2, n, m, o} := \varphi_{n,m}^D(\lambda_2 - \lambda_1, \lambda_3) l_o(\zeta) \mu_1 \mu_4 \lambda_2 \nabla \lambda_3 \odot \nabla \lambda_1, \tag{5.2.68b}$$

$$\boldsymbol{\varphi}_{T^3, n, m, o} := \varphi_{n,m}^D(\lambda_2 - \lambda_1, \lambda_3) l_o(\zeta) \mu_1 \mu_4 \lambda_3 \nabla \lambda_1 \odot \nabla \lambda_2, \tag{5.2.68c}$$

$n + m \leq k - 2, o \leq k :$

$$\boldsymbol{\varphi}_{T^4, n, m, o} := \varphi_{n,m}^D(\lambda_2 - \lambda_1, \lambda_3) l_o(\zeta) \lambda_1 \lambda_2 \lambda_3 \nabla \zeta \odot \nabla \zeta, \tag{5.2.68d}$$

$$\boldsymbol{\varphi}_{T^5, n, m, o} := \nabla(\varphi_{n,m}^D(\lambda_2 - \lambda_1, \lambda_3) \lambda_1 \lambda_2 \lambda_3) \odot \nabla \zeta, \tag{5.2.68e}$$

$n + m \leq k - 1, o \leq k :$

$$\boldsymbol{\varphi}_{T^6, n, m, o} := l_o(\zeta) \varphi_{n,m}^D(\lambda_2 - \lambda_1, \lambda_3) \lambda_1 (\lambda_1 \nabla \lambda_2 - \lambda_2 \nabla \lambda_1) \odot \nabla \zeta, \tag{5.2.68f}$$

$$\boldsymbol{\varphi}_{T^7, m, o} := l_o(\zeta) l_m(\lambda_3 - \lambda_2) \lambda_3 (\lambda_1 \nabla \lambda_2 - \lambda_2 \nabla \lambda_1) \odot \nabla \zeta. \tag{5.2.68g}$$

Proof. As in the previous proofs it can be easily shown that all shape functions are linearly independent. Thus, counting $9(k+1) + 3k(k+1) + 3((k+1)^2 + 2k(k+1)) + \frac{3}{2}k(k+1)k + \frac{1}{2}(k-1)k(k+1) + (k+1)k(k+1) = \frac{3}{2}(k+1)(k+2)(k+2) + \frac{1}{2}(k+2)(k+3)(k+1) + (k+1)(k+3)(k+1) = \dim V(\hat{T})$ concludes the proof. $\qquad\square$

Note, that the horizontal edge of the quadrilateral faces has to be chosen carefully depending on the orientation/rotation of the prism explaining the usage of f^* and $f^{\max}$ (see [239] and references therein for a detailed discussion).

In the lowest order case, $k = 0$, the Nédélec elements of first kind have to be used as part of the tensor product ansatz (5.2.61) to guarantee that the restriction on a quadrilateral facet delivers a valid 2D Regge element. For higher order, $k \geq 1$, it is also possible to use the Nédélec familiy of second kind, i.e., $\mathcal{N}_{II}^k$ instead of $\mathcal{N}_I^k$, which has less inner dofs (compared to the type one triangular elements with same amount of edge dofs) enabling two types of Regge prism elements.

Similarity to $H(\operatorname{div} \operatorname{div})$ elements: In two dimensions, analogically to $H(\operatorname{curl})$ and $H(\operatorname{div})$ elements, the rotated triangular and quadrilateral $H(\operatorname{div} \operatorname{div})$ elements lead to valid $H(\operatorname{curl} \operatorname{curl})$ elements. In [80] e.g., this fact is used to construct a triangular finite element for (3.1.29).

Additional bubbles and different construction based on de'Rham complex: For the quadrilateral and thus, hexahedral and prism we presented the minimal possible local space such that a (L^2-) convergence rate of $k + 1$ for element order k is given as the

Figure 5.14.: Lowest order facet space for triangle and tetrahedron.

polynomial space $[\mathcal{P}^k(T)]^{d \times d}_{\mathrm{sym}}$ is included. One may add additional internal bubbles to improve properties of these elements, especially if non-structured and thus curved or ill-shaped meshes are considered. These bubbles might be motivated by the following (exact) sequence similar to the de'Rham complex in two dimensions (for three dimensions see e.g., [85, 113])

$$[H^1]^d \xrightarrow{\nabla^{\mathrm{sym}}} H(\mathrm{curl}\,\mathrm{curl}) \xrightarrow{\mathrm{curl}^\top \mathrm{curl}} L^2.$$

Further, the used face and inner bubbles can also be (consistently!) constructed in terms of the complex, entailing possible advantages, compare e.g., the de'Rham based construction of H^1, $H(\mathrm{curl})$, and $H(\mathrm{div})$ elements in [239].

5.2.7. Finite element spaces for hybridization

For some techniques as Hybrid Discontinuous Galerkin (HDG) methods [53, 90, 12] or hybridization (enabling static condensation yielding symmetric positive definite systems for some classes of mixed problems) it is useful/essential to break the continuity condition of finite elements and reinforce it in weak sense. Therefore, so-called hybridization or facet spaces have to be used. When breaking the normal continuity of $H(\mathrm{div})$-conforming elements V_h^k the corresponding facet space for hybridization is given by, $\Gamma_N := \partial\Omega\backslash\Gamma_D$,

$$
\begin{aligned}
\mathcal{L}_h^k &:= \mathcal{P}^k(\mathcal{F}_h), \\
\mathcal{L}_{h,0}^k &:= \{\alpha \in \mathcal{L}_h^k \,|\, \alpha = 0 \text{ on } \Gamma_N\},
\end{aligned}
\tag{5.2.69}
$$

i.e., piece-wise polynomials on the skeleton $\mathcal{F}_h$, see Figure 5.14. Reordering the facet terms of the equation

$$\sum_{T \in \mathcal{T}_h} \int_{\partial T} u_h \cdot n \, \delta\alpha_h \, ds = 0 \text{ for all } \delta\alpha_h \in \mathcal{L}_{h,0}^k \tag{5.2.70}$$

for a discontinuous (dc) function in the RT or BDM space $u_h \in V_h^{k,dc}$ yields

$$0 = \sum_{F \in \mathcal{F}_h^{\mathrm{int}}} \int_F (u_h|_{T_1} - u_h|_{T_2}) \cdot n_E \, \delta\alpha_h \, ds + \sum_{F \in \mathcal{F}_h^{\mathrm{bnd}} \cap \Gamma_D} \int_F u_h \cdot n \, \delta\alpha_h \, ds = \sum_{F \in \mathcal{F}_h} \int_F [\![u_{h,n}]\!] \, \delta\alpha_h \, ds, \tag{5.2.71}$$

where $\mathcal{F}_h^{\mathrm{int}}$ and $\mathcal{F}_h^{\mathrm{bnd}}$ denote all interior and boundary facets, respectively. Thus, the normal continuity $[\![u_n]\!] = 0$ and homogeneous Dirichlet boundary $u_{h,n} = 0$ on Γ_D are forced. Note that the essential boundary changes from Γ_D to Γ_N.

For the $H(\text{div div})$ elements we follow [211] by equipping the facet space $\mathcal{L}_h^k$ with the normal vector n_F, see Definition 5.2, such that its functions are facet-wise two-valued differing only in the sign. More precisely, by defining this space as the normal-facet space Γ_h^k we have for $\alpha_h \in \Gamma_h^k$ that $\alpha_{h,n_{T_1}} = -\alpha_{h,n_{T_2}}$. Thus, a normal-normal continuous function with zero normal-normal trace on Γ_D of a function $\boldsymbol{\sigma}_h \in M_h^{dc,k}$ can be achieved by the equation

$$0 = \sum_{T \in \mathcal{T}_h} \int_{\partial T} \boldsymbol{\sigma}_{h,nn}\, \delta\alpha_{h,n}\, ds = \sum_{F \in \mathcal{F}_h} \int_F [\![\boldsymbol{\sigma}_{h,nn}]\!]\, \delta\alpha_h\, ds \text{ for all } \delta\alpha_h \in \Gamma_{h,0}^k. \qquad (5.2.72)$$

If an hierarchical basis is used for the $H(\text{div})$-conforming elements the facet shape functions can directly be used for the hybridization space. Thus we may set

$$\begin{aligned} \Gamma_h^k &= BDM_h^{\text{facet},k}, \\ \Gamma_{h,0}^k &= BDM_{h,0}^{\text{facet},k}. \end{aligned} \qquad (5.2.73)$$

5.3. Finite elements for dual spaces

For all finite elements we presented the dofs $\{\Psi_i\}$, which span the dual space. The shape functions $\{\varphi_i\}$ for a hierarchical basis, however, are in general not bi-orthogonal to the functionals, i.e, $\Psi_i(\varphi_j) \neq \delta_{ij}$. In this section we discuss how a projection operator based on the functionals and the corresponding dual shape functions can be constructed to interpolate arbitrary (sufficiently smooth) functions into the finite element space. This enables also the usage of finite elements for dual spaces directly involved in variational formulations. Further, we present an adaption to obtain a geometry-free procedure. We will apply this framework to the H^1-conforming, $H(\text{div})$-conforming BDM, and Regge elements. The other elements follow the same ideas. Further, we will restrict ourselves to tetrahedral elements, but stress that the concept can directly be adapted to other primitives provided the shape functions and functionals.

H^1 **dual space:** With the functionals (5.2.15) for a fixed polynomial degree $k > 0$ denoted by $\{\Psi_i^V\}_{i=1}^{N_V}, \{\Psi_i^E\}_{i=1}^{N_E}, \{\Psi_i^F\}_{i=1}^{N_F}, \{\Psi_i^T\}_{i=1}^{N_T}$ or all together as $\{\Psi_i\}_{i=1}^{N_k}$ and a hierarchical basis of shape functions $\{\varphi_i\}_{i=1}^{N_k} = \{\varphi_i^V\}_{i=1}^{N_V} \cup \{\varphi_i^E\}_{i=1}^{N_E} \cup \{\varphi_i^F\}_{i=1}^{N_F} \cup \{\varphi_i^T\}_{i=1}^{N_T}$ the interpolation operator reads

$$\begin{aligned} \mathcal{I}_h^k &: C^1(\Omega) \to U_h^k, \\ u &\mapsto \sum_{i=0}^{N_k} \alpha_i\, \varphi_i, \end{aligned} \qquad (5.3.1)$$

where the coefficients α_i are obtained by the following consideration: Let $u_h = \mathcal{I}_h^k(u)$ be the interpolation of a given function u. Then, u_h is the solution of the following system of
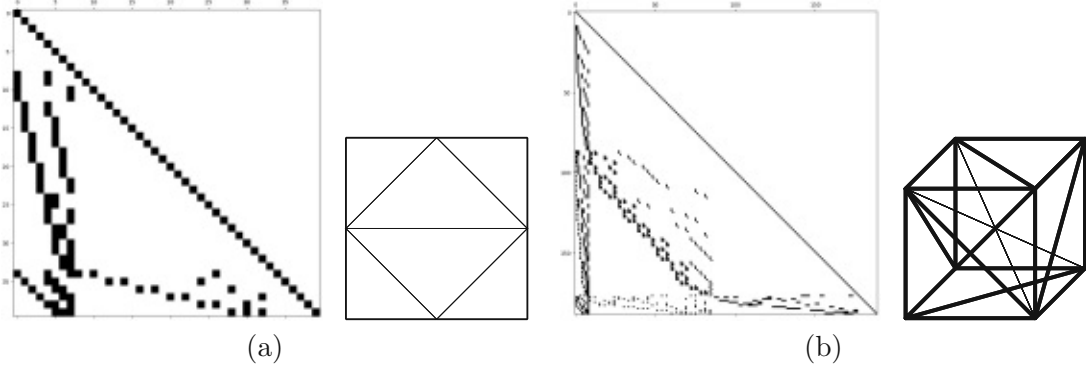
Figure 5.15.: Sparsity pattern of H^1 dual mass matrix $\boldsymbol{M}^D$ (a) Sparsity pattern of six triangles with order three elements. (b) Sparsity pattern of twelve tetrahedra with order four elements.

equations

$$u_h(V) = u(V)$$

$$\sum_{E \in \mathcal{E}_h} \int_E u_h \, q_{\mathcal{E}} \, d\lambda = \sum_{E \in \mathcal{E}_h} \int_E u \, q_{\mathcal{E}} \, d\lambda,$$

$$\sum_{F \in \mathcal{F}_h} \int_F u_h \, q_{\mathcal{F}} \, ds = \sum_{F \in \mathcal{F}_h} \int_E u \, q_{\mathcal{F}} \, ds, \qquad (5.3.2)$$

$$\sum_{T \in \mathcal{T}_h} \int_T u_h \, q_{\mathcal{T}} \, dx = \sum_{T \in \mathcal{T}_h} \int_T u \, q_{\mathcal{T}} \, dx,$$

for all vertices $V \in \mathcal{V}_h$, $q_{\mathcal{E}} \in \mathcal{P}^{k-2}(\mathcal{E}_h)$, $q_{\mathcal{F}} \in \mathcal{P}^{k-3}(\mathcal{F}_h)$, and $q_{\mathcal{T}} \in \mathcal{P}^{k-4}(\mathcal{T}_h)$. In matrix form we obtain the linear equation

$$\boldsymbol{M}^D \langle \alpha_i \rangle = f, \quad \boldsymbol{M}^D = \begin{pmatrix} \boldsymbol{M}_{VV}^D & \boldsymbol{M}_{VE}^D & \boldsymbol{M}_{VF}^D & \boldsymbol{M}_{VT}^D \\ \boldsymbol{M}_{EV}^D & \boldsymbol{M}_{EE}^D & \boldsymbol{M}_{EF}^D & \boldsymbol{M}_{ET}^D \\ \boldsymbol{M}_{FV}^D & \boldsymbol{M}_{FE}^D & \boldsymbol{M}_{FF}^D & \boldsymbol{M}_{FT}^D \\ \boldsymbol{M}_{TV}^D & \boldsymbol{M}_{TE}^D & \boldsymbol{M}_{TF}^D & \boldsymbol{M}_{TT}^D \end{pmatrix}, \quad f = \begin{pmatrix} f_V \\ f_E \\ f_F \\ f_T \end{pmatrix}, \qquad (5.3.3)$$

with $\langle \alpha_i \rangle$ denoting the corresponding coefficient vector of u_h and $(\boldsymbol{M}_{VV}^D)_{ij} = \Psi_i^V(\varphi_j^V)$, $(\boldsymbol{M}_{VE}^D)_{ij} = \Psi_i^V(\varphi_j^E)$, $(f_V)_i = \Psi_i^V(u)$ and analogously for the other components. There holds by construction, see e.g., [239] for an explicit construction of a hierarchical basis, $\Psi_i^V(\varphi_j^E) = \Psi_i^V(\varphi_j^F) = \Psi_i^V(\varphi_j^T) = 0$, $\Psi_i^E(\varphi_j^F) = \Psi_i^E(\varphi_j^T) = 0$, and $\Psi_i^F(\varphi_j^T) = 0$ and thus, e.g., $\boldsymbol{M}_{ET}^D = 0$, resulting in a lower block triangular dual mass matrix, see Figure 5.15. This structure can be exploited for inverting $\boldsymbol{M}^D$ efficiently. Note that the matrix is not symmetric, as in general e.g., $\Psi_i^T(\varphi_j^E) \neq 0$.

We mention that the interpolation operator is often defined/characterized element-wise

by the equations

$$u(V) = \mathcal{I}_h u(V), \qquad \text{for all } \mathcal{V}(T),$$

$$\int_E (u - \mathcal{I}_h u)\, q\, d\lambda = 0, \quad \text{for all } q \in \mathcal{P}^{k-2}(E), E \subset \mathcal{E}(T),$$

$$\int_F (u - \mathcal{I}_h u)\, q\, ds = 0, \quad \text{for all } q \in \mathcal{P}^{k-3}(F), F \subset \mathcal{F}(T), \qquad (5.3.4)$$

$$\int_T (u - \mathcal{I}_h u)\, q\, dx = 0, \quad \text{for all } q \in \mathcal{P}^{k-4}(T).$$

By transforming the dual shape basis in the correct way it is possible to obtain a geometry-free matrix, i.e., all element-matrices coincide. To be more precise, with the following transformations for the dual shape basis

$$q_E \circ \Phi = \frac{1}{J_E} \hat{q}_E, \qquad q_F \circ \Phi = \frac{1}{J_F} \hat{q}_F, \qquad q_T \circ \Phi = \frac{1}{J_T} \hat{q}_T, \qquad (5.3.5)$$

we obtain with a change of variables

$$\int_E \varphi^E q_E\, d\lambda = \int_{\hat{E}} \varphi^{\hat{E}} \hat{q}_E\, d\hat{\lambda}, \quad \int_F \varphi^F q_F\, ds = \int_{\hat{F}} \varphi^{\hat{F}} \hat{q}_F\, d\hat{s}, \quad \int_T \varphi^T q_T\, dx = \int_{\hat{T}} \varphi^{\hat{T}} \hat{q}_T\, d\hat{x}.$$

Therefore, we only need to compute (all permutations of) one element and fill the dual mass matrix $\boldsymbol{M}^D$ or use the information for a matrix-free algorithm.

$H(\mathrm{div})$ **BDM dual space:** The dual space for BDM elements follows the same ideas. Note, however, that the inner dual shapes (5.2.20) are more involved because the Nédélec space of first kind $\mathcal{N}_I$ is used. By using an appropriate (hierarchical) basis for BDM elements, i.e., $\Psi_i^F(\varphi_j^T) = 0$, a lower block triangular matrix is obtained. To be independent of the geometry the dual basis has to be transformed by

$$q_F \circ \Phi = \hat{q}_F, \qquad q_T \circ \Phi = \boldsymbol{G}^{-\top} \hat{q}_T. \qquad (5.3.6)$$

There holds with (5.1.5)

$$\int_F \varphi_F \cdot n\, q_F\, ds = \int_{\hat{F}} J_F \left(\frac{1}{J_T} \boldsymbol{G} \hat{\varphi}_F \right) \cdot \left(\frac{J_T}{J_F} \boldsymbol{G}^{-\top} \hat{n} \hat{q}_F \right) d\hat{s} = \int_{\hat{F}} \hat{\varphi}_F \cdot \hat{n} \hat{q}_F\, d\hat{s},$$

$$\int_T \varphi_T \cdot q_T\, dx = \int_{\hat{T}} \hat{\varphi}_T \cdot \hat{q}_T\, d\hat{x},$$

i.e., the covariant transformation for $H(\mathrm{curl})$-conforming elements is used motivating the choice of $\mathcal{N}_I$ as dof.

$H(\mathrm{curl\, curl})$ **dual space:** For a detailed construction in two dimensions we refer to [165]. There holds by our hierarchical construction from Section 5.2.6 $\Psi_i^E(\boldsymbol{\varphi}_j^F) = \Psi_i^E(\boldsymbol{\varphi}_j^T) = 0$

and $\Psi_i^F(\varphi_j^T) = 0$ and thus, we again obtain a lower block triangular dual mass matrix. The corresponding transformation rules for the dual basis are given by

$$q_E \circ \Phi := J_E \hat{q}_E, \qquad \boldsymbol{q}_F \circ \Phi := \frac{1}{J_F} \boldsymbol{G} \hat{\boldsymbol{q}}_F \boldsymbol{G}^\top, \qquad \boldsymbol{q}_T \circ \Phi := \frac{1}{J_T} \boldsymbol{G} \hat{\boldsymbol{q}}_T \boldsymbol{G}^\top, \quad (5.3.7)$$

which yields, involving (5.1.5),

$$\int_E \boldsymbol{\varphi}_E : q_E t \otimes t \, d\lambda = \int_{\hat{E}} J_E \boldsymbol{G}^{-\top} \hat{\boldsymbol{\varphi}}_E \boldsymbol{G}^{-1} : \frac{\hat{q}_E}{J_E} (\boldsymbol{G}\hat{t}) \otimes (\boldsymbol{G}\hat{t}) \, d\hat{\lambda} = \int_{\hat{E}} \hat{\boldsymbol{\varphi}}_E : \hat{q}_E \hat{t} \otimes \hat{t} \, d\hat{\lambda},$$

$$\int_F \boldsymbol{\varphi}_F : \boldsymbol{q}_F \, ds = \int_{\hat{F}} J_F \boldsymbol{G}^{-\top} \hat{\boldsymbol{\varphi}}_F \boldsymbol{G}^{-1} : \frac{1}{J_F} \boldsymbol{G} \hat{\boldsymbol{q}}_F \boldsymbol{G}^\top \, d\hat{s} = \int_{\hat{F}} \hat{\boldsymbol{\varphi}}_F : \hat{\boldsymbol{q}}_F \, d\hat{s},$$

$$\int_T \boldsymbol{\varphi}_T : \boldsymbol{q}_T \, dx = \int_{\hat{T}} J_T \boldsymbol{G}^{-\top} \hat{\boldsymbol{\varphi}}_T \boldsymbol{G}^{-1} : \frac{1}{J_T} \boldsymbol{G} \hat{\boldsymbol{q}}_T \boldsymbol{G}^\top \, d\hat{x} = \int_{\hat{T}} \hat{\boldsymbol{\varphi}}_T : \hat{\boldsymbol{q}}_T \, d\hat{x}.$$

Other dual spaces: The Nédélec space of second kind involves the RT space for faces and inner dofs in three dimensions (and only inner dofs in 2D). The Piola transformation is used for the $H(\mathrm{curl})$ dual shapes to obtain a matrix-free discretization. $H(\mathrm{div\,div})$ dual space elements are straight forward following the construction of the dual shape basis of $H(\mathrm{curl\,curl})$ together with the appropriate transformations.

5.4. Discretization of TDNNS method

After the finite element spaces have been introduced we can describe the discretized *tangential displacement and tangential-tangential stress continuous* (TDNNS) method of Section 4.3. Therefore, the normal-normal continuous $H(\mathrm{div\,div})$ space M_h (5.2.35) for the stress and the $H(\mathrm{curl})$-conforming tangential continuous Nédélec space of second kind V_h (5.2.26) for the displacement field are used. Note that the essential boundary conditions for $u_h \in V_h$ and $\boldsymbol{\sigma}_h \in M_h$ are the Dirichlet and Neumann boundary, respectively.

Following (4.3.1) the problem reads:

5.12 Problem. *For given external forces f and g and Dirichlet data u_D find stress and displacement fields $(\boldsymbol{\sigma}_h, u_h) \in M_h^k \times V_h^k$ such that $(\boldsymbol{\sigma}_h)_{nn} = g_n$ on Γ_N, $(u_h)_t = (u_D)_t$ on Γ_D and for all $(\delta\boldsymbol{\sigma}_h, \delta u_h) \in M_{h,0}^k \times V_{h,0}^k$*

$$\int_\Omega \mathbb{C}^{-1} \boldsymbol{\sigma}_h : \delta\boldsymbol{\sigma}_h \, dx + \langle \mathrm{div}(\delta\boldsymbol{\sigma}_h), u_h \rangle_{\mathcal{T}_h} = \int_{\Gamma_D} (u_D)_n \, (\boldsymbol{\sigma}_h)_{nn} \, ds, \qquad (5.4.1a)$$

$$\langle \mathrm{div}(\boldsymbol{\sigma}_h), \delta u_h \rangle_{\mathcal{T}_h} = -\int_\Omega f \cdot \delta u_h \, dx - \int_{\Gamma_N} g_t \cdot (\delta u_h)_t \, ds. \qquad (5.4.1b)$$

The corresponding Lagrangian is given by

$$\mathcal{L}(u_h, \boldsymbol{\sigma}_h) := -\frac{1}{2} \int_\Omega \mathbb{C}^{-1} \boldsymbol{\sigma}_h : \boldsymbol{\sigma}_h \, dx - \langle u_h, \mathrm{div}(\boldsymbol{\sigma}_h) \rangle_{\mathcal{T}_h} - W_{\mathrm{ext}}^{\mathrm{TDNNS}} \to \min_{u_h \in V_h^k} \max_{\boldsymbol{\sigma}_h \in M_h^k}, \quad (5.4.2)$$

with the work of external forces

$$W_{\text{ext}}^{\text{TDNNS}} = \int_\Omega f \cdot u_h \, dx + \int_{\Gamma_N} g_t \cdot (u_h)_t \, ds - \int_{\Gamma_D} (u_D)_n \, (\boldsymbol{\sigma}_h)_{nn}. \tag{5.4.3}$$

The duality pairing $\langle \cdot, \cdot \rangle_{\mathcal{T}_h}$ is defined in the sense of distributions as neither the divergence of the stress $\boldsymbol{\sigma}_h$ nor the gradient of the displacement field u_h is globally a regular function [171]

$$\langle \text{div}(\boldsymbol{\sigma}_h), u_h \rangle_{\mathcal{T}_h} := \sum_{T \in \mathcal{T}_h} \left(\int_T \text{div}(\boldsymbol{\sigma}_h) \cdot u_h \, dx - \int_{\partial T} (\boldsymbol{\sigma}_h)_{nt} \cdot (u_h)_t \, ds \right)$$
$$= - \sum_{T \in \mathcal{T}_h} \left(\int_T \boldsymbol{\sigma}_h : \nabla u_h \, dx - \int_{\partial T} (\boldsymbol{\sigma}_h)_{nn}(u_h)_n \, ds \right) = -\langle \boldsymbol{\epsilon}(u_h), \boldsymbol{\sigma}_h \rangle_{\mathcal{T}_h}.$$
$$\tag{5.4.4}$$

Note, that in the boundary integrals in (5.4.4) always one variable is continuous whereas the other jumps over elements. Therefore, the boundary terms are well-defined in the sense of distributions.

After discretization, the above saddle point problem leads to a linear system of equations with an indefinite system matrix of the form

$$\begin{pmatrix} A & B^\top \\ B & 0 \end{pmatrix} \begin{pmatrix} \underline{\boldsymbol{\sigma}} \\ \underline{u} \end{pmatrix} = \underline{f}, \tag{5.4.5}$$

where $\underline{\boldsymbol{\sigma}}$, $\underline{u}$, and $\underline{f}$ represent the coefficient vectors of the finite elements $\boldsymbol{\sigma}_h$ and u_h and the right-hand side f, respectively. The displacement u can be interpreted as Lagrange multiplier enforcing the force balance equation $-\text{div}(\boldsymbol{\sigma}) = f$.

Nevertheless, a positive definite system matrix can be regained using hybridization techniques. Therefore, the normal-normal continuity of the stresses is broken, such that the normal-normal component of $\boldsymbol{\sigma}_h$ may be discontinuous across interfaces and does not necessarily satisfy the boundary conditions on Γ_N anymore. To reinforce the lost continuity and boundary conditions a Lagrange multiplier α_h is introduced. The discontinuous stress space is denoted by M_h^{dc}. More precisely, let $\alpha_h \in \Gamma_h$ from the hybridization space (5.2.73). Further, α_h has to satisfy the essential boundary conditions on Γ_D. Then the hybridized TDNNS problem reads:

5.13 Problem. *For given external forces f and g and Dirichlet data u_D find stress, displacement, and hybridization fields $(\boldsymbol{\sigma}_h, u_h, \alpha_h) \in M_h^{\text{dc},k} \times V_h^k \times \Gamma_h^k$ such that $(\alpha_h)_n =$*

$(u_D)_n$, $(u_h)_t = (u_D)_t$ *on* Γ_D *and for all* $(\delta\boldsymbol{\sigma}_h, \delta u_h, \delta\alpha_h) \in M_h^{\mathrm{dc},k} \times V_{h,0}^k \times \Gamma_{h,0}^k$

$$\int_\Omega \mathbb{C}^{-1}\boldsymbol{\sigma}_h : \delta\boldsymbol{\sigma}_h \, dx + \langle \mathrm{div}(\delta\boldsymbol{\sigma}_h), u_h \rangle_{\mathcal{T}_h} - \sum_{T \in \mathcal{T}_h} \int_{\partial T} (\alpha_h)_n (\delta\boldsymbol{\sigma}_h)_{nn} \, ds = 0, \qquad (5.4.6a)$$

$$\langle \mathrm{div}(\boldsymbol{\sigma}_h), \delta u_h \rangle_{\mathcal{T}_h} \hspace{5cm} = F(\delta u_h),$$
$$(5.4.6b)$$

$$- \sum_{T \in \mathcal{T}_h} \int_{\partial T} (\delta\alpha_h)_n (\boldsymbol{\sigma}_h)_{nn} \, ds \hspace{3.5cm} = G(\delta\alpha_h),$$
$$(5.4.6c)$$

with $F(\delta u_h) := -\int_\Omega f \cdot \delta u \, dx - \int_{\Gamma_N} g_t \cdot (\delta u_h)_t \, ds$ *and* $G(\delta\alpha_h) := -\int_{\Gamma_N} g_n (\delta\alpha_h)_n \, ds$.

The Lagrangian changes to

$$\mathcal{L}(u_h, \boldsymbol{\sigma}_h, \alpha_h) := -\frac{1}{2} \int_\Omega \mathbb{C}^{-1}\boldsymbol{\sigma}_h : \boldsymbol{\sigma}_h \, dx - \langle u_h, \mathrm{div}(\boldsymbol{\sigma}_h) \rangle_{\mathcal{T}_h}$$
$$+ \sum_{T \in \mathcal{T}_h} \int_{\partial T} (\boldsymbol{\sigma}_h)_{nn} (\alpha_h)_n \, ds - W_{ext}^{\mathrm{TDNNSh}} \to \min_{u_h \in V_h^k} \min_{\alpha_h \in \Gamma_h^k} \max_{\boldsymbol{\sigma}_h \in M_h^{\mathrm{dc},k}}, \qquad (5.4.7)$$

and the work of external forces

$$W_{\mathrm{ext}}^{\mathrm{TDNNSh}} = \int_\Omega f \cdot u_h \, dx + \int_{\Gamma_N} (g_t \cdot (u_h)_t + g_n (\alpha_h)_n) \, ds. \qquad (5.4.8)$$

As described in Section 5.2.7, α_h enforces in equation (5.4.6c) the normal-normal continuity of $\boldsymbol{\sigma}_h$ and the boundary condition. Combining the surface terms in (5.4.6a) one observes that the Lagrange multiplier α_h has the physical meaning of the normal component of the displacement

$$\int_{\partial T} ((u_h)_n - (\alpha_h)_n) (\delta\boldsymbol{\sigma}_h)_{nn} \, ds. \qquad (5.4.9)$$

As for $\boldsymbol{\sigma}_h$ and α_h the same polynomial order is used, the hybridized system (5.4.6) is equivalent to the original one (5.4.1).

However, the discontinuous stress $\boldsymbol{\sigma}_h$ in (5.4.7) does not have any coupling dofs and thus, one can use static condensation to eliminate it at element level, reducing the number of total dofs drastically for the final system, and making it therefore symmetric and positive definite (spd) again

$$\begin{pmatrix} A & B^\top \\ B & 0 \end{pmatrix} \begin{pmatrix} \underline{\boldsymbol{\sigma}} \\ \left(\underline{\underline{u}} \atop \underline{\alpha} \right) \end{pmatrix} = \begin{pmatrix} 0 \\ \underline{f} \end{pmatrix},$$
$$(5.4.10)$$
$$\underline{\boldsymbol{\sigma}} = -A^{-1}B^\top \begin{pmatrix} \underline{u} \\ \underline{\alpha} \end{pmatrix}, \qquad -BA^{-1}B^\top \begin{pmatrix} \underline{u} \\ \underline{\alpha} \end{pmatrix} = \underline{f}.$$

From the first equation $\underline{\boldsymbol{\sigma}}$ can be explicitly expressed in terms of $\underline{u}$ and $\underline{\alpha}$. This identity is inserted into the second equation leading to the Schur-complement matrix $-BA^{-1}B^{\top}$. Note that A is a block diagonal matrix and thus cheap to invert.

After the linear TDNNS method has been introduced we are in the position to extend it to the large deformation (and thus nonlinear) regime.

6. Nonlinear elasticity

For the ease of presentation we will assume throughout this chapter that homogeneous Dirichlet data $u_D \equiv 0$ are prescribed on the whole boundary $\Gamma_D = \partial\Omega$, if not stated otherwise. Further, the subscript h is neglected for the finite element functions for a more compact notation. We strongly emphasis that all methods can easily be adopted including non-homogeneous Dirichlet data and mixed boundary conditions. For the hyperelastic potential Ψ we require that it is objective. Throughout this section we denote the finite element spaces (5.2.13), (5.2.14), (5.2.26), (5.2.35), (5.2.38), and (5.2.73) by U_h, Q_h, V_h, M_h, $\mathcal{R}_h$, and Γ_h, respectively.

We will start by summarizing mixed formulations available for nonlinear elasticity. Then, we will propose extensions of the linear TDNNS method for compressible and (nearly) incompressible materials.

6.1. State of the art

In analogy to the linear case we briefly summarize some extensions and new (mixed) methods from linear to finite elasticity.

Standard method: For the standard discretization the Lagrangian elements $[U_h^k]^d$ are taken. Together with the notation $\boldsymbol{F} = \boldsymbol{I} + \nabla u$, $\boldsymbol{C} = \boldsymbol{F}^\top \boldsymbol{F}$, and $\boldsymbol{\Sigma} = 2\partial_{\boldsymbol{C}}\Psi(\boldsymbol{C})$ we obtain:

> **6.1 Problem.** *Find $u \in [U_{h,0}^k]^d$ such that for all $\delta u \in [U_{h,0}^k]^d$*
>
> $$\int_\Omega \boldsymbol{F}\boldsymbol{\Sigma} : \nabla\delta u \, dx = \int_\Omega f \cdot \delta u \, dx. \qquad (6.1.1)$$

The corresponding minimization problem is given by

$$\mathcal{W}(u) := \int_\Omega \Psi(\boldsymbol{F}(u)) - f \cdot u \, dx \to \min_{u \in [U_h^k]^d} \qquad (6.1.2)$$

and one can directly use e.g., Newton's method to solve the nonlinear equation. To improve the convergence behavior mostly loadsteps are considered by starting with the zero solution and then increasing the right-hand side.

The problems discussed in Section 4.1 are inherited from the linear method. This motivates to extend mixed methods and their beneficial properties compared to the primal formulation to the geometric nonlinear case and nonlinear material laws.

Mixed, enhanced assumed strain, and HDG methods: A mixed three-field formulation including finite-deformation elasto-plasticity has been proposed in [208].

The enhanced strain method from [210] has been extended to nonlinear elasticity [209, 205]. A non-linear mixed-enhanced method with independent deformation gradient and first Piola–Kirchhoff stress was proposed and generalized to large deformation in [129, 130]. Recently, methods based on polyconvex strain energy-functionals, where the deformation gradient $\boldsymbol{F}$, cofactor matrix $\mathrm{cof}(\boldsymbol{F})$, and determinant J are treated separately in the context of mixed and enhanced assumed strain methods, have been introduced, see e.g., [176, 201, 54, 55].

A reduced-integration stabilized brick element for large deformations has been introduced in [189]. Therein, the stabilization technique is based on the enhanced strain method. A different brick solid-shell element based on reduced integration and hourglass stabilizations has been proposed in [187]. Lowest-order locking-free hybrid discontinuous Galerkin elements for finite elasticity have been recently developed in [237, 43]. This approach was shown in [188] to be equivalent to hourglass stabilization and reduced integration. An HDG method for thick and thin nonlinear elastic structures has been proposed in [223].

In [6] the compatible-strain mixed finite element method (CSMFEMs) for two-dimensional compressible finite elasticity problems has been proposed. This method falls in the class of three-field formulations and has also been generalized to three dimensions and incompressible elasticity in [203, 204]. Based on a Hilbert complex of nonlinear elasticity [7] the displacement u is chosen to be discretized with $H^1(\Omega)$-conforming elements, its gradient $\boldsymbol{K} = \nabla u$ by Nédélec and the first Piola–Kirchhoff stress tensor by Raviart–Thomas elements. In the incompressible setting the $L^2(\Omega)$-conforming space is taken for the pressure p.

6.2. Nonlinear TDNNS for compressible materials

For nonlinear material laws the TDNNS methods (5.4.2) and (5.4.7) cannot be directly applied in general. The gradient of the displacement field is a distribution rather than a L^2 function due to the weaker tangential continuity of u. Therefore, multiplication is not well-defined, which is, however, essential for nonlinear material laws. An updated Lagrangian scheme has been recently proposed and discussed in [175] to enable these sort of materials avoiding multiplication of distributions.

We will use the Hu–Washizu principle, see Section 4.4, introducing an additional unknown leading to a three- or five-field formulation based on [163]. We will propose three different approaches leading to valid methods. In the first one we lift the distributional gradient $\nabla u + \boldsymbol{I}$ to the deformation gradient $\boldsymbol{F}$ as a new unknown, which is again a square-integrable function. The second approach uses that for objective materials Theorem 2.2 guarantees that the energy potential Ψ depends on the Cauchy–Green strain tensor $\boldsymbol{C}$ taking it as an additional field. The third method combines the first two ideas by first introducing a lifting to an independent $\boldsymbol{F}$ followed by a projection to a new $\boldsymbol{C}$, i.e., a five-field formulation is used.

Throughout this section, we will use the notations $\boldsymbol{F}(u) := \boldsymbol{I} + \nabla u$, $\boldsymbol{C}(u) := \boldsymbol{F}(u)^\top \boldsymbol{F}(u)$, and $\boldsymbol{E}(u) := 0.5(\boldsymbol{C}(u) - \boldsymbol{I})$ indicating the dependence on the displacement, whereas $\boldsymbol{F}$, $\boldsymbol{C}$,

and $\boldsymbol{E}$ denote fields independent of u. Further, for simplicity, we assume a triangulation $\mathcal{T}_h$ consisting of triangles in 2D and tetrahedra in three dimensions, compare Remark 6.7.

6.2.1. Lifting to F

We start by defining the following constrained minimization problem for a continuous displacement field $\tilde{u} \in [U_h^k]^d$

$$\int_\Omega \Psi(\boldsymbol{F}) - f \cdot \tilde{u} \, dx \to \min_{\substack{\tilde{u} \in [U_h^k]^d \\ \boldsymbol{F} = \boldsymbol{F}(\tilde{u})}} . \tag{6.2.1}$$

The corresponding Lagrange functional is given by

$$\mathcal{L}(\tilde{u}, \boldsymbol{F}, \boldsymbol{P}) := \int_\Omega \Psi(\boldsymbol{F}) - f \cdot \tilde{u} \, dx - \int_\Omega (\boldsymbol{F} - \boldsymbol{I} - \nabla\tilde{u}) : \boldsymbol{P} \, dx. \tag{6.2.2}$$

By computing the first variation in direction $\delta\boldsymbol{F}$

$$\int_\Omega \partial_{\boldsymbol{F}}\Psi(\boldsymbol{F}) : \delta\boldsymbol{F} - \boldsymbol{P} : \delta\boldsymbol{F} \, dx \overset{!}{=} 0 \tag{6.2.3}$$

we observe that the Lagrange multiplier $\boldsymbol{P}$ is given by the first Piola–Kirchhoff stress tensor. For tangential-continuous displacement functions $u \in V_h$, however, the last integral in (6.2.2) is not well-defined, as ∇u does not exist globally in the sense of L^2-functions. For normal-normal continuous non-symmetric $\boldsymbol{P}$ the integral can be interpreted as a distribution suited for TDNNS elements. We combine the HHJ stress space M_h^k (5.2.35) with the discontinuous space Q_h^k (5.2.14) to $M_h^k \times [Q_h^k]_{\mathrm{skw}}^{d \times d}$ for the first Piola–Kirchhoff stress tensor and similar, with the discontinuous Regge space (5.2.38), $\mathcal{R}_h^{\mathrm{dc},k} \times [Q_h^k]_{\mathrm{skw}}^{d \times d}$ for the deformation gradient $\boldsymbol{F}$ leading to the first nonlinear TDNNS method:

6.2 Problem. *Find a solution* $(u, \boldsymbol{F}, \boldsymbol{P}) \in V_{h,0}^k \times [\mathcal{R}_h^{\mathrm{dc},k} \times [Q_h^k]_{\mathrm{skw}}^{d \times d}] \times [M_h^k \times [Q_h^k]_{\mathrm{skw}}^{d \times d}]$, *for the optimization problem*

$$\mathcal{L}^{\boldsymbol{F}}(u, \boldsymbol{F}, \boldsymbol{P}) \to \min_u \max_{\boldsymbol{P}} \min_{\boldsymbol{F}}, \tag{6.2.4}$$

$$\text{with } \mathcal{L}^{\boldsymbol{F}}(u, \boldsymbol{F}, \boldsymbol{P}) := \int_\Omega \Psi(\boldsymbol{F}) - f \cdot u \, dx + \langle\nabla u, \boldsymbol{P}\rangle_{\mathcal{T}_h} - \int_\Omega (\boldsymbol{F} - \boldsymbol{I}) : \boldsymbol{P} \, dx, \tag{6.2.5}$$

where $\langle\cdot, \cdot\rangle_{\mathcal{T}_h}$ *defined as in* (5.4.4).

Due to the lifting to a square-integrable $\boldsymbol{F}$ and the avoidance of the inversion of material laws the three-field formulation (6.2.4) can handle all kind of nonlinear materials. As we use discontinuous elements for the additional deformation gradient $\boldsymbol{F}$, it can be eliminated on element level for each linearized sub-problem arising during Newton's method, making the method competitive. To be more precise: Let A denote the stiffness matrix stemming from linearizing $\Psi(\boldsymbol{F})$ and B, C are the linearizations of $\int_\Omega (\boldsymbol{F} - \boldsymbol{I}) : \boldsymbol{P} \, dx$ and $\langle\nabla u, \boldsymbol{P}\rangle_{\mathcal{T}_h}$.

The resulting system then reads

$$
\begin{pmatrix} A & 0 & B^\top \\ 0 & 0 & C^\top \\ B & C & 0 \end{pmatrix}
\begin{pmatrix} \underline{\boldsymbol{F}} \\ \underline{u} \\ \underline{\boldsymbol{P}} \end{pmatrix}
= \begin{pmatrix} 0 \\ \underline{f} \\ 0 \end{pmatrix},
$$

where $\underline{\boldsymbol{F}}$, $\underline{u}$, $\underline{\boldsymbol{P}}$, and $\underline{f}$ are the corresponding coefficient vectors. Using the first equation we can eliminate $\underline{\boldsymbol{F}}$ by $\underline{\boldsymbol{P}}$ and insert the resulting expression in the third equation:

$$
A\underline{\boldsymbol{F}} + B^\top \underline{\boldsymbol{P}} = 0 \Rightarrow \underline{\boldsymbol{F}} = -A^{-1}B^\top \underline{\boldsymbol{P}},
$$
$$
B\underline{\boldsymbol{F}} + C\underline{u} = 0 \Rightarrow -BA^{-1}B^\top \underline{\boldsymbol{P}} + C\underline{u} = 0.
$$

Therefore, we obtain a system of equations involving only $\boldsymbol{P}$ and u

$$
\begin{pmatrix} -BA^{-1}B^\top & C \\ C^\top & 0 \end{pmatrix}
\begin{pmatrix} \underline{\boldsymbol{P}} \\ \underline{u} \end{pmatrix}
= \begin{pmatrix} 0 \\ \underline{f} \end{pmatrix}.
$$

Note, that A is block-diagonal and thus cheap to invert.

Additionally, we can apply hybridization techniques to eliminate $\boldsymbol{P}$. Therefore, as in the linear case, $\alpha \in \Gamma_h^k$ is added and the first Piola–Kirchhoff stress is then assumed piece-wise smooth but discontinuous, leading to:

6.3 Problem. *Find a solution* $(u, \boldsymbol{F}, \boldsymbol{P}, \alpha) \in V_{h,0}^k \times [\mathcal{R}_h^{\mathrm{dc},k} \times [Q_h^k]_{\mathrm{skw}}^{d \times d}] \times [M_h^{\mathrm{dc},k} \times [Q_h^k]_{\mathrm{skw}}^{d \times d}] \times \Gamma_{h,0}^k$ *for the optimization problem*

$$
\mathcal{L}_h^{\boldsymbol{F}}(u, \boldsymbol{F}, \boldsymbol{P}, \alpha) \to \min_u \min_\alpha \max_{\boldsymbol{P}} \min_{\boldsymbol{F}}, \tag{6.2.6}
$$

with $\mathcal{L}_h^{\boldsymbol{F}}(u, \boldsymbol{F}, \boldsymbol{P}, \alpha) := \mathcal{L}^{\boldsymbol{F}}(u, \boldsymbol{F}, \boldsymbol{P}) + \displaystyle\sum_{T \in \mathcal{T}_h} \int_{\partial T} \boldsymbol{P}_{nn} \alpha_n \, ds.$ (6.2.7)

6.4 Remark. *After the elimination of the discontinuous fields* $\boldsymbol{F}$ *and* $\boldsymbol{P}$*, a symmetric minimization problem in the displacement* u *and hybridization variable* α *is obtained, comparable to the linear case.*

We emphasize that the identity matrix $\boldsymbol{I}$ *can exactly be represented by the discontinuous elements used for* $\boldsymbol{F}$*. Therefore, one can also use* $\boldsymbol{K} := \boldsymbol{F} - \boldsymbol{I} = \nabla u$ *as independent field instead of* $\boldsymbol{F}$*.*

Gradient splitting: It is possible to further simplify Problem 6.3 by using the (non-physical) additive splitting of the deformation gradient into a symmetric and a skew-symmetric part, $\boldsymbol{F} = \boldsymbol{F}_{\mathrm{sym}} + \boldsymbol{F}_{\mathrm{skw}}$. The symmetric part $\boldsymbol{F}_{\mathrm{sym}}$ is related to the linearized strain tensor $\boldsymbol{\epsilon}(u)$, whereas the skew-symmetric part $\boldsymbol{F}_{\mathrm{skw}}$ is given by the curl of the displacement:

$$
\boldsymbol{F}(u) = \boldsymbol{F}_{\mathrm{sym}}(u) + \boldsymbol{F}_{\mathrm{skw}}(u), \quad \boldsymbol{F}_{\mathrm{sym}}(u) = \boldsymbol{I} + \boldsymbol{\epsilon}(u), \quad \boldsymbol{F}_{\mathrm{skw}}(u) = \mathrm{skw}(\mathrm{curl}(u)), \tag{6.2.8}
$$

with the skw-operator defined as

$$\mathrm{skw}(v) : \mathbb{R} \to \mathbb{R}^{2\times 2}_{\mathrm{skw}}, \qquad\qquad \mathrm{skw}(v) : \mathbb{R}^3 \to \mathbb{R}^{3\times 3}_{\mathrm{skw}},$$

$$v \mapsto \frac{1}{2}\begin{pmatrix} 0 & -v \\ v & 0 \end{pmatrix} \quad \text{in 2D}, \qquad v \mapsto \frac{1}{2}\begin{pmatrix} 0 & -v_3 & v_2 \\ v_3 & 0 & -v_1 \\ -v_2 & v_1 & 0 \end{pmatrix} \quad \text{in 3D}.$$

For $u \in V_h$ the curl-operator is well-defined, $\mathrm{curl}(u) \in [L^2(\Omega)]^{d^\star}$. Thus, there is no necessity to "lift" the skew-symmetric part $\boldsymbol{F}_{\mathrm{skw}}(u)$ to a new independent $\boldsymbol{F}_{\mathrm{skw}}$, as $\boldsymbol{F}_{\mathrm{skw}}(u)$ is already in $L^2(\Omega)$. The (hybridized) Lagrangian from Problem 6.3 can be adapted accordingly, now using only the symmetric part $\boldsymbol{P}_{\mathrm{sym}}$ of the first Piola–Kirchhoff stress as a Lagrange multiplier for the constraint $\boldsymbol{F}_{\mathrm{sym}} = \boldsymbol{F}_{\mathrm{sym}}(u)$:

6.5 Problem. *Find a solution* $(u, \boldsymbol{F}_{\mathrm{sym}}, \boldsymbol{P}_{\mathrm{sym}}, \alpha) \in V^k_{h,0} \times \mathcal{R}^{\mathrm{dc},k}_h \times M^{\mathrm{dc},k}_h \times \Gamma^k_{h,0}$ *for the optimization problem*

$$\mathcal{L}^{\boldsymbol{F},\mathrm{sym}}_h(u, \boldsymbol{F}_{\mathrm{sym}}, \boldsymbol{P}_{\mathrm{sym}}, \alpha) \to \min_u \min_\alpha \max_{\boldsymbol{P}_{\mathrm{sym}}} \min_{\boldsymbol{F}_{\mathrm{sym}}}, \tag{6.2.9}$$

$$\text{with } \mathcal{L}^{\boldsymbol{F},\mathrm{sym}}_h(u, \boldsymbol{F}_{\mathrm{sym}}, \boldsymbol{P}_{\mathrm{sym}}, \alpha) := \int_\Omega \Psi(\boldsymbol{F}_{\mathrm{sym}} + \mathrm{skw}(\mathrm{curl}(u))) - f \cdot u \, dx$$

$$+ \langle \nabla u, \boldsymbol{P}_{\mathrm{sym}} \rangle_{\mathcal{T}_h} - \int_\Omega (\boldsymbol{F}_{\mathrm{sym}} - \boldsymbol{I}) : \boldsymbol{P}_{\mathrm{sym}} \, dx$$

$$+ \sum_{T \in \mathcal{T}_h} \int_{\partial T} \boldsymbol{P}_{\mathrm{sym},nn} \alpha_n \, ds. \tag{6.2.10}$$

Note that the normal-normal continuity of the first Piola–Kirchhoff stress tensor $\boldsymbol{P}$ is equivalent to the normal-normal continuity of its symmetric part:

$$\boldsymbol{P}_{nn} = \boldsymbol{P}_{\mathrm{sym},nn} \qquad \text{and} \qquad \boldsymbol{P}_{\mathrm{skw},nn} = 0. \tag{6.2.11}$$

The stress elements M_h from the linear case are used for the discretization of $\boldsymbol{P}_{\mathrm{sym}}$. We motivate the choice of the (discontinuous) Regge elements $\mathcal{R}^{\mathrm{dc}}_h$ as finite element space for $\boldsymbol{F}_{\mathrm{sym}}$ instead of simply assuming $\boldsymbol{F}_{\mathrm{sym}} \in [Q_h]^{d\times d}_{\mathrm{sym}}$. Assuming non-curved elements the mapping of the gradient of $u \in V_h$ from the reference to a physical element is given by, compare (5.2.30),

$$(\nabla_x u) \circ \Phi = \boldsymbol{G}^{-\top} \nabla_{\hat{x}} \hat{u} \boldsymbol{G}^{-1}, \quad \mathrm{sym}(\nabla_x u) \circ \Phi = \boldsymbol{G}^{-\top} \mathrm{sym}(\nabla_{\hat{x}} \hat{u}) \boldsymbol{G}^{-1}, \tag{6.2.12}$$

where $\Phi : \hat{T} \to T$, $\boldsymbol{G} := \nabla_{\hat{x}} \Phi$, and $\hat{u}$ a Nédélec element on the reference element $\hat{T}$. We observe that the gradient gets transformed with a double covariant transformation, the same as used for Regge elements, see (5.2.39), yielding beneficial properties for e.g.,

anisotropic elements. For curved elements (6.2.12) changes to

$$(\nabla_x u) \circ \Phi = \nabla_{\hat{x}} \left(\boldsymbol{G}^{-\top} \hat{u} \right) \boldsymbol{G}^{-1}$$

$$= -\boldsymbol{G}^{-\top} \left(\sum_{k=1}^{d} \partial_{x_j} (\boldsymbol{G}^{\top})_{ik} (\boldsymbol{G}^{-\top} \hat{u})_k \right)_{i,j=1}^{d} \boldsymbol{G}^{-1} + \boldsymbol{G}^{-\top} \nabla_{\hat{x}} \hat{u} \boldsymbol{G}^{-1}$$

$$= \boldsymbol{G}^{-\top} \left(\nabla_{\hat{x}} \hat{u} - \left(\sum_{k=1}^{d} \partial_{x_j} (\boldsymbol{G}^{\top})_{ik} (\boldsymbol{G}^{-\top} \hat{u})_k \right)_{i,j=1}^{d} \right) \boldsymbol{G}^{-1}, \qquad (6.2.13)$$

where we used that $\partial_{x_i} \boldsymbol{G}^{-1} = -\boldsymbol{G}^{-1}(\partial_{x_i} \boldsymbol{G}) \boldsymbol{G}^{-1}$. Thus, also in the curved setting the transformation fits to Regge elements, however, also geometry information (the curvature) is then part of $\boldsymbol{F}_{\text{sym}} \in \mathcal{R}_h^{\text{dc}}$.

Another motivation is the tangential continuity of $u \in V_h$ and the resulting tangential-tangential continuity (∇u has a continuous tangential derivative of its tangential component $\nabla_t u_t$) of ∇u (and also $\boldsymbol{\epsilon}(u)$) fitting perfectly to the continuity condition of Regge elements, cf. (5.2.38).

6.6 Remark. *This additive splitting and simplification leads to fewer local degrees of freedom than the original hybridized Problem 6.3.*

One may recover $\boldsymbol{P}_{\text{skw}}$ as a post-processing step by using the identity

$$\partial_{\text{skw}(\text{curl}(u))} \Psi(\boldsymbol{F}_{\text{sym}} + \text{skw}(\text{curl}(u))) = \boldsymbol{P}_{\text{skw}}, \qquad (6.2.14)$$

stemming from the variation of (6.2.7) in direction $\text{skw}(\delta \boldsymbol{F})$.

6.7 Remark. *To guarantee that in the linear regime the problems are uniquely solvable the finite element space of $\boldsymbol{F}$ must contain the space of $\boldsymbol{P}$ (compare Theorem 6.17). For triangles and tetrahedra the HHJ and Regge space are of the same dimension for fixed polynomial order k. For quadrilaterals, and thus also hexahedra and prisms, the spaces differ in terms of different amount of inner bubbles. Therefore, e.g., for quadrilaterals one degree more has to be chosen for the Regge space for $\boldsymbol{F}$.*

6.2.2. Lifting to C

For objective materials Theorem 2.2 states that the energy potential Ψ depends only on the Cauchy–Green strain tensor $\boldsymbol{C}$. Thus, instead of solving the constrained minimization problem (6.2.1), we can consider for continuous displacements $\tilde{u} \in [U_h^k]^d$ the problem

$$\int_\Omega \Psi(\boldsymbol{C}) - f \cdot \tilde{u} \, dx \to \min_{\substack{\tilde{u} \in [U_h^k]^d, \\ \boldsymbol{C} = \boldsymbol{C}(\tilde{u})}}, \qquad (6.2.15)$$

with its Lagrangian

$$\mathcal{L}(\tilde{u}, \boldsymbol{C}, \boldsymbol{\Sigma}) := \int_\Omega \Psi(\boldsymbol{C}) - f \cdot \tilde{u} \, dx - \int_\Omega \frac{1}{2} \Big(\boldsymbol{C} - \underbrace{(\nabla \tilde{u} + \boldsymbol{I})^{\top} (\nabla \tilde{u} + \boldsymbol{I})}_{= \boldsymbol{C}(\tilde{u})} \Big) : \boldsymbol{\Sigma} \, dx. \qquad (6.2.16)$$

Now, the second Piola–Kirchhoff stress tensor $\boldsymbol{\Sigma}$ is the corresponding Lagrange multiplier. This can be readily checked by taking the first variation of (6.2.16) in direction $\delta \boldsymbol{C}$ together with (2.2.15)

$$\int_\Omega \partial_{\boldsymbol{C}} \Psi(\boldsymbol{C}) : \delta \boldsymbol{C} - \frac{1}{2} \boldsymbol{\Sigma} : \delta \boldsymbol{C} \, dx \overset{!}{=} 0, \tag{6.2.17}$$

explaining the factor 0.5 in (6.2.16). As already discussed in Section 6.2.1 the integral in (6.2.16) is not well-defined for displacement fields $u \in V_h$, which are only tangential-continuous. Further, the balance equation (2.2.8) implies the normal-continuity of the first Piola–Kirchhoff tensor, compare also $H(\mathrm{div})$-conforming finite elements, especially the coupling condition in Theorem 3.3. With this motivation, the second Piola–Kirchhoff stress tensor $\boldsymbol{\Sigma}$ and the Cauchy–Green strain tensor $\boldsymbol{C}$ are both assumed to be piece-wise smooth and discontinuous. Further, the hybridization variable $\alpha \in \Gamma_h$ is used to enforce the normal-normal continuity of $\boldsymbol{P} = \boldsymbol{F}\boldsymbol{\Sigma}$ instead of $\boldsymbol{\Sigma}$. This leads us to the following saddle point problem:

6.8 Problem. *Find a solution* $(u, \boldsymbol{C}, \boldsymbol{\Sigma}, \alpha) \in V_{h,0}^k \times \mathcal{R}_h^{\mathrm{dc},k} \times M_h^{\mathrm{dc},k} \times \Gamma_{h,0}^k$ *for the optimization problem*

$$\mathcal{L}_h^{\boldsymbol{C}}(u, \boldsymbol{C}, \boldsymbol{\Sigma}, \alpha) \to \min_u \min_\alpha \max_{\boldsymbol{\Sigma}} \min_{\boldsymbol{C}}, \tag{6.2.18}$$

$$\text{with } \mathcal{L}_h^{\boldsymbol{C}}(u, \boldsymbol{C}, \boldsymbol{\Sigma}, \alpha) := \int_\Omega \Psi(\boldsymbol{C}) - f \cdot u \, dx + \frac{1}{2} \langle \boldsymbol{C}(u), \boldsymbol{\Sigma} \rangle_0 - \frac{1}{2} \int_\Omega \boldsymbol{C} : \boldsymbol{\Sigma} \, dx$$

$$+ \sum_{T \in \mathcal{T}_h} \int_{\partial T} (\boldsymbol{F}(u)\boldsymbol{\Sigma})_{nn} \, \alpha_n \, ds \tag{6.2.19}$$

$$\text{and } \langle \boldsymbol{C}(u), \boldsymbol{\Sigma} \rangle_0 := \sum_{T \in \mathcal{T}_h} \left(\int_T \boldsymbol{C}(u) : \boldsymbol{\Sigma} \, dx - 2 \int_{\partial T} u_n (\boldsymbol{F}(u)\boldsymbol{\Sigma})_{nn} \, ds \right). \tag{6.2.20}$$

The duality pairing (6.2.20) is non-standard as it involves quadratic terms in (the gradient of) u and thus, is not bilinear. Further we implicitly proposed how distributions can be multiplied together in this special setting. Hence, the natural question of well-posedness arises. Therefore, we compute all first variations of Problem 6.8:

$$\int_\Omega \partial_{\boldsymbol{C}} \Psi(\boldsymbol{C}) : \delta \boldsymbol{C} - \frac{1}{2} \delta \boldsymbol{C} : \boldsymbol{\Sigma} \, dx \overset{!}{=} 0, \tag{6.2.21a}$$

$$\int_\Omega \frac{1}{2} (\boldsymbol{C}(u) - \boldsymbol{C}) : \delta \boldsymbol{\Sigma} \, dx + \sum_{T \in \mathcal{T}_h} \int_{\partial T} (\alpha - u)_n (\boldsymbol{F}(u)\delta\boldsymbol{\Sigma})_{nn} \, ds \overset{!}{=} 0, \tag{6.2.21b}$$

$$\sum_{T \in \mathcal{T}} \left(\int_T \boldsymbol{F}(u)\boldsymbol{\Sigma} : \nabla \delta u \, dx - \int_{\partial T} (\boldsymbol{F}(u)\boldsymbol{\Sigma})_{nn} \delta u_n - (\nabla \delta u \boldsymbol{\Sigma})_{nn} (\alpha - u)_n \, ds \right) - \int_\Omega f \cdot u \, dx \overset{!}{=} 0, \tag{6.2.21c}$$

$$\sum_{T \in \mathcal{T}_h} \int_{\partial T} (\boldsymbol{F}(u)\boldsymbol{\Sigma})_{nn} \delta \alpha_n \, ds \overset{!}{=} 0. \tag{6.2.21d}$$

6.9 Lemma. *Problem 6.8 is consistent.*

Proof. To prove consistency we have to show that the true (smooth) solution $\tilde{u}$ together with $\boldsymbol{C} := \boldsymbol{C}(\tilde{u})$, $\boldsymbol{\Sigma} := \boldsymbol{\Sigma}(\tilde{u})$, and $\alpha := \mathrm{tr}_n \tilde{u}$ solves (6.2.18) and equivalently (6.2.21). Considering the left-hand side of (6.2.21c) and inserting the solution $\tilde{u}$ we want to recover its strong form. First, the hybridization variable α is the normal trace of $\tilde{u}$ and thus, $(\tilde{u} - \alpha)_n = 0$ on ∂T. Integration by parts and reordering yields

$$\sum_{T \in \mathcal{T}_h} \left(\int_T -\mathrm{div}(\boldsymbol{F}(\tilde{u})\boldsymbol{\Sigma}) \cdot \delta u \, dx + \int_{\partial T} ((\boldsymbol{F}(\tilde{u})\boldsymbol{\Sigma})_n \delta u - (\boldsymbol{F}(\tilde{u})\boldsymbol{\Sigma})_{nn} \delta u_n) \, ds \right)$$

$$= \sum_{T \in \mathcal{T}_h} \left(\int_T -\mathrm{div}(\boldsymbol{F}(\tilde{u})\boldsymbol{\Sigma}) \cdot \delta u \, dx + \int_{\partial T} (\boldsymbol{F}(\tilde{u})\boldsymbol{\Sigma})_{nt} \cdot \delta u_t \, ds \right)$$

$$= \sum_{T \in \mathcal{T}_h} \int_T -\mathrm{div}(\boldsymbol{F}(\tilde{u})\boldsymbol{\Sigma}) \cdot \delta u \, dx + \sum_{E \in \mathcal{E}_h} \int_E [\![(\boldsymbol{F}(\tilde{u})\boldsymbol{\Sigma})_{nt}]\!] \cdot \delta u_t \, ds.$$

The first term states the element-wise balance equation, $-\mathrm{div}(\boldsymbol{F}(\tilde{u})\boldsymbol{\Sigma})|_T = f|_T$, and the second one the continuity of the normal-tangential components of the first Piola–Kirchhoff stress tensor which is satisfied for the exact solution. Reordering hybridization terms in (6.2.21d) yields

$$\sum_{E \in \mathcal{E}_h} \int_E [\![(\boldsymbol{F}(\tilde{u})\boldsymbol{\Sigma})_{nn}]\!] \delta \alpha \, ds = 0, \tag{6.2.22}$$

forcing also the normal-normal continuity and thus, the continuity of the normal-component of the first Piola–Kirchhoff stress tensor. Hence, also this interface condition is fulfilled. It immediately follows that the true solution $\tilde{u}$ also solves equations (6.2.21a) and (6.2.21b). $\qquad\square$

6.10 Remark. *Because of the discontinuity of the $\boldsymbol{\Sigma}$ and $\boldsymbol{C}$ fields, they can be eliminated at element level and the resulting system involves again only u and α. Thus, the same number of coupling dofs are used as for the lifting of $\boldsymbol{F}$ in the previous section.*

The motivation to use the Regge elements for the Cauchy–Green strain tensor is similar as before. The deformation gradient $\boldsymbol{F}(u)$ is tangential continuous for a continuous displacement field u. Therefore, the Green-strain tensor $\boldsymbol{C}(u)$ is tangential-tangential continuous. Further, for $u \in H(\mathrm{curl})$ we have with (6.2.12) $(\nabla_x u^\top \nabla_x u) \circ \Phi = \boldsymbol{G}^{-\top} \nabla_{\hat{x}} \hat{u}^\top \boldsymbol{G}^{-1} \boldsymbol{G}^{-\top} \nabla_{\hat{x}} \hat{u} \boldsymbol{G}^{-1}$ again a doubled covariant transformation from the reference to the physical element, $\Phi : \hat{T} \to T$, $\boldsymbol{G} = \nabla_{\hat{x}} \Phi$. The case of curved elements follow the same lines together with (6.2.13).

For the choice of the normal-normal continuous stress space M_h for the second Piola–Kirchhoff stress tensor we note that in the small strain case there holds $\boldsymbol{F}\boldsymbol{\Sigma} \approx \boldsymbol{\Sigma}$ and thus, the method reduces to a linear version of the TDNNS method which is discussed more precisely in the following.

Linearization: Starting from the first variations (6.2.21) under the assumption of small deformations, i.e., $u = \mathcal{O}(\varepsilon)$, $\alpha = \mathcal{O}(\varepsilon)$, $\nabla u = \mathcal{O}(\varepsilon)$, $\boldsymbol{\Sigma} = \mathcal{O}(\varepsilon)$, $\boldsymbol{C}(u) = 2\boldsymbol{\epsilon}(u) + \boldsymbol{I} + \mathcal{O}(\varepsilon^2)$, Problem 6.8 becomes:

6.11 Problem. *Find* $(u, \boldsymbol{E}, \boldsymbol{\Sigma}, \alpha) \in V_{h,0}^k \times \mathcal{R}_h^{\mathrm{dc},k} \times M_h^{\mathrm{dc},k} \times \Gamma_{h,0}^k$ *such that for all* $(\delta u, \delta\boldsymbol{E}, \delta\boldsymbol{\Sigma}, \delta\alpha) \in V_{h,0}^k \times \mathcal{R}_h^{\mathrm{dc},k} \times M_h^{\mathrm{dc},k} \times \Gamma_{h,0}^k$

$$\int_\Omega \partial_{\boldsymbol{E}}\Psi(\boldsymbol{E}) : \delta\boldsymbol{E} - \boldsymbol{\Sigma} : \delta\boldsymbol{E} \, dx \qquad\qquad = 0 \qquad\qquad (6.2.23\mathrm{a})$$

$$- \sum_{T \in \mathcal{T}_h} \left(\int_T (\boldsymbol{E} - \boldsymbol{\epsilon}(u)) : \delta\boldsymbol{\Sigma} \, dx + \int_{\partial T} (\delta\boldsymbol{\Sigma})_{nn}(u - \alpha)_n \, ds \right) = 0, \qquad (6.2.23\mathrm{b})$$

$$\sum_{T \in \mathcal{T}_h} \left(\int_T \boldsymbol{\Sigma} : \nabla\delta u \, dx - \int_{\partial T} \boldsymbol{\Sigma}_{nn}\delta u_n \, ds \right) \qquad\qquad = \int_\Omega f \cdot \delta u \, dx, \quad (6.2.23\mathrm{c})$$

$$\sum_{T \in \mathcal{T}_h} \int_{\partial T} \boldsymbol{\Sigma}_{nn}\delta\alpha_n \, ds \qquad\qquad\qquad\qquad = 0, \qquad\qquad (6.2.23\mathrm{d})$$

where we implicitly defined $\boldsymbol{E} := \frac{1}{2}(\boldsymbol{C} - \boldsymbol{I})$ *and* $\delta\boldsymbol{E} := \frac{1}{2}\delta\boldsymbol{C}$.

Assuming a quadratic potential, i.e., $\partial_{\boldsymbol{E}}\Psi(\boldsymbol{E}) = \mathbb{C}\boldsymbol{E}$, and eliminating $\boldsymbol{E}$ by $\boldsymbol{\Sigma}$ with (6.2.23a) recovers the hybridized TDNNS method (5.4.7). This elimination is possible if $M_h^{\mathrm{dc},k} \subset \mathcal{R}_h^{\mathrm{dc},k}$, compare Theorem 6.17. Thus, the linearized versions of (6.2.19) and (6.2.6) coincide. Note, that with a quadratic potential Problem 6.11 is the hybridized version of the Hu–Washizu principle Problem 4.4.1 with TDNNS elements (and discontinuous Regge elements instead of L^2-conforming ones).

6.12 Remark. *Note that due to the affine relation* $\boldsymbol{E} = 0.5(\boldsymbol{C} - \boldsymbol{I})$ *and*

$$\partial_{\boldsymbol{E}}\Psi(\boldsymbol{E}) : \delta\boldsymbol{E} = \partial_{\boldsymbol{C}}\Psi(\boldsymbol{C}) : \delta\boldsymbol{C} \qquad\qquad (6.2.24)$$

the problem

$$\int_\Omega \Psi(\boldsymbol{E}) - f \cdot \tilde{u} \, dx \to \min_{\substack{\tilde{u} \in [U_h^k]^d \\ \boldsymbol{E} = \boldsymbol{E}(\tilde{u})}} \qquad\qquad (6.2.25)$$

is equivalent to (6.2.15) *and thus, one can use* $\boldsymbol{E}$ *instead of* $\boldsymbol{C}$ *as additional field.*

Stabilization techniques: For large deformations the normal continuity of the displacement u is not guaranteed in weak sense, compare the boundary term in (6.2.21b). Therefore, to improve robustness of this method in the large deformation regime, one may add the following well-known stabilization term

$$\sum_{T \in \mathcal{T}_h} \int_{\partial T} \frac{c_1}{h}(u - \alpha)_n(u - \alpha)_n \, ds \qquad\qquad (6.2.26)$$

from Hybrid Discontinuous Galerkin (HDG) techniques [53, 90] to the Lagrangian (6.2.19). Here, h denotes the ratio of the element volume and the boundary area, $h = \frac{J_T}{J_F}$, compare (5.1.7), used especially for anisotropic elements and $c_1 > 0$ is a positive constant. As there holds $\tilde{u}_n = \alpha_n$ for the true solution (6.2.26) is consistent.

Another stabilization technique adds the consistent term

$$c_2 \sum_{T \in \mathcal{T}_h} \int_T (\boldsymbol{C} - \boldsymbol{C}(u)) : (\boldsymbol{C} - \boldsymbol{C}(u)) \, dx \tag{6.2.27}$$

enforcing the element-wise equality of the lifting with $c_2 > 0$ and thus supports the lifting. Note, that these terms on the one hand increase the stability but on the other hand lead to less accurate solutions if the stability parameters c_1 and c_2 are chosen too large.

6.2.3. Lifting to F and projection to C

As we will see in Section 6.5 the method presented in Section 6.2.1, where a lifting of $\boldsymbol{F}$ is considered, is more robust in numerical experiments compared to the approach in the previous section. Therefore, we expect more accurate solutions for the first method. On the other hand, the number of Newton iterations needed for one load step to converge is observed to be significantly higher than for the second method. This motivates to combine both ideas, leading to a lifting of $\boldsymbol{F}$, exactly as in the first method. Then, the resulting Cauchy–Green strain tensor $\boldsymbol{C}(\boldsymbol{F}) = \boldsymbol{F}^\top \boldsymbol{F}$ is going to be interpolated to a new independent field $\boldsymbol{C}$. This can be interpreted as a projection of $\boldsymbol{C}(\boldsymbol{F})$ to $\boldsymbol{C}$. Here, the method differs compared to the second approach, where $\boldsymbol{C}$ is a lifting rather than a projection.

Let as again start with a constraint minimization problem for the continuous displacement $\tilde{u} \in [U_h^k]^d$

$$\int_\Omega \Psi(\boldsymbol{C}) - f \cdot \tilde{u} \, dx \to \min_{\substack{\tilde{u} \in [U_h^k]^d \\ \boldsymbol{F} = \boldsymbol{F}(\tilde{u}) \\ \boldsymbol{C} = \boldsymbol{C}(\boldsymbol{F})}}, \tag{6.2.28}$$

with the corresponding Lagrangian

$$\mathcal{L}(\tilde{u}, \boldsymbol{F}, \boldsymbol{P}, \boldsymbol{C}, \boldsymbol{\Sigma}) := \int_\Omega \Psi(\boldsymbol{C}) - f \cdot \tilde{u} \, dx - \int_\Omega (\boldsymbol{F} - \nabla\tilde{u} - \boldsymbol{I}) : \boldsymbol{P} - \frac{1}{2}(\boldsymbol{C} - \boldsymbol{F}^\top \boldsymbol{F}) : \boldsymbol{\Sigma} \, dx. \tag{6.2.29}$$

Computing the variation in direction $\delta\boldsymbol{C}$ yields as in the previous section that the Lagrange multiplier $\boldsymbol{\Sigma}$, forcing the equality $\boldsymbol{C} = \boldsymbol{C}(\boldsymbol{F})$, is the second Piola–Kirchhoff stress tensor. With the variation in direction $\delta\boldsymbol{F}$ we deduce that $\boldsymbol{P}$ is given by the first Piola–Kirchhoff stress tensor

$$\int_\Omega \boldsymbol{P} : \delta\boldsymbol{F} - \boldsymbol{F}\boldsymbol{\Sigma} : \delta\boldsymbol{F} \, dx \overset{!}{=} 0. \tag{6.2.30}$$

The integral involving the gradient of the displacement in (6.2.29) is interpreted again as a distribution for $u \in V_h$ in the context of TDNNS elements. By combining the spaces $M_h^k \times [Q_h^k]_{\mathrm{skw}}^{d\times d}$ for the piece-wise smooth, non-symmetric and normal-normal continuous $\boldsymbol{P}$, and $\mathcal{R}_h^{\mathrm{dc},k} \times [Q_h^k]_{\mathrm{skw}}^{d\times d}$ for the deformation gradient $\boldsymbol{F}$, together with $\boldsymbol{\Sigma}$ and $\boldsymbol{C}$ piece-wise smooth discontinuous we obtain the following saddle point problem:

6.13 Problem. *Find a solution* $(u, \boldsymbol{F}, \boldsymbol{P}, \boldsymbol{C}, \boldsymbol{\Sigma}) \in V_{h,0}^k \times [\mathcal{R}_h^{\mathrm{dc},k} \times [Q_h^k]_{\mathrm{skw}}^{d \times d}] \times [M_h^k \times [Q_h^k]_{\mathrm{skw}}^{d \times d}] \times \mathcal{R}_h^{\mathrm{dc},k} \times \mathcal{R}_h^{\mathrm{dc},k}$ *for the optimization problem*

$$\mathcal{L}^{\boldsymbol{FC}}(u, \boldsymbol{F}, \boldsymbol{P}, \boldsymbol{C}, \boldsymbol{\Sigma}) \to \min_u \max_{\boldsymbol{P}} \min_{\boldsymbol{F}} \min_{\boldsymbol{C}} \max_{\boldsymbol{\Sigma}}, \tag{6.2.31}$$

$$\mathcal{L}^{\boldsymbol{FC}}(u, \boldsymbol{F}, \boldsymbol{P}, \boldsymbol{C}, \boldsymbol{\Sigma}) := \int_\Omega \Psi(\boldsymbol{C}) - f \cdot u \, dx - \langle \boldsymbol{F} - \nabla u - \boldsymbol{I}, \boldsymbol{P} \rangle_{\mathcal{T}_h}$$

$$- \int_\Omega \frac{1}{2}(\boldsymbol{C} - \boldsymbol{F}^\top \boldsymbol{F}) : \boldsymbol{\Sigma} \, dx, \tag{6.2.32}$$

where $\langle \cdot, \cdot \rangle_{\mathcal{T}_h}$ *is defined as in* (5.4.4).

We can pose the hybridized Lagrangian $\mathcal{L}_h^{\boldsymbol{FC}}(u, \boldsymbol{F}, \boldsymbol{P}, \boldsymbol{C}, \boldsymbol{\Sigma}, \alpha)$ according to Problem 6.3. Furthermore, as done in Section 6.2.1 the Lagrangian $\mathcal{L}_h^{\boldsymbol{FC},\mathrm{sym}}(u, \boldsymbol{F}_{\mathrm{sym}}, \boldsymbol{P}_{\mathrm{sym}}, \boldsymbol{C}, \boldsymbol{\Sigma}, \alpha)$ can be obtained by the gradient splitting and eliminating the skew-symmetric part of $\boldsymbol{F}$ and $\boldsymbol{P}$.

We focus on the additional term

$$\int_\Omega (\boldsymbol{C} - \boldsymbol{F}^\top \boldsymbol{F}) : \boldsymbol{\Sigma} \, dx, \tag{6.2.33}$$

which is well-defined for square-integrable fields. Therefore, $\boldsymbol{C}$ can be interpreted as the local L^2-projection of $\boldsymbol{F}^\top \boldsymbol{F}$ onto the space of polynomial order used for $\boldsymbol{\Sigma}$

$$\boldsymbol{C} = \mathcal{I}_{L^2}^k(\boldsymbol{F}^\top \boldsymbol{F}). \tag{6.2.34}$$

6.14 Remark. *Note that this method is equivalent to the first approach in Section 6.2.1, if the polynomial order for* $\boldsymbol{C}$ *and* $\boldsymbol{\Sigma}$ *are chosen sufficiently large, namely twice as the degree used for* $\boldsymbol{F}$.

6.15 Remark. *For this method the discontinuous fields* $\boldsymbol{\Sigma}$, $\boldsymbol{P}$, $\boldsymbol{C}$, *and* $\boldsymbol{F}$ *can be eliminated at element level leading to a symmetric minimization problem in* u *and* α. *Therefore, the number of coupling dofs coincide with those in Sections 6.2.1 and 6.2.2. The number of local dofs, however, is higher.*

Linearization: In the small strain regime $\mathcal{L}^{\boldsymbol{FC}}(u, \boldsymbol{F}, \boldsymbol{P}, \boldsymbol{C}, \boldsymbol{\Sigma})$ reduces to the linear TDNNS method (5.4.2). More precisely, taking all first variations of Problem 6.13 (left column) and linearizing by assuming that $u = \mathcal{O}(\varepsilon)$, $\nabla u = \mathcal{O}(\varepsilon)$, $\boldsymbol{F} = \boldsymbol{I} + \boldsymbol{F}_\varepsilon$ with $\boldsymbol{F}_\varepsilon = \mathcal{O}(\varepsilon)$, and

$\boldsymbol{\Sigma} = \mathcal{O}(\varepsilon)$, (right column) yields:

$$\int_\Omega (\partial_{\boldsymbol{C}}\Psi(\boldsymbol{C}) - \frac{1}{2}\boldsymbol{\Sigma}) : \delta\boldsymbol{C}\,dx = 0, \qquad \int_\Omega (\partial_{\boldsymbol{C}}\Psi(\boldsymbol{C}) - \frac{1}{2}\boldsymbol{\Sigma}) : \delta\boldsymbol{C}\,dx = 0, \qquad (6.2.35\text{a})$$

$$\langle \boldsymbol{P}, \nabla\delta u\rangle_{\mathcal{T}_h} = \int_\Omega f\cdot\delta u\,dx, \qquad \langle \boldsymbol{P}, \nabla\delta u\rangle_{\mathcal{T}_h} = \int_\Omega f\cdot\delta u\,dx, \qquad (6.2.35\text{b})$$

$$\int_\Omega (\boldsymbol{F}\boldsymbol{\Sigma} - \boldsymbol{P}) : \delta\boldsymbol{F}\,dx = 0, \qquad \int_\Omega (\boldsymbol{\Sigma} - \boldsymbol{P}) : \delta\boldsymbol{F}\,dx = 0, \qquad (6.2.35\text{c})$$

$$\langle \boldsymbol{F} - \nabla u - I, \delta\boldsymbol{P}\rangle_{\mathcal{T}_h} = 0, \qquad \langle \boldsymbol{F}_\varepsilon - \nabla u, \delta\boldsymbol{P}\rangle_{\mathcal{T}_h} = 0, \qquad (6.2.35\text{d})$$

$$\int_\Omega (\boldsymbol{C} - \boldsymbol{F}^\top\boldsymbol{F}) : \delta\boldsymbol{\Sigma}\,dx = 0, \qquad \int_\Omega (\boldsymbol{C} - \boldsymbol{I} - 2\,\text{sym}(\boldsymbol{F}_\varepsilon)) : \delta\boldsymbol{\Sigma}\,dx = 0. \qquad (6.2.35\text{e})$$

Thus, we obtain with (6.2.35c) and (6.2.35e) that $\boldsymbol{P} = \boldsymbol{\Sigma}$ is symmetric and $\boldsymbol{F}_\varepsilon = \frac{1}{2}(\boldsymbol{C} - \boldsymbol{I}) =: \boldsymbol{E}$. By eliminating $\boldsymbol{P}$ and $\boldsymbol{F}_\varepsilon$ we obtain the (non-hybridized version of the) linearized Problem 6.2.23. This eliminations require that the spaces for $\boldsymbol{\Sigma}$, $\boldsymbol{C}$, and $\boldsymbol{F}$ coincide and that the space of $\boldsymbol{P}$ is a subset of these.

As all three nonlinear TDNNS versions degenerate to the same three-field formulation in the small strain regime (under the appropriate assumptions on the finite element spaces and a quadratic potential Ψ) it is sufficient to pose one linearized problem:

6.16 Problem. *Find $(u, \boldsymbol{E}, \boldsymbol{\Sigma}) \in V_{h,0} \times \mathcal{R}_h^{\text{dc}} \times M_h$ such that for all $(\delta u, \delta\boldsymbol{E}, \delta\boldsymbol{\Sigma}) \in V_h \times \mathcal{R}_h^{\text{dc}} \times M_h$*

$$\int_\Omega \mathbb{C}\boldsymbol{E} : \delta\boldsymbol{E}\,dx \qquad\qquad - \int_\Omega \boldsymbol{\Sigma} : \delta\boldsymbol{E}\,dx = 0 \qquad (6.2.36\text{a})$$

$$\langle \nabla\delta u, \boldsymbol{\Sigma}\rangle_{\mathcal{T}_h} \qquad = \int_\Omega f\cdot\delta u\,dx, \qquad (6.2.36\text{b})$$

$$-\int_\Omega \boldsymbol{E} : \delta\boldsymbol{\Sigma}\,dx + \langle \nabla u, \delta\boldsymbol{\Sigma}\rangle_{\mathcal{T}_h} \qquad = 0. \qquad (6.2.36\text{c})$$

We prove that this Hu–Washizu problem (cf. Problem 4.6) is well-posed.

6.17 Theorem. *Under the assumption that $V_{h,0} \times M_h$ is a stable TDNNS pairing and $M_h \subset \mathcal{R}_h^{\text{dc}}$, Problem 6.16 is uniquely solvable.*

Proof. We define the following discrete norms

$$\|u\|_{V_h}^2 := \sum_{T\in\mathcal{T}_h} \|\nabla u\|_{L^2(T)}^2 + \sum_{F\in\mathcal{F}_h} \frac{1}{h_F}\|\llbracket u_n\rrbracket\|_{L^2(F)}^2, \quad \|\boldsymbol{\Sigma}\|_{M_h} := \|\boldsymbol{\Sigma}\|_{L^2}, \quad \|\boldsymbol{E}\|_{\mathcal{R}_h} := \|\boldsymbol{E}\|_{L^2}.$$

There holds the norm equivalence, see [171],

$$\|\boldsymbol{\Sigma}\|_{M_h}^2 \sim \sum_{T\in\mathcal{T}_h} \|\boldsymbol{\Sigma}\|_{L^2(T)}^2 + \sum_{F\in\mathcal{F}_h} h_F\|\boldsymbol{\Sigma}_{nn}\|_{L^2(F)}^2.$$

We apply Brezzi's Theorem 3.8 by defining the spaces

$$V := \mathcal{R}_h^{\mathrm{dc}} \times V_{h,0}, \qquad\qquad Q := M_h,$$

with the corresponding product norm on V. The bilinear forms

$$a\left((\boldsymbol{E}, u), (\delta\boldsymbol{E}, \delta u)\right) := \int_\Omega \mathbb{C}\boldsymbol{E} : \delta\boldsymbol{E}\, dx,$$

$$b\left((\boldsymbol{E}, u), \boldsymbol{\Sigma}\right) := \langle \nabla u, \boldsymbol{\Sigma} \rangle_{\mathcal{T}_h} - \int_\Omega \boldsymbol{E} : \boldsymbol{\Sigma}\, dx,$$

are continuous

$$|a\left((\boldsymbol{E}, u), (\delta\boldsymbol{E}, \delta u)\right)| \preceq \|(\boldsymbol{E}, u)\|_V \|(\delta\boldsymbol{E}, \delta u)\|_V \qquad \text{for all } (\boldsymbol{E}, u), (\delta\boldsymbol{E}, \delta u) \in V,$$

$$|b\left((\boldsymbol{E}, u), \boldsymbol{\Sigma}\right)| \preceq \|(\boldsymbol{E}, u)\|_V \|\boldsymbol{\Sigma}\|_Q \qquad \text{for all } (\boldsymbol{E}, u) \in V, \boldsymbol{\Sigma} \in Q.$$

The bilinear form $a(\cdot, \cdot)$ is coercive on the kernel space V_0 defined by

$$V_0 := \{(\boldsymbol{E}, u) \in V \mid b((\boldsymbol{E}, u), \boldsymbol{\Sigma}) = 0 \text{ for all } \boldsymbol{\Sigma} \in Q\},$$

as there holds, see [171, Lemma 7], with Cauchy–Schwarz

$$\|u\|_{V_h} \preceq \sup_{\boldsymbol{\Sigma} \in M_h} \frac{\langle \nabla u, \boldsymbol{\Sigma} \rangle_{\mathcal{T}_h}}{\|\boldsymbol{\Sigma}\|_{M_h}} \overset{V_0}{=} \sup_{\boldsymbol{\Sigma} \in M_h} \frac{\int_\Omega \boldsymbol{E} : \boldsymbol{\Sigma}\, dx}{\|\boldsymbol{\Sigma}\|_{M_h}} \le \|\boldsymbol{E}\|_{\mathcal{R}_h} \tag{6.2.37}$$

and further (with $\lambda_{\min}(|\mathbb{C}|)$ denoting the minimal eigenvalue of $\mathbb{C}$)

$$a((\boldsymbol{E}, u), (\boldsymbol{E}, u)) \ge \lambda_{\min}(|\mathbb{C}|) \|\boldsymbol{E}\|_{\mathcal{R}_h}^2$$

$$\overset{(6.2.37)}{\succeq} \lambda_{\min}(|\mathbb{C}|) \left(\|\boldsymbol{E}\|_{\mathcal{R}_h}^2 + \|u\|_{V_h}^2\right) = \lambda_{\min}(|\mathbb{C}|) \|(\boldsymbol{E}, u)\|_V^2.$$

The LBB condition follows by choosing, for arbitrary but fixed $\boldsymbol{\Sigma} \in Q$, $u = 0$ and $\boldsymbol{E} = -\boldsymbol{\Sigma}$ (which is possible as $M_h \subset \mathcal{R}_h^{\mathrm{dc}}$)

$$\sup_{(\boldsymbol{E}, u) \in V} \frac{b((\boldsymbol{E}, u), \boldsymbol{\Sigma})}{\|\boldsymbol{E}\|_{\mathcal{R}_h} + \|u\|_{V_h}} = \sup_{(\boldsymbol{E}, u) \in V} \frac{\langle \nabla u, \boldsymbol{\Sigma} \rangle_{\mathcal{T}_h} - \int_\Omega \boldsymbol{E} : \boldsymbol{\Sigma}\, dx}{\|\boldsymbol{E}\|_{\mathcal{R}_h} + \|u\|_{V_h}} \ge \frac{\int_\Omega \boldsymbol{\Sigma} : \boldsymbol{\Sigma}\, dx}{\|\boldsymbol{\Sigma}\|_{L^2}} = \|\boldsymbol{\Sigma}\|_{M_h}$$

and thus, due to Brezzi's Theorem, there exists a unique solution $((\boldsymbol{E}, u), \boldsymbol{\Sigma}) \in V \times Q$ which depends continuously on the right hand side

$$\|(\boldsymbol{E}, u)\|_V + \|\boldsymbol{\Sigma}\|_Q \preceq \|f\|_{L^2}.$$

$\square$

6.18 Remark. *For the hybridized version of Problem 6.16 the proof can readily be adapted from the hybridized TDNNS method.*

6.19 Remark. *One may interpret $\boldsymbol{\Sigma}$ in (6.2.33) as an element of the dual space of the Regge elements, which gives that $\boldsymbol{C}$ is the Regge interpolant*

$$\boldsymbol{C} = \mathcal{I}_{\mathcal{R}}^k(\boldsymbol{F}^\top \boldsymbol{F}), \tag{6.2.38}$$

where e.g., in two dimensions considering (5.2.40a)–(5.2.40b)

$$\langle \boldsymbol{\Sigma}, \boldsymbol{C} - \boldsymbol{F}^\top \boldsymbol{F} \rangle_{\mathcal{R}_h^* \times \mathcal{R}_h} := \sum_{T \in \mathcal{T}_h} \int_T (\boldsymbol{C} - \boldsymbol{F}^\top \boldsymbol{F}) : \boldsymbol{\Sigma}\, dx + \int_{\partial T} (\boldsymbol{C} - \boldsymbol{F}^\top \boldsymbol{F})_{tt} : \boldsymbol{\Sigma}_{tt}\, ds. \tag{6.2.39}$$

6.3. Nonlinear TDNNS for (nearly) incompressible materials

As already discussed in Chapter 4 nearly incompressible materials like rubber may lead to ill-posed problems as the Lamé parameter $\hat{\lambda}$ tends to infinity. In the linear setting a common strategy is to define a new variable, the pressure, $p := \hat{\lambda} \operatorname{div}(u)$, leading to a Stokes-like mixed saddle point problem, see Problem 4.1. Other approaches use elements which are robust with respect to the parameter $\hat{\lambda}$ as e.g., $H(\operatorname{div})$-conforming elements [104] or are based on a split of the strain into a deviatoric and spherical part. The construction of stable methods for incompressible materials in the large deformation regime is ongoing topic of research and also here, methods based on mixed formulations have been proposed, e.g., [22, 208, 54, 204, 128]. The large deformation counterpart of the deviatoric and spherical splitting is the multiplicative Flory split [103] of the deformation gradient $\boldsymbol{F}$ into its volumetric $J^{\frac{1}{d}}\boldsymbol{I}$ and isochoric $J^{-\frac{1}{d}}\boldsymbol{F}$ part.

As in the previous section we will use the notation $J(u) := \det(\boldsymbol{F}(u))$ to indicate the dependence on the displacement, whereas J denotes a field independent of u.

In the nonlinear case incompressibility is characterized by the equation

$$1 \overset{!}{=} J(u) = \det(\boldsymbol{F}) = \det(\boldsymbol{I} + \nabla u), \tag{6.3.1}$$

i.e., the volume of the material gets preserved during deformation. Throughout this section we assume a Neo–Hookean material law of the form

$$\Psi(\boldsymbol{F}, J) := \Psi^{\hat{\mu}}(\boldsymbol{F}) + \frac{\hat{\lambda}}{2}W(J)^2 := \frac{\hat{\mu}}{2}(\operatorname{tr}(\boldsymbol{F}^\top \boldsymbol{F} - \boldsymbol{I}) - 2\log(\det(\boldsymbol{F}))) + \frac{\hat{\lambda}}{2}W(J)^2, \quad (6.3.2)$$

where the function $W : \mathbb{R}^+ \to \mathbb{R}$ fulfills $W(J) = 0 \Leftrightarrow J = 1$ (the material laws (2.2.20) and (2.2.22) are of this form).

Motivated by the linear case (4.1.4) we can define the pressure $p := \hat{\lambda}W(J)$ leading to the following Lagrangian, which gets discretized e.g., by the Stokes stable Taylor–Hood elements [118].

6.20 Problem. *Find a solution* $(u, p) \in [U_{h,0}^k]^d \times U_h^{k-1}$ *for the optimization problem*

$$\mathcal{L}(u, p) \to \min_u \max_p, \tag{6.3.3}$$

$$\text{with } \mathcal{L}(u, p) := \int_\Omega \Psi^{\hat{\mu}}(\boldsymbol{F}(u)) - f \cdot u + p\, W(J(u)) - \frac{1}{2\hat{\lambda}}p^2 \, dx. \tag{6.3.4}$$

The problem is well-posed for the limit $\hat{\lambda} \to \infty$, however, the incompressibility constraint is only imposed weakly by

$$\int_\Omega W(J(u))\, \delta p \, dx \overset{!}{=} 0 \qquad \text{for all } \delta p, \tag{6.3.5}$$

due to the high polynomial degree of $W(J(u))$. Even in the linear case Taylor–Hood elements do not lead to (point-wise) exact divergence free solutions

$$\int_\Omega \operatorname{div}(u)\, q \, dx = 0 \quad \text{for all } q \in U_h^{k-1} \not\Rightarrow \operatorname{div}(u) \equiv 0.$$

Thus, exact incompressibility is not guaranteed. We mention that for exact divergence free solutions $\text{div}(u) \equiv 0$ the property $\text{div}(V_h) \subset Q_h$ has to hold, where V_h and Q_h denotes the displacement and pressure space, respectively.

Using tangential continuous elements for the displacement field u yields the same problem as in Section 6.2.2 of multiplying distributions. The reason for this is that in two dimensions the determinant is quadratic and in three dimensions even cubic in ∇u. Therefore, in the spirit of Section 6.2.2, we introduce the determinant of the deformation gradient as a new independent field. Like in previous sections, also a lifting to an independent $\boldsymbol{F}$ or $\boldsymbol{C}$ is needed to obtain a well-defined problem. Therefore, we consider the lifting to $\boldsymbol{F}$ from Section 6.2.1 and note that the other two approaches can also be directly adapted. Starting from a continuous displacement field we propose the following compressible and incompressible problems

$$\int_\Omega \Psi(\boldsymbol{F}, J) - f \cdot \tilde{u}\, dx \to \min_{\substack{\tilde{u} \in [U_h^k]^d, \\ \boldsymbol{F} = \boldsymbol{F}(u) \\ J = J(u)}}, \qquad \int_\Omega \Psi(\boldsymbol{F}, J) - f \cdot \tilde{u}\, dx \to \min_{\substack{\tilde{u} \in [U_h^k]^d, \\ \boldsymbol{F} = \boldsymbol{F}(u) \\ J = J(u) \\ J = 1}}, \qquad (6.3.6a)$$

with the corresponding Lagrange functionals

$$\mathcal{L}(\tilde{u}, \boldsymbol{F}, \boldsymbol{P}, J, \theta) := \int_\Omega \Psi(\boldsymbol{F}, J) - f \cdot \tilde{u}\, dx - \int_\Omega (\boldsymbol{F} - \nabla \tilde{u} - \boldsymbol{I}) : \boldsymbol{P} - (J - J(\tilde{u}))\theta\, dx, \tag{6.3.7a}$$

$$\mathcal{L}(\tilde{u}, \boldsymbol{F}, \boldsymbol{P}, J, \theta, p) := \int_\Omega \Psi^{\hat{\mu}}(\boldsymbol{F}) - f \cdot \tilde{u}\, dx - \int_\Omega (\boldsymbol{F} - \nabla \tilde{u} - \boldsymbol{I}) : \boldsymbol{P} - (J - J(\tilde{u}))\theta + W(J)p\, dx. \tag{6.3.7b}$$

Note that for the nearly incompressible case the term $-\frac{1}{2\hat{\lambda}}p^2$ can be added to (6.3.7b). In the incompressible limit $\boldsymbol{P}$ is the constitutive part of the stress stemming from the variation in direction $\delta \boldsymbol{F}$

$$\int_\Omega \partial_{\boldsymbol{F}} \Psi^{\hat{\mu}}(\boldsymbol{F}) : \delta \boldsymbol{F} - \boldsymbol{P} : \delta \boldsymbol{F}\, dx \overset{!}{=} 0 \quad \text{for all } \delta \boldsymbol{F}. \tag{6.3.8}$$

Together with the contribution θ of the incompressibility constraint coming from the variation of (6.3.7b) in direction δJ

$$\int_\Omega \partial_J W(J)p\, \delta J - \theta \delta J\, dx \overset{!}{=} 0 \quad \text{for all } \delta J, \tag{6.3.9}$$

the total stress is given through the variation in direction $\delta \tilde{u}$

$$\int_\Omega (\boldsymbol{P} + \theta \operatorname{cof}(\boldsymbol{F}(\tilde{u}))) : \nabla \delta \tilde{u}\, dx - \int_\Omega f \cdot \delta \tilde{u}\, dx \overset{!}{=} 0 \quad \text{for all } \delta \tilde{u}, \tag{6.3.10}$$

where we used the identity

$$\partial_u J(u)(\delta u) = J(u)\boldsymbol{F}^{-\top}(u) : \nabla \delta u = \operatorname{cof}(\boldsymbol{F}(u)) : \nabla \delta u. \tag{6.3.11}$$

Note that $\mathrm{cof}(\boldsymbol{F}(\tilde{u})) = \boldsymbol{F}(\tilde{u})^{-\top}$ as $J = 1$ for the critical points of the Lagrangian. Thus, the full first Piola–Kirchhoff stress tensor reads $\widetilde{\boldsymbol{P}} = \boldsymbol{P} + \theta\,\mathrm{cof}(\boldsymbol{F}(\tilde{u}))$. Also in the compressible case (6.3.7a) the total stress is given by $\tilde{\boldsymbol{P}}$. As already discussed in Section 6.2.2 only the first Piola–Kirchhoff stress tensor has to be normal-continuous. Therefore, discontinuous elements for $\boldsymbol{P}$ and θ are used and the hybrid variable α is used to enforce the normal-normal continuity of $\widetilde{\boldsymbol{P}}$.

For the compressible case with a tangential-continuous displacement field the problem reads:

6.21 Problem. *Find a solution* $(u, \boldsymbol{F}, \boldsymbol{P}, J, \theta, \alpha) \in V_{h,0}^k \times [\mathcal{R}_h^{\mathrm{dc},k} \times [Q_h^k]_{\mathrm{skw}}^{d\times d}] \times [M_h^{\mathrm{dc},k} \times [Q_h^k]_{\mathrm{skw}}^{d\times d}] \times Q_h^{k-1} \times Q_h^{k-1} \times \Gamma_{h,0}^k$ *for the optimization problem*

$$\mathcal{L}^J(u, \boldsymbol{F}, \boldsymbol{P}, J, \theta, \alpha) \to \min_u \min_J \max_\theta \min_\alpha \min_{\boldsymbol{F}} \max_{\boldsymbol{P}}, \tag{6.3.12}$$

with $\mathcal{L}^J(u, \boldsymbol{F}, \boldsymbol{P}, J, \theta, \alpha) := \displaystyle\int_\Omega \Psi(\boldsymbol{F}, J) - f \cdot u - (\boldsymbol{F} - \boldsymbol{I}) : \boldsymbol{P}\,dx + \langle \nabla u, \boldsymbol{P}\rangle_{\mathcal{T}_h}$

$$+ \sum_{T \in \mathcal{T}_h} \int_{\partial T} (\boldsymbol{P} + \theta\,\mathrm{cof}(\boldsymbol{F}(u)))_{nn}\alpha_n\,ds - \langle J - J(u), \theta\rangle_0, \tag{6.3.13}$$

$$\langle J - J(u), \theta\rangle_0 := \sum_{T \in \mathcal{T}_h}\left(\int_T (J - J(u))\theta\,dx + \int_{\partial T} u_n \mathrm{cof}(\boldsymbol{F}(u))_{nn}\theta\,ds\right), \tag{6.3.14}$$

and $\langle \cdot, \cdot\rangle_{\mathcal{T}_h}$ *defined as in* (5.4.4).

Taking the first variation of (6.3.7a) in direction δJ we deduce that $\theta = \hat{\lambda}W(J)\partial_J W(J)$, which is the work conjugate stress to J, compare [54]. Taking all first variations yields the following system of equations

$$\langle \nabla\delta u, \boldsymbol{P}\rangle_{\mathcal{T}_h} + \sum_{T \in \mathcal{T}_h}\int_T \theta\,\mathrm{cof}(\boldsymbol{F}(u)) : \nabla\delta u\,dx$$

$$-\int_{\partial T} \delta u_n \mathrm{cof}(\boldsymbol{F}(u))_{nn}\theta + (u - \alpha)_n(\partial_u\mathrm{cof}(\boldsymbol{F}(u))(\delta u))_{nn}\theta\,ds \overset{!}{=} \int_\Omega f \cdot \delta u\,dx, \tag{6.3.15a}$$

$$\int_\Omega (\hat{\lambda}W(J)\partial_J W(J) - \theta)\delta J\,dx \overset{!}{=} 0, \tag{6.3.15b}$$

$$-\sum_{T \in \mathcal{T}_h}\left(\int_T (J - J(u))\delta\theta\,dx + \int_{\partial T}(u - \alpha)_n\mathrm{cof}(\boldsymbol{F}(u))_{nn}\delta\theta\,ds\right) \overset{!}{=} 0, \tag{6.3.15c}$$

$$\sum_{T \in \mathcal{T}_h}\int_{\partial T}(\boldsymbol{P} + \theta\,\mathrm{cof}(\boldsymbol{F}(u)))_{nn}\delta\alpha_n\,ds \overset{!}{=} 0, \tag{6.3.15d}$$

$$\int_\Omega \partial_{\boldsymbol{F}}\Psi(\boldsymbol{F}, J)(\delta\boldsymbol{F}) - \boldsymbol{P} : \delta\boldsymbol{F}\,dx \overset{!}{=} 0, \tag{6.3.15e}$$

$$\int_\Omega (\boldsymbol{I} - \boldsymbol{F}) : \delta\boldsymbol{P}\,dx + \langle\nabla u, \delta\boldsymbol{P}\rangle_{\mathcal{T}_h} + \sum_{T \in \mathcal{T}_h}\int_{\partial T}\delta\boldsymbol{P}_{nn}\alpha_n\,ds \overset{!}{=} 0. \tag{6.3.15f}$$

Note, that $\mathrm{cof}(\boldsymbol{F}(u))_{nn} = \det(\boldsymbol{F}(u)_{tt})$ is single-valued, as the tangential derivative of the tangential continuous displacement u is a continuous function. Here, $\boldsymbol{F}(u)_{tt}$ denotes the
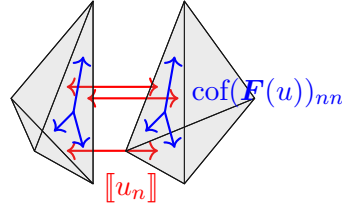
Figure 6.1.: Change of volume in-plane (blue) and out-of-plane (red) between two elements.

tangential-tangential 2×2 sub-matrix of $\boldsymbol{F}(u)$ in three dimensions and a scalar in 2D. The boundary term $\mathrm{cof}(\boldsymbol{F}(u))_{nn}[\![u_n]\!]$ measures the change of volume induced by the in-plane deformation, $\mathrm{cof}(\boldsymbol{F}(u))_{nn} = \det(\boldsymbol{F}(u)_{tt})$, and the out-of-plane displacement via the jump $[\![u_n]\!]$, cf. Figure 6.1. As a result also the change of volume between elements is considered for the lifting to J and not only the element-wise contribution:

$$J = \begin{cases} \det(\boldsymbol{I} + \nabla u) & \text{on } T, \\ \mathrm{cof}(\boldsymbol{F}(u))_{nn}[\![u_n]\!]_F & \text{on } F. \end{cases} \tag{6.3.16}$$

The polynomial orders for the spaces in Problem 6.21 are chosen such that for all variables the (optimal) convergence rate $\mathcal{O}(h^k)$ in the corresponding (natural) norms is expected (stemming from linear theory). We note that it is possible to increase the orders for J and θ, cf. Theorem 6.26. As we again multiplied distributions and defined a new nonlinear duality pairing, we have to show that the problem is consistent.

6.22 Lemma. *Problem 6.21 is consistent.*

Proof. To show consistency of (6.3.15) we proceed as in Lemma 6.9 and set for the exact (smooth) solution $\tilde{u}$, $\boldsymbol{F} := \boldsymbol{F}(\tilde{u})$, $J := J(\tilde{u})$, $\theta := \hat{\lambda}\partial_J W(J(\tilde{u}))$, $\boldsymbol{P} := \partial_{\boldsymbol{F}}\Psi(\boldsymbol{F}(\tilde{u}), J(\tilde{u}))$, and $\alpha := \mathrm{tr}_n\tilde{u}$. Starting with the left-hand side of (6.3.15a), noting that $(\tilde{u} - \alpha)_n = 0$, yields

$$\langle \nabla \delta u, \boldsymbol{P}\rangle + \sum_{T \in \mathcal{T}_h}\left(\int_T \theta \, \mathrm{cof}(\boldsymbol{F}(\tilde{u})) : \nabla \delta u \, dx - \int_{\partial T} \delta u_n \mathrm{cof}(\boldsymbol{F}(u))_{nn}\theta \, ds\right)$$

$$= \langle \nabla \delta u, \boldsymbol{P}\rangle + \sum_{T \in \mathcal{T}_h}\left(\int_T -\mathrm{div}(\theta \, \mathrm{cof}(\boldsymbol{F}(\tilde{u}))) \cdot \delta u \, dx + \int_{\partial T}(\delta u \, \mathrm{cof}(\boldsymbol{F}(\tilde{u}))_n - \delta u_n \mathrm{cof}(\boldsymbol{F}(\tilde{u}))_{nn})\theta \, ds\right)$$

$$= \langle \nabla \delta u, \boldsymbol{P}\rangle + \sum_{T \in \mathcal{T}_h}\left(\int_T -\mathrm{div}(\theta \, \mathrm{cof}(\boldsymbol{F}(\tilde{u}))) \cdot \delta u \, dx + \int_{\partial T} \delta u_t \cdot \mathrm{cof}(\boldsymbol{F}(\tilde{u}))_{nt}\theta \, ds\right)$$

$$= \sum_{T \in \mathcal{T}_h}\int_T -\mathrm{div}(\boldsymbol{P} + \theta \, \mathrm{cof}(\boldsymbol{F}(\tilde{u}))) \cdot \delta u \, dx + \sum_{E \in \mathcal{E}_h}\int_E \delta u_t \cdot [\![(\boldsymbol{P} + \theta \, \mathrm{cof}(\boldsymbol{F}(\tilde{u})))_{nt}]\!] \, ds.$$

The first term is the piece-wise force balance equation and the jump term enforces the normal-tangential continuity and together with (6.3.15a) the continuity of the normal components of the first Piola–Kirchhoff stress tensor. For the exact solution these conditions are fulfilled. Analogously, one can easily see that the other equations are also fulfilled. $\square$

For the (nearly) incompressible case we follow the same ideas as before posing the problem:

6.23 Problem. *Find a solution* $(u, \boldsymbol{F}, \boldsymbol{P}, J, \theta, \alpha, p) \in V_{h,0}^k \times [\mathcal{R}_h^{\mathrm{dc},k} \times [Q_h^k]_{\mathrm{skw}}^{d \times d}] \times [M_h^{\mathrm{dc},k} \times [Q_h^k]_{\mathrm{skw}}^{d \times d}] \times Q_h^{k-1} \times Q_h^{k-1} \times \Gamma_{h,0}^k \times Q_h^{k-1}$ *for the optimization problem*

$$\mathcal{L}^p(u, \boldsymbol{F}, \boldsymbol{P}, J, \theta, \alpha, p) \to \min_u \min_J \max_\theta \min_\alpha \min_{\boldsymbol{F}} \max_{\boldsymbol{P}} \max_p, \qquad (6.3.17)$$

with $\mathcal{L}^p(u, \boldsymbol{F}, \boldsymbol{P}, J, \theta, \alpha, p) := \displaystyle\int_\Omega \Psi^{\hat{\mu}}(\boldsymbol{F}) - f \cdot u - (\boldsymbol{F} - \boldsymbol{I}) : \boldsymbol{P} - \frac{1}{2\hat{\lambda}} p^2 + W(J) p \, dx$

$$+ \langle \nabla u, \boldsymbol{P} \rangle_{\mathcal{T}_h} + \sum_{T \in \mathcal{T}_h} \int_{\partial T} (\boldsymbol{P} + \theta \operatorname{cof}(\boldsymbol{F}(u)))_{nn} \alpha_n \, ds - \langle J - J(u), \theta \rangle_0, \quad (6.3.18)$$

where $\langle \cdot, \cdot \rangle_{\mathcal{T}_h}$ *and* $\langle \cdot, \cdot \rangle_0$ *are defined as in* (5.4.4) *and* (6.3.14), *respectively.*

Similar to Problem 6.20 the pressure p is used to enforce $J = 1$ in a weak sense. However, due to the lifting from $J(u)$ to J involving also boundary terms not only the element-wise incompressibility is forced.

Again, we used complete discontinuous stresses $\boldsymbol{P}$ together with the hybridization variable α enforcing the normal-normal continuity, $(\boldsymbol{P} + \theta \operatorname{cof}(\boldsymbol{F}(u)))_{nn}$, of the total stress. The consistency follows analogously to Lemma 6.22.

Linearization: We consider the small strain assumptions $u = \mathcal{O}(\varepsilon)$, $\nabla u = \mathcal{O}(\varepsilon)$, $J = 1 + J_\varepsilon$ ($J_\varepsilon = \mathcal{O}(\varepsilon)$), $\operatorname{cof}(\boldsymbol{F}(u)) = \boldsymbol{I} + \mathcal{O}(\varepsilon)$, $J(u) = 1 + \operatorname{div}(u) + \mathcal{O}(\varepsilon^2)$, $\boldsymbol{F} = \boldsymbol{I} + \boldsymbol{F}_\varepsilon$ ($\boldsymbol{F}_\varepsilon = \mathcal{O}(\varepsilon)$), and $\theta = \mathcal{O}(\varepsilon)$. The incompressible part of material laws (2.2.20) and (2.2.22) reduce both to $W(J) \partial_J W(J) \approx J_\varepsilon$ in the linear regime and thus, we obtain for the compressible Problem 6.21:

$$\langle \nabla \delta u, \boldsymbol{P} \rangle_{\mathcal{T}_h} + \sum_{T \in \mathcal{T}_h} \left(\int_T \theta \operatorname{div}(\delta u) \, dx - \int_{\partial T} \delta u_n \theta \, ds \right) = \int_\Omega f \cdot \delta u \, dx, \qquad (6.3.19\mathrm{a})$$

$$\int_\Omega (\hat{\lambda} J_\varepsilon - \theta) \delta J \, dx = 0, \qquad (6.3.19\mathrm{b})$$

$$\sum_{T \in \mathcal{T}_h} \left(- \int_T (J_\varepsilon - \operatorname{div}(u)) \delta\theta \, dx + \int_{\partial T} (u - \alpha)_n \delta\theta \, ds \right) = 0, \qquad (6.3.19\mathrm{c})$$

$$\sum_{T \in \mathcal{T}_h} \int_{\partial T} (\boldsymbol{P}_{nn} + \theta) \delta\alpha_n \, ds = 0, \qquad (6.3.19\mathrm{d})$$

$$\int_\Omega (2\hat{\mu} \operatorname{sym}(\boldsymbol{F}_\varepsilon) - \boldsymbol{P}) : \delta\boldsymbol{F} \, dx = 0, \qquad (6.3.19\mathrm{e})$$

$$\int_\Omega \boldsymbol{F}_\varepsilon : \delta\boldsymbol{P} \, dx + \langle \nabla u, \delta\boldsymbol{P} \rangle_{\mathcal{T}_h} + \sum_{T \in \mathcal{T}_h} \int_{\partial T} \delta\boldsymbol{P}_{nn} \alpha_n \, ds = 0, \qquad (6.3.19\mathrm{f})$$

where we used that $\partial_{\boldsymbol{F}} \Psi^{\hat{\mu}}(\boldsymbol{F}) \approx 2\hat{\mu} \operatorname{sym}(\boldsymbol{F}_\varepsilon)$.

For the (nearly) incompressible case, variation (6.3.15b) and thus linearization (6.3.19b) changes and a new equation induced by the pressure appears:

$$\int_\Omega (p - \theta)\delta J\, dx \qquad = 0, \tag{6.3.20a}$$

$$\int_\Omega \left(J_\varepsilon - \frac{1}{2\hat\lambda}p \right)\delta p\, dx = 0. \tag{6.3.20b}$$

Note, that the lifting J_ε in (6.3.19c) consists of a volume and a jump term, including the change of displacement in normal direction between two elements

$$J_\varepsilon = \begin{cases} \operatorname{div}(u) & \text{on } T, \\ [\![u_n]\!]_F & \text{on } F. \end{cases} \tag{6.3.21}$$

Thus, in the incompressible case the element-wise incompressibility as well as the normal-flow through elements is forced to be zero, i.e., the balance of mass is globally considered and not only (locally) element-wise, compare also $H(\operatorname{div})$-conforming elements in the context of incompressible Stokes equations [145].

By defining $\boldsymbol{E} := \operatorname{sym}(\boldsymbol{F}_\varepsilon)$ and renaming $\boldsymbol{\Sigma} := \boldsymbol{P}$, which is now symmetric, and $J := J_\varepsilon$ we obtain the following linearized problems:

6.24 Problem. *Find a solution $(u, \boldsymbol{E}, \boldsymbol{\Sigma}, J, \theta, \alpha) \in V_{h,0}^k \times \mathcal{R}_h^{\mathrm{dc},k} \times M_h^{\mathrm{dc},k} \times Q_h^{k-1} \times Q_h^{k-1} \times \Gamma_{h,0}^k$ for the optimization problem*

$$\mathcal{L}_{\mathrm{lin}}^J(u, \boldsymbol{E}, \boldsymbol{\Sigma}, J, \theta, \alpha) = \int_\Omega \hat\mu \|\boldsymbol{E}\|_F^2 - f \cdot u - \boldsymbol{E} : \boldsymbol{\Sigma} - (J - \operatorname{div}(u))\theta - \frac{\hat\lambda}{2}J^2\, dx$$

$$+ \langle \nabla u, \boldsymbol{\Sigma} \rangle_{\mathcal{T}_h} + \sum_{T \in \mathcal{T}_h} \int_{\partial T} (\boldsymbol{\Sigma} + \theta \boldsymbol{I})_{nn}\alpha_n - u_n\theta\, ds. \tag{6.3.22}$$

6.25 Problem. *Find a solution $(u, \boldsymbol{E}, \boldsymbol{\Sigma}, J, \theta, \alpha, p) \in V_{h,0}^k \times \mathcal{R}_h^{\mathrm{dc},k} \times M_h^{\mathrm{dc},k} \times Q_h^{k-1} \times Q_h^{k-1} \times \Gamma_{h,0}^k \times Q_h^{k-1}$ for the optimization problem*

$$\mathcal{L}_{\mathrm{lin}}^p(u, \boldsymbol{E}, \boldsymbol{\Sigma}, J, \theta, \alpha, p) = \int_\Omega \hat\mu \|\boldsymbol{E}\|_F^2 - f \cdot u - \boldsymbol{E} : \boldsymbol{\Sigma} - (J - \operatorname{div}(u))\theta - \frac{1}{2\hat\lambda}p^2 + pJ\, dx$$

$$+ \langle \nabla u, \boldsymbol{\Sigma} \rangle_{\mathcal{T}_h} + \sum_{T \in \mathcal{T}_h} \int_{\partial T} (\boldsymbol{\Sigma} + \theta \boldsymbol{I})_{nn}\alpha_n - u_n\theta\, ds. \tag{6.3.23}$$

6.26 Theorem. *Let $V_{h,0} \times M_h^{\mathrm{dc}} \times \Gamma_{h,0}$ be a stable TDNNS pairing, $M_h^{\mathrm{dc}} \subset \mathcal{R}_h^{\mathrm{dc}}$, the spaces for θ and J coincide, and the pressure space is a subset of those. Then both, Problem 6.24 and Problem 6.25, are uniquely solvable.*

Proof. We start by proving the existence and uniqueness of solutions of Problem (6.24). Let $(u, \alpha) \in V_{h,0} \times \Gamma_{h,0}$, $\boldsymbol{\Sigma} \in M_h^{\mathrm{dc}}$, $\boldsymbol{E} \in \mathcal{R}_h^{\mathrm{dc}}$, $J, \theta \in Q_h$, define the discrete norms

$$\|(u, \alpha)\|_{V_h \times \Gamma_h}^2 := \sum_{T \in \mathcal{T}_h} \|\nabla u\|_{L^2(T)}^2 + \sum_{F \in \mathcal{F}_h} \frac{1}{h_F} \|[\![(u - \alpha)_n]\!]\|_{L^2(F)}^2,$$

$$\|\boldsymbol{\Sigma}\|_{M_h} := \|\boldsymbol{\Sigma}\|_{L^2}, \quad \|\boldsymbol{E}\|_{\mathcal{R}_h} := \|\boldsymbol{E}\|_{L^2},$$

and equip Q_h with the L^2-norm. There holds the norm equivalences

$$\|\boldsymbol{\Sigma}\|_{M_h}^2 \sim \sum_{T \in \mathcal{T}_h} \|\boldsymbol{\Sigma}\|_{L^2(T)}^2 + \sum_{F \in \mathcal{F}_h} h_F \|\boldsymbol{\Sigma}_{nn}\|_{L^2(F)}^2, \quad \|\theta\|_{L^2}^2 \sim \sum_{T \in \mathcal{T}_h} \|\theta\|_{L^2(T)}^2 + \sum_{F \in \mathcal{F}_h} h_F \|[\![\theta]\!]\|_{L^2(F)}^2.$$

We define the following spaces for Brezzi's Theorem

$$V := \mathcal{R}_h^{\mathrm{dc}} \times V_{h,0} \times \Gamma_{h,0} \times Q_h, \qquad\qquad Q := M_h^{\mathrm{dc}} \times Q_h,$$

with the corresponding product norms and the bilinear forms

$$a((\boldsymbol{E}, u, \alpha, J), (\delta\boldsymbol{E}, \delta u, \delta\alpha, \delta J)) := \int_\Omega 2\hat{\mu}\, \boldsymbol{E} : \delta\boldsymbol{E} + \hat{\lambda}\, J\delta J\, dx$$

$$b((\boldsymbol{E}, u, \alpha, J), (\boldsymbol{\Sigma}, \theta)) := \sum_{T \in \mathcal{T}_h} \int_T (\mathrm{div}(u) - J)\theta + \boldsymbol{\Sigma} : (\nabla u - \boldsymbol{E})\, dx$$

$$+ \int_{\partial T} (\boldsymbol{\Sigma}_{nn} + \theta)(\alpha - u)_n\, ds.$$

It can be readily checked that these are continuous. For the kernel coercivity we have

$$V_0 := \{(\boldsymbol{E}, u, \alpha, J) \in V : b((\boldsymbol{E}, u, \alpha, J), (\boldsymbol{\Sigma}, \theta)) = 0 \text{ for all } (\boldsymbol{\Sigma}, \theta) \in Q\}$$

and the hybridized version of [171, Lemma 7]

$$\|(u, \alpha)\|_{V_h \times \Gamma_h} \preceq \sup_{\boldsymbol{\sigma} \in M_h^{\mathrm{dc}}} \frac{\sum_{T \in \mathcal{T}_h} \int_T \nabla u : \boldsymbol{\sigma}\, dx + \int_{\partial T} \boldsymbol{\sigma}_{nn}(\alpha - u)_n\, ds}{\|\boldsymbol{\sigma}\|_{L^2}}.$$

We use V_0 by explicitly setting $\theta = 0$

$$\|(u, \alpha)\|_{V_h \times \Gamma_h} \preceq \sup_{\boldsymbol{\Sigma} \in M_h^{\mathrm{dc}}} \frac{\sum_{T \in \mathcal{T}_h} \int_T \nabla u : \boldsymbol{\Sigma}\, dx + \int_{\partial T} \boldsymbol{\Sigma}_{nn}(\alpha - u)_n\, ds}{\|\boldsymbol{\Sigma}\|_{L^2}}$$

$$\overset{V_0}{=} \sup_{\boldsymbol{\Sigma} \in M_h^{\mathrm{dc}}} \frac{\int_\Omega \boldsymbol{E} : \boldsymbol{\Sigma}\, dx}{\|\boldsymbol{\Sigma}\|_{L^2}} \leq \|\boldsymbol{E}\|_{\mathcal{R}_h}. \tag{6.3.24}$$

Further there holds by setting $\boldsymbol{\Sigma} = 0$ in V_0

$$\|J\|_{L^2} = \sup_{\theta \in Q_h} \frac{\int_\Omega J\theta\, dx}{\|\theta\|_{L^2}} \overset{V_0}{=} \sup_{\theta \in Q_h} \frac{\sum_{T \in \mathcal{T}_h} \int_T \mathrm{div}(u)\theta\, dx + \int_{\partial T} \theta(\alpha - u)_n\, ds}{\|\theta\|_{L^2}}$$

$$\preceq \|(u, \alpha)\|_{V_h \times \Gamma_h} \overset{(6.3.24)}{\preceq} \|\boldsymbol{E}\|_{\mathcal{R}_h}. \tag{6.3.25}$$

Therefore, the kernel coercivity holds

$$a((\boldsymbol{E}, u, \alpha, J), (\boldsymbol{E}, u, \alpha, J)) \succeq \|(\boldsymbol{E}, u, \alpha, J)\|_V \quad \text{for all } (\boldsymbol{E}, u, \alpha, J) \in V_0.$$

For the LBB condition we get for all arbitrary but fixed $(\boldsymbol{\Sigma}, \theta) \in Q$

$$\sup_{(\boldsymbol{E}, u, \alpha, J) \in V} \frac{b((\boldsymbol{E}, u, \alpha, J), (\boldsymbol{\Sigma}, \theta))}{\|(\boldsymbol{E}, u, \alpha, J)\|_V} \overset{(u,\alpha)=0}{\geq} \sup_{(\boldsymbol{E}, J) \in \mathcal{R}_h \times Q_h} \frac{\int_\Omega J\theta - \boldsymbol{E} : \boldsymbol{\Sigma} \, dx}{\|\boldsymbol{E}\|_{\mathcal{R}_h} + \|J\|_{L^2}}$$

$$\overset{\boldsymbol{E}=-\boldsymbol{\Sigma}, J=\theta}{\succeq} \|(\boldsymbol{\Sigma}, \theta)\|_Q.$$

The choices are valid due to the requirement of the spaces. Thus, due to Brezzi's Theorem, there exists a unique solution $((\boldsymbol{E}, u, \alpha, J), (\boldsymbol{\Sigma}, \theta)) \in V \times Q$ which depends continuously on the right-hand side

$$\|(\boldsymbol{E}, u, \alpha, J)\|_V + \|(\boldsymbol{\Sigma}, \theta)\|_Q \preceq c\|f\|_{L^2}.$$

Next, we show existence and uniqueness of Problem 6.25 by first proving that the incompressible case "$\hat{\lambda} = \infty$" is well-posed and then deduce directly with the extended Brezzi Theorem 3.9 that Problem 6.25 is uniquely solvable (with stability constant independently of $\hat{\lambda}$) for $1 < \hat{\lambda} < \infty$.

We equip the pressure space $\tilde{Q}_h \subset Q_h$ with the L^2-norm and define on the product spaces

$$V := \mathcal{R}_h^{\mathrm{dc}} \times V_{h,0} \times \Gamma_{h,0} \times Q_h, \qquad\qquad Q := M_h^{\mathrm{dc}} \times Q_h \times \tilde{Q}_h,$$

the bilinear forms

$$a^p((\boldsymbol{E}, u, \alpha, J), (\delta\boldsymbol{E}, \delta u, \delta\alpha, \delta J)) := \int_\Omega 2\hat{\mu}\, \boldsymbol{E} : \delta\boldsymbol{E} \, dx,$$

$$b^p((\boldsymbol{E}, u, \alpha, J), (\boldsymbol{\Sigma}, \theta, p)) := \sum_{T \in \mathcal{T}_h} \Big(\int_T (\mathrm{div}(u) - J)\theta + pJ + \boldsymbol{\Sigma} : (\nabla u - \boldsymbol{E}) \, dx$$

$$+ \int_{\partial T} (\boldsymbol{\Sigma}_{nn} + \theta)(\alpha - u)_n \, ds \Big),$$

which are obviously continuous. The estimates (6.3.24) and (6.3.25) also hold on

$$V_0^p := \{(\boldsymbol{E}, u, \alpha, J) \in V : b^p((\boldsymbol{E}, u, \alpha, J), (\boldsymbol{\Sigma}, \theta, p)) = 0 \text{ for all } (\boldsymbol{\Sigma}, \theta, p) \in Q\}$$

as $V_0^p \subset V_0$ and thus the kernel coercivity follows immediately. For the LBB condition let $\boldsymbol{\Sigma}$, θ, and p be arbitrary but fixed. We solve (5.4.6) with a different right-hand side as auxiliary problem: Find $(\boldsymbol{\sigma}, u, \alpha) \in M_h^{\mathrm{dc}} \times V_{h,0} \times \Gamma_{h,0}$ such that for all $(\delta\boldsymbol{\sigma}, \delta u, \delta\alpha) \in M_h^{\mathrm{dc}} \times V_{h,0} \times \Gamma_{h,0}$

$$\int_\Omega \boldsymbol{\sigma} : \delta\boldsymbol{\sigma} \, dx - \sum_{T \in \mathcal{T}_h} \int_T \nabla u : \delta\boldsymbol{\sigma} + \int_{\partial T} (\alpha - u)_n (\delta\boldsymbol{\sigma})_{nn} \, ds = 0,$$

$$-\sum_{T \in \mathcal{T}_h} \int_T \nabla\delta u : \boldsymbol{\sigma} \, dx - \int_{\partial T} \delta u_n \boldsymbol{\sigma}_{nn} \, ds = -\sum_{T \in \mathcal{T}_h} \int_T \nabla\delta u : (\boldsymbol{\Sigma} + \theta\boldsymbol{I}) \, dx - \int_{\partial T} \delta u_n (\boldsymbol{\Sigma} + \theta\boldsymbol{I})_{nn} \, ds,$$

$$-\sum_{T \in \mathcal{T}_h} \int_{\partial T} \delta\alpha_n \boldsymbol{\sigma}_{nn} \, ds = -\sum_{T \in \mathcal{T}_h} \int_{\partial T} \delta\alpha_n (\boldsymbol{\Sigma} + \theta\boldsymbol{I})_{nn} \, ds,$$
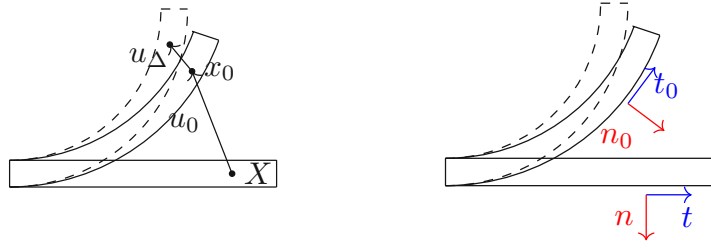
Figure 6.2.: Reference configuration, intermediate configuration and actual configuration (left) and normal and tangential vector on reference and intermediate configuration (right).

where $\boldsymbol{\sigma} = \boldsymbol{\Sigma} + \theta \boldsymbol{I}$ is part of the unique solution $(\boldsymbol{\sigma}, u, \alpha)$. Further, we have the stability estimate $\|(u, \alpha)\|_{V_h \times \Gamma_h}\| \preceq (\|\boldsymbol{\Sigma}\|_{M_h} + \|\theta\|_{L^2})$ and by choosing $\delta\boldsymbol{\sigma} = \boldsymbol{\Sigma} + \theta \boldsymbol{I}$ as test function we obtain

$$\sum_{T \in \mathcal{T}_h} \left(\int_T \nabla u : (\boldsymbol{\Sigma} + \theta \boldsymbol{I}) + \int_{\partial T} (\alpha - u)_n (\boldsymbol{\Sigma} + \theta \boldsymbol{I})_{nn} \, ds \right) = \|\boldsymbol{\Sigma} + \theta \boldsymbol{I}\|_{L^2}.$$

We fix the corresponding u and α, which yields with the choices $J = p$, $\boldsymbol{E} = -4\boldsymbol{\Sigma}$ and Young's[1] inequality

$$
\sup_{(\boldsymbol{E}, u, \alpha, J) \in V} \frac{b^p((\boldsymbol{E}, u, \alpha, J), (\boldsymbol{\Sigma}, \theta, p))}{\|(\boldsymbol{E}, u, \alpha, J)\|_V} \geq \sup_{(\boldsymbol{E}, J) \in \mathcal{R}_h^{\mathrm{dc}} \times Q_h} \frac{\int_\Omega pJ - J\theta - \boldsymbol{\Sigma} : \boldsymbol{E} \, dx + \|\boldsymbol{\Sigma} + \theta \boldsymbol{I}\|_{L^2}}{\|E\|_{\mathcal{R}_h} + \|J\|_{L^2} + c \left(\|\boldsymbol{\Sigma}\|_{M_h} + \|\theta\|_{L^2} \right)}
$$

$$
\succeq \frac{\|p\|_{L^2}^2 - \langle p, \theta \rangle_{L^2} + 5\|\boldsymbol{\Sigma}\|_{L^2}^2 + 2\langle \boldsymbol{\Sigma}, \theta \boldsymbol{I} \rangle_{L^2} + \|\theta\|_{L^2}^2}{\|\boldsymbol{\Sigma}\|_{\mathcal{R}_h} + \|p\|_{L^2} + \|\theta\|_{L^2}}
$$

$$
\geq \frac{\frac{1}{2}\|p\|_{L^2}^2 + (\frac{1}{2} - \varepsilon)\|\theta\|_{L^2}^2 + (5 - \frac{1}{\varepsilon})\|\boldsymbol{\Sigma}\|_{L^2}^2}{\|\boldsymbol{\Sigma}\|_{\mathcal{R}_h} + \|p\|_{L^2} + \|\theta\|_{L^2}}
$$

$$
\overset{\varepsilon = \frac{1}{4}}{\succeq} \|(\boldsymbol{\Sigma}, \theta, p)\|_Q,
$$

which concludes the proof. $\qquad\square$

6.27 Remark. *Note that we need the estimate $\|J\|_{L^2} \leq \|\boldsymbol{E}\|_{\mathcal{R}_h}$ in the proof as $\hat{\lambda}$ can be zero. If $\hat{\lambda} \neq 0$ the kernel coercivity of Problem 6.24 follows directly also without this estimate.*

6.4. Updated Lagrangian

When large rotations occur, normal and tangential directions vary strongly when going from reference to spatial configuration. This may lead to problems as the proposed methods highly depend on these vectors. We observed sub-optimal behavior for thin structured elements for the methods with lifting to $\boldsymbol{F}$ or $\boldsymbol{F}/\boldsymbol{C}$. For the method with lifting to $\boldsymbol{C}$

---

[1] Young: $-ab \geq -\frac{1}{2\varepsilon}a^2 - \frac{\varepsilon}{2}b^2$ for all $a, b \in \mathbb{R}$, $\varepsilon > 0$

even breakdown has been observed as the rotations approached about 90°. To mitigate these problems, an updated Lagrangian scheme can be applied, where in each load step the configuration obtained in the last load step is used as intermediate configuration, compare Figure 6.2. As rotations during a single load step to be less than 90° can be assumed, better behavior of the method is expected. For a precise description of the updated Lagrangian method we refer to [163, 175].

6.5. Numerical examples

In this section the methods from Section 6.2.1, 6.2.2, and 6.2.3 are denoted by $\boldsymbol{F}$, $\boldsymbol{C}$, and $\boldsymbol{FC}$, respectively. As already mentioned before, we observed that the $\boldsymbol{F}$-based method is more robust compared to the $\boldsymbol{C}$-based method giving slightly better results, however, at the cost of more Newton iterations for every load step. The $\boldsymbol{FC}$-based method incorporates both advantages, the robustness of $\boldsymbol{F}$- and the faster Newton convergence of $\boldsymbol{C}$-based method. The drawback of this approach is to be locally more expensive, due to the higher number of local dofs.

For all benchmarks quadratic polynomial order for the displacement field u, $k = 2$, is used. We emphasize, however, that also the lowest order polynomial degree $k = 1$ can be used as well as higher polynomial orders. We compare the methods also with standard Lagrangian elements of polynomial order $k = 2$ for the displacement u solving (6.1.2). We denote it by method "std". Note that for the same grids the coupling dofs of our methods are nearly doubled compared to the standard Lagrangian method in two dimensions as there are asymptotically three times more edges than vertices, $\#E \approx 3\#V$, where the dofs are placed (compare Figure 5.2 and Figure 5.4). In the three dimensional case the coupling type dofs are approximately four times more due to the fact that $\#E \approx 7\#V$.

To solve the nonlinear problems a Newton method with possible damping is used together with a load step scheme, where the right-hand side is scaled by a factor starting from zero and then gets increased gradually to one. The stiffness matrices appearing during the Newton iterations are symmetric due to solving constraint minimization problems. Furthermore, as we use static condensation, the resulting smaller system is also a minimization problem involving only the displacement based unknowns u and α, enabling the use of the built in *sparsecholesky* solver of NGSolve.

The following benchmark examples and results for the compressible regime are taken from [163], to which we refer also for more examples including applications of the updated Lagrangian scheme. Full code examples are available[2].

6.5.1. Shearing Plate

We apply shear loads to a clamped square plate with length $1\,\mathrm{mm}$, see Figure 6.3. This benchmark has been considered e.g., in [6, 186]. The exact displacement field is assumed to be

$$U_{\mathrm{ex}} = \begin{pmatrix} \frac{1}{2}y^3 + \frac{1}{2}\sin\left(\frac{\pi y}{2}\right) \\ 0 \end{pmatrix}$$

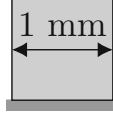[2]www.gitlab.com/mneunteufel/nonlinear_elasticity

Figure 6.3.: Geometry of shearing plate example.

	ne	dof	coupl. dof	$\|U - U_{\mathrm{ex}}\|_{L^2}$	$\|\boldsymbol{F} - \boldsymbol{F}_{\mathrm{ex}}\|_{L^2}$
$\boldsymbol{F}$	14	852	138	4.11e-04	7.01e-03
	56	3390	534	5.86e-05	1.99e-03
	230	13860	2130	6.24e-06	4.53e-04
	938	56400	8562	6.64e-07	1.03e-04
	3724	223680	33756	8.22e-08	2.57e-05
$\boldsymbol{C}$	14	852	138	5.12e-04	1.64e-02*
	56	3390	534	6.15e-05	4.63e-03*
	230	13860	2130	6.62e-06	1.08e-03*
	938	56400	8562	7.04e-07	2.50e-04*
	3724	223680	33756	8.70e-08	6.17e-05*
$\boldsymbol{FC}$	14	1692	138	4.11e-04	7.01e-03
	56	6750	534	5.86e-05	1.99e-03
	230	27660	2130	6.24e-06	4.53e-04
	938	112680	8562	6.64e-07	1.03e-04
	3724	447120	33756	8.22e-08	2.57e-05

Table 6.1.: Results for shearing plate example. For all methods the number of elements, number of dofs and coupling dofs, and the L^2-error of the displacement and deformation gradient are presented. *: For the $\boldsymbol{C}$-based method $\|\boldsymbol{C} - \boldsymbol{C}_{\mathrm{ex}}\|_{L^2}$ is computed.

and the Neo-Hookean material law (2.2.22) with parameters $\hat{\mu} = \hat{\lambda} = 1 \,\mathrm{N\,mm}^{-2}$ is used. With the exact solution U_{ex} at hand the corresponding right hand sides f and g can be easily computed. Unstructured triangular meshes are used and the final deformation is depicted in Figure 6.4. The results for all methods can be found in Table 6.1. Figure 6.5 shows the absolute error of the displacement $\|U - U_{\mathrm{ex}}\|_{L^2}$ and deformation gradient $\|\boldsymbol{F} - \boldsymbol{F}_{\mathrm{ex}}\|_{L^2}$. Note that for the $\boldsymbol{C}$-based method the quantity $\|\boldsymbol{C} - \boldsymbol{C}_{\mathrm{ex}}\|_{L^2}$ is computed instead, as the approach does not use the deformation gradient $\boldsymbol{F}$. Thus, the corresponding error curve is slightly shifted above compared to the others. The expected optimal rates for all methods are observed, cubic for the displacement U and quadratic for $\boldsymbol{F}$ and $\boldsymbol{C}$, respectively. For the $\boldsymbol{C}$-based method we needed stabilization (6.2.26) with $c_1 = 1$ to guarantee convergence also for finer grids.

6.5.2. Cook's Membrane

We consider the well-established Cook's membrane problem, see Figure 6.6, which has been used as a benchmark problem by [6, 186]. Material parameters for the hyperelastic
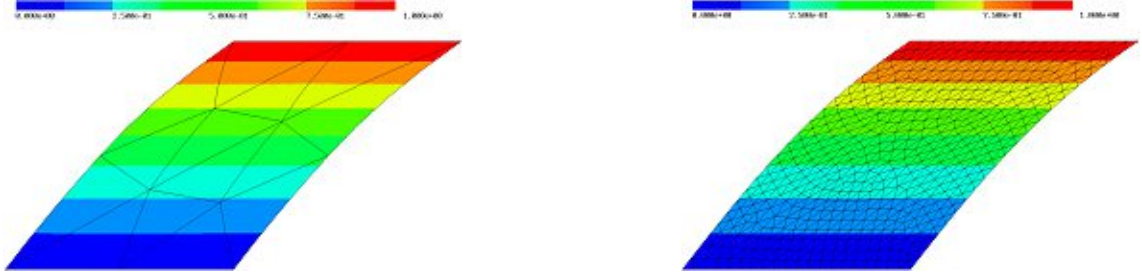
Figure 6.4.: Final deformation of shearing plate example with 14 and 934 elements.
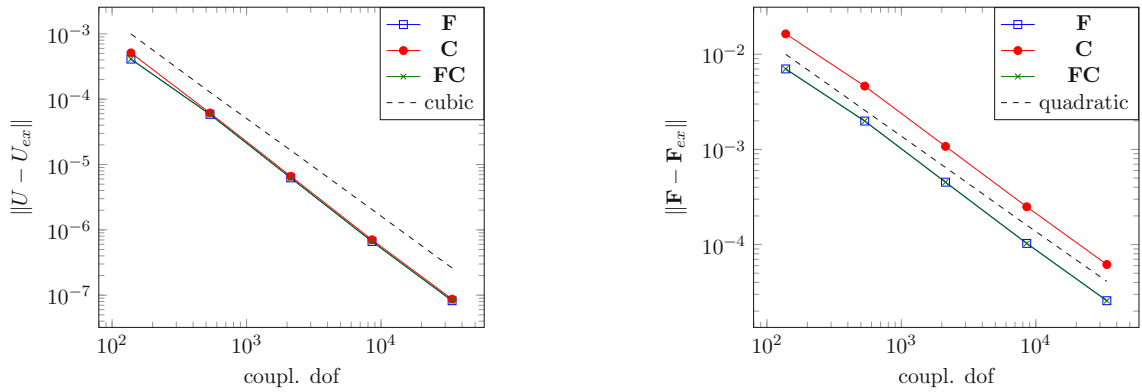

Figure 6.5.: L^2-errors of the methods with respect to the coupling dofs for shearing plate example. Left: Displacement error $\|U - U_{\mathrm{ex}}\|_{L^2}$. Right: Error of deformation gradient $\|\boldsymbol{F} - \boldsymbol{F}_{\mathrm{ex}}\|_{L^2}$ for $\boldsymbol{F}$- and $\boldsymbol{FC}$-based method and Cauchy–Green strain tensor $\|\boldsymbol{C} - \boldsymbol{C}_{\mathrm{ex}}\|_{L^2}$ for $\boldsymbol{C}$-based method.

potential (2.2.20) are $\hat{\mu} = 80.194\,\text{N}\,\text{mm}^{-2}$ and $\hat{\lambda} = 40\,889.8\,\text{N}\,\text{mm}^{-2}$, i.e., the material behaves nearly incompressible. The quantity of interest is given by the vertical deflection at point A, cf. Figure 6.6. Different shear forces $f = 8, 16, 24, 32\,\text{N}\,\text{mm}^{-2}$ are considered and structured quadrilateral meshes with 2×2, 4×4, 8×8, 16×16, 32×32 grids are used. It is well-known that on the top left corner a strong singularity leads to reduced convergence rates. Therefore, mostly adaptive (triangular) or nested meshes are used to resolve the singularity. For the proposed methods, however, already a coarse 2×2 uniform quadrilateral grid produces accurate results being already in the correct magnitude, see Figure 6.7. In Figure 6.8 a comparison between the standard and $\boldsymbol{F}$-based method for $f = 32$ is shown, where a significant difference in the vertical deflection can be seen for the coarse mesh. We observe that the quadrilateral on the top left deforms also on the clamped left boundary, as the components are not prescribed point-wise giving the proposed methods more flexibility.
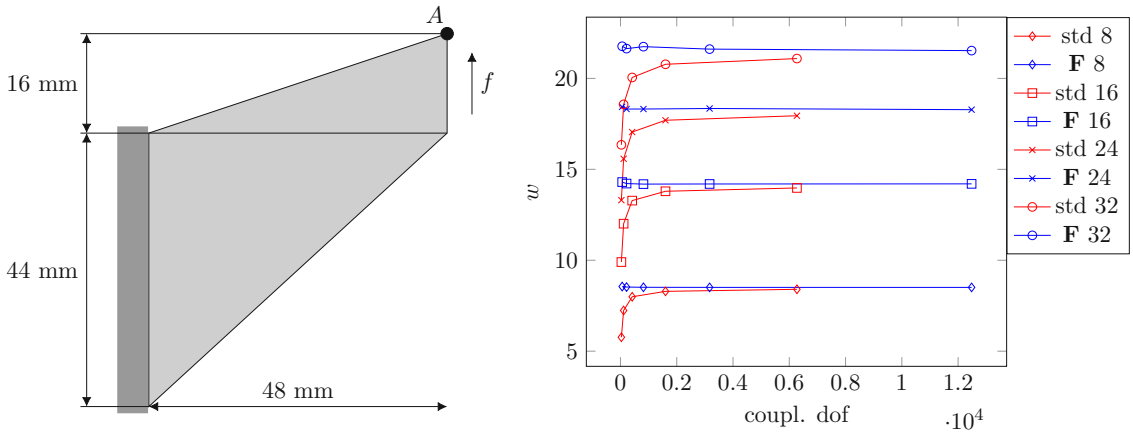

Figure 6.6.: Geometry of Cook's membrane example.

Figure 6.7.: Vertical deflection w at point A for Cook's membrane example for $f = 8, 16, 24, 32$ with standard and $\boldsymbol{F}$-based method.

For the $\boldsymbol{C}$-based method, however, stabilization techniques (6.2.26) and (6.2.27) are used with parameters $c_1 = 1$ and $c_2 = \frac{\hat{\mu}}{2}$, respectively. With them, only on the finest grid for the large forces $f = 24, 32$ Newton's method did not converge, showing the more robust behavior of the $\boldsymbol{F}$ and $\boldsymbol{FC}$ methods. The results for forces $f = 16, 24, 32$ can be found in Table 6.2. All results are comparable with those in [6, 186].

6.5.3. Cylindrical Shell

The benchmark presented in [189, 186] has to be adapted in terms of the force and boundary condition as line forces and traces are not well-defined in terms of Sobolev spaces in three spatial dimensions. The same geometry and material parameters are considered. A quarter of a cylindrical structure with $r_i = 9 - \text{t}/2\,\text{mm}$, $l = 15\,\text{mm}$, and thickness $t = 2\,\text{mm}$ or $0.2\,\text{mm}$, see Figure 6.9, and $\hat{\mu} = 6000\,\text{N}\,\text{mm}^{-2}$ and $\hat{\lambda} = 24\,000\,\text{N}\,\text{mm}^{-2}$ together with the hyperelastic potential (2.2.20). Clamped boundary conditions are prescribed at the bottom
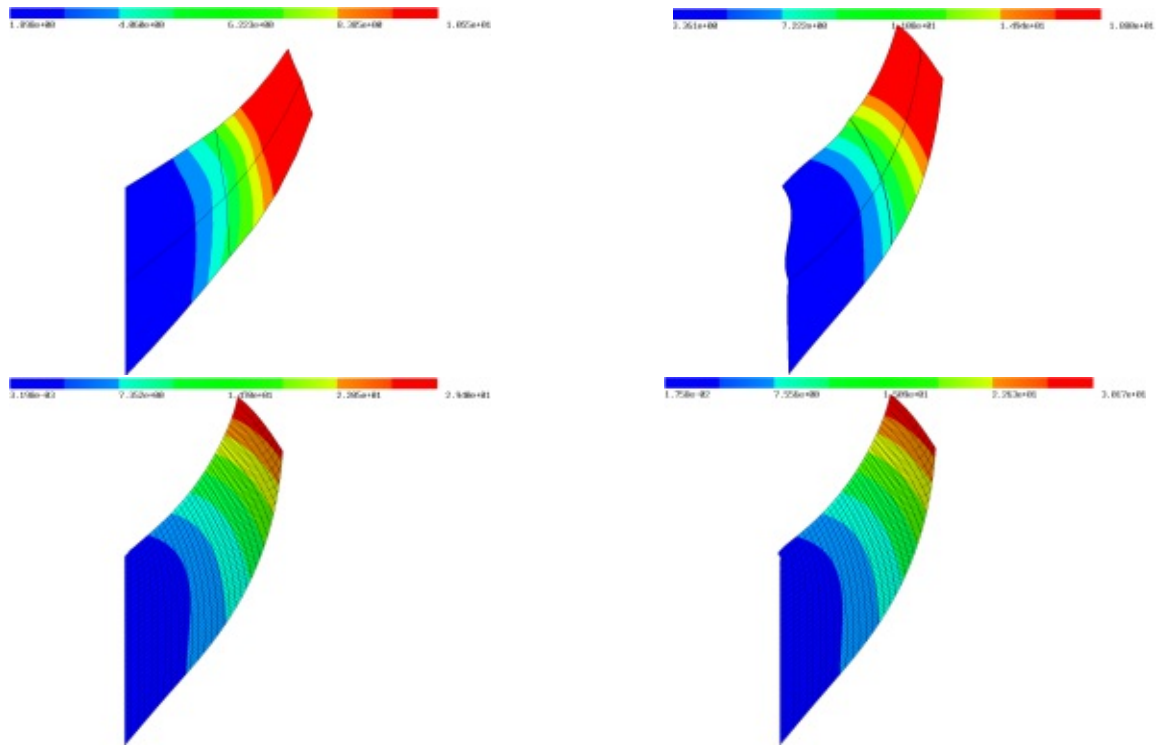
Figure 6.8.: Final deformation for Cook's membrane example with $f = 32$ standard method (left) and $\boldsymbol{F}$-based method (right) for 2×2 (top) and 32×32 (bottom) grid.

	coupl. dof	w	$\|U\|_{L^2}$	w	$\|U\|_{L^2}$	w	$\|U\|_{L^2}$
		$f = 16$		$f = 24$		$f = 32$	
std	32	9.902	153.983	13.305	212.422	16.348	265.766
	112	12.012	199.393	15.579	269.195	18.574	329.713
	416	13.281	232.024	17.052	315.428	20.053	385.690
	1600	13.794	246.522	17.700	337.958	20.778	415.150
	6272	13.977	252.014	17.948	346.933	21.093	427.745
$\boldsymbol{F}$	60	14.299	261.363	18.439	363.620	21.769	453.584
	216	14.218	259.260	18.317	359.827	21.639	448.622
	816	14.188	258.691	18.317	360.305	21.747	453.602
	3168	14.195	259.070	18.346	361.587	21.612	448.416
	12480	14.201	259.345	18.281	359.313	21.530	445.142
$\boldsymbol{C}$	60	13.872	249.196	17.980	346.236	21.237	429.732
	216	14.031	253.808	18.109	351.697	21.354	436.172
	816	14.094	255.716	18.159	354.099	21.405	439.173
	3168	14.123	256.705	18.189	355.628	21.455	441.717
	12480	14.142	257.391	-	-	-	-
$\boldsymbol{FC}$	60	14.295	261.013	18.424	362.626	21.734	451.528
	216	14.205	258.870	18.292	358.944	21.596	446.903
	816	14.179	258.389	18.584	370.337	21.769	455.071
	3168	14.300	262.429	18.345	361.562	21.573	446.896
	12480	14.204	259.429	18.265	358.718	21.531	445.182

Table 6.2.: Results for Cook's membrane example for $f = 16, 24, 32$ with 2×2, 4×4, 8×8, 16×16, and 32×32 grids. For all methods the number of coupling dofs, the vertical deflection at point A and the L^2 norm of the displacement are presented.
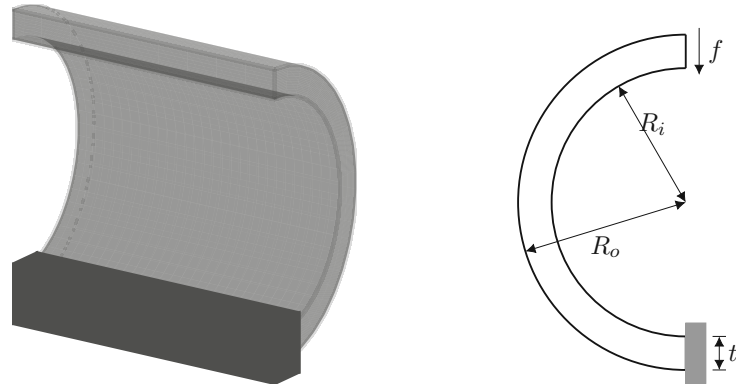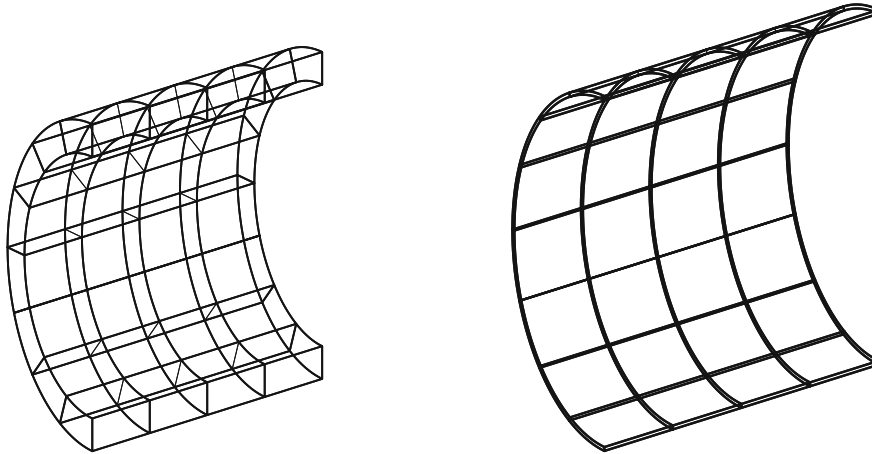
Figure 6.9.: 3D geometry of cylindrical shell example and 2D cross-section.

Figure 6.10.: Curved meshes with $8 \times 4 \times 1$ grid for cylindrical shell example for $t = 2$ and $t = 0.2$.

area and an area shear force $f = 240\,\mathrm{N\,mm^{-2}}$ ($f = 2.7\,\mathrm{N\,mm^{-2}}$ for $t = 0.2\,\mathrm{mm}$) is applied on the top. Structured hexahedra meshes with $8 \times 4 \times 1$, $16 \times 8 \times 1$, $32 \times 16 \times 1$ grids are used, see Figure 6.10. For the standard method also a $64 \times 32 \times 1$ grid is used such that the the overall number of dofs are comparable.

The vertical deflection at point A is depicted in Figure 6.12 and the final deformations are shown in Figure 6.11. The results can be found in Table 6.3. We observed a locking behavior, see Section 8, for the standard method, which becomes more significant for the small thickness. All of the three presented methods give already satisfying results for the coarsest mesh. The reference values were computed with the standard method and degree $k = 4$ on the finest grid, where locking is circumvented due to the high polynomial degree. We note, that the methods do not converge towards the reference solution for $t = 2$ as only one layer in the thin direction is used. For the thinner structure, $t = 0.2$, the values coincide. As already mentioned, the $\boldsymbol{F}$-based method may suffer from a larger number of Newton iterations to reach the requested precision, whereas the $\boldsymbol{C}$- and $\boldsymbol{FC}$-based method
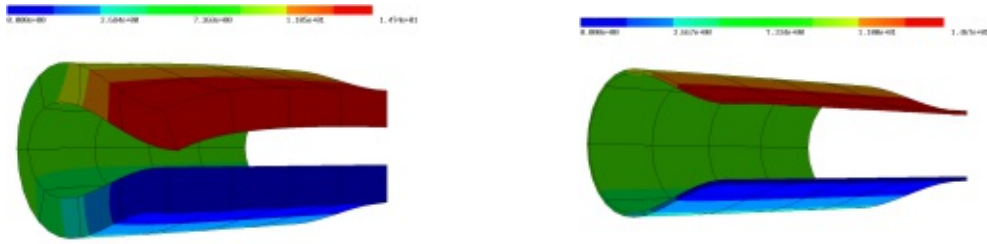
Figure 6.11.: Final configuration of cylindrical shell example for $t = 2$ and $t = 0.2$ with $16 \times 8 \times 1$ grid.
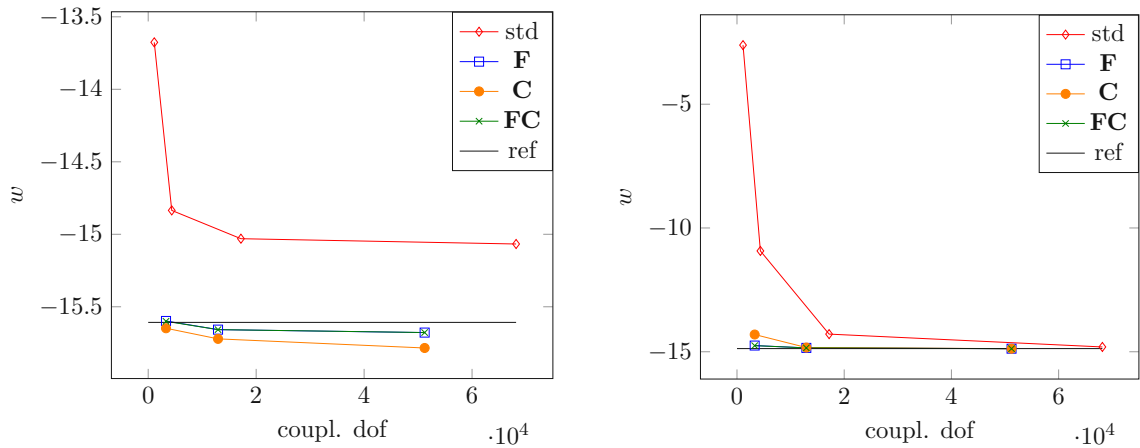
Figure 6.12.: Vertical deflection of cylindrical shell example at point A.

	coupl. dof	w	$\|U\|_{L^2}$	w	$\|U\|_{L^2}$
		$t = 2$		$t = 0.2$	
std	1125	-13.676	211.958	-2.613	14.350
	4365	-14.835	231.071	-10.927	58.065
	17181	-15.030	234.734	-14.287	76.437
	68157	-15.067	235.513	-14.806	79.387
F	3300	-15.598	244.530	-14.749	78.920
	12936	-15.658	245.756	-14.844	79.571
	51216	-15.678	246.149	-14.876	79.825
C	300	-15.648	245.779	-14.304	76.878
	12936	-15.721	246.883	-14.830	79.521
	51216	-15.784	247.951	-14.876	79.825
FC	3300	-15.600	244.586	-14.753	78.946
	12936	-15.658	245.757	-14.844	79.576
	51216	-15.678	246.143	-14.876	79.825

Table 6.3.: Results for cylindrical shell example. For all methods the number of coupling dofs, the vertical deflection at point A and the L^2 norm of the displacement are given.

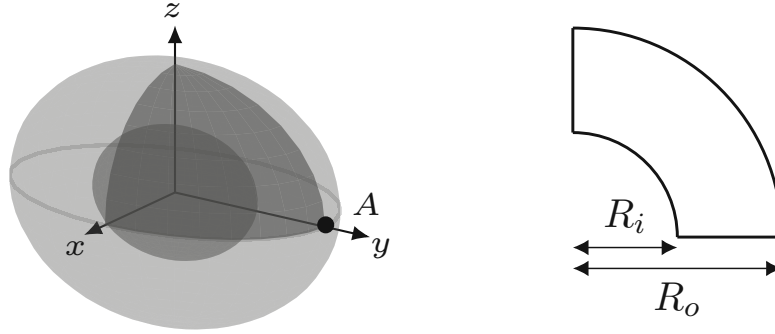| t	std	$\boldsymbol{F}$	$\boldsymbol{C}$	$\boldsymbol{FC}$
2	6	5	5	5
0.2	7	7-8	4-5	4-5

Table 6.4.: Number of Newton iterations for $32 \times 16 \times 1$ grid in cylindrical shell example.

Figure 6.13.: 3D geometry of inflation of a hollow spherical ball example and 2D cross-section.

have a better convergence behavior. In Table 6.4 the numbers of Newton iterations can be found, where twelve overall load steps were considered. Also the standard method needs more iterations than the $\boldsymbol{C}$- and $\boldsymbol{FC}$-based variant.

6.5.4. Inflation of a Hollow Spherical Ball

A hollow spherical ball is subjected to the boundary condition $u_{\text{in}} = (\gamma - 1)\vec{x}$ on the inner boundary, whereas the outer boundary is left free. The inner and outer radius are given by $R_{\text{i}} = 0.5\,\text{mm}$ and $R_{\text{o}} = 1\,\text{mm}$, respectively, cf. [204]. We consider Problem 6.23 together with $W(J) = \frac{1}{2}(1 - J)^2$ and $\hat{\mu} = 1\,\text{N}\,\text{mm}^{-2}$. The final configuration is reached for $\gamma = 3$, starting from $\gamma = 1$, the initial configuration. Due to symmetry, only one eight of the ball is considered, see Figure 6.13. Unstructured curved tetrahedral meshes are used as shown in Figure 6.14. The exact solution reads

$$\vec{u}_{\text{ex}}(\vec{x}) = \left(\frac{r(R)}{R} - 1\right)\vec{x}, \qquad p_{\text{ex}}(\vec{x}) = -\hat{\mu}\frac{R_o^4}{r^4(R_o)} + \frac{\hat{\mu}}{2}\left(g(R) - g(R_o)\right), \qquad (6.5.1)$$

where $R = \|\vec{x}\|_2$, $r(R) = \left(R^3 + (\hat{\lambda}^3 - 1)R_i^3\right)^{\frac{1}{3}}$ and $g(R) = R(3r^3(R) + (\hat{\lambda}^3 - 1)R_i^3/r^4(R)$.

The results can be found in Table 6.5 and Figure 6.15. Again, the deflection is in the right regime for the coarse grid for the lifting method.
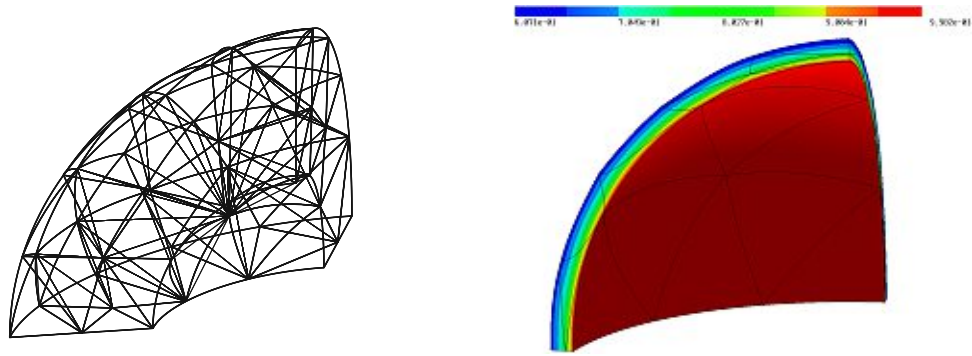
Figure 6.14.: Curved mesh (left) and final configuration with 85 elements for inflation of a hollow spherical ball example.

	coupl. dof	w	$\|U - U_{\mathrm{ex}}\|_{L^2}$	coupl. dofs	w	$\|U - U_{\mathrm{ex}}\|_{L^2}$
std	583	0.606	7.30×10^{-3}	1531	0.617	3.13×10^{-3}
	12094	0.620	1.64×10^{-4}			
$\boldsymbol{F}$	2196	0.620	2.59×10^{-3}	6099	0.620	1.35×10^{-3}
	55173	0.620	1.01×10^{-4}			

Table 6.5.: Results for inflation of a hollow spherical ball example. The number of coupling dofs, the radial deflection at point A, and the L^2-error of the displacement are presented.

Figure 6.15.: L^2 displacement error for inflation of a hollow spherical ball example.

7. Shells

7.1. Introduction

The appearance of shell structures, where one direction is significantly smaller than the others, are common in nature and technology. The scaling reaches from s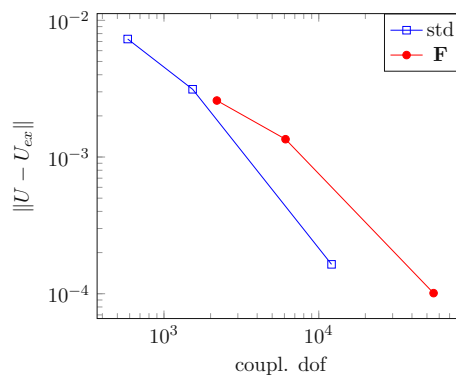mall like cell membranes to large as e.g., parts of cars and air planes. So-called thin-walled structures, see Figure 7.1, as plates and shells entail several numerical difficulties. One would need anisotropic (curved) elements to discretize the geometry or an enormous amount of isotropic elements. These approaches, however, lead to possible locking phenomena or a not justified large number of elements and thus, expensive computational costs.

Therefore, models were developed where only the mid-surface of the structure gets discretized and assumptions are made to "neglect" the thin direction, i.e., a dimension reduction. A derivation from continuum theory to obtain a shell model by simplifications and kinematic assumptions was given for plates by Kirchhoff [136] and Love [149]. Koiter [138] derived consistent equations for shells from continuum mechanics and Naghdi [160] proposed shell models of arbitrary order. Another idea coming from Cosserat [92] directly starts with a 2D model and postulating the balance equations. Therein the shell is described by its mid-surface and an additional independent director field on it. This geometrically exact shell models can be used in the linear [193] and nonlinear regime [206]. Giving a full overview of existing shell models and elements is a nearly impossible task and not topic of this thesis. We refer to the immense amount of literature, e.g., [238], where a general overview of shell elements is given.

The behavior of shell models should coincide with the full model, especially in the limit $t \to 0$, when the thickness tends to zero. Besides asymptotic analysis in the thickness parameter t the derivation of beam, plate, and shell models from 3D elasticity has also been done via Γ-convergence (see [140] and references therein). Models with extensions to varying thicknesses have also been proposed. Throughout this work, however, we assume a homogeneous thickness.

As the thickness t becomes small the shell falls in one of two different categories: the membrane dominated (inhibited pure bending) or bending dominated (non-inhibited pure bending) case [71]. This behavior enforced by the appearance of different powers of the thickness t in the equations may lead to so-called membrane and shear locking necessitating special numerical treatments and will be discussed in Chapter 8.

7.2. Differential geometry and shell description

A mathematical description of the mid-surface of a shell necessitates notation and results from differential geometry. We provide some basic results and definitions and refer to the

Figure 7.1.: Thin-walled shell structure with thickness t.

literature of differential geometry, e.g., [213], and especially shells [72, 49, 88, 206, 207, 71, 49, 235]. In this work, we will use a coordinate free description of quantities on the surface, comparable to the notation in [231], and only differ explicitly between vector fields in the tangential and in normal direction. Our notation is also comparable to *tangential differential calculus* (TDC) [93] applied to membrane problems [112] and especially to Kirchhoff and Reissner–Mindlin shells, see [200, 199] and references therein. As the notation of curvilinear coordinates is widely used, we also provide a very brief overview of this description form and state the essential results and formulas in this framework.

7.2.1. Initial configuration of shells

To describe a shell structure we start with the definition of a surface, or more generally of a (sub-)manifold.

Definition 7.1. Let $0 \le k < n$. A differentiable function $\varphi : \omega \to \mathbb{R}^n$ with $\omega \subset \mathbb{R}^k$ open is called an *embedding* if $\nabla \varphi \in \mathbb{R}^{n \times k}$ has full rank, i.e., $\nabla \varphi$ is injective. $\mathcal{S} \subset \mathbb{R}^n$ is a k-dimensional *submanifold* of $\mathbb{R}^n$ if for every $x \in \mathcal{S}$ there exists an embedding $\varphi : V \to U$ from $V \subset \mathbb{R}^k$ open to an open neighborhood $U \subset \mathbb{R}^n$ of x such that $\mathcal{S} \cap U = \varphi(V)$. For $n = 3$ and $k = 2$ we call $\mathcal{S}$ a *surface* and for $k = 1$ a *curve*. A surface $\mathcal{S}$ is called *orientable* if there exists a globally continuous normal vector field $\nu : \mathcal{S} \to \mathbb{S}^2$.

In the following we assume w.l.o.g. that the manifold $\mathcal{S}$ can be parameterized with a single embedding and note that the results can easily be extended by using an atlas, i.e., a set of embeddings covering the whole manifold. Further, we will consider orientable surfaces and weaken this assumption only in the case of surfaces with kinks and branched shells. Therefore, e.g., Möbius-strips are forbidden.

Looking at a plate structure as depicted in Figure 7.2 (a) one can describe every point X in it by its mid-surface ω and going along the normal vector, $X = x + z\nu$. Therefore, the question arises if we can describe every thin-walled structure in this form. The answer is positive, if the structure is smooth and "thin" enough.

7.1 Theorem. *Let $\omega \subset \mathbb{R}^2$ a domain and let $\varphi \in C^3(\overline{\omega}, \mathbb{R}^3)$ be an embedding. Then there exists $t > 0$ such that the mapping $\Theta : \overline{\Omega} \to \mathbb{R}^3$, $\Omega := \omega \times (-t/2, t/2)$ defined by*

$$\Theta(x, z) := \varphi(x) + z\nu(x) \qquad \forall (x, z) \in \overline{\Omega} \tag{7.2.1}$$
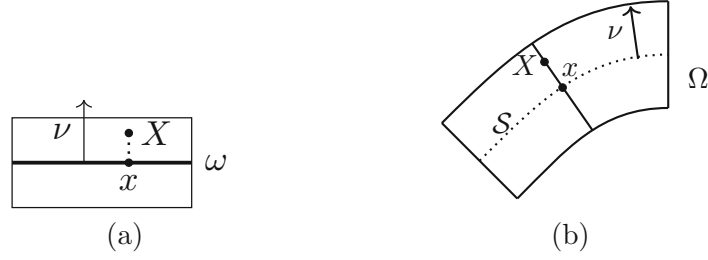
Figure 7.2.: Description of shell structures by its mid-surface $\mathcal{S}$ and normal vector ν. Every point X can be represented in the form $X = x + z\nu$. (a) Flat structure. (b) Curved structure.

> is a C^2-diffeomorphism from $\overline{\Omega}$ onto $\Theta(\overline{\Omega})$ and $\det(\tau_1, \tau_2, \nu) > 0$ in $\overline{\Omega}$, where $\tau_i = \frac{\partial \Theta}{\partial x_i}$ and $\nu = \frac{\tau_1 \times \tau_2}{\|\tau_1 \times \tau_2\|_2}$.

Proof. See e.g., [88, Theorem 4.1-1]. □

The requirement on the thickness t depends on the curvature of the shell, compare also Remark 7.5. Theorem 7.1 justifies to split a shell Ω into its mid-surface $\mathcal{S}$ and the corresponding normal vector ν

$$\Omega = \{X = x + z\,\nu(x)\,|\,x \in \mathcal{S},\, z \in [-t/2, t/2]\}, \tag{7.2.2}$$

as depicted in Figure 7.2 (b), compare also [97, Lemma 2.8].

Definition 7.2. We call a surface $\mathcal{S}$, fulfilling the requirements of Theorem 7.1, together with its normal vector field $\nu : \mathcal{S} \to \mathbb{S}^2$ the *initial configuration* of a shell and $(\mathcal{S}, \tilde{\nu})$ with a unit vector field $\tilde{\nu} : \mathcal{S} \to \mathbb{S}^2$, also called *director*, a *configuration of a shell.*

To compute derivatives of functions on the surface $\mathcal{S}$ we either need to pull them back to the flat case by the Moore–Penrose pseudo-inverse or extend the function to the full space, use the classical derivative, and project the result back to the surface.

Definition 7.3. Let $\mathcal{S} \subset \mathbb{R}^n$ be a smooth k-dimensional sub-manifold, $p \in \mathcal{S}$, $f : \mathcal{S} \to \mathbb{R}$ and $\varphi : \mathbb{R}^k \to \mathcal{S}$ a smooth embedding. Then we call the function f *differentiable*, $f \in C^1(\mathcal{S})$, at $p \in \mathcal{S}$, w.l.o.g. $\varphi(0) = p$, if

$$\nabla_\tau f(p) := \nabla((f \circ \varphi)(0))(\nabla \varphi(0))^\dagger \tag{7.2.3}$$

is differentiable in classical sense and call $\nabla_\tau f$ the *tangential* or *surface gradient* of f. Here, $(\nabla \varphi)^\dagger \in \mathbb{R}^{k \times n}$ denotes the *Moore–Penrose pseudo-inverse* of $\nabla \varphi \in \mathbb{R}^{n \times k}$.

The definition is independent of the particular embedding φ and can be extended easily to vector valued functions $f : \mathcal{S} \to \mathbb{R}^n$. A manifold is equipped at each point $p \in \mathcal{S}$ with a tangent space:
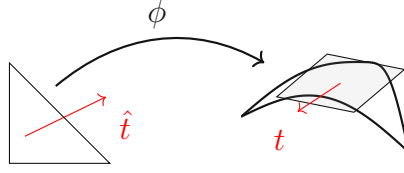
Figure 7.3.: Push forward by $\nabla\phi$ of a tangent vector $\hat{t}$ onto tangent space of a surface.

Definition 7.4. Let $\mathcal{S}$ be a surface with normal vector field ν. Then, for every point $p \in \mathcal{S}$ the *tangent space* $T_p\mathcal{S}$ is defined by the set of all vectors which are perpendicular to $\nu(p)$

$$T_p\mathcal{S} = \{\nu(p)\}^{\perp} := \{v \in \mathbb{R}^3 \,|\, v \perp \nu(p)\} \tag{7.2.4}$$

and the tangential bundle of $\mathcal{S}$ is given by $T\mathcal{S} := \cup_{p \in \mathcal{S}}\{p\} \times T_p\mathcal{S}$. Further, the projection operator onto $T\mathcal{S}$ is defined by

$$\boldsymbol{P}_\tau := \boldsymbol{I} - \nu \otimes \nu : \mathbb{R}^3 \to T\mathcal{S}. \tag{7.2.5}$$

The definition of the tangent space can be extended directly to $n-1$-dimensional submanifolds. Note, that with a given embedding $\varphi : \mathbb{R}^{n-1} \to \mathcal{S}$ there holds

$$T_p\mathcal{S} = \nabla\varphi(p)\mathbb{R}^{n-1} := \{\nabla\varphi(p)\eta \,|\, \eta \in \mathbb{R}^{n-1}\}. \tag{7.2.6}$$

Thus, $\nabla\varphi$ can be seen as a *push forward* mapping tangent vectors in the plane to tangent vectors onto the manifold, see Figure 7.3.

With Theorem 7.1 and (7.2.5) for given $f : \mathcal{S} \to \mathbb{R}$ an extension $F : \mathbb{R}^3 \to \mathbb{R}$ can be defined such that $\boldsymbol{P}_\tau F = f$. With this at hand we define the tangential derivative as

$$\nabla_\tau f = \boldsymbol{P}_\tau \nabla F, \tag{7.2.7}$$

which is independent of the choice of the extension F, see [97]. Note that (7.2.7) is an equivalent definition to (7.2.3). For vector valued functions $f : \mathcal{S} \to \mathbb{R}^3$ the surface gradient via extension is given by $\nabla_\tau f = \nabla F \boldsymbol{P}_\tau$. From a finite element point of view Definition 7.3 fits perfectly in the design of a reference element $\hat{T} \subset \mathbb{R}^2$, where the derivative is computed and then mapped via the pseudo-inverse (see Section 7.5), whereas (7.2.7) might be better suited for e.g., theoretical results.

Definition 7.5. The *surface divergence* of a vector valued function $u \in [C^1(\mathcal{S})]^d$ is defined by $\mathrm{div}_\tau(u) := \mathrm{tr}(\nabla_\tau u)$. For $d = 3$ the *surface curl* of a vector valued function u is given by $\mathrm{curl}_\tau(u) := (\nabla_\tau \times U) \cdot \nu = \mathrm{div}_\tau(u \times \nu)$ and for a scalar $\phi \in C^1(\mathcal{S})$ $\mathrm{Curl}_\tau(\phi) := \nu \times \nabla_\tau\phi$, where ν is the outer normal vector and U an extension of u into the neighborhood of $\mathcal{S}$.

With the projection operator $\boldsymbol{P}_\tau$ onto the tangent space at hand we can define the covariant surface derivative:

Definition 7.6. Let $\mathcal{S} \subset \mathbb{R}^n$ be a smooth $n-1$-dimensional sub-manifold, $\boldsymbol{P}_\tau$ the projection onto the tangent space, and $f : \mathcal{S} \to \mathbb{R}^n$ a differentiable vector field. The *covariant surface gradient* of f is defined by

$$\nabla_\tau^{\mathrm{cov}} f := \boldsymbol{P}_\tau \nabla_\tau f \tag{7.2.8}$$

or via extension $F : \mathbb{R}^n \to \mathbb{R}^n$ as $\nabla_\tau^{\mathrm{cov}} f := \boldsymbol{P}_\tau \nabla_\tau F \boldsymbol{P}_\tau$.

Note, that for a vector field f on $\mathcal{S}$ there holds $\nu^\top \nabla_\tau^{\mathrm{cov}} f = 0$ and $\nabla_\tau^{\mathrm{cov}} f \, \nu = 0$, but in general $\nu^\top \nabla_\tau f \neq 0$ (only $\nabla_\tau f \, \nu = 0$).

To measure distances, angles, and curvatures on manifolds the following fundamental forms are introduced.

Definition 7.7. Let $\mathcal{S}$ be a shell, $v, w \in T\mathcal{S}$, and $\tilde{\nu} : \mathcal{S} \to \mathbb{S}^2$ a director field. Then the (generalized) first, second, and third fundamental forms are given by

$$I(v,w) := \langle v, w \rangle, \tag{7.2.9a}$$

$$II_{\tilde{\nu}}(v,w) := \frac{1}{2}\left(\langle \nabla_\tau \tilde{\nu}\, v, w\rangle + \langle v, \nabla_\tau \tilde{\nu}\, w\rangle\right), \tag{7.2.9b}$$

$$III_{\tilde{\nu}}(v,w) := \langle \nabla_\tau \tilde{\nu}\, v, \nabla_\tau \tilde{\nu}\, w\rangle, \tag{7.2.9c}$$

where $\langle \cdot, \cdot \rangle$ denotes the Euclidean scalar product in $\mathbb{R}^3$. Further, the shear form $\sigma_{\tilde{\nu}} : T\mathcal{S} \to \mathbb{R}$ is defined for all $p \in \mathcal{S}$ by

$$(\sigma_{\tilde{\nu}})_p : T_p\mathcal{S} \to \mathbb{R}, \quad v \mapsto \langle \tilde{\nu}(p), v\rangle. \tag{7.2.10}$$

Note, that for the normal vector ν on $\mathcal{S}$ there holds $II_\nu(\cdot, \cdot) = \langle \nabla_\tau \nu\, \cdot, \cdot \rangle$ and $\sigma_\nu \equiv 0$. $\nabla_\tau \nu$ is the Weingarten tensor, also called the shape operator $\mathfrak{S} : T\mathcal{S} \to T\mathcal{S}$. It is further referred to as curvature tensor as the second derivatives of the underlying embedding of the shell contain the curvature information.

7.2.2. Curvilinear coordinates for shells

We compactly introduce the ingredients to describe a shell in curvilinear coordinates and refer to Appendix A and the literature, e.g., [72] and references therein, for a comprehensive introduction. Throughout the thesis we will use the notation $\vec{u}$ for a vector u if curvilinear coordinates are considered.

Let φ be an embedding of a surface. Then the two vectors

$$\vec{a}_\alpha := \frac{\partial \varphi(\xi^1, \xi^2)}{\partial \xi^\alpha} \tag{7.2.11}$$

are linearly independent and form a basis of the tangent space of the surface, compare Definition 7.4. Together with the normal vector $\vec{a}_3 := \frac{\vec{a}_1 \times \vec{a}_2}{\|\vec{a}_1 \times \vec{a}_2\|_2}$ the 3D chart (7.2.1) reads

$$\Theta(\xi^1, \xi^2, \xi^3) = \varphi(\xi^1, \xi^2) + \xi^3 \vec{a}_3(\xi^1, \xi^2). \tag{7.2.12}$$

The set $\{\vec{a}_1, \vec{a}_2\}$ is called the *covariant basis* of the surface and the *contravariant basis* $\{\vec{a}^1, \vec{a}^2\}$ is given by the relation $\vec{a}_\alpha \cdot \vec{a}^\beta = \delta_\beta^\alpha$, $\alpha, \beta = 1, 2$.

The components of the first, second, and third fundamental forms $\boldsymbol{a}$, $\boldsymbol{b}$, $\boldsymbol{c}$, cf. (7.2.9) with $\tilde{\nu} = \nu$, are given by

$$a_{\alpha\beta} = \vec{a}_\alpha \cdot \vec{a}_\beta, \qquad b_{\alpha\beta} = \vec{a}_3 \cdot \vec{a}_{\alpha,\beta} = -\vec{a}_{3,\beta} \cdot \vec{a}_\alpha, \qquad c_{\alpha\beta} = b_\alpha^\lambda b_{\lambda\beta},$$

where $b_\beta^\alpha = a^{\alpha\lambda}b_{\lambda\beta} = \vec{a}_{,\beta}^\alpha \cdot \vec{a}_3$. Note that from the relation $\|\vec{a}_3\|_2 = 1$ we can deduce that $\vec{a}_{3,\alpha} = -b_\alpha^\lambda \vec{a}_\lambda$.

With the *surface Christoffel symbols* $\Gamma_{\beta\alpha}^\lambda := \vec{a}_{\beta,\alpha} \cdot \vec{a}^\lambda = -\vec{a}_\beta \cdot \vec{a}_{,\alpha}^\lambda$ the surface derivative, compare Definition 7.3, of a vector field $\vec{u}$ in curvilinear coordinates is given by

$$\vec{u}_{,\alpha} := \left(u_{\beta,\alpha} - \Gamma_{\beta\alpha}^\lambda u_\lambda\right)\vec{a}^\beta + b_\alpha^\lambda u_\lambda \vec{a}_3.$$

The components of the surface covariant derivative of $\vec{u}$, cf. Definition 7.6, are defined by

$$u_{\beta|\alpha} := u_{\beta,\alpha} - \Gamma_{\beta\alpha}^\lambda u_\lambda.$$

The 3D covariant base vectors induced by the 3D chart (7.2.12) are

$$\vec{g}_\alpha = \frac{\partial \Theta}{\partial \xi^\alpha} = \vec{a}_\alpha + \xi^3 \vec{a}_{3,\alpha} = \left(\delta_\alpha^\lambda - \xi^3 b_\alpha^\lambda\right)\vec{a}_\lambda, \qquad \vec{g}_3 = \frac{\partial \Theta}{\partial \xi^3} = \vec{a}_3$$

and the components of the corresponding 3D metric tensor $\boldsymbol{g}$ are given by

$$g_{\alpha\beta} = a_{\alpha\beta} - 2\xi^3 b_{\alpha\beta} + (\xi^3)^2 c_{\alpha\beta}, \qquad g_{\alpha 3} = 0, \qquad g_{33} = 1. \tag{7.2.13}$$

The connections between the 3D and surface quantities are given by evaluating the three-dimensional objects at the mid-surface: $a_{\alpha\beta} = (g_{\alpha\beta})|_{\xi^3=0}$, $\Gamma_{\alpha\beta}^\lambda = (\bar{\Gamma}_{\alpha\beta}^\lambda)|_{\xi^3=0}$, and $b_{\alpha\beta} = (\bar{\Gamma}_{\alpha\beta}^3)|_{\xi^3=0}$ ($\bar{\Gamma}$ defined as in (A.0.1)).

7.2.3. Deformed configuration

Definition 7.8. Let $(\overline{\mathcal{S}}, \overline{\nu})$ be the initial configuration of a shell. A deformation $\Phi = (\phi, \hat{\nu})$ of $\overline{\mathcal{S}}$ is given by

$$\begin{aligned} \Phi : \overline{\mathcal{S}} \times [-t/2, t/2] &\to \mathbb{R}^3, \\ (x, z) &\mapsto \phi(x) + z\hat{\nu}(x), \end{aligned} \tag{7.2.14}$$

where ϕ is the deformation of the mid-surface and $\hat{\nu} : \overline{\mathcal{S}} \to \mathbb{S}^2$ a differentiable unit vector field. We call $\mathcal{S} := \phi(\overline{\mathcal{S}})$ together with $\tilde{\nu} := \hat{\nu} \circ \phi^{-1}$ a *deformed configuration* of the shell.

In the following we will also use the additive splitting of the deformation ϕ into the identity function and the displacement u, $\phi = \mathrm{id} + u$.

As the shell gets deformed we need to transform the normal and tangential vectors from the initial to the current deformation. Therefore, we collect some useful properties. The cofactor matrix can be defined via the relation

$$\mathrm{cof}(\boldsymbol{A}) := \det(\boldsymbol{A})\boldsymbol{A}^{-\top} \qquad \text{for all } \boldsymbol{A} \in \mathrm{GL}(3) \tag{7.2.15}$$

or equivalently as the matrix whose (i,j)-th entry corresponds to the determinant of the 2×2 sub-matrix resulting from deleting the i-th row and j-th column of $\boldsymbol{A}$. Thus, the cofactor matrix is also well-defined for non invertible matrices. From identity (7.2.15) there directly follows (by a density argument) that $\mathrm{cof}(\boldsymbol{A}\boldsymbol{B}) = \mathrm{cof}(\boldsymbol{A})\mathrm{cof}(\boldsymbol{B})$, $\mathrm{cof}(\boldsymbol{A}^\top) = \mathrm{cof}(\boldsymbol{A})^\top$, $\mathrm{cof}(\boldsymbol{A}^{-1}) = \mathrm{cof}(\boldsymbol{A})^{-1}$ (if $\boldsymbol{A} \in \mathrm{GL}(3)$).

7.2 Lemma. *Let $\boldsymbol{A} \in \mathbb{R}^{3\times3}$ with $\mathrm{rank}(\boldsymbol{A}) = 2$ and $v \in \mathbb{R}^3$ with $v \in \ker(\boldsymbol{A})$. Then there holds, with $\boldsymbol{P}_\tau^\perp = \nu \otimes \nu$ the complementary orthogonal projection of $\boldsymbol{P}_\tau = \boldsymbol{I} - \nu \otimes \nu$, where $\nu := \frac{v}{\|v\|_2}$,*

1. $\boldsymbol{A}^\top \mathrm{cof}(\boldsymbol{A}) = 0.$

2. $\mathrm{cof}(\boldsymbol{P}_\tau) = \boldsymbol{P}_\tau^\perp.$

3. $\|\mathrm{cof}(\boldsymbol{A})v\|_2 = \|v\|_2 \|\mathrm{cof}(\boldsymbol{A})\|_F.$

Proof.

1. As the set of regular matrices $\mathrm{GL}(3)$ is dense in the set of all matrices there exists for all $\boldsymbol{A} \in \mathbb{R}^{3\times3}$ and $\varepsilon > 0$ some $\boldsymbol{A}_\varepsilon \in \mathrm{GL}(3)$ such that $\|\boldsymbol{A}_\varepsilon - \boldsymbol{A}\|_F < \varepsilon$. Therefore, with (7.2.15) and continuity of the determinant, there holds

$$\boldsymbol{A}^\top \mathrm{cof}(\boldsymbol{A}) = \lim_{\varepsilon \to 0} \boldsymbol{A}_\varepsilon^\top \mathrm{cof}(\boldsymbol{A}_\varepsilon) = \lim_{\varepsilon \to 0} \det(\boldsymbol{A}_\varepsilon) = 0.$$

2. We choose $\tau_1, \tau_2 \in \mathbb{R}^3$ such that $\boldsymbol{B} := \begin{pmatrix} \tau_1 & \tau_2 & \nu \end{pmatrix} \in \mathrm{SO}(3)$. The claim follows directly as $\mathrm{cof}(\boldsymbol{A}) = \boldsymbol{A}$ for $\boldsymbol{A} \in \mathrm{SO}(3)$ and

$$\mathrm{cof}(\boldsymbol{P}_\tau) = \mathrm{cof}(\boldsymbol{B})\mathrm{cof}(\begin{pmatrix} 1 & 0 & 0 \\ 0 & 1 & 0 \\ 0 & 0 & 0 \end{pmatrix})\mathrm{cof}(\boldsymbol{B}^{-1}) = \boldsymbol{B}\begin{pmatrix} 0 & 0 & 0 \\ 0 & 0 & 0 \\ 0 & 0 & 1 \end{pmatrix}\boldsymbol{B}^{-1} = \boldsymbol{P}_\tau^\perp.$$

3. With $\mathrm{cof}(\boldsymbol{A})\tau_i = \mathrm{cof}(\boldsymbol{A}\boldsymbol{P}_\tau)\tau_i = \mathrm{cof}(\boldsymbol{A})\boldsymbol{P}_\tau^\perp \tau_i = 0$ for $i = 1, 2$ and τ_i as in 2), we get

$$\|\mathrm{cof}(\boldsymbol{A})\nu\|_2^2 = \nu^\top \mathrm{cof}(\boldsymbol{A}^\top \boldsymbol{A})\nu = \nu^\top \mathrm{cof}(\boldsymbol{A}^\top \boldsymbol{A})\nu + \sum_{i=1}^{2} \tau_i^\top \mathrm{cof}(\boldsymbol{A}^\top \boldsymbol{A})\tau_i$$

$$= \mathrm{tr}(\mathrm{cof}(\boldsymbol{A}^\top \boldsymbol{A})) = \|\mathrm{cof}(\boldsymbol{A})\|_F^2.$$

$\square$

7.3 Lemma. *Let $\overline{\mathcal{S}}$ be a shell with normal vector field $\overline{\nu}$ and $\phi : \overline{\mathcal{S}} \to \mathbb{R}^3$ a diffeomorphism. For the resulting deformed shell $\mathcal{S} := \phi(\overline{\mathcal{S}})$ let ν be the corresponding normal vector and $\tau \in T_p\mathcal{S}$ a normalized tangent vector at $p \in \mathcal{S}$. Then, with $\boldsymbol{F}_{\overline{\tau}} := \nabla_{\overline{\tau}}\phi$ and $\mu := \nu \times \tau$, there exists $\overline{\tau} \in T_{\phi^{-1}(p)}\overline{\mathcal{S}}$ such that*

$$\tau \circ \phi = \frac{\boldsymbol{F}_{\overline{\tau}}\overline{\tau}}{\|\boldsymbol{F}_{\overline{\tau}}\overline{\tau}\|_2}, \qquad \nu \circ \phi = \frac{\mathrm{cof}(\boldsymbol{F}_{\overline{\tau}})\overline{\nu}}{\|\mathrm{cof}(\boldsymbol{F}_{\overline{\tau}})\overline{\nu}\|_2} = \frac{\mathrm{cof}(\boldsymbol{F}_{\overline{\tau}})\overline{\nu}}{\|\mathrm{cof}(\boldsymbol{F}_{\overline{\tau}})\|_F}, \quad \mu \circ \phi = \frac{\boldsymbol{F}_{\overline{\tau}}^{\dagger\top}\overline{\mu}}{\|\boldsymbol{F}_{\overline{\tau}}^{\dagger\top}\overline{\mu}\|_2},$$

$$(7.2.16)$$

where $\overline{\mu} = \overline{\nu} \times \overline{\tau}$.

Proof. The former claim is the definition of mapping of tangent vectors via push forward and thus obvious. For the second claim let $p \in \mathcal{S}$ and $\eta \in T_p\mathcal{S}$ be arbitrary. Then

$$\eta \circ \phi \cdot \nu \circ \phi = \frac{1}{\|\boldsymbol{F}_{\overline{\tau}}\overline{\eta}\|_2 \|\text{cof}(\boldsymbol{F}_{\overline{\tau}})\overline{\nu}\|_2} \overline{\eta}^\top \boldsymbol{F}_{\overline{\tau}}^\top \text{cof}(\boldsymbol{F}_{\overline{\tau}})\overline{\nu} \stackrel{\text{Lemma } 7.2}{=} 0.$$

For the latter we compute

$$\mu \circ \phi \cdot \nu \circ \phi = \frac{1}{\|\boldsymbol{F}_{\overline{\tau}}^{\dagger\top}\overline{\mu}\|_2 \|\text{cof}(\boldsymbol{F}_{\overline{\tau}})\overline{\nu}\|_2} \overline{\mu}^\top \boldsymbol{F}_{\overline{\tau}}^\dagger \text{cof}(\boldsymbol{F}_{\overline{\tau}})\overline{\nu} = 0,$$

$$\mu \circ \phi \cdot \tau \circ \phi = \frac{1}{\|\boldsymbol{F}_{\overline{\tau}}^{\dagger\top}\overline{\mu}\|_2 \|\boldsymbol{F}_{\overline{\tau}}\overline{\tau}\|_2} \overline{\mu}^\top \boldsymbol{F}_{\overline{\tau}}^\dagger \boldsymbol{F}_{\overline{\tau}}\overline{\tau} = \frac{1}{\|\boldsymbol{F}_{\overline{\tau}}^{\dagger\top}\overline{\mu}\|_2 \|\boldsymbol{F}_{\overline{\tau}}\overline{\tau}\|_2} \overline{\mu}^\top \overline{\tau} = 0,$$

where we used that $\boldsymbol{F}_{\overline{\tau}}^\dagger \text{cof}(\boldsymbol{F}_{\overline{\tau}}) = \boldsymbol{F}_{\overline{\tau}}^\dagger \boldsymbol{P}_{\overline{\tau}}\text{cof}(\boldsymbol{F}_{\overline{\tau}}) \stackrel{\text{Lemma } 7.2}{=} 0$ and $\boldsymbol{F}_{\overline{\tau}}^\dagger \boldsymbol{F}_{\overline{\tau}} = \boldsymbol{P}_{\overline{\tau}}$. As the three vector fields are perpendicular and normalized there holds $\det(\nu \circ \phi, \tau \circ \phi, \mu \circ \phi) = \pm 1$. To show that the orientation is preserved we extend the vectors to full space, compare (7.2.7), by using a full rank matrix $\boldsymbol{F} \in \mathbb{M}_+(3)$ and $\boldsymbol{A} := (\boldsymbol{I} - \frac{\boldsymbol{F}^{-\top}\overline{\nu}}{\|\boldsymbol{F}^{-\top}\overline{\nu}\|_2} \otimes \frac{\boldsymbol{F}^{-\top}\overline{\nu}}{\|\boldsymbol{F}^{-\top}\overline{\nu}\|_2})\boldsymbol{F}^{-\top}$

$$\frac{\boldsymbol{F}^{-\top}\overline{\nu}}{\|\boldsymbol{F}^{-\top}\overline{\nu}\|_2}, \qquad \frac{\boldsymbol{F}\overline{\tau}}{\|\boldsymbol{F}\overline{\tau}\|_2}, \qquad \frac{\boldsymbol{A}\overline{\mu}}{\|\boldsymbol{A}\overline{\mu}\|_2}.$$

By neglecting the denominators we obtain

$$\det(\boldsymbol{F}^{-\top}\overline{\nu}, \boldsymbol{F}\overline{\tau}, \boldsymbol{A}\overline{\mu}) = \det(\boldsymbol{F}^{-\top}\overline{\nu}, \boldsymbol{F}\overline{\tau}, \boldsymbol{F}^{-\top}\overline{\mu})$$
$$= \det(\boldsymbol{F}^{-\top})\det(\overline{\nu}, \boldsymbol{F}^\top \boldsymbol{F}\overline{\tau}, \overline{\mu})$$
$$= \det(\boldsymbol{F}^{-\top})\overline{\mu} \times \overline{\nu} \cdot (\boldsymbol{F}^\top \boldsymbol{F}\overline{\tau}) = \det(\boldsymbol{F}^{-\top})\|\boldsymbol{F}\overline{\tau}\|_2^2 > 0.$$

$\square$

7.4 Lemma. *Let $\overline{\mathcal{S}}$ be a shell with normal vector field $\overline{\nu}$ and $\phi : \overline{\mathcal{S}} \to \mathbb{R}^3$ a diffeomorphism of the form $\phi = \text{id} + u$. For the resulting deformed shell $\mathcal{S} := \phi(\overline{\mathcal{S}})$ let ν, τ, and μ defined as in Lemma 7.3. Assume that $\nabla_{\overline{\tau}}u = \mathcal{O}(\varepsilon)$. Then the linearization of these vectors is given by*

$$\nu \circ \phi = \overline{\nu} - \nabla_{\overline{\tau}}u^\top \overline{\nu} + \mathcal{O}(\varepsilon^2), \tag{7.2.17a}$$

$$\tau \circ \phi = \overline{\tau} + (\boldsymbol{I} - \overline{\tau} \otimes \overline{\tau})\nabla_{\overline{\tau}}u\,\overline{\tau} + \mathcal{O}(\varepsilon^2), \tag{7.2.17b}$$

$$\mu \circ \phi = \overline{\mu} + ((\boldsymbol{I} - \overline{\tau} \otimes \overline{\tau})\nabla_{\overline{\tau}}u - \nabla_{\overline{\tau}}u^\top)\overline{\mu} + \mathcal{O}(\varepsilon^2). \tag{7.2.17c}$$

Proof. The claim can be proved by using the first variations of ν, τ, and μ given in Appendix B, e.g., (B.0.1). However, it is faster to extend the deformation gradient $\boldsymbol{F}_{\overline{\tau}}$ to a full rank matrix $\boldsymbol{F}$ and compute

$$\partial_u(\nu \circ \phi)(\delta u)|_{u=0} = \partial_u\left(\frac{\boldsymbol{F}^{-\top}\overline{\nu}}{\|\boldsymbol{F}^{-\top}\overline{\nu}\|}\right)(\delta u)|_{u=0}$$
$$= \left(-\frac{\boldsymbol{F}^{-\top}\nabla\delta u^\top \boldsymbol{F}^{-\top}\overline{\nu}}{\|\boldsymbol{F}^{-\top}\overline{\nu}\|} + \boldsymbol{F}^{-\top}\overline{\nu}\frac{1}{\|\boldsymbol{F}^{-\top}\overline{\nu}\|^3}\langle \boldsymbol{F}^{-\top}\overline{\nu}, \boldsymbol{F}^{-\top}\nabla\delta u^\top \boldsymbol{F}^{-\top}\rangle\right)|_{u=0}$$
$$= -\nabla\delta u^\top \overline{\nu} + (\nabla\delta u)_{\overline{\nu}\overline{\nu}}\overline{\nu} = -(\boldsymbol{I} - \overline{\nu} \otimes \overline{\nu})\nabla\delta u^\top \overline{\nu} = -\nabla_{\overline{\tau}}\delta u^\top \overline{\nu},$$

where we used that $\partial_{x_i} \boldsymbol{F}^{-1} = -\boldsymbol{F}^{-1}\partial_{x_i}\boldsymbol{F}\boldsymbol{F}^{-1}$. The proof of the others follow the same lines. □

To evaluate the fundamental and shear forms given in Definition 7.7 for a deformed shell $\mathcal{S} = \Phi(\overline{\mathcal{S}})$ so-called pull backs are used. Therefore, let $\overline{v}, \overline{w} \in T\overline{\mathcal{S}}$, $\overline{\nu}$ the normal vector on $\overline{\mathcal{S}}$ and $\tilde{\nu} : \mathcal{S} \to \mathbb{S}^2$. Then, with the notation ∇_τ for the derivative on $\mathcal{S}$ and $\nabla_{\overline{\tau}}$ for the derivative on $\overline{\mathcal{S}}$ we have

$$\Phi^* I(\overline{v}, \overline{w}) := \langle \nabla_{\overline{\tau}}\Phi\,\overline{v}, \nabla_{\overline{\tau}}\Phi\,\overline{w}\rangle, \tag{7.2.18a}$$

$$\Phi^* II_{\tilde{\nu}}(\overline{v}, \overline{w}) := \frac{1}{2}\left(\langle \nabla_\tau\tilde{\nu}\circ\Phi\,\nabla_{\overline{\tau}}\Phi\,\overline{v}, \nabla_\tau\Phi\,\overline{w}\rangle + \langle\nabla_{\overline{\tau}}\Phi\,\overline{v}, \nabla_\tau\tilde{\nu}\circ\Phi\,\nabla_{\overline{\tau}}\Phi\,\overline{w}\rangle\right), \tag{7.2.18b}$$

$$\Phi^* III_{\tilde{\nu}}(\overline{v}, \overline{w}) := \langle \nabla_\tau\tilde{\nu}\circ\Phi\,\nabla_{\overline{\tau}}\Phi\,\overline{v}, \nabla_\tau\tilde{\nu}\circ\Phi\,\nabla_{\overline{\tau}}\Phi\,\overline{w}\rangle, \tag{7.2.18c}$$

$$\Phi^* \sigma_{\tilde{\nu}}(\cdot) := \sigma_{\tilde{\nu}}(\nabla_{\overline{\tau}}\Phi\,\cdot). \tag{7.2.18d}$$

Matrix representations of the (pull-backed) forms are given, $\boldsymbol{F}_{\overline{\tau}} := \nabla_{\overline{\tau}}\Phi$, by

$$\overline{I} \mathrel{\hat{=}} \boldsymbol{P}_{\overline{\tau}}^\top\boldsymbol{P}_{\overline{\tau}} = \boldsymbol{P}_{\overline{\tau}}, \qquad \overline{II}_{\overline{\nu}} \mathrel{\hat{=}} \nabla_{\overline{\tau}}\overline{\nu}, \qquad \overline{III}_{\overline{\nu}} \mathrel{\hat{=}} \nabla_{\overline{\tau}}\overline{\nu}\nabla_{\overline{\tau}}\overline{\nu}, \qquad \sigma_{\overline{\nu}} \equiv 0,$$

$$\Phi^* I \mathrel{\hat{=}} \boldsymbol{F}_{\overline{\tau}}^\top\boldsymbol{F}_{\overline{\tau}}, \qquad\qquad\qquad \Phi^* II_{\tilde{\nu}} \mathrel{\hat{=}} \mathrm{sym}(\boldsymbol{F}_{\overline{\tau}}^\top\nabla_\tau\tilde{\nu}\circ\Phi\,\boldsymbol{F}_{\overline{\tau}}), \tag{7.2.19}$$

$$\Phi^* III_{\tilde{\nu}} \mathrel{\hat{=}} \boldsymbol{F}_{\overline{\tau}}^\top\nabla_\tau\tilde{\nu}\circ\Phi^\top\nabla_\tau\tilde{\nu}\circ\Phi\,\boldsymbol{F}_{\overline{\tau}}, \qquad \Phi^* \sigma_{\tilde{\nu}} \mathrel{\hat{=}} \boldsymbol{F}_{\overline{\tau}}^\top\tilde{\nu}\circ\Phi.$$

In the following we will write e.g., I instead of $\Phi^* I$ for a more compact notation.

7.3. Shell models

As mentioned at the beginning of this section, deriving a 2D shell formulation from 3D elasticity is a highly non-trivial topic of research. We will briefly introduce a Galerkin semi-discretization and then follow [231, 232] to derive a geometrically exact shell model comparable with [206] in the shear deformable case and [88] when using the Kirchhoff–Love hypothesis (see Section 7.3.4).

7.3.1. Galerkin semi-discretization

A (high-order) semi-discretization of shells is based on the approximation along the thickness direction by a power series of the displacement [160]

$$u(x, z) = u_0(x) + \sum_{i=1}^{\infty} z^i w_i(x), \qquad x \in \mathcal{S},\, z \in [-t/2, t/2]. \tag{7.3.1}$$

Using a finite sum gives the approximation

$$u(x, z) \approx u_0(x) + \sum_{i=1}^{N} z^i w_i(x). \tag{7.3.2}$$

These methods are called (for $N > 1$) hierarchical models (or p-methods).

The multilayer approach (h-method) divides the shell in thickness direction into layers and uses e.g., piece-wise linear polynomials in every layer

$$u(x, z) \approx \sum_{i=1}^{N} \tilde{\phi}_i(z) w_i(x), \tag{7.3.3}$$

where $\tilde{\phi}_i$ is a hat-function being 1 at one specific layer and 0 at the others.

In this work we consider only (7.3.2) with $N = 1$, where the Reissner–Mindlin and Kirchhoff–Love models described later are included.

7.3.2. A geometrically nonlinear derivation

Let $\overline{\mathcal{S}}$ be the initial configuration of a shell and $\overline{\nu}$ the corresponding normal vector field. We use (7.3.2) with $N = 1$ and assume that the deformation in Definition 7.8 is of the following form

$$\begin{aligned} \Phi : \overline{\mathcal{S}} \times [-t/2, t/2] &\to \mathbb{R}^3 \\ (x, z) &\mapsto \phi(x) + \mathbf{R}(\overline{\nu}(x), \phi(x)), \end{aligned} \tag{7.3.4}$$

where ϕ is the deformation of the mid-surface and

$$\mathbf{R} : \mathbb{S}^2 \times \mathcal{S} \to \mathbb{S}^2 \tag{7.3.5}$$

can be understood as a nonlinear rotation of the normal vector (compare the Reissner–Mindlin assumptions in Section 7.3.3). To simplify notation we neglect the x and ϕ dependency of $\mathbf{R}$.

We split the full 3D gradient of the deformation Φ into its tangential and normal component, namely

$$\nabla \Phi = \nabla_{\overline{\tau}} \Phi + \nabla_z \Phi \tag{7.3.6}$$

and denote the projection onto the normal direction by $\mathbf{P}_z := \mathbf{P}_{\overline{\tau}}^{\perp} = \overline{\nu} \otimes \overline{\nu}$.

The Cauchy–Green strain tensor (metric tensor) of the full 3D deformed shell is given by $\mathbf{C} = \nabla \Phi^{\top} \nabla \Phi$. Together with $\nabla_z(z\mathbf{R}(\overline{\nu})) = \mathbf{R}(\overline{\nu}) \otimes \overline{\nu}$ and the notation $\mathbf{F}_{\overline{\tau}} := \nabla_{\overline{\tau}} \phi$ we obtain

$$\begin{aligned} \mathbf{C} &= (\mathbf{F}_{\overline{\tau}} + z\nabla_{\overline{\tau}}\mathbf{R}(\overline{\nu}) + \mathbf{R}(\overline{\nu}) \otimes \overline{\nu})^{\top} (\mathbf{F}_{\overline{\tau}} + z\nabla_{\overline{\tau}}\mathbf{R}(\overline{\nu}) + \mathbf{R}(\overline{\nu}) \otimes \overline{\nu}) \\ &= \mathbf{F}_{\overline{\tau}}^{\top} \mathbf{F}_{\overline{\tau}} + 2z \operatorname{sym}\left(\mathbf{F}_{\overline{\tau}}^{\top} \nabla_{\overline{\tau}}\mathbf{R}(\overline{\nu})\right) + z^2 \nabla_{\overline{\tau}}\mathbf{R}(\overline{\nu})^{\top} \nabla_{\overline{\tau}}\mathbf{R}(\overline{\nu}) \\ &\quad + \mathbf{F}_{\overline{\tau}}^{\top} \mathbf{R}(\overline{\nu}) \otimes \overline{\nu} + (\mathbf{R}(\overline{\nu}) \otimes \overline{\nu})^{\top} \mathbf{F}_{\overline{\tau}} + \underbrace{\mathbf{R}(\overline{\nu})^{\top} \mathbf{R}(\overline{\nu})}_{=1} \mathbf{P}_z, \end{aligned} \tag{7.3.7}$$

where we used that from $\|\mathbf{R}(\overline{\nu})\|_2 = 1$ there follows $\nabla_{\overline{\tau}}\mathbf{R}(\overline{\nu})\mathbf{R}(\overline{\nu}) = 0$. Note, that with the chain rule there holds $\nabla_{\tau}\tilde{\nu} \circ \phi \, \mathbf{F}_{\overline{\tau}} = \nabla_{\overline{\tau}}(\tilde{\nu} \circ \phi) = \nabla_{\overline{\tau}}\mathbf{R}(\overline{\nu})$. Thus, with Definition 7.7, we can identify

$$\mathbf{C} = I + 2z II_{\mathbf{R}(\overline{\nu})} + z^2 III_{\mathbf{R}(\overline{\nu})} + \left(\sigma_{\mathbf{R}(\overline{\nu})} \otimes \overline{\nu} + \overline{\nu} \otimes \sigma_{\mathbf{R}(\overline{\nu})}\right) + \mathbf{P}_z. \tag{7.3.8}$$
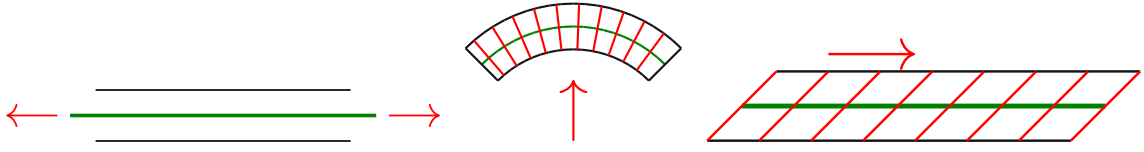
Figure 7.4.: Sketched membrane, bending, and shearing energy of a shell.

For the undeformed configuration we obtain

$$\overline{C} = \overline{I} + 2z\overline{II}_{\overline{\nu}} + z^2\overline{III}_{\overline{\nu}} + P_z, \tag{7.3.9}$$

compare also the 3D metric tensor (7.2.13) in curvilinear coordinates.

The Green strain tensor is given by

$$E = \frac{1}{2}\left(C - \overline{C}\right) \tag{7.3.10}$$

and together with the linear material law of St. Venant–Kirchhoff the whole energy of the deformed shell reads

$$\mathcal{W} := \frac{1}{2}\int_{-\frac{t}{2}}^{\frac{t}{2}}\int_{\overline{S}} \|E\|_M^2 \, ds_z \, dz. \tag{7.3.11}$$

For a discussion of justification for using a linear material law we refer to e.g., [168]. Using Steiner's formula [214]

$$ds_z = \left(1 - 2zH + z^2K\right)ds \tag{7.3.12}$$

with the mean and Gauß curvature H and K, respectively, yields

$$\mathcal{W} = \frac{1}{2}\int_{\overline{S}}\left(\int_{-\frac{t}{2}}^{\frac{t}{2}} \|E\|_M^2 \, dz - 2H\int_{-\frac{t}{2}}^{\frac{t}{2}} z\|E\|_M^2 \, dz + K\int_{-\frac{t}{2}}^{\frac{t}{2}} z^2\|E\|_M^2 \, dz\right)ds. \tag{7.3.13}$$

We assume that $t/L \ll 1$ (L denoting the characteristic length), $\|I - \overline{I}\|_M \leq t$, and $K \leq t$, i.e., that the membrane energy and Gauß curvature are small. Then, using asymptotic analysis neglecting all terms of order $\mathcal{O}(t^4)$ or higher gives the energy [231, 206]

$$\mathcal{W} = \frac{1}{2}\int_{\overline{S}}\left(\frac{t}{4}\|I - \overline{I}\|_M^2 + \frac{t^3}{12}\|II_{R(\overline{\nu})} - \overline{II}\|_M^2 + t\kappa G|\sigma_{R(\overline{\nu})}|^2\right)ds. \tag{7.3.14}$$

Here, $G = \frac{\hat{E}}{2(1+\hat{\nu})}$ and κ denote the shearing modulus and shear correction factor, respectively. The shear correction factor $\kappa < 1$, used to compensate high-order effects of the shear stresses which are not constant through the thickness, is mostly set to 5/6 in practice [49]. Note that the shear correction factor does not appear during the derivation in terms of asymptotic analysis and is added afterwards. For the plate derivation based on variational methods in [4] the factor 5/6 directly appears in front of the shearing part.

The three terms in (7.3.14) correspond to the membrane, bending, and shearing energy, cf. Figure 7.4. Under the assumptions of Reissner–Mindlin, see Section 7.3.3, the material norm is of the form

$$\| \cdot \|_{\boldsymbol{M}}^2 := \frac{\hat{E}}{1 - \hat{\nu}^2} \left(\hat{\nu} \operatorname{tr}(\cdot)^2 + (1 - \hat{\nu}) \operatorname{tr}(\cdot^2) \right). \tag{7.3.15}$$

Using the matrix representations (7.2.19) together with $\boldsymbol{E}_{\overline{\tau}} := 0.5(\boldsymbol{F}_{\overline{\tau}}^\top \boldsymbol{F}_{\overline{\tau}} - \boldsymbol{P}_{\overline{\tau}})$ gives the following form of (7.3.14)

$$\mathcal{W} = \int_{\mathcal{S}} \left(\frac{t}{2} \| \boldsymbol{E}_{\overline{\tau}} \|_{\boldsymbol{M}}^2 + \frac{t^3}{24} \| \operatorname{sym}(\boldsymbol{F}_{\overline{\tau}}^\top \nabla_{\overline{\tau}} \boldsymbol{R}(\overline{\nu})) - \nabla_{\overline{\tau}} \overline{\nu} \|_{\boldsymbol{M}}^2 + \frac{t\kappa G}{2} | \boldsymbol{F}_{\overline{\tau}}^\top \boldsymbol{R}(\overline{\nu}) |^2 \right) ds. \tag{7.3.16}$$

7.5 Remark. *From Steiner's formula (7.3.12) we observe that the shell has to be sufficiently thin such that the expression $1 - 2zH + z^2 K$ stays always strictly positive, depending on the radius of curvature of the smallest modulus of the surface, compare Theorem 7.1.*

7.3.3. Naghdi shell, Reissner–Mindlin plate, and Timoshenko beam

We use (7.3.16) as starting point to derive formulations of (nonlinear) Naghdi shells, the two-dimensional Reissner–Mindlin plate, and the Timoshenko beam in one dimension. In the following we use the displacement field $u := \phi - \operatorname{id}$ as unknown.

The hypothesis of Reissner–Mindlin [156, 191], which we will use gradually in the following, are stated as follows:

(H1) Lines normal to the mid-surface are deformed linearly, i.e., they lie on a straight line.

(H2) The deformation in normal direction is independent of the normal coordinate.

(H3) Points on the mid-surface get only deformed in normal direction.

(H4) The normal stress $\boldsymbol{\sigma}_{33}$ vanishes (often called plane-stress assumption).

A rigorous justification of hypothesis (H4) started in 1959 [158] and has been completed decades later by [4] and [60] using the two-energies principle. Therein it was proven for plates that the full 3D solution converges to the Kirchhoff–Love and Reissner–Mindlin model as the thickness t tends to 0. There holds, under the assumption of a convex middle-surface or a smooth boundary,

$$\| u^{3d} - u^{RM} \| \leq \mathcal{O}(t^{\frac{1}{2}}), \qquad \| u^{3d} - u^{KL} \| \leq \mathcal{O}(t^{\frac{1}{2}}), \tag{7.3.17}$$

and $\| (\boldsymbol{\sigma}^{3d})_{33} \| = \mathcal{O}(t^{\frac{1}{2}}) \| \boldsymbol{\sigma}^{3d} \|$, which can be seen as a justification of the hypothesis.

Under assumption (H4) and using (2.4.1) we can eliminate the strain component $\boldsymbol{\epsilon}_{33}$ by

$$\boldsymbol{\epsilon}_{33} = \frac{\hat{\nu}}{\hat{\nu} - 1} (\boldsymbol{\epsilon}_{11} + \boldsymbol{\epsilon}_{22}). \tag{7.3.18}$$

Inserting this into the other equations of (2.4.1) yields

$$
\begin{pmatrix} \boldsymbol{\sigma}_{11} \\ \boldsymbol{\sigma}_{22} \\ \boldsymbol{\sigma}_{12} \\ \boldsymbol{\sigma}_{13} \\ \boldsymbol{\sigma}_{23} \end{pmatrix} = \frac{\hat{E}}{1 - \hat{\nu}^2} \begin{pmatrix} 1 & \hat{\nu} & & & 0 \\ \hat{\nu} & 1 & & & \\ & & 1 - \hat{\nu} & & \\ & & & 1 - \hat{\nu} & \\ 0 & & & & 1 - \hat{\nu} \end{pmatrix} \begin{pmatrix} \boldsymbol{\epsilon}_{11} \\ \boldsymbol{\epsilon}_{22} \\ \boldsymbol{\epsilon}_{12} \\ \boldsymbol{\epsilon}_{13} \\ \boldsymbol{\epsilon}_{23} \end{pmatrix} \tag{7.3.19}
$$

and splitting this into the in-plane $(\boldsymbol{\sigma}_{11}, \boldsymbol{\sigma}_{22}, \boldsymbol{\sigma}_{12})$ and shearing $(\boldsymbol{\sigma}_{13}, \boldsymbol{\sigma}_{23})$ parts gives the material norm (7.3.15) and shear modulus G.

Nonlinear Naghdi shell: With (H1) and (H2) the director $\tilde{\nu} \circ \phi = \boldsymbol{R}(\overline{\nu}, u)$ is given by a (nonlinear) rotation matrix $\boldsymbol{R} \in \mathrm{SO}(3)$. Although rotational matrices with finite rotations can be well described by e.g., Euler parameters, Quaternions, or Rodrigues parameters, we will consider a different approach better suited for the finite elements involved in the later proposed methods. The rotation can be split by first rotating the normal vector such that it is orthogonal to the deformed mid-plane (compare the Kirchhoff–love hypothesis (H5) in Section 7.3.4) and then a second rotation, the shear, is applied, i.e.,

$$
\boldsymbol{R}(\overline{\nu}, u, \gamma) = \tilde{\boldsymbol{R}}(\gamma)\nu \circ \phi = \tilde{\boldsymbol{R}}(\gamma)\frac{\mathrm{cof}(\boldsymbol{F}_{\overline{\tau}})\overline{\nu}}{\|\mathrm{cof}(\boldsymbol{F}_{\overline{\tau}})\overline{\nu}\|_2} \quad \text{or} \quad \boldsymbol{R}(\overline{\nu}, u, \gamma) = \frac{\mathrm{cof}(\boldsymbol{F}_{\overline{\tau}})\overline{\nu} + \gamma}{\|\mathrm{cof}(\boldsymbol{F}_{\overline{\tau}})\overline{\nu} + \gamma\|_2}, \tag{7.3.20}
$$

where $\gamma = (\gamma_1, \gamma_2)$ are the two shearing parameters and $\tilde{\boldsymbol{R}}(\gamma) \in \mathrm{SO}(3)$. This hierarchical approach can be simplified under the assumption that the shearing term is small (see [167])

$$
\boldsymbol{R}(\overline{\nu}, u, \gamma) = \frac{\mathrm{cof}(\boldsymbol{F}_{\overline{\tau}})\overline{\nu}}{\|\mathrm{cof}(\boldsymbol{F}_{\overline{\tau}})\overline{\nu}\|_2} + \gamma, \tag{7.3.21}
$$

providing the advantage of an additive (instead of a multiplicative) splitting.

Note that $\gamma \in \{\nu \circ \phi\}^{\perp}$ is perpendicular to the deformed normal vector. Thus we need to pull the shear back via the classical push forward $\boldsymbol{F}_{\overline{\tau}}$ or the covariant transformation $(\boldsymbol{F}_{\overline{\tau}}^{\dagger})^{\top}$

$$
\gamma \circ \phi := \boldsymbol{F}_{\overline{\tau}}\overline{\gamma}, \qquad\qquad \gamma \circ \phi := (\boldsymbol{F}_{\overline{\tau}}^{\dagger})^{\top}\overline{\gamma}. \tag{7.3.22}
$$

Defining the director as $\boldsymbol{R}(\overline{\nu}, u, \overline{\gamma})$, we obtain the nonlinear Naghdi shell energy (without a right-hand side)

$$
\mathcal{W}_{RM} = \int_{\overline{\mathcal{S}}} \left(\frac{t}{2}\|\boldsymbol{E}_{\overline{\tau}}\|_{\boldsymbol{M}}^2 + \frac{t^3}{24}\|\mathrm{sym}(\boldsymbol{F}_{\overline{\tau}}^{\top}\nabla_{\overline{\tau}}\boldsymbol{R}(\overline{\nu}, u, \overline{\gamma})) - \nabla_{\overline{\tau}}\overline{\nu}\|_{\boldsymbol{M}}^2 + \frac{t\kappa G}{2}|\boldsymbol{F}_{\overline{\tau}}^{\top}\boldsymbol{R}(\overline{\nu}, u, \overline{\gamma})|^2 \right) ds. \tag{7.3.23}
$$

Linear Naghdi shell: For infinitesimal rotations there holds $\tilde{\nu} \circ \phi = \boldsymbol{R}(\overline{\nu}, u) \approx (\boldsymbol{I} + \mathrm{skw}(\beta_1, \beta_2))\overline{\nu}$ as the tangent space at the identity for the special orthogonal group $\mathrm{SO}(3)$ is the set of skew-symmetric matrices, compare also Figure 7.5 for the classical linearization
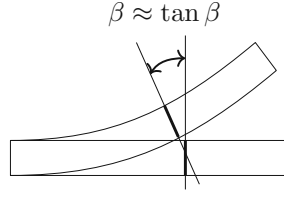
Figure 7.5.: Linearized angle.

of the angle. There holds $\mathrm{skw}(\beta_1, \beta_2)\overline{\nu} \perp \overline{\nu}$ and thus, we can identify it with a vector field $\beta := \mathrm{skw}(\beta_1, \beta_2)\overline{\nu}$ in the tangent bundle $T\overline{\mathcal{S}}$, i.e., $\beta \perp \overline{\nu}$ and thus, $\tilde{\nu} \circ \phi \approx \overline{\nu} + \beta$.

We can also start with the linear approximation $\gamma \circ \phi \approx \overline{\gamma}$, cf. (7.3.22). Linearizing the deformed normal vector (7.2.17a) $\nu \circ \phi \approx \overline{\nu} - \nabla_{\overline{\tau}} u^\top \overline{\nu}$ we get $\tilde{\nu} \circ \phi \approx \overline{\nu} - \nabla_{\overline{\tau}} u^\top \overline{\nu} + \overline{\gamma}$ with $\overline{\gamma} \in T\overline{\mathcal{S}}$ the shear and we can define the rotation $\beta := -\nabla_{\overline{\tau}} u^\top \overline{\nu} + \overline{\gamma}$. Thus, the shearing term in (7.3.23) simplifies to

$$\boldsymbol{F}_{\overline{\tau}}^\top \boldsymbol{R}(\overline{\nu}, u, \overline{\gamma}) \approx \nabla_{\overline{\tau}} u^\top \overline{\nu} + \beta - \nabla_{\overline{\tau}} u^\top \beta \approx \nabla_{\overline{\tau}} u^\top \overline{\nu} + \beta, \tag{7.3.24}$$

as $\nabla_{\overline{\tau}} u^\top \beta = \mathcal{O}(\varepsilon^2)$. Further, with

$$\boldsymbol{F}_{\overline{\tau}}^\top \nabla_{\overline{\tau}} \boldsymbol{R}(\overline{\nu}, u, \overline{\gamma}) - \nabla_{\overline{\tau}} \overline{\nu} \approx \boldsymbol{F}_{\overline{\tau}}^\top \nabla_{\overline{\tau}}(\overline{\nu} + \beta) - \nabla_{\overline{\tau}} \overline{\nu} = \boldsymbol{F}_{\overline{\tau}}^\top \nabla_{\overline{\tau}} \beta + \nabla_{\overline{\tau}} u^\top \nabla_{\overline{\tau}} \overline{\nu}$$
$$\approx \boldsymbol{P}_{\overline{\tau}} \nabla_{\overline{\tau}} \beta + \nabla_{\overline{\tau}} u^\top \nabla_{\overline{\tau}} \overline{\nu} = \nabla_{\overline{\tau}}^{\mathrm{cov}} \beta + \nabla_{\overline{\tau}} u^\top \nabla_{\overline{\tau}} \overline{\nu} \tag{7.3.25}$$

the bending energy changes to

$$\|\mathrm{sym}(\boldsymbol{F}_{\overline{\tau}}^\top \nabla_{\overline{\tau}} \boldsymbol{R}(\overline{\nu}, u, \overline{\gamma})) - \nabla_{\overline{\tau}} \overline{\nu}\|_{\boldsymbol{M}}^2 \approx \|\mathrm{sym}(\nabla_{\overline{\tau}}^{\mathrm{cov}} \beta + \nabla_{\overline{\tau}} u^\top \nabla_{\overline{\tau}} \overline{\nu})\|_{\boldsymbol{M}}^2. \tag{7.3.26}$$

Thus we obtain the linearized Naghdi shell energy

$$\mathcal{W}_{\mathrm{RM}}^{\mathrm{lin}} = \int_{\overline{\mathcal{S}}} \left(\frac{t}{2} \|\mathrm{sym}(\nabla_{\overline{\tau}}^{\mathrm{cov}} u)\|_{\boldsymbol{M}}^2 + \frac{t^3}{24} \|\mathrm{sym}(\nabla_{\overline{\tau}}^{\mathrm{cov}} \beta + \nabla_{\overline{\tau}} u^\top \nabla_{\overline{\tau}} \overline{\nu})\|_{\boldsymbol{M}}^2 + \frac{t \kappa G}{2} |\nabla_{\overline{\tau}} u^\top \overline{\nu} + \beta|^2 \right) ds, \tag{7.3.27}$$

where we used the linearized membrane energy

$$\|\boldsymbol{E}_{\overline{\tau}}\|_{\boldsymbol{M}}^2 \approx \|\mathrm{sym}(\nabla_{\overline{\tau}}^{\mathrm{cov}} u)\|_{\boldsymbol{M}}^2. \tag{7.3.28}$$

In curvilinear coordinates the corresponding (variational) problem of (7.3.27) reads, cf. [72]: Find (for given right-hand side f) $\vec{u}$ and $\vec{\beta}$ such that for all $\delta \vec{u}$ and $\delta \vec{\beta}$

$$\int_{\overline{\mathcal{S}}} C^{\alpha\beta\lambda\mu} \left(t \gamma_{\alpha\beta}(\vec{u}) \gamma_{\lambda\mu}(\delta\vec{u}) + \frac{t^3}{12} \chi_{\alpha\beta}(\vec{u}, \vec{\beta}) \chi_{\lambda\mu}(\delta\vec{u}, \delta\vec{\beta}) \right) + \kappa t D^{\alpha\lambda} \zeta_\alpha(\vec{u}, \vec{\beta}) \zeta_\lambda(\delta\vec{u}, \delta\vec{\beta}) \, ds$$
$$= \int_{\overline{\mathcal{S}}} f \cdot \delta\vec{u} \, ds, \tag{7.3.29}$$

where

$$\gamma_{\alpha\beta}(\vec{u}) := \frac{1}{2} \left(u_{\alpha|\beta} + u_{\beta|\alpha} \right) - b_{\alpha\beta} u_3, \tag{7.3.30a}$$

$$\chi_{\alpha\beta}(\vec{u}, \vec{\beta}) := \frac{1}{2} \left(\beta_{\alpha|\beta} + \beta_{\beta|\alpha} - b_\beta^\lambda u_{\lambda|\alpha} - b_\alpha^\lambda u_{\lambda|\beta} \right) + c_{\alpha\beta} u_3, \tag{7.3.30b}$$

$$\zeta_\alpha(\vec{u}, \vec{\beta}) := \frac{1}{2}(\beta_\alpha + u_{3,\alpha} + b_\alpha^\lambda u_\lambda), \tag{7.3.30c}$$

and

$$C^{\alpha\beta\lambda\mu} := \frac{\hat{E}}{2(1+\hat{\nu})}\left(a^{\alpha\lambda}a^{\beta\mu} + a^{\alpha\mu}a^{\beta\lambda} + \frac{2\hat{\nu}}{1-\hat{\nu}}a^{\alpha\beta}a^{\lambda\mu}\right), \tag{7.3.31a}$$

$$D^{\alpha\lambda} = \frac{2\hat{E}}{1+\hat{\nu}}a^{\alpha\lambda}. \tag{7.3.31b}$$

7.6 Remark. *Note, that with the kinematic assumptions (H1) – (H2) in the linear regime the total displacement is given by*

$$\vec{U}(\xi^1,\xi^2,\xi^3) = \vec{u}(\xi^1,\xi^2) + \xi^3\beta_\lambda(\xi^1,\xi^2)a^\lambda(\xi^1,\xi^2)$$

leading to the same formulation (7.3.29) *[72, 199].*

Using the shear $\gamma := \overline{\gamma} = \nabla_{\overline{\tau}}u^\top\overline{\nu} + \beta$, (7.3.27) changes to

$$\mathcal{W}_{\mathrm{RM}}^{\mathrm{lin}} = \int_{\overline{\mathcal{S}}}\left(\frac{t}{2}\|\mathrm{sym}(\nabla_{\overline{\tau}}^{\mathrm{cov}}u)\|_{\boldsymbol{M}}^2 + \frac{t^3}{24}\|\mathrm{sym}(\nabla_{\overline{\tau}}^{\mathrm{cov}}\gamma - \boldsymbol{P}_{\overline{\tau}}\boldsymbol{\mathcal{H}}_{\overline{\nu}})\|_{\boldsymbol{M}}^2 + \frac{t\kappa G}{2}|\gamma|^2\right)ds, \tag{7.3.32}$$

where $\boldsymbol{\mathcal{H}}_{\overline{\nu}} := \sum_{i=1}^3(\nabla_{\overline{\tau}}^2 u_i)\overline{\nu}_i$ with $\nabla_{\overline{\tau}}^2$ denoting the surface Hessian, see e.g., [97, 200]. As it involves a second order operator leading to a fourth order problem, (7.3.27) is mostly used instead of (7.3.32).

Reissner–Mindlin plate: By assuming that the shell is a flat plate, i.e., the normal vector is constant (w.l.o.g. $\overline{\nu} = \begin{pmatrix}0 & 0 & 1\end{pmatrix}^\top$), (7.3.27) decouples into a 2D membrane problem and the 2D Reissner–Mindlin plate model with $\Omega := \overline{\mathcal{S}} \subset \mathbb{R}^2$:

$$\int_\Omega \mathbb{C}_M\boldsymbol{\epsilon}(\tilde{u}) : \boldsymbol{\epsilon}(\delta\tilde{u})\,dx = \int_\Omega \tilde{f}\cdot\delta\tilde{u}\,dx, \tag{7.3.33}$$

$$\int_\Omega \mathbb{C}_B\boldsymbol{\epsilon}(\beta) : \boldsymbol{\epsilon}(\delta\beta) + t\kappa G\left(\nabla w + \beta\right)\cdot\left(\nabla\delta w + \delta\beta\right)dx = \int_\Omega f_3\delta w\,dx, \tag{7.3.34}$$

where $\tilde{u} := \begin{pmatrix}u_1 & u_2\end{pmatrix}^\top$, $w := u_3$, $\boldsymbol{\epsilon}(\cdot)$ the symmetric part of the gradient, and derivatives are taken only in the first two directions. Further, $\mathbb{C}_B\boldsymbol{\epsilon} := \frac{\hat{E}}{12(1-\hat{\nu}^2)}((1-\hat{\nu})\boldsymbol{\epsilon} + \hat{\nu}\,\mathrm{tr}(\boldsymbol{\epsilon}))$, $\mathbb{C}_M\boldsymbol{\epsilon} := \frac{12}{t^2}\mathbb{C}_B\boldsymbol{\epsilon}$.

Due to three displacement and two rotational degrees of freedom the Reissner–Mindlin plate is also denoted as 5-parameter model. There holds, compare (7.3.2),

$$u_1 = v_1 + zw_1, \quad u_2 = v_2 + zw_2, \quad u_3 = v_3 \tag{7.3.35}$$

and thus, $\boldsymbol{\epsilon}_{33} = \frac{\partial u_3}{\partial z} = 0$, whereas $\boldsymbol{\epsilon}_{11}$ and $\boldsymbol{\epsilon}_{22}$ are linear polynomials. From (2.4.1) we have that $\boldsymbol{\sigma}_{33} = \hat{\lambda}(\boldsymbol{\epsilon}_{11} + \boldsymbol{\epsilon}_{22})$ leading to an asymptotically incorrect model. Thus, the hypothesis (H4), $\boldsymbol{\sigma}_{33} = 0$, has been used leading to $\boldsymbol{\epsilon}_{33} = \frac{\hat{\nu}}{\hat{\nu}-1}(\boldsymbol{\epsilon}_{11} + \boldsymbol{\epsilon}_{22}) \neq 0$. Due to this discrepancy the normal-normal component of the strain is condensed out of the material law equation.

One may hope that by using linear polynomials in z for u_3, called $(1,1,1)$-model, overcomes this problem of modifying the 3D material law. However, it turns out that a quadratic approach, $(1,1,2)$-model, is needed to directly use 3D material models [46].

The hypothesis (H3) is used to neglect the membrane problem (7.3.33) yielding solely (7.3.34) involving only two rotational unknowns and the vertical deflection.

Timoshenko beam: Reducing the plate to one dimension the so-called Timoshenko beam is recovered (together with a membrane problem of the form (7.3.33))

$$\int_\Omega D\beta'(\delta\beta)' + t\kappa G\,(w'+\beta)((\delta w)' + \delta\beta)\,dx = \int_\Omega f\delta w\,dx, \qquad (7.3.36)$$

where $D := \frac{t^3\hat{E}}{12(1-\hat{\nu}^2)}$ is the bending rigidity.

As discussed in Section 8.2, already for this simplified model shear locking appears and needs to be treated accordingly.

7.3.4. Koiter shell, Kirchhoff–Love plate, and Euler–Bernoulli beam

Additionally to the hypothesis (H1) – (H4) the Kirchhoff–Love hypothesis reads

(H5) Normals to the undeformed middle surface move to normals of the deformed middle surface without any change in length.

Nonlinear Koiter shell: With hypothesis (H1), (H2), and (H5) and Lemma 7.3 the director $\tilde{\nu}\circ\phi$ is of the form

$$\tilde{\nu}\circ\phi = \frac{1}{\|\mathrm{cof}(\boldsymbol{F}_{\overline{\tau}})\|_F}\mathrm{cof}(\boldsymbol{F}_{\overline{\tau}})\overline{\nu}. \qquad (7.3.37)$$

Thus, the shearing energy is zero and the nonlinear Koiter shell energy is given by

$$\mathcal{W}_{\mathrm{KL}} = \int_{\overline{\mathcal{S}}}\left(\frac{t}{2}\|\boldsymbol{E}_{\overline{\tau}}\|_{\boldsymbol{M}}^2 + \frac{t^3}{24}\|\mathrm{sym}(\boldsymbol{F}_{\overline{\tau}}^\top\nabla_{\overline{\tau}}\left(\frac{\mathrm{cof}(\boldsymbol{F}_{\overline{\tau}})\overline{\nu}}{\|\mathrm{cof}(\boldsymbol{F}_{\overline{\tau}})\|_F}\right)) - \nabla_{\overline{\tau}}\overline{\nu}\|_{\boldsymbol{M}}^2\right)ds. \qquad (7.3.38)$$

Linear Koiter shell: Linearization (7.2.17a) gives $\tilde{\nu}\circ\phi = \overline{\nu} - \nabla_{\overline{\tau}}u^\top\overline{\nu} + \mathcal{O}(\varepsilon^2)$ yielding with the linearized membrane energy (7.3.28)

$$\overline{\mathcal{W}}_{\mathrm{KL}}^{\mathrm{lin}} = \int_{\overline{\mathcal{S}}}\left(\frac{t}{2}\|\mathrm{sym}(\nabla_{\overline{\tau}}^{\mathrm{cov}}u)\|_{\boldsymbol{M}}^2 + \frac{t^3}{24}\|\mathrm{sym}(\nabla_{\overline{\tau}}^{\mathrm{cov}}(\nabla_{\overline{\tau}}u^\top\overline{\nu}))\|_{\boldsymbol{M}}^2\right)ds. \qquad (7.3.39)$$

In classical shell theory the term $\nabla_{\overline{\tau}}u^\top\nabla_{\overline{\tau}}\overline{\nu}$ is neglected for the linearized bending energy [207]. Thus, (7.3.39) simplifies to (compare also [200])

$$\mathcal{W}_{\mathrm{KL}}^{\mathrm{lin}} = \int_{\overline{\mathcal{S}}}\left(\frac{t}{2}\|\mathrm{sym}(\nabla_{\overline{\tau}}^{\mathrm{cov}}u)\|_{\boldsymbol{M}}^2 + \frac{t^3}{24}\|\mathrm{sym}(\boldsymbol{P}_{\overline{\tau}}\,\boldsymbol{\mathcal{H}}_{\overline{\nu}})\|_{\boldsymbol{M}}^2\right)ds. \qquad (7.3.40)$$

Note, that in the limit $t\to 0$ in (7.3.27) we obtain $\beta = -\nabla_{\overline{\tau}}u^\top\overline{\nu}$ recovering (7.3.40) as then $\nabla_{\overline{\tau}}^{\mathrm{cov}}\beta + \nabla_{\overline{\tau}}u^\top\nabla_{\overline{\tau}}\overline{\nu} = -\boldsymbol{P}_{\overline{\tau}}\boldsymbol{\mathcal{H}}_{\overline{\nu}}$. The same holds for the shearing formulation (7.3.32).

The problem in curvilinear coordinates reads [72]: Find (for given right-hand side f) $\vec{u}$ such that for all $\delta\vec{u}$

$$\int_{\overline{\mathcal{S}}}C^{\alpha\beta\lambda\mu}\left(t\,\gamma_{\alpha\beta}(\vec{u})\gamma_{\lambda\mu}(\delta\vec{u}) + \frac{t^3}{12}\rho_{\alpha\beta}(\vec{u})\rho_{\lambda\mu}(\delta\vec{u})\right)ds = \int_{\overline{\mathcal{S}}}f\cdot\delta\vec{u}\,ds, \qquad (7.3.41)$$

where $C^{\alpha\beta\lambda\mu}$, $\gamma_{\alpha\beta}$ are as in (7.3.30a), (7.3.31a) and

$$\rho_{\alpha\beta}(\vec{u}) := u_{3|\alpha\beta} + b^\mu_{\alpha|\beta} u_\mu + b^\mu_\alpha u_{\mu|\beta} + b^\mu_\beta u_{\mu|\alpha} - c_{\alpha\beta} u_3, \qquad (7.3.42)$$

with

$$u_{3|\alpha\beta} = u_{3,\alpha\beta} - \Gamma^\mu_{\alpha\beta} u_{3,\mu}, \qquad\qquad b^\mu_{\alpha|\beta} = b^\mu_{\alpha,\beta} + \Gamma^\mu_{\beta\lambda} b^\lambda_\alpha - \Gamma^\lambda_{\alpha\beta} b^\mu_\lambda.$$

Kirchhoff–Love plate: By assuming that the shell is a flat plate $\Omega \subset \mathbb{R}^2$ and $\overline{\nu} = \begin{pmatrix} 0 & 0 & 1 \end{pmatrix}^\top$, (7.3.40) decouples into the membrane problem (7.3.33) and the Kirchhoff–Love plate model:

$$\int_\Omega \mathbb{C}_B \nabla^2 w : \nabla^2 \delta w \, dx = \int_\Omega f \, \delta w \, dx. \qquad (7.3.43)$$

As in the Kirchhoff–Love model only the 3 displacement parameters appear it is also called 3-parameter model.

Euler–Bernoulli beam: In one dimension the Kirchhoff–Love plate degenerates to the Euler–Bernoulli beam

$$\int_\Omega D w''(\delta w)'' \, dx = \int_\Omega f \, \delta w \, dx. \qquad (7.3.44)$$

Note, that compared to the Timoshenko beam (7.3.36) no shear locking appears, (as no shearing term is involved).

7.4. Discrete differential geometry

Up to now we have considered smooth surfaces for the derivation of the different shell models. When discretizing the initial configuration of a smooth shell the resulting elements are continuously connected, but not necessarily in a smooth way. As the curvature of a surface depends on the derivative of the normal vector field, i.e., the second derivative of the embedding, the natural question of how to define curvature on discrete geometries arise and is discussed in this section from a finite element (and distributional) point of view.

7.4.1. Discrete surfaces

Let $\mathcal{T}_h$ be a piece-wise smooth and globally continuous surface triangulation approximating the smooth manifold $\mathcal{S}$ such that the vertices of $\mathcal{T}_h$ lie exactly on $\mathcal{S}$. More precisely, let $\mathcal{T}_h = \{T_i\}_{i=1}^N$ with T_i smooth manifolds and piece-wise smooth boundary ∂T and define $T\mathcal{T}_h := \cup_i TT_i$ as the tangential bundle of $\mathcal{T}_h$. Thus, we can define on every element T a (globally not necessarily continuous) normal vector ν and on the edges (normalized) tangential vectors τ_L and τ_R such that the element-normal (co-normal) vectors $\mu_L := \nu_L \times \tau_L$ and $\mu_R := \nu_R \times \tau_R$ are pointing outward of T_L and T_R, respectively, see Figure 7.6. We neglect the subscripts L and R, if the corresponding element T is obvious. Remember that
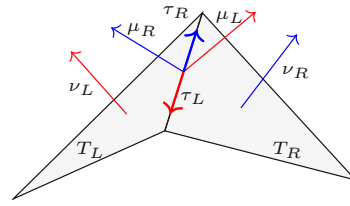
Figure 7.6.: Normal, tangential and element-normal vectors ν, τ and μ on two neighbored elements.
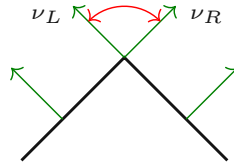

Figure 7.7.: Jump of normal vector over two affine elements.

integrating over volume, surfaces, or edges (vertices in 2D) is denoted by dx, ds, or $d\lambda$, respectively.

Let $\mathcal{T}_{h,k}$ be a triangulation of $\mathcal{S}$ with polynomial approximation order $k \geq 1$. If the order of approximation is obvious or not essential, we simply write $\mathcal{T}_h$. To curve the mesh in such a way that an optimal isoparametric finite element approximations we refer to [146] (compare also [97]). A projection-based interpolation procedure for curving geometries is given in [94].

7.4.2. Discrete curvatures

For an affine triangulation $\mathcal{T}_{h,1}$ the discrete outer normal vector ν is piece-wise constant and thus, $\nabla_\tau \nu|_T = 0$ for all $T \in \mathcal{T}_h$. Moreover, the normal vector may jump over the interfaces, see Figure 7.7. Hence, the discrete shape operator can at best be a distribution, which requires a detailed derivation. This is motivated by discrete differential geometry, e.g., [109], where the angle is also used as part of the curvature computation.

We start with an affine 1D curve in two dimensions and w.l.o.g. consider two line segments and one point $P = (0,0)$, where the normal vector jumps with angle α as depicted in Figure 7.8 (a). Our goal is to derive an approximation of the curvature formula at the point P. To this end, we construct a family of C^1-smooth approximation of the curve parametrised by $\varepsilon > 0$. Starting with an ε-circle centered at P, we define the unique circle that goes through the same intersection points with the curve as the ε-circle and cuts it in a 90 degree angle, see Figure 7.8 (b). This circle with radius $r_\varepsilon = \varepsilon \frac{1+\cos(\alpha)}{\sin(\alpha)}$ and midpoint $M_\varepsilon = (\varepsilon, -r_\varepsilon)$ is then used as C^1-approximation of the junction, cf. Figure 7.8 (c). Thus, we can define the continuous and piece-wise smooth approximated normal
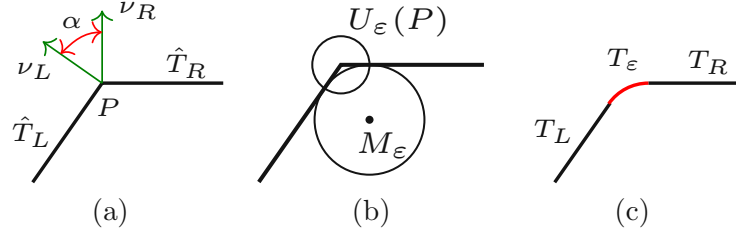
Figure 7.8.: Construction of approximation of discrete jump. (a) The affine curve with jump angle α. (b) The construction of the circles. (c) The final approximated smooth curve.

vector field $\nu_\varepsilon : \mathcal{T}_\varepsilon \to \mathbb{S}^1$ and the corresponding shape operator

$$\nu_\varepsilon(x) = \begin{cases} \nu_L & \text{for } x \in T_L, \\ \frac{x - M_\varepsilon}{\|x - M_\varepsilon\|} & \text{for } x \in T_\varepsilon, \\ \nu_R & \text{for } x \in T_R, \end{cases} \qquad -\nabla_\tau \nu_\varepsilon = \begin{cases} 0 & \text{for } x \in T_L, \\ -\frac{1}{r_\varepsilon} \mu_\varepsilon \otimes \mu_\varepsilon & \text{for } x \in T_\varepsilon, \\ 0 & \text{for } x \in T_R, \end{cases} \tag{7.4.1}$$

with $\mu_\varepsilon := \frac{1}{\|x - M_\varepsilon\|} \begin{pmatrix} -(x_2 - M_{\varepsilon,2}) \\ (x_1 - M_{\varepsilon,1}) \end{pmatrix}$ the tangential vector on T_ε, $T_L := \hat{T}_L \backslash U_\varepsilon(P)$ and $T_R := \hat{T}_R \backslash U_\varepsilon(P)$ and $\mathbb{S}^1$ denotes the unit-sphere in 2D. Note that $\mu_\varepsilon = -\mu_L$ and $\mu_\varepsilon = \mu_R$ on the interfaces $\overline{T}_\varepsilon \cap \overline{T}_L$ and $\overline{T}_\varepsilon \cap \overline{T}_R$, where μ_L and μ_R are the element-normal vectors, cf. Figure 7.6. Further, there exists a continuous and bijective mapping $\Phi_\varepsilon : \mathcal{T}_h \to \mathcal{T}_\varepsilon$

$$\Phi_\varepsilon(x) := \begin{cases} x & \text{for } x \in \mathcal{T}_h \backslash U_\varepsilon(P), \\ \frac{r_\varepsilon}{\|x - M_\varepsilon\|}(x - M_\varepsilon) & \text{for } x \in \mathcal{T}_h \cap U_\varepsilon(P), \end{cases} \tag{7.4.2}$$

with $\Phi_\varepsilon \xrightarrow{\varepsilon \to 0} \mathrm{id}$.

To compute the limit $\varepsilon \to 0$ for the curvature we define the corresponding test function on the triangulation $\boldsymbol{\Psi} : \mathcal{T}_h \to \mathbb{R}^{2 \times 2}$ to be element-normal element-normal continuous, i.e., $\mu_L^\top \boldsymbol{\Psi} \mu_L =: \boldsymbol{\Psi}_{\mu_L \mu_L} = \boldsymbol{\Psi}_{\mu_R \mu_R}$ on the skeleton $\mathcal{E}_h$. Thus, the element-normal element-normal component "does not see" the junction of the discretized geometry. Further it should be symmetric, as the shape operator is, and thus has the form $\boldsymbol{\Psi} = \Psi \mu \otimes \mu$ with $\Psi : \mathbb{R}^2 \to \mathbb{R}$ a continuous function. The test function on the smoothed surface $\mathcal{T}_\varepsilon$ reads $\boldsymbol{\Psi}_\varepsilon = \Psi \mu_\varepsilon \otimes \mu_\varepsilon$. Then, with the transformation and Lebesgue dominated convergence theorem we obtain

$$\begin{aligned} \langle -\nabla_\tau \nu, \boldsymbol{\Psi} \rangle_{\mathcal{T}_{h,1}} &:= \lim_{\varepsilon \to 0} \langle -\nabla_\tau \nu_\varepsilon, \boldsymbol{\Psi}_\varepsilon \rangle_{\mathcal{T}_\varepsilon} \\ &= \lim_{\varepsilon \to 0} \int_{\Gamma_\varepsilon} -\frac{1}{r_\varepsilon} \mu_\varepsilon \otimes \mu_\varepsilon : \Psi \mu_\varepsilon \otimes \mu_\varepsilon \, ds \\ &= \lim_{\varepsilon \to 0} \int_{\Gamma_1} -\Psi(M_\varepsilon + r_\varepsilon x) \, ds(x) = -\underbrace{|\Gamma_1|}_{=\alpha} \Psi(P) \\ &= -\int_P \sphericalangle(\nu_L, \nu_R) \Psi \, d\lambda, \end{aligned}$$

(a)   (b)

Figure 7.9.: Construction of approximation of discrete jump in 3D. (a) The affine curve with junction. (b) The approximated smooth surface.

with the notation $\sphericalangle(\nu_L, \nu_R) := \arccos(\nu_L \cdot \nu_R)$ for the angle and

$$\Gamma_\varepsilon := \{M_\varepsilon + r_\varepsilon \begin{pmatrix} \cos(s) \\ \sin(s) \end{pmatrix}, \, s \in (\frac{\pi}{2}, \frac{\pi}{2} + \alpha)\}, \quad \Gamma_1 := \{\begin{pmatrix} \cos(s) \\ \sin(s) \end{pmatrix}, \, s \in (\frac{\pi}{2}, \frac{\pi}{2} + \alpha)\}. \quad (7.4.3)$$

Thus, the discrete shape operator on a triangulation $\mathcal{T}_{h,k}$ can be defined as

$$\langle -\nabla_\tau \nu, \boldsymbol{\Psi} \rangle_{\mathcal{T}_{h,k}} := -\sum_{T \in \mathcal{T}_h} \int_T \nabla_\tau \nu_s|_T : \boldsymbol{\Psi} \, ds - \sum_{E \in \mathcal{E}_h} \int_E \sphericalangle(\nu_L, \nu_R) \boldsymbol{\Psi}_{\mu\mu} \, d\lambda. \quad (7.4.4)$$

Note, that for a high-order approximation of the surface the jump term becomes less important in terms of curvature information, however, as we will see, it is crucial for numerical stability.

The generalization to two-dimensional sub-manifolds in three dimensions is done in an analogous manner, see Figure 7.9. For the vertices one might also use a smoothing by an ε-sphere, compute the normal vector on this regularized surface, and then use the limit $\varepsilon \to 0$ as distributional value on the vertex. This limit, however, is zero as the surface of the sphere converges with quadratic order to zero whereas the norm of the shape operator $\nabla \nu_\varepsilon$ is only of order $\mathcal{O}(\varepsilon^{-1})$. Therefore, as in the two-dimensional case, the test function $\boldsymbol{\Psi} : \mathcal{T}_h \to \mathbb{R}^{3 \times 3}_{\text{sym}}$ has to be element-normal element-normal continuous, i.e., $0 = [\![\boldsymbol{\Psi}_{\mu\mu}]\!] := \boldsymbol{\Psi}_{\mu\mu}|_{T_L} - \boldsymbol{\Psi}_{\mu\mu}|_{T_R}$, and symmetric. The construction of such surface finite element spaces is given in the following section. We note that other algorithms in discrete differential geometry use also vertex patches to compute the curvature, see e.g., [109].

From a finite element point of view the discrete normal vector ν on the (curved) elements is globally tangential-continuous. The corresponding shape operator is thus tangential-tangential continuous. As it is also symmetric we can use the prescribed procedure as a lifting from the distributional Weingarten tensor to a more regular 2D Regge finite element mapped onto the surface, where the HHJ space acts as Lagrange multiplier, compare also Section 6.2. E.g., to compute the norm of the curvature tensor we can use

$$\mathcal{L}(\boldsymbol{\kappa}, \boldsymbol{\sigma}) = \frac{1}{2} \|\boldsymbol{\kappa}\|^2_{L^2} - \int_{\mathcal{T}_h} \boldsymbol{\kappa} : \boldsymbol{\sigma} \, ds + \langle \nabla_\tau \nu, \boldsymbol{\sigma} \rangle_{\mathcal{T}_h}, \quad (7.4.5)$$

where $\boldsymbol{\kappa}$ and $\boldsymbol{\sigma}$ are in the tangential-tangential continuous Regge and normal-normal continuous HHJ finite element space mapped onto the surface. For shells we are more interested in the difference of the curvature between the initial and deformed configuration to measure the bending energy. This can be achieved with the moment tensor $\boldsymbol{\sigma}$ acting as Lagrange

$$\kappa = \alpha \qquad\qquad \kappa = 2\sin\left(\tfrac{\alpha}{2}\right) \qquad\qquad \kappa = 2\tan\left(\tfrac{\alpha}{2}\right)$$
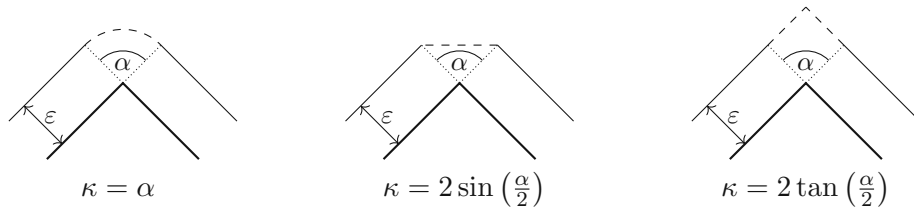
Figure 7.10.: Three different consistent discrete curvatures based on Steiner's offset formula.

multiplier without the lifted curvature tensors $\bar{\boldsymbol{\kappa}}$ and $\boldsymbol{\kappa}$. Thus, we will not follow the idea of a lifting and consider a Hellinger–Reissner type formulation

$$\mathcal{W}(\boldsymbol{\sigma}) = -\frac{1}{2}\|\boldsymbol{\sigma}\|_{L^2}^2 + \langle \nabla_\tau \nu, \boldsymbol{\sigma}\rangle_{\mathcal{T}_h}. \tag{7.4.6}$$

7.7 Remark. *Note, that the question where to place the normal vector (and directors for shells) is not uniformly answered. Instead of placing them at the elements a common strategy is to average the normal vector e.g., at vertices to obtain a globally continuous field. Then the gradient would be globally well-defined in weak sense, however, for kinks and branched shells there is no unique way to average the normal vector [49]. As discussed, e.g., in [231], the directors can be placed also on edges for an improved approximation property of the exact geometry if a piece-wise affine triangulation is used.*

7.8 Remark. *For the definition of curvature of a curve Steiner's offset formula can also be considered. Depending on how the offset curve gets continuously continued different kind of curvatures at the jump are obtained, see e.g., [107, 42] and Figure 7.10. All three versions coincide in the limit of smooth surfaces $\alpha \to 0$. The third one is the only, where the curvature tends to infinity for $\alpha \to \pi$. The first approach leads to the same curvature as our variational derivation. It is possible to consider also the other curvature definitions, however as we will see, the difference of the angles between the initial and deformed configuration will always be close to zero.*

7.5. Finite elements on surfaces

Before introducing finite element spaces on surfaces we need to define the function spaces on manifolds and start with the integration by parts formula. For a comprehensive introduction of finite elements on surfaces we refer to [97].

7.9 Theorem (Integration by parts on manifolds). *Let $\mathcal{S}$ by an $n-1$-dimensional submanifold of $\mathbb{R}^n$ with smooth boundary $\partial\mathcal{S}$. Further let ν be the normal vector, μ the co-normal, and $f \in C^1(\overline{\mathcal{S}})$ a differentiable function up to the boundary. Then there holds with the mean curvature $H = \operatorname{tr}(\nabla_\tau \nu)$*

$$\int_{\mathcal{S}} \nabla_\tau f \, ds = \int_{\mathcal{S}} f \, H\nu \, ds + \int_{\partial\mathcal{S}} f\mu \, d\lambda. \tag{7.5.1}$$

Proof. See e.g., [97, Theorem 2.10.]. □

Definition 7.9. The set of square-integrable functions on the surface $\mathcal{S}$ is defined as

$$L^2(\mathcal{S}) := \{u : \mathcal{S} \to \mathbb{R} \,|\, \|u\|_{L^2(\mathcal{S})} < \infty\}. \tag{7.5.2}$$

A function $f \in L^2(\mathcal{S})$ is weakly differentiable, $u = \nabla_\tau f \in [L^2(\mathcal{S})]^n$, if for all $\Psi \in [C_0^\infty(\mathcal{S})]^n$ there holds

$$\int_\mathcal{S} f \operatorname{div}_\tau(\Psi) \, ds = - \int_\mathcal{S} u \cdot \Psi \, ds + \int_\mathcal{S} H f \, \Psi \cdot \nu \, ds \tag{7.5.3}$$

and the Sobolev space $H^1(\mathcal{S})$ is given by

$$H^1(\mathcal{S}) := \{u \in L^2(\mathcal{S}) \,|\, \nabla_\tau u \in [L^2(\mathcal{S})]^n\}. \tag{7.5.4}$$

For vector valued function spaces on surfaces we first define

$$[L^2(\mathcal{S})]^3_\tau := \{u \in [L^2(\mathcal{S})]^3 \,|\, u \cdot \nu = 0\}, \tag{7.5.5a}$$

$$[L^2(\mathcal{S})]^{3\times3}_\tau := \{\boldsymbol{\sigma} \in [L^2(\mathcal{S})]^{3\times3} \,|\, \boldsymbol{\sigma}\nu = \nu^\top \boldsymbol{\sigma} = 0\} \tag{7.5.5b}$$

as the set of square-integrable tangential vector and matrix fields on $\mathcal{S}$ and then

$$H(\operatorname{div}, \mathcal{S}) := \{u \in [L^2(\mathcal{S})]^3_\tau \,|\, \operatorname{div}_\tau(u) \in L^2(\mathcal{S})\}, \tag{7.5.6a}$$

$$H(\operatorname{curl}, \mathcal{S}) := \{u \in [L^2(\mathcal{S})]^3_\tau \,|\, \operatorname{curl}_\tau(u) \in L^2(\mathcal{S})\}, \tag{7.5.6b}$$

and analogously $H(\operatorname{div}\operatorname{div}, \mathcal{S})$ and $H(\operatorname{curl}\operatorname{curl}, \mathcal{S})$. The following sequences are exact and comparable to the flat two-dimensional case, see Definition 7.5 and [194],

$$\begin{aligned}
\mathbb{R} &\xrightarrow{\operatorname{id}} H^1(\mathcal{S}) \xrightarrow{\nabla_\tau} H(\operatorname{curl}, \mathcal{S}) \xrightarrow{\operatorname{curl}_\tau} L^2(\mathcal{S}) \xrightarrow{0} 0, \\
\mathbb{R} &\xrightarrow{\operatorname{id}} H^1(\mathcal{S}) \xrightarrow{\operatorname{Curl}_\tau} H(\operatorname{div}, \mathcal{S}) \xrightarrow{\operatorname{div}_\tau} L^2(\mathcal{S}) \xrightarrow{0} 0.
\end{aligned} \tag{7.5.7}$$

The finite element spaces introduced in Chapter 5 fall into two categories:

1. Spaces where the trace of a 3D element results in a 2D element of the same space.

2. Spaces where the trace of a 3D element does not lead to a valid 2D element of the same space.

The spaces H^1, $H(\operatorname{curl})$, and $H(\operatorname{curl}\operatorname{curl})$ belong to the first class, whereas L^2, $H(\operatorname{div})$, $H(\operatorname{div}\operatorname{div})$, and $H(\operatorname{curl}\operatorname{div})$ are contained in the second category.

Nevertheless, we generally describe how 2D flat elements (triangles and quadrilaterals) can be mapped onto surfaces. Therefore, let $\hat{T} \subset \mathbb{R}^2$ be the reference element and $\Phi_T : \hat{T} \to \mathcal{T}_h \subset \mathbb{R}^3$ a (not necessarily affine but smooth) mapping onto a surface element, i.e., Φ_T can be seen as an embedding ($\nabla\Phi_T \in \mathbb{R}^{3\times2}$ has full rank).

Let $\hat{u}$ be an H^1-conforming finite element on $\hat{T}$. Then, with $u \circ \Phi_T := \hat{u}$ a H^1-conforming finite element is defined as the continuity of $\hat{u}$ is directly inherited by u directly to u. The L^2-conforming elements follow the same idea, see Figure 7.5.
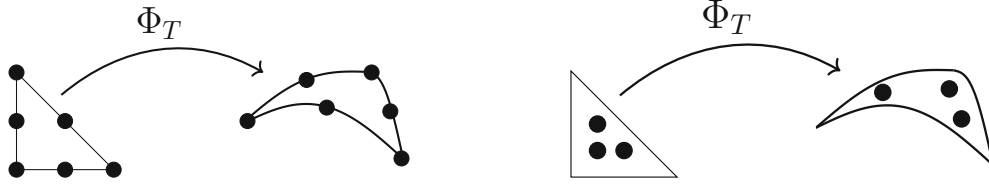
Figure 7.11.: Mapping of H^1- and L^2-conforming elements from reference triangle onto a curved physical surface element.

Thus, we can define

$$Q_h^k(\mathcal{T}_h) := \{u \in L^2(\mathcal{T}_h) \,|\, \forall T \in \mathcal{T}_h \,\exists \hat{u} \in \mathcal{P}^k(\hat{T}) :\, u|_T \circ \Phi_T = \hat{u}\}, \tag{7.5.8}$$

$$U_h^k(\mathcal{T}_h) := \{u \in H^1(\mathcal{T}_h) \,|\, \forall T \in \mathcal{T}_h \,\exists \hat{u} \in \mathcal{P}^k(\hat{T}) :\, u|_T \circ \Phi_T = \hat{u},\, u \text{ continuous}\}. \tag{7.5.9}$$

To preserve the normal or tangential continuity of $H(\mathrm{div})$- or $H(\mathrm{curl})$-conforming finite elements the Piola and Covariant transformations (5.2.21) and (5.2.30) are adapted

$$u \circ \Phi_T := \frac{1}{J}\boldsymbol{G}\hat{u}, \qquad \boldsymbol{G} = \nabla\Phi_T \in \mathbb{R}^{3\times2}, \quad J = \sqrt{\det(\boldsymbol{G}^\top\boldsymbol{G})}, \tag{7.5.10}$$

$$v \circ \Phi_T = (\boldsymbol{G}^\dagger)^\top\hat{v}, \qquad \boldsymbol{G}^\dagger = (\boldsymbol{G}^\top\boldsymbol{G})^{-1}\boldsymbol{G}^\top, \tag{7.5.11}$$

with the Moore–Penrose pseudo inverse $\boldsymbol{G}^\dagger$. Therefore

$$V_h^k(\mathcal{T}_h) := \{u \in H(\mathrm{curl}, \mathcal{T}_h) \,|\, \forall T \in \mathcal{T}_h \,\exists \hat{u} \in [\mathcal{P}^k(\hat{T})]^2 :\, u|_T \circ \Phi_T = (\boldsymbol{G}^\dagger)^\top\hat{u},\, \llbracket u_t \rrbracket = 0\},$$
$$\tag{7.5.12}$$

$$W_h^k(\mathcal{T}_h) := \{u \in H(\mathrm{div}, \mathcal{T}_h) \,|\, \forall T \in \mathcal{T}_h \,\exists \hat{u} \in [\mathcal{P}^k(\hat{T})]^2 :\, u|_T \circ \Phi_T = \frac{1}{J}\boldsymbol{G}\hat{u},\, \llbracket u_\mu \rrbracket = 0\}.$$
$$\tag{7.5.13}$$

In the same spirit the transformation rules for $H(\mathrm{div\,div})$ and $H(\mathrm{curl\,curl})$ elements on surfaces are given by

$$\boldsymbol{\sigma} \circ \Phi_T := \frac{1}{J^2}\boldsymbol{G}\hat{\boldsymbol{\sigma}}\boldsymbol{G}^\top, \qquad\qquad \boldsymbol{\tau} \circ \Phi_T = (\boldsymbol{G}^\dagger)^\top\hat{\boldsymbol{\tau}}\boldsymbol{G}^\dagger. \tag{7.5.14}$$

The finite element spaces $M_h^k(\mathcal{T}_h)$ and $\mathcal{R}_h^k(\mathcal{T}_h)$ are defined accordingly. To simplify notation we neglect the dependency of $\mathcal{T}_h$, if no misunderstandings are possible.

Note that $\boldsymbol{G}$ in (7.5.10) acts as a push forward of the tangent vector field $\hat{u}$, if $\mathbb{R}^2$ is identified as a sub-manifold of $\mathbb{R}^3$, compare Figure 7.3. Thus, the transformed u is a tangent vector field on the surface, which can be used to construct e.g., divergence-free tangential methods for incompressible flows on surfaces [144].

7.10 Remark. *As a consequence the tensor $\boldsymbol{\sigma}$ acts also on the tangent space of the surface, i.e., $\boldsymbol{\sigma} : T\mathcal{T}_h \times T\mathcal{T}_h \to \mathbb{R}$ and $\boldsymbol{\sigma}\nu = \nu^\top\boldsymbol{\sigma} = 0$.*

The definitions of the facet space (5.2.69) and normal-facet space (5.2.73) on surfaces, denoted by $F_h^k(\mathcal{T}_h)$ and $\Gamma_h^k(\mathcal{T}_h)$, follow immediately. Note, that for the normal-facet space

the Piola transformation has to be used to transform the involved normal vector.

7.11 Remark. *The dual shapes presented in Section 5.3 can also directly be applied in terms of surface spaces. Only the transformations (to obtain e.g., a geometry-free matrix) need to be adapted accordingly, e.g., the inverse of the Jacobi matrix $\boldsymbol{G}^{-1}$ has to be replaced by the Moore–Penrose pseudo-inverse $\boldsymbol{G}^{\dagger}$.*

7.12 Remark. *A polynomial (non-affine) mapping Φ of order k yields the requirement to have e.g, a H^1-conforming finite element space of order k, i.e., an isoparametric discretization to represent polynomials on the surface should be used. Otherwise, non-optimal convergence-rates or extreme locking behavior (see Chapter 8) may be the consequence.*

7.6. Hellan–Herrmann–Johnson stress space for plates

As preparation for the (nonlinear) shells, we describe how the HHJ stress space (5.2.35) is used to discretize the fourth order Kirchhoff–Love plate without H^2-conforming (and thus C^1-) elements and the Reissner–Mindlin plate together with rotations β in the Nédélec space avoiding shear locking (see Section 8.2).

7.6.1. HHJ method for Kirchhoff–Love plates

Assuming a flat plate $\Omega \subset \mathbb{R}^2$ and an external force f acting orthogonal on Ω, see Figure 7.12, the following strong form of the fourth order problem (7.3.43) describes the vertical deflection w of a plate considering linearized bending:

$$\operatorname{div}(\operatorname{div}(\boldsymbol{\sigma})) = f, \qquad \boldsymbol{\sigma} := \mathbb{C}_B \nabla^2 w \quad \text{in } \Omega, \tag{7.6.1a}$$

$$w = 0, \quad \frac{\partial w}{\partial n} = 0 \qquad\qquad \text{on } \Gamma_c, \tag{7.6.1b}$$

$$w = 0, \quad \boldsymbol{\sigma}_{nn} = 0 \qquad\qquad \text{on } \Gamma_s, \tag{7.6.1c}$$

$$\boldsymbol{\sigma}_{nn} = 0, \quad \frac{\partial \boldsymbol{\sigma}_{nt}}{\partial t} + \operatorname{div}(\boldsymbol{\sigma}) \cdot n = 0 \qquad \text{on } \Gamma_f, \tag{7.6.1d}$$

$$[\![\boldsymbol{\sigma}_{nt}]\!]_x = \boldsymbol{\sigma}_{n_1 t_1}(x) - \boldsymbol{\sigma}_{n_2 t_2}(x) = 0 \qquad \forall x \in \mathcal{V}_{\Gamma_f}, \tag{7.6.1e}$$

where the boundary $\Gamma = \partial\Omega$ splits into a clamped, simply supported, and free boundary Γ_c, Γ_s, and Γ_f, respectively. $\mathcal{V}_{\Gamma_f}$ denotes the set of corner points where the two adjacent edges belong to Γ_f. Physically, $\boldsymbol{\sigma}_{nn}$ is the normal bending moment, $\partial_t(t^\top \boldsymbol{\sigma} n) + n^\top \operatorname{div}(\boldsymbol{\sigma})$ the effective transverse shear force, and $t^\top \boldsymbol{\sigma} n$ the torsion moment. Further, the shear force q is given by $q = -\operatorname{div}(\boldsymbol{\sigma})$. For simplicity we assume a totally clamped plate, $\Gamma_c = \partial\Omega$, in the following. Then, the weak formulation reads:

7.13 Problem. *Find $w \in H_0^2(\Omega)$ such that for all $\delta w \in H_0^2(\Omega)$*

$$\int_\Omega \mathbb{C}_B \nabla^2 w : \nabla^2 \delta w \, dx = \int_\Omega f w \, dx. \tag{7.6.2}$$
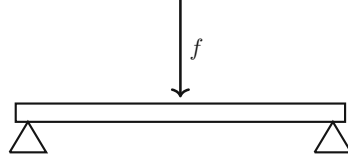
Figure 7.12.: Plate with external force f.

The construction of H^2-conforming finite elements is a difficult task as they have to be globally C^1 instead of being "just" continuous over interfaces. Examples of such elements are the Argyris and Bell triangles or the Bogner–Fox–Schmit quadrilateral. The Hsieh–Clough–Tocher element falls in the category of so-called macro-elements, where one triangle is divided into three smaller ones. The famous Morley triangle [159] is a nonconforming finite element, where the normal derivative is used as degree of freedom at the edges.

In [182] a Helmholtz decomposition of (3.1.27) is used to split the fourth order equation (7.6.1) into three second order problems enabling the use of Sobolev spaces with simpler finite elements.

The HHJ method for fourth order Kirchhoff plates has been developed and first analyzed in [114, 116, 127]. Superconvergence results and postprocessing procedures were developed and analyzed until the early 90's by several authors [67, 66, 91, 10, 216] and 20 years later the method regained interest. An adaptive FEM algorithm based on a residual a posteriori error estimator has been developed in [120] and an equilibrate based a posteriori error estimator, where the best possible reliability constant is achieved, was proposed in [59]. The convergence of the V-cycle multigrid method for this method was proved in [79]. Recently, the Kirchhoff plate equation on curved domains and surfaces using the HHJ method has been analyzed in [19, 229].

The HHJ method overcomes the issue of C^1-conformity by introducing the moment tensor

$$\boldsymbol{\sigma} := \mathbb{C}_B \nabla^2 w \qquad (7.6.3)$$

as an additional tensor field leading to a mixed saddle point problem:

7.14 Problem. *Find* $(w, \boldsymbol{\sigma}) \in H_0^1(\Omega) \times H(\operatorname{div}\operatorname{div}, \Omega)$ *such that for all* $(\delta w, \delta \boldsymbol{\sigma}) \in H_0^1(\Omega) \times H(\operatorname{div}\operatorname{div}, \Omega)$

$$\int_\Omega \mathbb{C}_B^{-1}\boldsymbol{\sigma} : \delta\boldsymbol{\sigma}\, dx + \langle \nabla w, \operatorname{div}(\delta\boldsymbol{\sigma})\rangle_{H(\operatorname{curl})^* \times H(\operatorname{curl})} = 0, \qquad (7.6.4a)$$

$$\langle \nabla \delta w, \operatorname{div}(\boldsymbol{\sigma})\rangle_{H(\operatorname{curl})^* \times H(\operatorname{curl})} \qquad\qquad = -\int_\Omega f\delta w. \qquad (7.6.4b)$$

Note, that due to $\nabla H^1 \subset H(\operatorname{curl})$ the duality pairing is well-defined, compare (3.1.26a). With U_h and M_h as in (5.2.13) and (5.2.35) the discretized problem is given by:

7.15 Problem. *Find* $(w_h, \boldsymbol{\sigma}_h) \in U_{h,0}^{k+1} \times M_h^k$ *such that for all* $(\delta w_h, \delta \boldsymbol{\sigma}_h) \in U_{h,0}^{k+1} \times M_h^k$

$$\int_\Omega \mathbb{C}_B^{-1} \boldsymbol{\sigma}_h : \delta \boldsymbol{\sigma}_h \, dx + \langle \nabla w_h, \mathrm{div}(\delta \boldsymbol{\sigma}_h) \rangle_{\mathcal{T}_h} = 0, \tag{7.6.5a}$$

$$\langle \nabla \delta w_h, \mathrm{div}(\boldsymbol{\sigma}_h) \rangle_{\mathcal{T}_h} = -\int_\Omega f \delta w_h. \tag{7.6.5b}$$

The duality pairing is defined as in (5.4.4)

$$\langle \nabla w, \mathrm{div}(\boldsymbol{\sigma}) \rangle_{\mathcal{T}_h} = \sum_{T \in \mathcal{T}_h} \int_T \nabla w \cdot \mathrm{div}(\boldsymbol{\sigma}) \, dx - \int_{\partial T} (\nabla w)_t \cdot \boldsymbol{\sigma}_{nt} \, ds$$

$$= -\sum_{T \in \mathcal{T}_h} \int_T \nabla^2 w : \boldsymbol{\sigma} \, dx + \int_{\partial T} (\nabla w)_n \boldsymbol{\sigma}_{nn} \, ds = -\langle \nabla^2 w, \boldsymbol{\sigma} \rangle_{\mathcal{T}_h}.$$

We cite the following a priori estimates [91] and therein references (where a slightly different space in the continuous setting instead of $H(\mathrm{div\,div})$ is used). An extension to mixed boundary conditions has been done e.g., in [52] using mesh-dependent norms [25]. For regularity results of the plate problem we refer to [51].

7.16 Theorem. *Let* $(\boldsymbol{\sigma}, w)$ *be the solution of Problem 7.14,* $(\boldsymbol{\sigma}_h, w_h)$ *the solution of Problem 7.15 and* $\tilde{w} \in H^{k+2}(\Omega) \cap H_0^2(\Omega)$ *the solution of Problem 7.13. Then*

$$\|\boldsymbol{\sigma} - \boldsymbol{\sigma}_h\|_{L^2} + \|w - w_h\|_{H^1} \le ch^k \left(|\tilde{w}|_{H^{k+1}} + |\tilde{w}|_{H^{k+2}} \right) \tag{7.6.6}$$

and

$$\|w - w_h\|_{L^2} \le ch^{k+1} \left(|\tilde{w}|_{H^{k+1}} + |\tilde{w}|_{H^{k+2}} \right). \tag{7.6.7}$$

One can break the normal-normal continuity of the moment tensor $\boldsymbol{\sigma}$ and add an additional Lagrange multiplier living on the skeleton $\mathcal{E}_h$ of $\mathcal{T}_h$ to reinforce the continuity, compare the hybridized TDNNS Problem 5.13. This enables static condensation, eliminating the dofs of $\boldsymbol{\sigma}_h$ on element level, leading to a positive definite system involving only w_h and α_h. The added Lagrange multiplier α_h has the physical meaning of the normal derivative of w and in [91] a first convergence result for arbitrary polynomial order of $\|(\alpha_h)_n - \frac{\partial w}{\partial n}\| \to 0$ for $h \to 0$ has been proposed.

For the more regular $H(\mathrm{div\,div}, \Omega; L^2)$ space (3.1.28), where $\mathrm{div}(\mathrm{div}(\boldsymbol{\sigma}))$ is assumed to be in $L^2(\Omega)$, the saddle point Problems 7.14 and 7.15 are stable together with discontinuous displacement fields $w \in L^2(\Omega)$ [80, 81].

In [26] it was shown that, if a domain with smooth boundary gets approximated by a polygonal domain, the solutions do not necessarily converge towards the solution of the smooth domain. This so-called Babuška paradox shows that one cannot expect convergence if a lowest-order, i.e., an affine, discretization of the geometry is considered. In [19], however, it was shown that the HHJ method does not suffer from this behavior giving it a geometrically non-conforming sight.

7.6.2. TDNNS method for Reissner–Mindlin plates

When dividing the Reissner–Mindlin plate equation (7.3.34) by t^3 we obtain the following minimization problem in the vertical deflection w and rotational vector field β

$$\mathcal{W}_{RM}(w,\beta) = \frac{1}{2}\|\epsilon(\beta)\|^2_{\mathbb{C}_B} + \frac{\kappa G}{2t^2}\|\nabla w - \beta\|^2_{L^2} - \langle f, w\rangle_{H^{-1}\times H^1} \to \min!, \qquad (7.6.8)$$

where we used the notation $\|\epsilon(\beta)\|^2_{\mathbb{C}_B} := \int_\Omega (\mathbb{C}_B\epsilon(\beta)) : \epsilon(\beta)\, dx$.

The TDNNS method developed for linear elasticity and discussed in Sections 4.3 and 5.4 has already been successfully applied to Reissner–Mindlin plates [173]. The therein used moment tensor gets interpolated into the HHJ stress space. To avoid shear locking for small thickness parameters t, see Section 8.2, the rotations are assumed to be in the $H(\mathrm{curl})$ space rather than in $[H^1]^2$, $\beta \in H(\mathrm{curl}, \Omega)$. The gradient of a $H(\mathrm{curl})$ function, however, is not square-integrable and thus the linearized moment stress tensor $\boldsymbol{\sigma}$ is introduced leading to the problem:

7.17 Problem. *Find* $(w, \boldsymbol{\sigma}, \beta) \in H^1_0(\Omega) \times H(\mathrm{div\,div}, \Omega) \times H_0(\mathrm{curl}, \Omega)$ *such that for all* $(\delta w, \delta\boldsymbol{\sigma}, \delta\beta) \in H^1_0(\Omega) \times H(\mathrm{div\,div}, \Omega) \times H_0(\mathrm{curl}, \Omega)$

$$\int_\Omega \mathbb{C}_B^{-1}\boldsymbol{\sigma} : \delta\boldsymbol{\sigma}\, dx + \langle \beta, \mathrm{div}(\delta\boldsymbol{\sigma})\rangle_{H(\mathrm{curl})^* \times H(\mathrm{curl})} = 0, \qquad (7.6.9a)$$

$$\langle \delta\beta, \mathrm{div}(\boldsymbol{\sigma})\rangle_{H(\mathrm{curl})^* \times H(\mathrm{curl})} - \frac{\kappa G}{t^2}\int_\Omega (\nabla w - \beta)\cdot(\nabla\delta w - \delta\beta)\, dx = -\int_\Omega f\delta w. \qquad (7.6.9b)$$

With (5.2.13), (5.2.35), and (5.2.26) the discretized problem reads:

7.18 Problem. *Find* $(w_h, \boldsymbol{\sigma}_h, \beta_h) \in U^{k+1}_{h,0} \times M^k_h \times V^k_{h,0}$ *such that for all* $(\delta w_h, \delta\boldsymbol{\sigma}_h, \delta\beta_h) \in U^{k+1}_{h,0} \times M^k_h \times V^k_{h,0}$

$$\int_\Omega \mathbb{C}_B^{-1}\boldsymbol{\sigma}_h : \delta\boldsymbol{\sigma}_h\, dx + \langle \beta_h, \mathrm{div}(\delta\boldsymbol{\sigma}_h)\rangle_{\mathcal{T}_h} = 0, \qquad (7.6.10a)$$

$$\langle \delta\beta_h, \mathrm{div}(\boldsymbol{\sigma}_h)\rangle_{\mathcal{T}_h} - \frac{\kappa G}{t^2}\int_\Omega (\nabla w_h - \beta_h)\cdot(\nabla\delta w_h - \delta\beta_h)\, dx = -\int_\Omega f\delta w_h. \qquad (7.6.10b)$$

Note that the same duality pairings in (7.6.4) and (7.6.9) (respectively (7.6.5) and (7.6.10)) are used as $\nabla H^1 \subset H(\mathrm{curl})$. Due to the De'Rham complex this relation is inherited to the discrete counterparts.

Using the shear $\gamma = \nabla w - \beta$ instead of the rotation β as unknown, compare (7.3.32), Problem 7.17 changes to the equivalent form:

7.19 Problem. *Find* $(w, \boldsymbol{\sigma}, \gamma) \in H^1_0(\Omega) \times H(\mathrm{div\,div}, \Omega) \times H_0(\mathrm{curl}, \Omega)$ *such that for*

---

all $(\delta w, \delta \boldsymbol{\sigma}, \delta \gamma) \in H_0^1(\Omega) \times H(\operatorname{div} \operatorname{div}, \Omega) \times H_0(\operatorname{curl}, \Omega)$

$$\int_\Omega \mathbb{C}_B^{-1} \boldsymbol{\sigma} : \delta \boldsymbol{\sigma} \, dx + \langle \nabla w - \gamma, \operatorname{div}(\delta \boldsymbol{\sigma}) \rangle_{H(\operatorname{curl})^* \times H(\operatorname{curl})} = 0, \qquad (7.6.11\mathrm{a})$$

$$\langle \nabla \delta w - \delta \gamma, \operatorname{div}(\boldsymbol{\sigma}) \rangle_{H(\operatorname{curl})^* \times H(\operatorname{curl})} - \frac{\kappa G}{t^2} \int_\Omega \gamma \cdot \delta \gamma \, dx = -\int_\Omega f \delta w. \qquad (7.6.11\mathrm{b})$$

Here we can see the close relation to the HHJ formulation for the Kirchhoff–Love plate: We obtain that in the limit $t \to 0$ there holds $|\gamma| \to 0$ (or equivalently $|\nabla w - \beta| \to 0$) and thus, Problem 7.14 is (formally) recovered. In [173] the auxiliary variable $\tilde{\gamma} := \frac{\kappa G}{t^2}(\nabla w - \beta)$, which can be seen as a kind of normalized shear stress, is introduced as additional unknown and equation to prove convergence independently of the thickness parameter t, i.e., shear locking is circumvented, see also Section 8.2:

7.20 Theorem. *Let* $(w, \boldsymbol{\sigma}, \beta) \in H_0^1(\Omega) \times H(\operatorname{div} \operatorname{div}, \Omega) \times H_0(\operatorname{curl}, \Omega)$ *the exact solution of Problem 7.17 and* $(w_h, \boldsymbol{\sigma}_h, \beta_h)$ *the corresponding finite element solution. Then there holds the a priori estimate for* $1 \le m \le k$

$$\|w - w_h\|_{H^1} + \|\beta - \beta_h\|_{H(\operatorname{curl})} + \|\boldsymbol{\sigma} - \boldsymbol{\sigma}_h\|_{M_h} + t\|\tilde{\gamma} - \tilde{\gamma}_h\|_{L^2}$$
$$\le c h^m \left(\|\beta\|_{H^{m+1}} + \|\boldsymbol{\sigma}\|_{H^m} + t\|\tilde{\gamma}\|_{H^m} \right), \qquad (7.6.12)$$

with $c \ne c(t)$.

7.7. Hellan–Herrmann–Johnson stress space for nonlinear shells

In this section we propose an extension of the HHJ method from Kirchhoff–Love plates (7.6.5) to nonlinear shells. We show that linearization leads to the HHJ method for linear Koiter shells (7.3.40) and in the case of a flat plate the classical HHJ method is recovered. Further, we discuss the treatment of structures with kinks and branched shells which do not necessitate additional requirements and can be handled naturally due to the special jump term arising in the method. Then we extend the method to nonlinear Naghdi shells by introducing additional shearing variables in such a way that in the limit $t \to 0$ the HHJ method for nonlinear Koiter shells is regained and in the linear case a natural extension of the TDNNS method for Reissner–Mindlin plates (7.6.10) is achieved.

7.7.1. HHJ for nonlinear Koiter shells

The difficulty of constructing simple C^1-conforming Kirchhoff–Love shell elements led to the development of the well-known discrete Kirchhoff triangle and quadrilateral (DKT and DKQ) elements, where the Kirchhoff constraint, compare (H5) in Section 7.3.4, is enforced in a discrete way at the vertices [38] or along the edges. The (nonconforming) famous Morley triangle [159] consists of additional rotational degrees of freedoms at the edges besides displacement dofs at the vertices. In [41] (high-order) formulations of a family of DK shell elements of various shapes as triangles, quadrilaterals, pentagons, and hexahedra were proposed. A generalization of the Morley triangle to finite rotations has been developed in

[226]. The class of rotation-free (RF) elements eliminate the rotational degrees of freedom by using out-of-plane translation degrees of freedom (dofs). The so-called *basic shell triangle* (BST) and *basic shell nodal* (BSN) elements use a triangle as control domain, linked to its neighbored triangles, or a vertex patch, respectively [166]. An extension to quadrilaterals and finite rotations via an updated Lagrangian was given in [68] and an improvement of the element shape dependency forced by the control patches has been developed [105]. An alternative approach based on discontinuous Galerkin (DG) methods [99], where the continuity of derivatives is enforced weakly via stabilization terms on interior boundaries, has been extended to linear Koiter shells [111]. In [227] a penalty formulation is used to enforce the C^1-continuity in terms of penalizing the angle difference enabling also kinks and branched shell structures. In *Isogeometric Analysis* (IGA) [122] nonuniform rational B-splines (NURBS) are used as basis functions which are constructed to be smooth (at least C^1). This has been exploited to directly implement (nonlinear) Kirchhoff–Love formulations on shells [200], where kinks are treated by angle preservation over so-called patches [134]. A hierarchical family of isogeometric shell elements was presented in [98].

In this section we propose a method, compare also [164], for nonlinear Koiter shells based on the HHJ stress space for the moment tensor, circumventing the necessity of C^1-conforming elements. To this end the jump term, following the discussion and results of Section 7.4.2, plays a crucial role.

We start with shell energy (7.3.38), the notation $\nu \circ \phi = \frac{\mathrm{cof}(\boldsymbol{F}_{\overline{\tau}})\overline{\nu}}{\|\mathrm{cof}(\boldsymbol{F}_{\overline{\tau}})\|_F}$, and material law (7.3.15)

$$\mathcal{W}_{\mathrm{KL}}(u_h) = \int_{\overline{\mathcal{S}}} \left(\frac{t}{2}\|\boldsymbol{E}_{\overline{\tau}}\|_{\boldsymbol{M}}^2 + \frac{t^3}{24}\|\mathrm{sym}(\boldsymbol{F}_{\overline{\tau}}^{\top}\nabla_{\overline{\tau}}(\nu\circ\phi)) - \nabla_{\overline{\tau}}\overline{\nu}\|_{\boldsymbol{M}}^2 \right) ds. \qquad (7.7.1)$$

In the following we neglect for ease of presentation the subscript h for the finite element functions. For a possibly curved but not C^1 triangulation $\mathcal{T}_h$ of $\overline{\mathcal{S}}$ consisting of triangles and quadrilaterals we use, as discussed in Section 7.4.2, the distributional form of the difference of the shape operators (7.4.4), leading to the saddle point problem

$$\mathcal{L}(u, \boldsymbol{\sigma}) = \frac{t}{2}\|\boldsymbol{E}_{\overline{\tau}}\|_{\boldsymbol{M}}^2 - \frac{6}{t^3}\|\boldsymbol{\sigma}\|_{\boldsymbol{M}^{-1}}^2 + \langle \boldsymbol{F}_{\overline{\tau}}^{\top}\nabla_{\overline{\tau}}(\nu\circ\phi) - \nabla_{\overline{\tau}}\overline{\nu}, \boldsymbol{\sigma}\rangle_{\mathcal{T}_h} \qquad (7.7.2)$$

$$:= \frac{t}{2}\|\boldsymbol{E}_{\overline{\tau}}\|_{\boldsymbol{M}}^2 - \frac{6}{t^3}\|\boldsymbol{\sigma}\|_{\boldsymbol{M}^{-1}}^2 + \sum_{T\in\mathcal{T}_h}\int_T (\boldsymbol{F}_{\overline{\tau}}^{\top}\nabla_{\overline{\tau}}(\nu\circ\phi) - \nabla_{\overline{\tau}}\overline{\nu}) : \boldsymbol{\sigma}\, ds$$

$$+ \sum_{E\in\mathcal{E}_h}\int_E (\sphericalangle(\nu_L, \nu_R)\circ\phi - \sphericalangle(\overline{\nu}_L, \overline{\nu}_R))\, \boldsymbol{\sigma}_{\overline{\mu\mu}}\, d\lambda, \qquad (7.7.3)$$

compare Figure 7.6 for the normal vector ν_L and ν_R on neighbored elements.

The Lagrange parameter $\boldsymbol{\sigma}$ has the physical meaning of the moment tensor, which is the energetic conjugate of the difference of the curvatures of the deformed and initial configuration. Note that the thickness parameter t appears now also in the denominator and the inverse material tensor given by

$$\| \cdot \|_{\boldsymbol{M}^{-1}}^2 := \frac{1+\hat{\nu}}{\hat{E}}\int_{\mathcal{T}_h}(\mathrm{tr}(\cdot^2) - \frac{\hat{\nu}}{2\hat{\nu}+1}\mathrm{tr}(\cdot)^2)\, ds \qquad (7.7.4)$$

is used. In the smooth case the Lagrange functional is equivalent to the original minimization problem and thus consistent:

7.21 Theorem. *Assume that $\mathcal{T}_h$ is a globally smooth manifold, $\mathcal{T}_h \in C^1$, and $\boldsymbol{\sigma} \in [L^2(\mathcal{T}_h)]^{3\times 3}_{\mathrm{sym},\tau}$, $u \in [H^2(\mathcal{T}_h)]^3$. Then, solving the saddle point problem* (7.7.2) *is equivalent to minimizing the energy* (7.7.1).

Proof. We compute the variations of the Lagrange functional in (7.7.2), noting that for a smooth triangulation $\mathcal{T}_h$ the jump term vanishes,

$$\partial_{\boldsymbol{\sigma}}\mathcal{L}(u,\boldsymbol{\sigma})(\delta\boldsymbol{\sigma}) = \int_{\mathcal{T}_h} -\frac{12}{t^3}\boldsymbol{M}^{-1}\boldsymbol{\sigma}:\delta\boldsymbol{\sigma} + (\boldsymbol{F}_{\overline{\tau}}^{\top}\nabla_{\overline{\tau}}(\nu\circ\phi) - \nabla_{\overline{\tau}}\overline{\nu}):\delta\boldsymbol{\sigma}\,ds \overset{!}{=} 0, \quad (7.7.5a)$$

$$\partial_u\mathcal{L}(u,\boldsymbol{\sigma})(\delta u) = \partial_u(\frac{t}{2}\|\boldsymbol{E}_{\overline{\tau}}\|^2_{\boldsymbol{M}})(\delta u) + \int_{\mathcal{T}_h}\boldsymbol{\sigma}:\partial_u(\boldsymbol{F}_{\overline{\tau}}^{\top}\nabla_{\overline{\tau}}(\nu\circ\phi) - \nabla_{\overline{\tau}}\overline{\nu})(\delta u)\,ds \overset{!}{=} 0. \tag{7.7.5b}$$

Expressing $\boldsymbol{\sigma}$ from (7.7.5a)

$$\boldsymbol{\sigma} = \frac{t^3}{12}\boldsymbol{M}(\boldsymbol{F}_{\overline{\tau}}^{\top}\nabla_{\overline{\tau}}(\nu\circ\phi) - \nabla_{\overline{\tau}}\overline{\nu})$$

and inserting this into (7.7.5b) yields

$$0 = \partial_u(\frac{t}{2}\|\boldsymbol{E}_{\overline{\tau}}\|^2_{\boldsymbol{M}})(\delta u) + \int_{\mathcal{T}_h}\frac{t^3}{12}\boldsymbol{M}(\boldsymbol{F}_{\overline{\tau}}^{\top}\nabla_{\overline{\tau}}(\nu\circ\phi) - \nabla_{\overline{\tau}}\overline{\nu}):\partial_u(\boldsymbol{F}_{\overline{\tau}}^{\top}\nabla_{\overline{\tau}}(\nu\circ\phi) - \nabla_{\overline{\tau}}\overline{\nu})(\delta u)$$

$$= \partial_u(\frac{t}{2}\|\boldsymbol{E}_{\overline{\tau}}\|^2_{\boldsymbol{M}})(\delta u) + \partial_u(\frac{t^3}{24}\|\boldsymbol{F}_{\overline{\tau}}^{\top}\nabla_{\overline{\tau}}(\nu\circ\phi) - \nabla_{\overline{\tau}}\overline{\nu}\|^2_{\boldsymbol{M}})(\delta u) = \partial_u\mathcal{W}_{\mathrm{KL}}(u)(\delta u).$$

Thus, we conclude that (7.7.1) and (7.7.2) are equivalent. $\qquad\square$

We reduced the fourth order minimization problem (7.7.1) to a second order mixed saddle point problem. With some computations, we finally obtain the following Lagrange functional.

7.22 Problem. *Find $(u,\boldsymbol{\sigma}) \in [U_h^k]^3 \times M_h^{k-1}$ which solve the saddle point problem*

$$\mathcal{L}(u,\boldsymbol{\sigma}) = \frac{t}{2}\|\boldsymbol{E}_{\overline{\tau}}\|^2_{\boldsymbol{M}} - \frac{6}{t^3}\|\boldsymbol{\sigma}\|^2_{\boldsymbol{M}^{-1}} - \sum_{T\in\mathcal{T}_h}\int_T(\boldsymbol{\mathcal{H}}_{\nu\circ\phi} + (1 - \overline{\nu}\cdot\nu\circ\phi)\nabla_{\overline{\tau}}\overline{\nu}):\boldsymbol{\sigma}\,ds$$

$$+ \sum_{E\in\mathcal{E}_h}\int_E(\sphericalangle(\nu_L,\nu_R)\circ\phi - \sphericalangle(\overline{\nu}_L,\overline{\nu}_R))\boldsymbol{\sigma}_{\overline{\mu\mu}}\,d\lambda, \tag{7.7.6}$$

where $\boldsymbol{\mathcal{H}}_{\nu\circ\phi} := \sum_{i=1}^3(\nabla_{\overline{\tau}}^2 u_i)\nu_i\circ\phi$, cf. (7.3.40).

Proof. Equivalence of (7.7.6) and (7.7.2) follows by differentiating the identity $\boldsymbol{F}_{\overline{\tau}}^{\top}\nu\circ\phi = 0$ and some computations

$$\int_T\boldsymbol{\sigma}:\boldsymbol{F}_{\overline{\tau}}^{\top}\nabla_{\overline{\tau}}(\nu\circ\phi)\,ds = -\int_T\begin{pmatrix}\boldsymbol{H}_1:\boldsymbol{\sigma}\\\boldsymbol{H}_2:\boldsymbol{\sigma}\\\boldsymbol{H}_3:\boldsymbol{\sigma}\end{pmatrix}\cdot\nu\circ\phi\,ds,$$

where $\boldsymbol{H}_i := \nabla_{\overline{\tau}}^2 u_i + \nabla_{\overline{\tau}}((\boldsymbol{P}_{\overline{\tau}})_i)$, $(\boldsymbol{P}_{\overline{\tau}})_i$ denoting the i-th column of $\boldsymbol{P}_{\overline{\tau}}$. With $\boldsymbol{P}_{\overline{\tau}} = \boldsymbol{I} - \overline{\nu} \otimes \overline{\nu}$ we obtain

$$
\nu \circ \phi \cdot \begin{pmatrix} \boldsymbol{H}_1 : \boldsymbol{\sigma} \\ \boldsymbol{H}_2 : \boldsymbol{\sigma} \\ \boldsymbol{H}_3 : \boldsymbol{\sigma} \end{pmatrix} = \sum_{i=1}^{3} \nu_i \circ \phi \nabla_{\overline{\tau}}((\boldsymbol{P}_{\overline{\tau}})_i + \nabla_{\overline{\tau}} u_i) : \boldsymbol{\sigma} = -\sum_{i=1}^{3} \nu_i \circ \phi (\nabla_{\overline{\tau}}(\overline{\nu} \otimes \overline{\nu})_i - \nabla_{\overline{\tau}}^2 u_i) : \boldsymbol{\sigma}
$$

$$
= -\sum_{i=1}^{3} \nu_i \circ \phi ((\nabla_{\overline{\tau}} \overline{\nu}_i) \otimes \overline{\nu} + \overline{\nu}_i \nabla_{\overline{\tau}} \overline{\nu} - \nabla_{\overline{\tau}}^2 u_i) : \boldsymbol{\sigma}
$$

$$
= -((\nu \circ \phi \cdot \overline{\nu}) \nabla_{\overline{\tau}} \overline{\nu} - \sum_{i=1}^{3} \nu_i \circ \phi \nabla_{\overline{\tau}}^2 u_i) : \boldsymbol{\sigma} = -((\nu \circ \phi \cdot \overline{\nu}) \nabla_{\overline{\tau}} \overline{\nu} - \boldsymbol{\mathcal{H}}_{\nu \circ \phi}) : \boldsymbol{\sigma},
$$

where we used that $\nabla_{\overline{\tau}} \overline{\nu}_i \otimes \overline{\nu} : \boldsymbol{\sigma} \equiv 0$ as $\boldsymbol{\sigma}$ acts on the tangent bundle, see Remark 7.10. $\qquad \square$

7.23 Remark. *In case of a flat plane as initial configuration* (7.7.6) *simplifies to*

$$
\mathcal{L}(u, \boldsymbol{\sigma}) = \frac{t}{2} \|\boldsymbol{E}_{\overline{\tau}}\|_{\boldsymbol{M}}^2 - \frac{6}{t^3} \|\boldsymbol{\sigma}\|_{\boldsymbol{M}^{-1}}^2 - \sum_{T \in \mathcal{T}_h} \int_T \boldsymbol{\mathcal{H}}_{\nu \circ \phi} : \boldsymbol{\sigma} \, ds + \sum_{E \in \mathcal{E}_h} \int_E (\sphericalangle(\nu_L, \nu_R) \circ \phi) \boldsymbol{\sigma}_{\overline{\mu}\overline{\mu}} \, d\lambda,
$$

$$(7.7.7)$$

as $\overline{\nu} = const$ *and* $\sphericalangle(\overline{\nu}_L, \overline{\nu}_R) = 0$.

As mentioned before, the resulting system is a saddle point problem, which would lead to an indefinite matrix after assembling. To overcome this problem, we can use completely discontinuous elements for the moment tensor $\boldsymbol{\sigma}$ and introduce a hybridization variable $\alpha \in \Gamma_h^{k-1}$ ((5.2.73) mapped onto the surface) to reinforce the normal-normal continuity of $\boldsymbol{\sigma}$:

7.24 Problem. *Find* $(u, \boldsymbol{\sigma}, \alpha) \in [U_h^k]^3 \times M_h^{\mathrm{dc},k-1} \times \Gamma_h^{k-1}$ *for the saddle point problem*

$$
\mathcal{L}^h(u, \boldsymbol{\sigma}, \alpha) = \frac{t}{2} \|\boldsymbol{E}_{\overline{\tau}}\|_{\boldsymbol{M}}^2 - \frac{6}{t^3} \|\boldsymbol{\sigma}\|_{\boldsymbol{M}^{-1}}^2 - \sum_{T \in \mathcal{T}_h} \int_T (\boldsymbol{\mathcal{H}}_{\nu \circ \phi} + (1 - \overline{\nu} \cdot \nu \circ \phi) \nabla_{\overline{\tau}} \overline{\nu}) : \boldsymbol{\sigma} \, ds
$$

$$
+ \sum_{E \in \mathcal{E}_h} \int_E (\sphericalangle(\nu_L, \nu_R) \circ \phi - \sphericalangle(\overline{\nu}_L, \overline{\nu}_R)) \langle\!\langle \boldsymbol{\sigma}_{\overline{\mu}\overline{\mu}} \rangle\!\rangle \, d\lambda + \int_E \alpha_{\overline{\mu}} [\![\boldsymbol{\sigma}_{\overline{\mu}\overline{\mu}}]\!] \, d\lambda,
$$

$$(7.7.8)$$

with $\langle\!\langle \boldsymbol{\sigma}_{\overline{\mu}\overline{\mu}} \rangle\!\rangle := \frac{1}{2}(\boldsymbol{\sigma}_{\overline{\mu}_L \overline{\mu}_L} + \boldsymbol{\sigma}_{\overline{\mu}_R \overline{\mu}_R})$ *denoting the mean value of* $\boldsymbol{\sigma}_{\overline{\mu}\overline{\mu}}$.

Due to the hybridization variable α, we can use static condensation to eliminate the degrees of freedom of the moment tensor $\boldsymbol{\sigma}$ locally, which leads to a minimization problem (in u and α) again. The new unknown α has the physical meaning of the changed angle, the rotation, between elements.
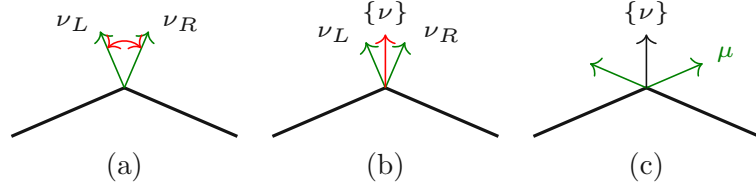
Figure 7.13.: Angle computation: (a) Angle between ν_L and ν_R. (b) Averaged normal vector with normal vector ν. (c) Averaged normal vector with element normal vector μ.

Computational aspects: For the computation of the jump term we use that

$$\sum_{E \in \mathcal{E}_h} \int_E \sphericalangle(\nu_L, \nu_R) \circ \phi - \sphericalangle(\overline{\nu}_L, \overline{\nu}_R) \, d\lambda = \sum_{T \in \mathcal{T}_h} \int_{\partial T} \sphericalangle(\{\nu\}, \nu) \circ \phi - \sphericalangle(\{\overline{\nu}\}, \overline{\nu}) \, d\lambda \qquad (7.7.9)$$

$$= \sum_{T \in \mathcal{T}_h} \int_{\partial T} \sphericalangle(\{\overline{\nu}\}, \overline{\mu}) - \sphericalangle(\{\nu\}, \mu) \circ \phi \, d\lambda, \qquad (7.7.10)$$

as $\sphericalangle(\{\nu\}, \nu) = \frac{\pi}{2} - \sphericalangle(\{\nu\}, \mu)$, see Figure 7.13. Here, $\{\nu\} := \frac{1}{\|\nu_L + \nu_R\|_2}(\nu_L + \nu_R)$ denotes the averaged normal vector. This algebraic equivalent reformulation is numerically much more stable as the derivative of $\arccos(x)$ has singularities at $x = \pm 1$ and we expect (for the triangulation of a smooth surface) $\{\nu\} \cdot \nu \approx 1$, whereas for $\{\nu\} \cdot \mu \approx 0$ the derivatives of arccos are well-defined.

To compute the deformed averaged normal vector $\{\nu\} \circ \phi$ on an edge, information of the two neighbored elements is needed at once, which would require e.g., Discontinuous Galerkin techniques leading to a denser stiffness matrix. Instead, one can use the information of the last (loadstep) solution $\{\nu\}^n$, cf. Figure 7.14. This, and also (7.7.9), is based on the following simple geometric observation:

7.25 Lemma. *Let $a, b \in \mathbb{R}^3$ with $\|a\|_2 = \|b\|_2 = 1$. Further let $c \in \mathbb{R}^3$ with $\|c\|_2 = 1$ and c "lies between" a and b, i.e., there exists $t \in (0, 1)$ such that $c \in \text{span}\{t\, a + (1-t)b\}$. Then there holds*

$$\arccos(a \cdot b) = \arccos(a \cdot c) + \arccos(c \cdot b). \qquad (7.7.11)$$

In three spatial dimensions, to fulfill the requirement of Lemma 7.25 that $\{\nu\}^n$ "lies between" μ_R and μ_L, i.e., to measure the correct angle, we have to project $\{\nu\}^n$ to the plane orthogonal to the tangent vector τ by using the orthogonal projection $\boldsymbol{P}_{\tau_E}^{\perp} = \boldsymbol{I} - \tau \circ \phi \otimes \tau \circ \phi$, and then re-normalize it leading to the (nonlinear) operator

$$P_{\tau_E}^{\perp}(\{\nu\}^n) := \frac{1}{\|\boldsymbol{P}_{\tau_E}^{\perp}\{\nu\}^n\|_2} \boldsymbol{P}_{\tau_E}^{\perp}\{\nu\}^n. \qquad (7.7.12)$$

Note that $\boldsymbol{P}_{\tau_E}^{\perp}$ is single-valued on each edge and $\tau \circ \phi$ itself depends on the unknown deformation. By using (7.7.12) we have to ensure that $\{\nu\}^n$ lies between the two element-normal vectors, see Figure 7.14. For smooth manifolds the angle between the element-normal vectors tends to 180 degree as $h \to 0$. Hence, this assumption is fulfilled, if the
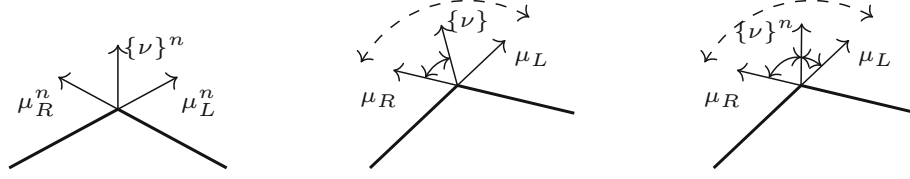
Figure 7.14.: Angle computation with the current averaged normal vector $\{\nu\}$ and the averaged normal vector $\{\nu\}^n$ from the previous step.

elements do not rotate more than half of their included angle during one loadstep, which is an acceptable and realistic assumption.

Therefore, for given averaged normal vector $\{\nu\}^n$ Problem 7.24 changes to

---

7.26 Problem. *Let $\{\nu\}^n$ be given. Find $(u, \boldsymbol{\sigma}, \alpha) \in [U_h^k]^3 \times M_h^{\mathrm{dc},k-1} \times \Gamma_h^{k-1}$ for the saddle point problem*

$$\mathcal{L}_{\{\nu\}^n}^h(u, \boldsymbol{\sigma}, \alpha) = \frac{t}{2}\|\boldsymbol{E}_{\overline{\tau}}\|_{\boldsymbol{M}}^2 - \frac{6}{t^3}\|\boldsymbol{\sigma}\|_{\boldsymbol{M}^{-1}}^2 + \sum_{T \in \mathcal{T}_h}\Big(-\int_T (\boldsymbol{\mathcal{H}}_{\nu\circ\phi} + (1 - \overline{\nu}\cdot\nu\circ\phi)\nabla_{\overline{\tau}}\overline{\nu}) : \boldsymbol{\sigma}\, ds$$

$$-\int_{\partial T}\Big(\sphericalangle(P_{\tau_E}^{\perp}(\{\nu\}^n), \mu)\circ\phi - \sphericalangle(\{\overline{\nu}\}, \overline{\mu}) - \alpha_{\overline{\mu}}\Big)\boldsymbol{\sigma}_{\overline{\mu\mu}}\, d\lambda\Big). \quad (7.7.13)$$

Note, that $P_{\tau_E}^{\perp}(\{\nu\}^n)\cdot\mu\circ\phi = \frac{\{\nu\}^n\cdot\mu\circ\phi}{\|P_{\tau_E}^{\perp}(\{\nu\}^n)\|_2}$ as $\tau\circ\phi \perp \mu\circ\phi$.

The averaged normal vector $\{\nu\}^n$ can easily be computed by the following (local) problem, where boundaries with clamped or symmetry boundary conditions have to be treated as Dirichlet boundary.

7.27 Problem. *For given (non-continuous) normal vector field ν^n find $\eta \in [F_h^k]^3$ such that $\eta = \overline{\nu}$ on Γ_D and for all $\delta\eta \in [F_{h,0}^k]^3$*

$$\sum_{T \in \mathcal{T}_h}\int_{\partial T}\eta\,\delta\eta\, d\lambda = \sum_{T \in \mathcal{T}_h}\int_{\partial T}\nu^n\,\delta\eta\, d\lambda. \quad (7.7.14)$$

Then define $\{\nu\}^n := \frac{\eta}{\|\eta\|_2}$.

Final algorithm: The final algorithm consists of the following steps:

1. For given displacement u^n and $\nu^n = \nu(u^n)$ compute the averaged normal vector $\{\nu\}^n$ via Problem 7.27.

2. Find $(u, \boldsymbol{\sigma}, \alpha)$ by solving Problem 7.26.

For the very first Newton iteration the projection operator $P_{\tau_E}^{\perp}$ has no effect on the residuum (the first variation) and the stiffness matrix simplifies immensely compared to the following Newton iterations as $\{\nu\}^n \perp \tau^n = \tau(u^n)$, see Appendix B. Therefore, if

the averaging procedure is performed after every Newton iteration the effort of computing variations of the jump terms is reduced at the cost of solving additional local problems. Another advantage is that the restriction of the rotation of elements in one loadstep is weakened to the restriction in one single Newton iteration step, which is practically always fulfilled.

The direct use of the angle yields that the solutions are independent of the number of loadsteps, as long as Newton's method converges, in contrast to a classical updated Lagrangian formulation. The usage of the angle directly follows from the distributional curvature in Section 7.4.2. The idea to use an angle for finite rotations has already been investigated in literature. E.g., in [226] the edge degrees of the Morley triangle [159] are interpreted as angles $\bar{\varphi}$ and an additional director d on the edges is introduced to measure the change of angle

$$\bar{\varphi} = \arctan\left(\frac{d \cdot \mu}{\nu \cdot d}\right),$$
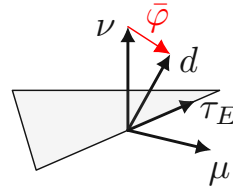
Figure 7.15.: Angle computation with director d.

which is updated in every Newton iteration, compare Figure 7.15. Therefore, instead of averaging, in [226] the director gets transformed by a rotational matrix $\boldsymbol{T}$ based on the well-known Euler–Rodrigues formula

$$\boldsymbol{T} = \boldsymbol{I} + \frac{\sin(\theta)}{\theta}\boldsymbol{\Theta} + \frac{1}{2}\left(\frac{\sin\left(\frac{\theta}{2}\right)}{\frac{\theta}{2}}\right)^2\boldsymbol{\Theta}^2, \qquad \boldsymbol{\Theta} = \mathrm{skw}(\boldsymbol{\theta}), \qquad \theta = \|\boldsymbol{\theta}\|_2, \qquad \boldsymbol{\theta} \in \mathbb{R}^3.$$

Angle linearization: If the initial configuration stems from a smooth surface we expect the angles of the form $\sphericalangle(\{\nu\}, \mu)$ tending to $\frac{\pi}{2}$ for the mesh-size $h \to 0$, i.e., $\{\nu\} \cdot \mu \to 0$. With Taylor we obtain

$$\sphericalangle(\{\nu\}, \mu) = \frac{\pi}{2} - \{\nu\} \cdot \mu + \mathcal{O}(|\{\nu\} \cdot \mu|^3) \quad \text{for } |\{\nu\} \cdot \mu| \to 0. \tag{7.7.15}$$

Therefore, a possible simplification of the jump term can be achieved by

$$\mathcal{L}^h_{\{\nu\}^n}(u, \boldsymbol{\sigma}, \alpha) = \frac{t}{2}\|\boldsymbol{E}_{\bar{\tau}}\|^2_{\boldsymbol{M}} - \frac{6}{t^3}\|\boldsymbol{\sigma}\|^2_{\boldsymbol{M}^{-1}} - \sum_{T \in \mathcal{T}_h}\int_T(\boldsymbol{\mathcal{H}}_{\nu \circ \phi} + (1 - \bar{\nu} \cdot \nu \circ \phi)\nabla_{\bar{\tau}}\bar{\nu}) : \boldsymbol{\sigma}\, ds$$

$$+ \int_{\partial T}(P^\perp_{\tau_E}(\{\nu\}^n) \cdot \mu \circ \phi - \{\bar{\nu}\} \cdot \bar{\mu} + \alpha_{\bar{\mu}})\boldsymbol{\sigma}_{\overline{\mu\mu}}\, d\lambda. \tag{7.7.16}$$

Note that if an approximation $\mathcal{T}_{h,k}$ of $\mathcal{S}$ with higher order $k > 1$ is given, the assumption $\{\nu\} \cdot \mu \approx 0$ is fulfilled already for quite coarse meshes (depending on the curvature of $\overline{\mathcal{S}}$ and $\mathcal{S}$). For large deformations or rotations, however, this simplification might lead to slightly different results depending on the number of loadsteps comparable to an updated Lagrangian scheme.
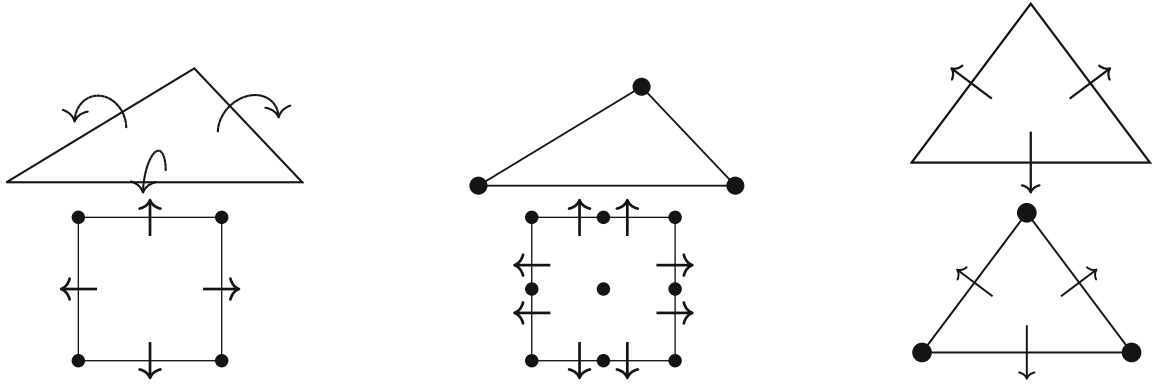
Figure 7.16.: Lowest order $H(\mathrm{div\,div})$, H^1 and normal facet elements for the moment, displacement and hybridization variable (top) and lowest order, quadratic hybridized quadrilateral shell element, and Morley triangle element (bottom).

Boundary conditions: As we use H^1-conforming elements for the displacement field u the Dirichlet boundary condition $u = u_D$ can be used to prescribe the displacement on the boundary. For $\boldsymbol{\sigma} \in H(\mathrm{div\,div})$ we can prescribe the normal-normal component $\boldsymbol{\sigma}_{\overline{\mu\mu}}$. For free boundaries homogeneous Dirichlet data, $\boldsymbol{\sigma}_{\overline{\mu\mu}} = 0$, are used in combination with the do-nothing Neumann condition for u. If homogeneous Dirichlet data for u and $\boldsymbol{\sigma}$ are prescribed we obtain a simply supported boundary. Do-nothing Neumann conditions for $\boldsymbol{\sigma}$ together with $u = 0$ are used for clamped boundaries. Symmetry boundary conditions can be achieved with the do-nothing Neumann condition for $\boldsymbol{\sigma}$ and the usual symmetry conditions for the displacement field u. By setting non-homogeneous Dirichlet data for $\boldsymbol{\sigma}$ one can prescribe a moment. In the case of a complete discontinuous moment tensor together with the hybridization variable α, the boundary conditions for $\boldsymbol{\sigma}$ have to be incorporated in terms of α, which has the physical meaning of the changed angle (rotation). Note that the essential and natural boundary conditions swap, i.e., the clamped boundary condition is now set directly as homogeneous Dirichlet data, $\alpha_{\overline{\mu}} = 0$, and the prescribed moment is handled naturally as a right-hand side.

Shell element: Combining the displacement $u \in [U_h^k(\mathcal{T}_h)]^3$, the moment tensor $\boldsymbol{\sigma} \in M_h^{k-1}(\mathcal{T}_h)$ and, eventually, the hybridization space $\Gamma_h^{k-1}(\mathcal{T}_h)$ leads to the final shell element. In Figure 7.16 the hybridized lowest order (linear) and quadratic element for quadrilaterals is depicted. Note, that the degrees of freedom of the hybridized lowest order triangle shell element are equivalent to the (nonlinear) Morley element [159, 226]. If we use the lowest order elements on triangles for (7.7.6) then the Hessian term vanishes, as only linear polynomials are used, i.e., the curvature is measured only via the change of angles. For quadrilaterals the Hessian is constant on each element in this case.

To solve (7.7.6) we have to assemble the corresponding stiffness matrix. As it is formulated in terms of a Lagrange functional, the first and second variations must be computed, which is a bit challenging due to the non-linearity but doable, see Appendix B. If, however, the finite element software supports energy based integrators, where the variations are calculated automatically, one can use directly the Lagrange functional (7.7.6). If this is

not the case we recommend using the averaging procedure after every Newton step as then the stiffness matrix simplifies immensely. Further, the resulting stiffness matrix is always symmetric as it stems from a Lagrange functional.

The hidden interface condition for the displacement u in strong form is not needed for the method itself. However, if one uses e.g., residual error estimators, the boundary conditions are crucial. For a computation one might start with the first variations from Appendix B and then integrate by parts. For Zienkiewicz–Zhu error estimators [242] the stresses given by

$$\boldsymbol{\sigma}_{\text{mem}} = t\boldsymbol{M}\boldsymbol{E}_{\overline{\tau}}, \qquad \boldsymbol{\sigma}_{\text{bend}} = \boldsymbol{\sigma}, \qquad \boldsymbol{\sigma}_{\text{shear}} = 0 \tag{7.7.17}$$

get interpolated into a finite element space with appropriate continuity and the difference is then used as error indicator.

7.7.2. Branched shells and kinks

Up to now we have described the method for smooth surfaces. As shown below, however, that in the case of kinks and branched shells the (hybridized version of the) proposed method can directly be applied without additional treatments.

For a recent and comprehensive review of junctions in shells we refer to [177] and references therein. As discussed in [49] the placement of the directors is challenging for shells with kinks and especially for branched shells as there is no unique way to determine one director, if more branches come together. A common strategy is to use e.g., additional drilling rotations [124]. In [102] rotation-free triangular shell elements were extended to finite rotations by computing the angles between the elements via the control domain. The angle preservation over kinks is achieved in [227] via a penalty formulation enabling also branched shell structures. In IGA kinks are treated by preserving the angles over patches [134].

For the proposed method the averaging procedure to obtain $\{\nu\}^n$ is valid independently of the amount of elements/branches attached to one single edge.

If we compute the variations of (7.7.6) with respect to $\boldsymbol{\sigma}$, we obtain in strong form that the angle from the initial configuration gets weakly preserved. Formally, if we choose test functions $\delta\boldsymbol{\sigma}$ which are zero everywhere except on the edge E we obtain

$$\int_E (\sphericalangle(\nu_L, \nu_R) \circ \phi - \sphericalangle(\overline{\nu}_L, \overline{\nu}_R))\delta\boldsymbol{\sigma}_{\mu\mu} \, d\lambda \overset{!}{=} 0 \qquad \text{for all } \delta\boldsymbol{\sigma} \tag{7.7.18}$$

and thus in strong form

$$\sphericalangle(\nu_L, \nu_R) \circ \phi = \sphericalangle(\overline{\nu}_L, \overline{\nu}_R). \tag{7.7.19}$$

Here, the normal-normal continuity of the moment tensor $\boldsymbol{\sigma}$ is the key ingredient, as it "does not see" the kink and the normal-normal component of the moment gets preserved, which is an important interface condition for kinks. As the junctions are treated by edge

integral terms, the method can handle triangulations consisting of triangles and quadrilaterals at the same time.

7.28 Remark. *Note, that in the case of junctions angle simplification* (7.7.15) *cannot be used any more, as* $|\{\nu\} \cdot \mu| \nrightarrow 0$ *for* $h \to 0$ *at the kinks.*

Furthermore, also branching shells, where one edge is shared by more than two elements can be simulated with the method without any extra treatment in a natural way. Now the condition for the moments is that the sum of all incoming moments is equal to the sum of all outflow moments, i.e., the law of moment conservation. Thus, it may happen that one branch is not affected by moments, compare Section 7.8.4 and Figure 7.28 for an example where all moments induced by a force applied at one branch get completely compensated by the branch where the structure is fixed. The third involved branch undergoes a pure rotation and thus no moments appear.

Normally, depending on the amount of involved branches, different number of e.g., Lagrange parameters have to be used. For the hybridized version, however, no further treatment is necessary. The non-hybridized version on the other hand does not work directly in the case of branched shells.

7.7.3. HHJ for linear Koiter shells

For the small deformation regime we show that Problem 7.24 (or equivalently Problem 7.26) reduces to the (hybridized) HHJ method of the linear Koiter shell formulation (7.3.40) under the assumption that the exact geometry $\overline{\mathcal{S}}$ is approximated sufficiently well.

7.29 Problem. *Find* $(u, \boldsymbol{\sigma}, \alpha) \in [U_h^k]^3 \times M_h^{\mathrm{dc},k-1} \times \Gamma_h^{k-1}$ *for the saddle point problem*

$$\mathcal{L}_{\mathrm{lin}}^h(u, \boldsymbol{\sigma}, \alpha) = \frac{t}{2}\|\mathrm{sym}(\nabla_{\overline{\tau}}^{\mathrm{cov}} u)\|_{\boldsymbol{M}}^2 - \frac{6}{t^3}\|\boldsymbol{\sigma}\|_{\boldsymbol{M}^{-1}}^2 + \sum_{T \in \mathcal{T}_h} \Big(-\int_T \boldsymbol{\mathcal{H}}_{\overline{\nu}} : \boldsymbol{\sigma}\, ds$$

$$+ \int_{\partial T} ((\nabla_{\overline{\tau}} u^\top \overline{\nu})_{\overline{\mu}} + \alpha_{\overline{\mu}}) \boldsymbol{\sigma}_{\overline{\mu}\overline{\mu}}\, d\lambda \Big). \tag{7.7.20}$$

7.30 Theorem. *Assume that* $\mathcal{T}_{h,k}$ *discretizes a smooth surface* $\overline{\mathcal{S}}$ *with* h *and* k *such that* $\{\overline{\nu}\} \cdot \overline{\mu}_L = \{\overline{\nu}\} \cdot \overline{\mu}_R = \mathcal{O}(\varepsilon)$. *Then there holds: Problem 7.29 is the linearization of Problem 7.24.*

Proof. As we started with the nonlinear Koiter shell (7.3.38) it suffices to show that the special jump terms of (7.7.8) reduces to the jump term of (7.7.20). For ease of presentation we neglect the ϕ dependency and write e.g., μ for $\mu \circ \phi$.

With (7.7.15) and setting $\{\nu\}^n = \{\overline{\nu}\}$ we start with the term $P_{\tau_E}^\perp(\{\overline{\nu}\}) \cdot \mu - \{\overline{\nu}\} \cdot \overline{\mu}$. Noting that $\{\overline{\nu}\} \cdot \overline{\tau} = 0$ yields

$$P_{\tau_E}^\perp(\{\overline{\nu}\}) \cdot \mu = \frac{\{\overline{\nu}\} \cdot \mu}{\|\{\overline{\nu}\} - (\{\overline{\nu}\} \cdot \tau)\tau\|_2}$$

and with (7.2.17b)

$$(\{\overline{\nu}\} \cdot \tau)\tau \approx (\{\overline{\nu}\} \cdot \overline{\tau})\overline{\tau} + (\{\overline{\nu}\} \cdot \overline{\tau})(\boldsymbol{I} - \overline{\tau} \otimes \overline{\tau})\nabla_{\overline{\tau}} u\overline{\tau} + (\{\overline{\nu}\} \cdot ((\boldsymbol{I} - \overline{\tau} \otimes \overline{\tau})\nabla_{\overline{\tau}} u\overline{\tau}))\overline{\tau}$$
$$= (\{\overline{\nu}\} \cdot ((\boldsymbol{I} - \overline{\tau} \otimes \overline{\tau})\nabla_{\overline{\tau}} u\overline{\tau}))\overline{\tau} = (\{\overline{\nu}\} \cdot (\nabla_{\overline{\tau}} u\overline{\tau}))\overline{\tau}.$$

We obtain, using (7.2.17c),

$$P_{\tau_E}^{\perp}(\{\overline{\nu}\}) \cdot \mu - \{\overline{\nu}\} \cdot \overline{\mu} \approx \{\overline{\nu}\} \cdot (\overline{\mu} - \nabla_{\overline{\tau}} u\overline{\mu}) + \{\overline{\nu}\} \cdot \overline{\mu}\langle\{\overline{\nu}\}, (\{\overline{\nu}\} \cdot (\nabla_{\overline{\tau}} u\overline{\tau}))\overline{\tau}\rangle - \{\overline{\nu}\} \cdot \overline{\mu}$$
$$= -\{\overline{\nu}\} \cdot \nabla_{\overline{\tau}} u\overline{\mu}.$$

With $\{\overline{\nu}\} = \overline{\nu} + \mathcal{O}(\varepsilon)$ the claim follows. $\qquad\square$

7.31 Remark. *As already mentioned, the geometry assumption is easily fulfilled if a high-order approximation $k > 1$ is used. Furthermore, if this condition is not fulfilled the geometry approximation error might dominate the linearization error.*

Theorem 7.30 generalizes the result in [164], where it has been shown that the linearization in the case of a flat plate leads to the classical HHJ method for Kirchhoff–Love plates. Note that the geometry assumption is automatically fulfilled for a plate as initial configuration.

7.32 Corollary. *Let $\overline{\mathcal{S}}$ be a flat plate $\overline{\mathcal{S}} \subset \mathbb{R}^2$. Then the HHJ method for plates given by Problem 7.15 is the linearized bending term of Problem 7.24.*

Proof. Follows directly from Theorem 7.30 as $\{\overline{\nu}\} \cdot \overline{\mu} = 0$. $\qquad\square$

7.33 Remark. *In the linearized problem the hybridization variable α has the physical meaning of the linearized angle $\frac{\partial u}{\partial \mu}$. This dof is also used in the (nonconforming) Morley triangle. Thus the higher order (hybridized) HHJ method can be interpreted as an extension of the Morley element.*

7.34 Remark. *In [183] Problem 7.29 is discretized by using a Helmholtz decomposition of $H(\mathrm{div\,div})$ solving three second order problems involving standard Sobolev spaces instead.*
For an analysis of Problem 7.29 one may extend the results from [229] for the bending term and the membrane term involving standard Lagrangian elements. Due to the coupling with the fundamental forms, compare (7.3.42), a rigorous proof without additional assumption might, however, be extremely challenging.

7.7.4. HHJ for nonlinear Naghdi shells

To include also transverse shear effects the DK elements have been extended by using e.g., *Assumed Natural Strain* (ANS) or Discrete Shear methods [40, 39]. Another class based on a special interpolation are the discrete Kirchhoff–Mindlin triangle and quadrilateral (DKMT and DKMQ) elements [131], which have been combined with the optimal membrane triangular element OPT [101] as a facet shell element in nonlinear analysis [133]. Recently, the DKMQ elements have also been directly applied to shells [132, 228]. By

using a co-rotational approach [100] these elements can be extended to the large deformation regime. Methods based on incompatible (nonconforming) linear rotation fields are applicable also for finite deformations [148, 169, 69]. The so-called *mixed interpolation of tensorial components* (MITC) elements originally developed for plate elements [34, 35, 32] and extended to shell elements [36, 73] are widely used and several works and improvements have been published including extensions to finite deformations, e.g., [126].

In this section we add an additional shearing parameter $\gamma \in H(\mathrm{curl})$ and use a hierarchical approach to extend the nonlinear HHJ method from Koiter to Naghdi shells. We will see that in the linearized case the method reduces to the TDNNS method for Reissner–Mindlin plates extended to linear shells. The shearing parameter $\tilde{\gamma} \circ \phi$ is of dimension two and perpendicular to the deformed normal vector, i.e., lives in the deformed tangent space. This motivates to use the space $H(\mathrm{curl})$ mapped onto the surface and use the corresponding covariant transformation $\tilde{\gamma} \circ \phi = (\boldsymbol{F}_{\overline{\tau}}^{\dagger})^{\top} \gamma$.

We start as in Section 7.7.1 with the shell energy (7.3.23), where $\tilde{\nu} \circ \phi = \frac{\mathrm{cof}(\boldsymbol{F}_{\overline{\tau}})\overline{\nu} + (\boldsymbol{F}_{\overline{\tau}}^{\dagger})^{\top}\gamma}{\|\mathrm{cof}(\boldsymbol{F}_{\overline{\tau}})\overline{\nu} + (\boldsymbol{F}_{\overline{\tau}}^{\dagger})^{\top}\gamma\|_2}$ (compare also (7.3.22)), and material law (7.3.15)

$$\mathcal{W}_{\mathrm{RM}}(u_h, \gamma_h) = \int_{\overline{\mathcal{S}}} \frac{t}{2} \|\boldsymbol{E}_{\overline{\tau}}\|_{\boldsymbol{M}}^2 + \frac{t^3}{24} \|\mathrm{sym}(\boldsymbol{F}_{\overline{\tau}}^{\top} \nabla_{\overline{\tau}}(\tilde{\nu} \circ \phi)) - \nabla_{\overline{\tau}}\overline{\nu}\|_{\boldsymbol{M}}^2 + \frac{t\kappa G}{2} \|\boldsymbol{F}_{\overline{\tau}}^{\top} \tilde{\nu} \circ \phi\|_2^2 \, ds. \tag{7.7.21}$$

We again neglect the subscript h for the finite element functions in the following. The procedure for handling distributional forms of the difference of the shape operators (7.4.4) can be directly extended to the curvature difference induced by the director fields, leading to the saddle point problem

$$\mathcal{L}(u, \gamma, \boldsymbol{\sigma}) = \frac{t}{2} \|\boldsymbol{E}_{\overline{\tau}}\|_{\boldsymbol{M}}^2 - \frac{6}{t^3} \|\boldsymbol{\sigma}\|_{\boldsymbol{M}^{-1}}^2 + \sum_{T \in \mathcal{T}_h} \int_T (\boldsymbol{F}_{\overline{\tau}}^{\top} \nabla_{\overline{\tau}}(\nu \circ \phi) - \nabla_{\overline{\tau}}\overline{\nu}) : \boldsymbol{\sigma} \, ds$$

$$+ \frac{t\kappa G}{2} \|\boldsymbol{F}_{\overline{\tau}}^{\top} \tilde{\nu} \circ \phi\|_2^2 + \sum_{E \in \mathcal{E}_h} \int_E (\sphericalangle(\tilde{\nu}_L, \tilde{\nu}_R) \circ \phi - \sphericalangle(\overline{\nu}_L, \overline{\nu}_R)) \, \boldsymbol{\sigma}_{\overline{\mu}\overline{\mu}} \, d\lambda. \tag{7.7.22}$$

One may now proceed as in Section 7.7.1 yielding a method for nonlinear Naghdi shells. We, however, simplify the highly nonlinear expression of $\tilde{\nu} \circ \phi$ by assuming that the shearing parameter is small as discussed and applied in [167], $(\boldsymbol{F}_{\overline{\tau}}^{\dagger})^{\top}\gamma = \mathcal{O}(\varepsilon)$, yielding $\tilde{\nu} \approx \nu \circ \phi + (\boldsymbol{F}_{\overline{\tau}}^{\dagger})^{\top}\gamma$ with $\nu \circ \phi$ the deformed surface normal vector as in the previous sections. Then, the volume term $\int_T (\boldsymbol{F}_{\overline{\tau}}^{\top} \nabla_{\overline{\tau}}\tilde{\nu} \circ \phi - \nabla_{\overline{\tau}}\overline{\nu}) : \boldsymbol{\sigma} \, ds$ in (7.7.22) can be simplified analogously to (7.7.6)

$$\int_T \nabla_{\overline{\tau}}\tilde{\nu} \circ \phi : (\boldsymbol{F}_{\overline{\tau}}\boldsymbol{\sigma}) \, ds = \int_T (\boldsymbol{\mathcal{H}}_{\tilde{\nu}\circ\phi} - \tilde{\nu} \circ \phi \cdot \overline{\nu} \, \nabla_{\overline{\tau}}\overline{\nu}) : \boldsymbol{\sigma} - (\boldsymbol{F}_{\overline{\tau}}^{\dagger})^{\top}\gamma \cdot (\boldsymbol{F}_{\overline{\tau}} \, \mathrm{div}_{\overline{\tau}}(\boldsymbol{\sigma})) \, ds$$

$$+ \int_{\partial T} (\boldsymbol{F}_{\overline{\tau}}^{\dagger})^{\top}\gamma \cdot (\boldsymbol{F}_{\overline{\tau}}\boldsymbol{\sigma}\overline{\mu}) \, d\lambda$$

$$= \int_T (\boldsymbol{\mathcal{H}}_{\tilde{\nu}\circ\phi} - \tilde{\nu} \circ \phi \cdot \overline{\nu} \, \nabla_{\overline{\tau}}\overline{\nu}) : \boldsymbol{\sigma} - \gamma \cdot \mathrm{div}_{\overline{\tau}}(\boldsymbol{\sigma}) \, ds + \int_{\partial T} \gamma \cdot \boldsymbol{\sigma}_{\overline{\mu}} \, d\lambda.$$

The boundary term measuring the change of angle reduces to

$$\int_{\partial T} \left(\sphericalangle(\nu \circ \phi, \{\nu\}) - \gamma_{\overline{\mu}} - \sphericalangle(\overline{\nu}, \{\overline{\nu}\}) \right) \boldsymbol{\sigma}_{\overline{\mu\mu}} \, d\lambda$$

and also the shearing energy simplifies

$$\|\boldsymbol{F}_{\overline{\tau}} \tilde{\nu} \circ \phi\|_2^2 = \|\gamma\|_2^2. \tag{7.7.23}$$

Thus, the problem of nonlinear Naghdi shells reads with V_h^k as in (7.5.12)

7.35 Problem. *Find* $(u, \gamma, \boldsymbol{\sigma}) \in [U_h^k]^3 \times V_h^{k-1} \times M_h^{k-1}$ *which solve the saddle point problem, with* $\tilde{\nu} \circ \phi := \nu \circ \phi + (\boldsymbol{F}_{\overline{\tau}}^{\dagger})^{\top} \gamma$,

$$\mathcal{L}(u, \gamma, \boldsymbol{\sigma}) = \frac{t}{2} \|\boldsymbol{E}_{\overline{\tau}}\|_{\boldsymbol{M}}^2 + \sum_{T \in \mathcal{T}_h} \int_T \left(\boldsymbol{\mathcal{H}}_{\tilde{\nu}\circ\phi} + (1 - \tilde{\nu} \circ \phi \cdot \overline{\nu}) \nabla_{\overline{\tau}} \overline{\nu} \right) : \boldsymbol{\sigma} - \gamma \cdot \mathrm{div}_{\overline{\tau}}(\boldsymbol{\sigma}) \, ds$$

$$+ \frac{t\kappa G}{2} \|\gamma\|_2^2 + \int_{\partial T} \left(\sphericalangle(\nu, \{\nu\}) \circ \phi - \sphericalangle(\overline{\nu}, \{\overline{\nu}\}) \right) \boldsymbol{\sigma}_{\overline{\mu\mu}} + \gamma \cdot \boldsymbol{\sigma}_{\overline{\mu\tau}} \, d\lambda. \tag{7.7.24}$$

7.36 Remark. *Note that we can compute the Moore–Penrose pseudo-inverse via*

$$\boldsymbol{F}_{\overline{\tau}}^{\dagger} = \left(\boldsymbol{F}_{\overline{\tau}}^{\top} \boldsymbol{F}_{\overline{\tau}} + \boldsymbol{P}_{\overline{\tau}}^{\perp} \right)^{-1} \boldsymbol{F}_{\overline{\tau}}^{\top} \tag{7.7.25}$$

as we know that the kernel of $\boldsymbol{F}_{\overline{\tau}}$ *is spanned by* $\overline{\nu}$ *(see also the Tikhonov regularization).*

It is straight forward to rewrite the boundary part in terms of a projection of the averaged normal vector, as we have in this hierarchical approach an additive splitting of the Koiter formulation and the additional shearing parameter:

7.37 Problem. *Let* $\{\nu\}^n$ *be given and* $\tilde{\nu} \circ \phi := \nu \circ \phi + (\boldsymbol{F}_{\overline{\tau}}^{\dagger})^{\top} \gamma$. *Find* $(u, \boldsymbol{\sigma}, \gamma, \alpha) \in [U_h^k]^3 \times M_h^{\mathrm{dc},k-1} \times \times V_h^{k-1} \times \Gamma_h^{k-1}$ *for the saddle point problem*

$$\mathcal{L}_{\{\nu\}^n}^h(u, \boldsymbol{\sigma}, \gamma, \alpha) = \frac{t}{2} \|\boldsymbol{E}_{\overline{\tau}}\|_{\boldsymbol{M}}^2 - \frac{6}{t^3} \|\boldsymbol{\sigma}\|_{\boldsymbol{M}^{-1}}^2 + \frac{t\kappa G}{2} \|\gamma\|_2^2$$

$$+ \sum_{T \in \mathcal{T}_h} \int_T \left(\boldsymbol{\mathcal{H}}_{\tilde{\nu}\circ\phi} + (1 - \tilde{\nu} \circ \phi \cdot \overline{\nu}) \nabla_{\overline{\tau}} \overline{\nu} \right) : \boldsymbol{\sigma} - \gamma \cdot \mathrm{div}_{\overline{\tau}}(\boldsymbol{\sigma}) \, ds$$

$$- \int_{\partial T} \left(\sphericalangle(P_{\tau_E}^{\perp}(\{\nu\}^n), \mu) \circ \phi - \sphericalangle(\{\overline{\nu}\}, \overline{\mu}) - \alpha_{\overline{\mu}} \right) \boldsymbol{\sigma}_{\overline{\mu\mu}} + \gamma \cdot \boldsymbol{\sigma}_{\overline{\mu\tau}} \, d\lambda. \tag{7.7.26}$$

7.7.5. HHJ/TDNNS for linear Naghdi shells

With the small deformation assumption we directly have that $(\boldsymbol{F}_{\overline{\tau}}^{\dagger})^{\top} \gamma \approx \gamma = \mathcal{O}(\varepsilon)$. Therefore, the additive splitting $\tilde{\nu} \circ \phi = \nu \circ \phi + \gamma$ is automatically justified. The linear Naghdi shell problem (7.3.32) with the HHJ stress space reads:

7.38 Problem. *Find* $(u, \boldsymbol{\sigma}) \in [U_h^k]^3 \times V_h^{k-1} \times M_h^{k-1}$ *for the saddle point problem*

$$
\mathcal{L}_{\text{lin}}^h(u, \boldsymbol{\sigma}, \gamma) = \frac{t}{2}\|\text{sym}(\nabla_{\overline{\tau}}^{\text{cov}} u)\|_{\boldsymbol{M}}^2 + \frac{t\kappa G}{2}\|\gamma\|_2^2 - \frac{6}{t^3}\|\boldsymbol{\sigma}\|_{\boldsymbol{M}^{-1}}^2
$$
$$
+ \sum_{T \in \mathcal{T}_h} \Big(-\int_T (\boldsymbol{\mathcal{H}}_{\overline{\nu}} - \nabla_{\overline{\tau}}\gamma) : \boldsymbol{\sigma}\, ds + \int_{\partial T} ((\nabla_{\overline{\tau}} u^\top \overline{\nu})_{\overline{\mu}} + \gamma_{\overline{\mu}})\boldsymbol{\sigma}_{\overline{\mu\mu}}\, d\lambda \Big).
$$
$$
(7.7.27)
$$

Due to the hierarchical ansatz we immediately obtain that the proposed method for non-linear Naghdi shells degenerates to the linear Problem 7.38:

7.39 Corollary. *Assume that the requirements of Theorem 7.30 are fulfilled. Then Problem 7.38 is the linearization of Problem 7.35. In particular, if the initial configuration $\overline{\mathcal{S}}$ is a flat plate, then the TDNNS method for Reissner–Mindlin plates Problem 7.18 is recovered.*

Corollary 7.39 states that Problem 7.38 generalizes the TDNNS method for Reissner–Mindlin plates proposed in [173] to general linear Naghdi shells. Further, Problem 7.37 can be interpreted as a nonlinear extension of the TDNNS method to shells.

7.8. Numerical examples

We show some numerical examples to demonstrate the performance of the presented methods. First, we confirm numerically that in the linear regime the proposed methods for nonlinear Koiter and Naghdi shells converge to their linear versions, compare Theorem 7.30 and Corollary 7.39. Further, the convergence of the nonlinear Naghdi shell model to the Koiter shell is tested for decreasing thickness $t \to 0$. Then nonlinear benchmarks are discussed. We refer to [164], where the following results are partly taken from, for several further numerical examples. For quadratic displacements u immense membrane locking is observed. Therefore, we use special procedures discussed in detail in Chapter 8 to avoid this locking behavior. For cubic or higher order displacement fields strong locking effects are not observed for moderately fine grids.

7.8.1. Convergence behaviors

For the convergence studies we consider the twisted beam example [152]. Therein, a beam is twisted by 90 degrees and clamped on the left side, and a point load F in x- or z-direction is applied on the middle of the right boundary. The material and geometrical properties are $\hat{E} = 2.9 \times 10^7$, $\hat{\nu} = 0.22$, $L = 12$, $b = 1.1$, see Figure 7.17. We use cubic displacement fields on a 60×10 structured triangular grid with $t = 0.032$, $F = f\, P_x$ and decrease the force magnitude. As observed in Figure 7.18 the nonlinear methods converge to their linear counterparts with a quadratic convergence rate in the force magnitude. Next, we decrease the thickness t and scale the force appropriately with t^3 as the twisted beam example is in the so-called bending dominated regime (see Chapter 8). We observe a convergence of quadratic rate in the thickness, cf. Figure 7.19. This is expected as in terms of asymptotical
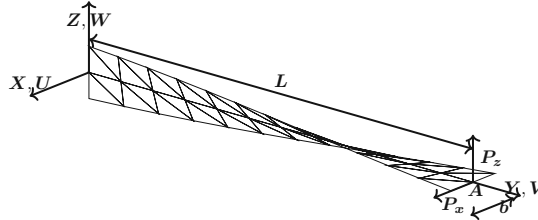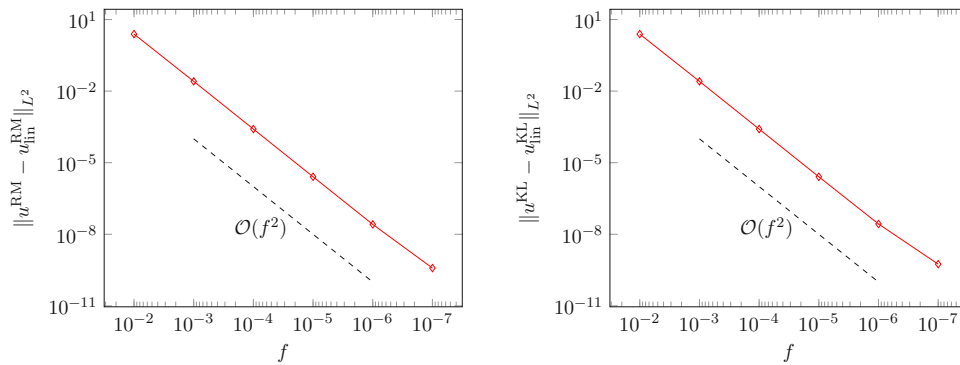
Figure 7.17.: Geometry of twisted beam with a 12×2 triangular grid.

Figure 7.18.: Convergence of nonlinear Naghdi and Koiter method towards linear counterparts for twisted beam with $k = 3$, 60×10 triangular grid, $t = 0.0032$, $F = f P_x$, and $f = 1 \times 10^{-2}, 1 \times 10^{-3}, \ldots, 1 \times 10^{-7}$.
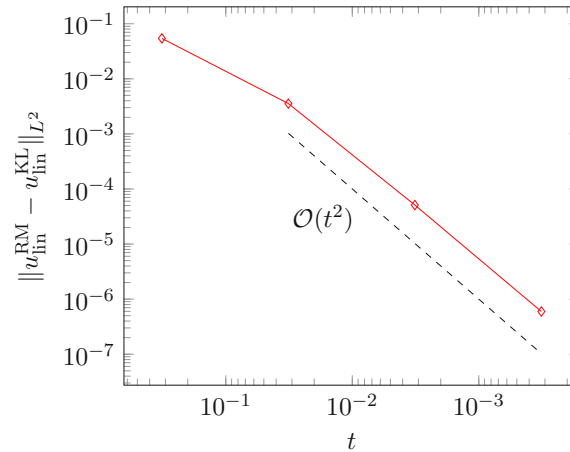
Figure 7.19.: Convergence of nonlinear Naghdi to Koiter method for twisted beam with $k = 3$, 60×10 triangular grid, $t = 0.32, 0.032, 0.0032, 0.00032$, and $F = 0.3125 \, t^3 \, P_x$.
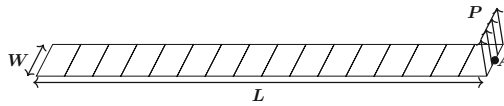
Figure 7.20.: Geometry of cantilever subjected to end shear force benchmark.

analysis the Kirchhoff–Love model can be seen as an low order approximation of the full 3D model, whereas the Reissner–Mindlin theory is of higher order. With these results we can also deduce that the linear Naghdi shell converges to the linear Koiter model for decreasing thickness. Examples with exact solutions to test for numerical convergence in the linear regime can be found e.g., in [225].

7.8.2. Cantilever subjected to end shear force

A cantilever fixed on the left side is subjected to an end shear force P on the right boundary. The material and geometrical properties are given by $\hat{E} = 1.2 \times 10^6$, $\hat{\nu} = 0$, $L = 10$, $W = 1$, $t = 0.1$ and $P_{\max} = 4$, see Figure 7.20. Different structured quadrilateral grids are used. The reference values are taken from [222]. In Figure 7.21 the initial and deformed configuration of the mesh is depicted. In Figure 7.22 and Table 7.1 the results for quadratic displacements can be found. In Figure 7.23 a convergence plot is given.
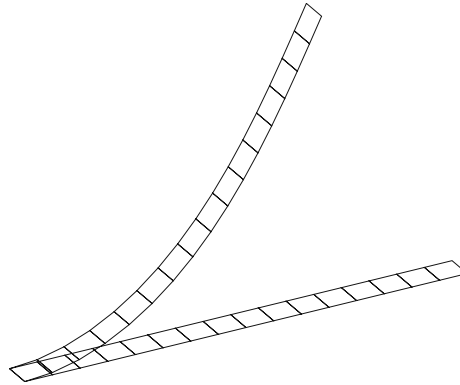
Figure 7.21.: Initial and final configuration of cantilever subjected to end shear force.

$P/P_{\max}$	-U	W	$P/P_{\max}$	-U	W
0.05	0.026	0.664	0.55	1.811	5.210
0.10	0.104	1.311	0.60	2.007	5.452
0.15	0.225	1.926	0.65	2.195	5.669
0.20	0.382	2.498	0.70	2.375	5.864
0.25	0.565	3.021	0.75	2.546	6.040
0.30	0.765	3.494	0.80	2.710	6.199
0.35	0.974	3.919	0.85	2.867	6.344
0.40	1.187	4.299	0.90	3.015	6.476
0.45	1.399	4.638	0.95	3.157	6.597
0.50	1.608	4.940	1.00	3.292	6.708

Table 7.1.: Horizontal and vertical deflection of cantilever subjected to end shear force with 16×1 grid.
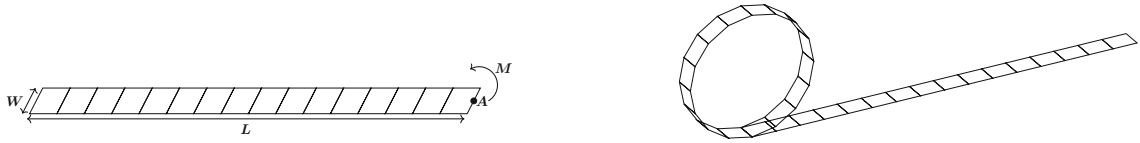
Figure 7.24.: Geometry, initial and final configuration of cantilever subjected to end moment benchmark.
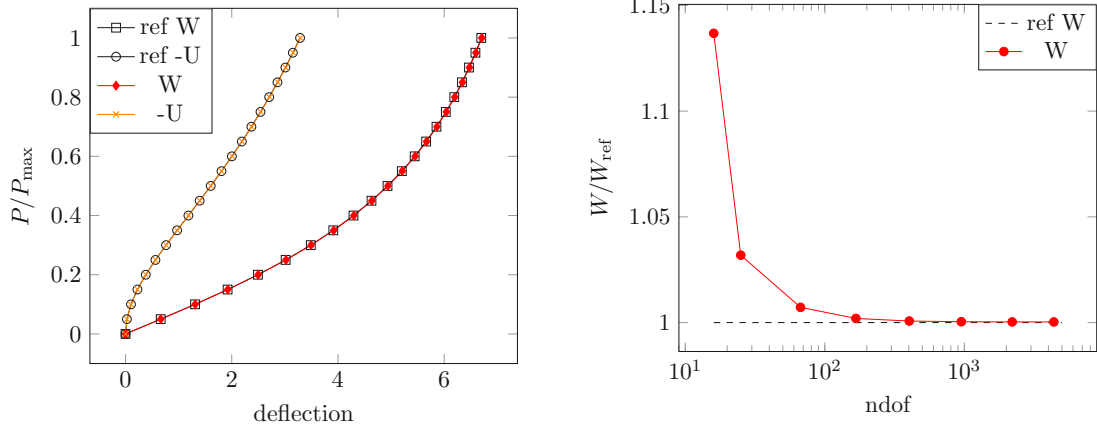
Figure 7.22.: Horizontal and vertical load-deflection for cantilever subjected to end shear force with 16×1 grid.
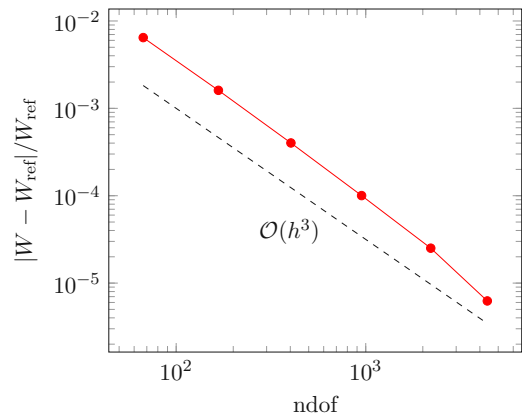

Figure 7.23.: Convergence with respect to number of degrees of freedom of vertical load-deflection for cantilever subjected to end shear force with 1×1, 2×1, 4×2, ..., 128×6 grid.

7.8.3. Cantilever subjected to end moment

A cantilever clamped on the left boundary is subjected to a moment force M on the right. On the other boundaries we use symmetry boundary conditions. The material and geometrical properties are given by $\hat{E} = 1.2 \times 10^6$, $\hat{\nu} = 0$, $L = 12$, $W = 1$, $t = 0.1$ and $M_{\max} = 50\pi/3$, see Figure 7.24.

The results for quadratic displacement fields u can be found in Figure 7.25 and Table 7.2. As an analytic solution is known for this benchmark a convergence plot is given in Figure 7.26, where we observe a cubic convergence rate for the deflection, which is the optimal one for quadratic displacements (compare the Aubin–Nitsche technique for the L^2-norm).

$M/M_{\max}$	U	U_{ex}	W	W_{ex}	$M/M_{\max}$	U	U_{ex}	W	W_{ex}
0.05	-0.196	-0.196	1.870	1.870	0.55	-13.075	-13.073	6.788	6.775
0.10	-0.773	-0.774	3.648	3.648	0.60	-13.875	-13.871	5.772	5.758
0.15	-1.698	-1.699	5.249	5.248	0.65	-14.384	-14.377	4.678	4.665
0.20	-2.916	-2.918	6.600	6.598	0.70	-14.603	-14.595	3.583	3.571
0.25	-4.357	-4.361	7.643	7.639	0.75	-14.556	-14.546	2.556	2.546
0.30	-5.942	-5.945	8.338	8.333	0.80	-14.280	-14.270	1.656	1.650
0.35	-7.582	-7.585	8.671	8.664	0.85	-13.826	-13.818	0.931	0.926
0.40	-9.191	-9.194	8.646	8.637	0.90	-13.254	-13.247	0.407	0.405
0.45	-10.687	-10.688	8.291	8.281	0.95	-12.625	-12.621	0.099	0.098
0.50	-12.000	-12.000	7.652	7.639	1.00	-12.000	-12.000	0.000	0.000

Table 7.2.: Horizontal and vertical deflection of cantilever subjected to end moment for 16×1 grid.
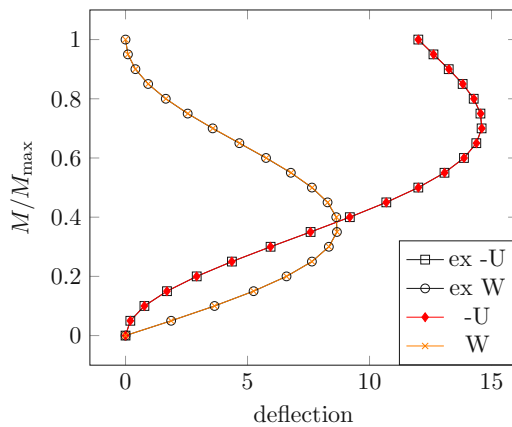
Figure 7.25.: Horizontal and vertical load-deflection for cantilever subjected to end moment with 16×1 grid.

Figure 7.26.: Relative error with respect to number of degrees of freedom of vertical load-deflection for cantilever subjected to end moment with 4×2, 8×3, ..., 128×6 grid for $M/M_{\max} = 0.25$.

7.8.4. T-section cantilever

For the last example we consider a T-section cantilever, where more than two elements share an edge. The material and geometrical properties are $\hat{E} = 6 \times 10^6$, $\hat{\nu} = 0$, $t = 0.1$, $L = 1$, $W = 1$, and $H = 1$. The structure is clamped on the bottom and a shear force $P_{\max} = 1 \times 10^4$ is applied on the left boundary, compare Figure 7.27. For this example we used a cubic displacement field.

Due to the shear force P a moment is induced on the left top branch, which goes over the kink to the bottom branch where the structure is fixed and the moments get compensated. No moments appear on the right top branch and thus, it only rotates and the curvature
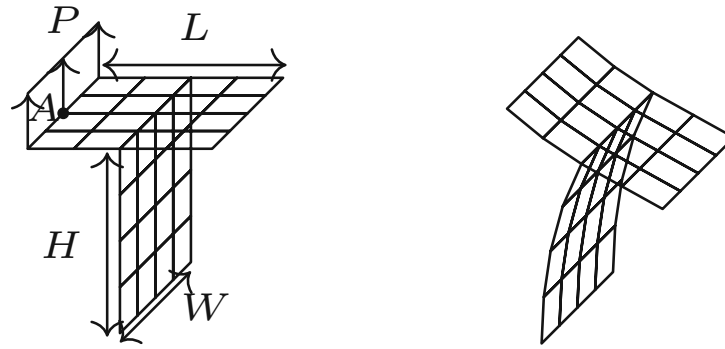
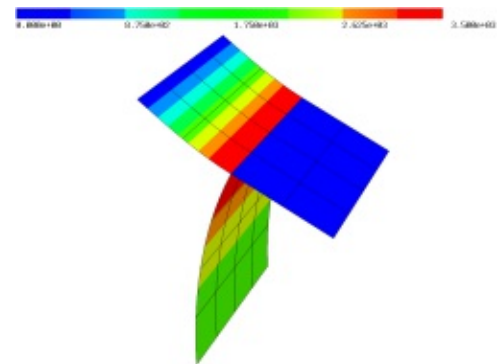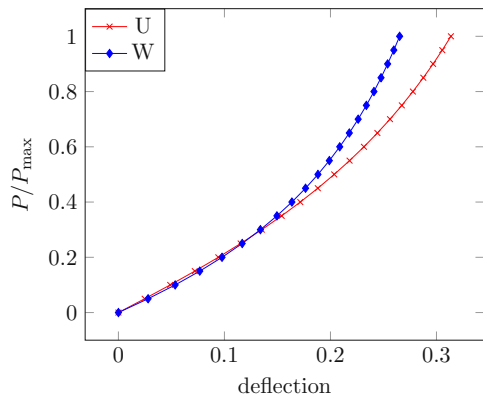Figure 7.27.: Geometry of T-section cantilever and deformed configuration.

Figure 7.28.: Horizontal and vertical deflection at point A for T-section cantilever with cubic displacement field (left) and norm of moment tensor $\boldsymbol{\sigma}$ (right).

is zero also after the deformation. The deflections of the point A and the moments are depicted in Figure 7.28.

8. (Membrane) Locking

As already mentioned in Chapter 7 the small thickness parameter t is involved in formulations of plates and shells. Due to the lack of finite element approximations fulfilling the implicitly given constraints of the underlying physical model so-called locking phenomena occur [28, 82]. As the thickness becomes small, $t \to 0$, the shell falls in one of the following different categories: the membrane dominated, bending dominated, or mixed case [71, 72]. This depends heavily on the type of geometry, prescribed boundary conditions and given external forces and is sometimes difficult to predict. For shells, shear and membrane locking can be observed in the bending dominated case. The former, induced by the Kirchhoff constraint, see (H5) in Section 7.3.4, in the limit case of vanishing thickness, has been extensively discussed and analyzed [8, 31, 65, 173]. In the case of plates rigorous mathematical proofs that shear locking is prevented have been stated and a variety of successfully shear locking free plate and shell elements have been proposed based on several approaches: an incomplete list of common formulations to alleviate shear locking includes reduced integration schemes in combination with hourglass stabilization techniques [241, 170], assumed strain methods [123, 151, 170, 119, 35, 125], and multifield formulations [224, 210], where the strains and/or stresses are additionally considered as independent fields.

In the case of membrane locking, also called inextensional locking, the curved elements are not able to exactly represent pure bending modes after discretization. As a result unintentional parasitic membrane modes are incited. Due to the different scaling of the energy terms with respect to the parameter t, the artificially induced membrane energy starts dominating the bending energy. This effect becomes critical for small thicknesses and the numerical solution tends to be trivially zero. Therefore, the general goal is to alleviate membrane locking by weakening the membrane energy carefully without introducing so-called spurious zero energy modes, which have zero membrane energy, spoiling the solution. Available methods rely on various techniques. Frequently, ideas from procedures to avoid shear locking are transferred and adapted. E.g., stabilized reduced integration schemes [217, 218] directly relax the membrane constraints by under-integration as each integration point can be interpreted as additional equation. Assumed strain methods [47, 135, 72] evaluate the strain components only at judiciously chosen points, which can be interpreted as an interpolation procedure. Mixed methods adding e.g., the membrane force tensor as additional unknown [11, 75, 76, 98] follow a similar idea. The therein involved spaces, however, are explicitly described instead of proposing only interpolation or tying points. These three different approaches lead sometimes to equivalent methods [153, 57, 48]. The discrete strain gap method [139], where the normal strains are modified to eliminating parasitic strain modes, are related to assumed strain approaches. It is motivated by the discrete shear gap (DSG) method used to circumvent shear locking [50]. In [45] these methods are taken as motivation to double the unknown variables to construct locking free methods independent of the discretization scheme. A framework based on discrete models

has been proposed in [181].

To prove in terms of rigorous numerical analysis that a method is robust with respect to membrane locking independently of the thickness and asymptotic regime is hard compared to shear locking. The main reason for this is that shear locking can be observed already for simple plate and beam problems, whereas for membrane locking to occur curved shells have to be considered, involving geometric quantities as the Weingarten tensor. Currently, results are mostly available only for special geometries or restrictive assumptions [11, 178, 106, 83, 75]. A numerical inf-sup test for mixed shell elements has been proposed in [37].

It is well known that by increasing the polynomial degree for the displacement field, i.e., p and hp-refinement strategies [178, 220, 110], the problem of membrane locking can be reduced. For low order triangular elements, however, only little impact of the reduced integration techniques has been observed [83].

We discuss the appearance of membrane and shear locking and take a closer look at the Timoshenko beam and Reissner–Mindlin plate, where the effect of shear locking and how it can be circumvented is discussed. Then we propose a novel method based on Regge elements, where the resulting Regge interpolation operator is used to construct membrane locking free methods for shells, staying stable in the membrane dominated regime, by interpolating the (nonlinear) Green strain tensor in the membrane energy term. Several of the above mentioned methods for successfully circumventing shear locking are constructed such that they reflect the intrinsic tangential continuity of the rotational fields. The presented approach preserves the problem-specific tangential-tangential continuity condition of the membrane strain and follow [165]. Further, a tying point procedure to accomplish the interpolation without explicitly constructing Regge elements is presented revealing a connection to MITC triangular shell elements. With the interpolation operator or tying point procedure at hand, the proposed method can easily be incorporated into existing shell elements and finite element code.

8.1. Locking phenomena

The terminology *locking* is used in the engineering literature as the finite element solutions like e.g., displacements are way too small compared to the true solution. The numerical solution is also called to be too stiff.

From a mathematical point of view locking occurs if the constant in Cea's Lemma

$$\|u - u_h\|_X \le c(t) \inf_{v_h \in X_h} \|u - v_h\|_X \tag{8.1.1}$$

depends on a small parameter t, i.e., the solutions do not converge uniformly in the parameter as $h \to 0$. Rigorous mathematical analysis of the locking effects can be found e.g., in [8, 202] and for plate models in [221].

For a huge class of problems the involved terms get scaled differently by the critical parameter as is the case for plates and shells, where the membrane and shear term are scaled linearly with t and the bending energy by t^3, compare (7.3.16). Other examples are nearly incompressible elastic materials, where the Lamé parameter λ tends to infinity, see Chapter 4, leading to so-called volume locking (also called Poisson locking). In the theory

of developable surfaces [212] membrane locking is challenging. Several further examples where locking appears can be found e.g., in [30].

We follow [58] and choose as a model problem $a_0 : X \times X \to \mathbb{R}$ to be a continuous but not coercive bilinear form on a Hilbert space X and $B : X \to L^2(\Omega)$ a continuous and linear operator. For a continuous right-hand side f we have the problem:

8.1 Problem. *For $0 < t \leq 1$, find $u \in X$ such that for all $\delta u \in X$*

$$a_0(u, \delta u) + \frac{1}{t^2} \int_\Omega Bu \, B\delta u \, dx = \int_\Omega f \, \delta u \, dx. \qquad (8.1.2)$$

We assume that $a(u, \delta u) := a_0(u, \delta u) + t^{-2} \int_\Omega Bu \, B\delta u \, dx$ is coercive and therefore, for every fixed t the Lax–Milgram Lemma 3.7 guarantees a unique solution u^t. The operator B has usually a non-trivial, infinite-dimensional kernel. Thus, if we formally let $t \to 0$, the term $t^{-2} \int_\Omega Bu \, B\delta u \, dx$ can be interpreted as penalty forcing that the limit solution u^0 lies in the kernel of B, $B u^0 = 0$. However, if we use a finite element space $X_h \subset X$ the kernel of the operator might be locked, $X_h \cap \ker B = \emptyset$. Due to the approximation property of X_h we only can hope that the finite element functions are "near" to the kernel, i.e., $Bu = 0 \Rightarrow \|B\mathcal{I}_h u\|_{L^2} \leq \mathcal{O}(h)$. If we can prove that for all $u_h \in X_h$ the inequality

$$\|B u_h\|_{L^2} \geq c(h)\|u_h\|_X \qquad (8.1.3)$$

holds then the coercivity constant of (8.1.2) is given by

$$a(u_h, u_h) \geq \underbrace{\left(\alpha_0 + \frac{c(h)^2}{t^2}\right)}_{=:\alpha} \|u_h\|_X^2. \qquad (8.1.4)$$

Thus, we can expect locking [27] and with the stability estimate

$$\|u_h\|_X \leq \frac{1}{\alpha}\|f\|_{X^*} \leq \frac{t^2}{c(h)^2}\|f\|_{X^*} \qquad (8.1.5)$$

we can see that small parameters t produce small solutions as long as $t \ll h$, explaining the terminology "locking". When the mesh size is in the same regime as the parameter t the so-called pre-asymptotic range, see e.g., Figures 8.1 and 8.4, is left and the expected convergence rates can be observed.

From (8.1.4) we can see that the coercivity constant becomes large when $t \to 0$. Therefore, the problem can be seen as ill-posed. We call a method *robust* if it converges uniformly in the small parameter t as $h \to 0$.

To overcome the locking behavior without using a fine grid such that $h \leq t$ several approaches have been proposed. E.g.,

1. Rewrite the problem as a mixed saddle point problem: If we define $\mu := \frac{1}{t^2} Bu$ Problem 8.1 changes to

8.2 Problem. *For $0 < t \le 1$, find $(u, \mu) \in X \times Q$ such that for all $(\delta u, \delta \mu) \in X \times Q$*

$$a_0(u, \delta u) \quad + \int_\Omega B \delta u \, \mu \, dx = \int_\Omega f \, \delta u \, dx, \qquad (8.1.6a)$$

$$\int_\Omega Bu \, \delta \mu \, dx - t^2 \int_\Omega \mu \, \delta \mu \, dx = 0. \qquad (8.1.6b)$$

Now, the limit $t \to 0$ is well-defined and if the (finite element) spaces fit the requirements of Theorem 3.9 (which is not always trivial to show) we have a robust method.

2. Using a reduction operator: One can try inserting an operator R relaxing the kernel constraint of operator B:

8.3 Problem. *For $0 < t \le 1$, find $u \in X$ such that for all $\delta u \in X$*

$$a_0(u, \delta u) + \frac{1}{t^2} \int_\Omega RBu \, RB\delta u \, dx = \int_\Omega f \, \delta u \, dx. \qquad (8.1.7)$$

3. Adding more finite element functions: In the enhanced assumed strain methods [210] additional (non-conforming) functions are added to the space X_h to increase the number of functions lying in the kernel of B. From a physical point of view these enhanced strains are chosen such that parasitic modes stemming from the compatible strains inducing locking are compensated or eliminated.

These methods are sometimes equivalent [153, 57, 48]. E.g., equation (8.1.6b) induces a projection operator

$$\mu = \frac{1}{t^2} \mathcal{I}_{L^2}(B \, u) =: \frac{1}{t^2} RBu, \qquad (8.1.8)$$

which leads in the discretized case to the minimization problem

$$\mathcal{W}(u_h) = \frac{1}{2} a_0(u_h, u_h) + \frac{1}{2t^2} \|RBu_h\|_{L^2}^2 - \int_\Omega f \, u_h \, dx \to \min!, \qquad (8.1.9)$$

cf. Problem 8.3, with $R : L^2(\Omega) \to Q_h$ a reduced integration operator, where Q_h is defined as in (5.2.14).

For shells, we can define the subspace

$$U_0 := \{(u, \beta) \mid E_{\text{mem}}(u, u) = 0 \wedge E_{\text{shear}}((u, \beta), (u, \beta)) = 0\}, \qquad (8.1.10)$$

where $E_{\text{mem}}(\cdot, \cdot)$ and $E_{\text{shear}}(\cdot, \cdot)$ are the bilinear forms induced by the membrane and shear energy $\frac{1}{2} \|\boldsymbol{E}_{\overline{\tau}}\|_{\boldsymbol{M}}^2$ and $\frac{\kappa G}{2} \|\boldsymbol{F}_{\overline{\tau}}^\top \boldsymbol{R}(u, \beta)\|_{\boldsymbol{M}}^2$, respectively, compare (7.3.23). For $(u, \beta) \in U_0$ the membrane and shear strains vanish. Depending heavily on the geometry of the shell and the prescribed boundary conditions there holds either $U_0 = \{0\}$ or $U_0 \ne \{0\}$. For

the first case, called inhibit pure bending or membrane dominated, $E_{\text{mem}}(\cdot, \cdot) + E_{\text{shear}}(\cdot, \cdot)$ induces a norm and it has been proven in [71, 72] that the right-hand side f has to be of order $\mathcal{O}(t)$ to obtain a well-defined limit solution for $t \to 0$. In terms of locking the second case $U_0 \neq \{0\}$ is more challenging and interesting. Here, pure bending is not inhibited and thus, the shell is called to be in a bending dominated regime. Then the appropriate scaling of the right-hand side is t^3, $f = t^3 \tilde{f}$ with $\tilde{f} = \mathcal{O}(1)$, and dividing all terms by t^3 yields

$$E_{\text{bend}}((u, \beta), (\delta u, \delta \beta)) + \frac{1}{t^2} \left(E_{\text{mem}}(u, \delta u) + E_{\text{shear}}((u, \beta), (\delta u, \delta \beta)) \right) = \int_\Omega \tilde{f} \, \delta u \, dx, \, \forall (\delta u, \delta \beta). \tag{8.1.11}$$

Thus we are in the setting of Problem 8.1. Therefore, in the limit $t \to 0$ the solution is forced to have zero membrane and shear energy. This leads to possible membrane and shear locking in the finite element setting. Note, that in case of plates and beams the membrane term decouples from the shear and bending energy and thus, only shear locking occurs, compare (7.3.33)–(7.3.34).

8.4 Remark. *To be precise, there is no one-to-one correspondence between inhibited pure bending/ non-inhibited pure bending, and membrane dominated/bending dominated. If the applied loading is non-admissible or does not activate corresponding modes, the shell is said to be in a mixed state [71, 33].*

8.5 Remark. *We emphasize that depending on the prescribed boundary conditions boundary layers may appear for Naghdi shells and Reissner–Mindlin plates, whose scaling depends on the thickness parameter t. Thus, to obtain optimal convergence rates these layers have to be resolved by e.g., nested meshes. This, however, is out of scope of this thesis and we refer to the literature, e.g., [17, 179].*

8.2. Timoshenko beam, Reissner–Mindlin plate, and shear locking

For the Kirchhoff plate (7.3.43) and Bernoulli beam (7.3.44) shear locking does not occur as the Kirchhoff–Love hypothesis (H5) forces that the directors stay always perpendicular to the mid-surface and therefore, the shearing energy is always zero. As shear locking is much better (mathematically) understood than membrane locking we discuss this phenomenon first. One reason is that shear locking appears already for simple beam or plate examples, whereas membrane locking occurs only in the case of curved elements. Another motivation to discuss shear locking in more detail first is the reduction operator used for MITC (plate) elements to circumvent shear locking as the proposed method for avoiding membrane locking is related to a MITC tying point procedure.

Timoshenko beam: The Timoshenko beam (7.3.36) is a one-dimensional example where shear locking appears if low-order elements are used. Let $\Omega = (0, l)$ be a beam with length l and thickness t. Neglecting material constants we obtain:

8.6 Problem (Timoshenko beam). *Minimize for* $(w, \beta) \in H^1(\Omega) \times [H^1(\Omega)]^2$

$$\mathcal{W}(w, \beta) = \frac{1}{2} \|\beta'\|^2_{L^2(\Omega)} + \frac{1}{2t^2} \|w' - \beta\|^2_{L^2(\Omega)} - \int_\Omega f\, w \, dx \to \min! \qquad (8.2.1)$$

The first term is the bending and the second one the shearing energy. The operator B in the context of Problem 8.1.2 is given by $B(w, \beta) := w' - \beta$.

One can show, see [58], that the kernel $\{(w, \beta) \in H^1(\Omega) \times [H^1(\Omega)]^2 \,|\, B(w, \beta) = 0\}$, which consists exactly of the deformations fulfilling the Kirchhoff–Love hypothesis (H5), is infinite-dimensional. Further, for piece-wise linear elements there holds $\|w'_h - \beta_h\|_{L^2} \geq ch\,(\|w_h\|_{H^1} + \|\beta_h\|_{H^1})$ and therefore locking occurs, compare (8.1.3). Introducing the shear term $\gamma := t^{-2}\,(w' - \beta) \in L^2(\Omega)$ and rewriting (8.2.1) as a saddle point problem leads to:

8.7 Problem. *Find* $(w, \beta, \gamma) \in H^1(\Omega) \times [H^1(\Omega)]^2 \times L^2(\Omega)$ *such that for all* $(\delta w, \delta\beta, \delta\gamma) \in H^1(\Omega) \times [H^1(\Omega)]^2 \times L^2(\Omega)$

$$\int_0^l \beta'\delta\beta' \, dx \quad\quad + \int_0^l (\delta w' - \delta\beta)\gamma \, dx = \int_0^l f\delta w \, dx, \qquad (8.2.2a)$$

$$\int_0^l (w' - \beta)\delta\gamma \, dx - t^2 \int_0^l \gamma\delta\gamma \, dx \quad\quad = 0. \qquad (8.2.2b)$$

On the kernel $B_0 = \{(w, \beta) \in H^1(\Omega) \times [H^1(\Omega)]^2 \,|\, w' = \beta\}$ there holds with Friedrichs's inequality (3.2.1)

$$\|\beta'\|^2_{L^2} = \frac{1}{2}|\beta|_{H^1} + \frac{1}{2}|\beta|_{H^1} \geq c\,(\|\beta\|_{H^1} + \|\beta\|_{L^2}) \geq c\,(\|\beta\|_{H^1} + \|w\|_{H^1}). \qquad (8.2.3)$$

Further, following [58], for given $\gamma \in L^2(\Omega)$ define $\rho(x) := x(l - x)$ and

$$A := \int_0^l \gamma(s) \, ds \Big/ \int_0^l \rho(s) \, ds, \quad w(x) := \int_0^x \gamma(s) \, ds - A \int_0^x \rho(s) \, ds, \quad \beta(x) := -A\rho(x).$$

Then, there holds $\|w'\|_{L^2} \leq c\|\gamma\|_{L^2}$, $\|\beta'\|_{L^2} \leq c\|\gamma\|_{L^2}$, and $w' - \beta = \gamma$. Thus, the LBB condition is fulfilled

$$\sup_{(w,\beta)\in H^1\times[H^1]^2} \frac{\int_0^l (w' - \beta)\gamma \, dx}{\|w\|_{H^1} + \|\beta\|_{H^1}} \geq \frac{\|\gamma\|^2_{L^2}}{\|w'\|_{L^2} + \|\beta'\|_{L^2}} \geq \frac{1}{2c}\|\gamma\|_{L^2}. \qquad (8.2.4)$$

Brezzi's Theorem 3.9 now gives the robust estimate

$$\|\beta\|_{H^1} + \|w\|_{H^1} + \frac{1}{t^2}\|w' - \beta\|_{L^2} \leq c\|f\|_{H^{-1}}, \quad c \neq c(t). \qquad (8.2.5)$$

Using lowest-order Lagrange elements for w and β and lowest-order discontinuous L^2-conforming elements for γ gives a stable discretization of Problem 8.7, which can easily be shown.

As mentioned before, the saddle point problem is often equivalent to applying a reduction operator R. Here, $R : L^2(\Omega) \to Q_h^0$ evaluates the shear term $w' - \beta$ on the mid-points of
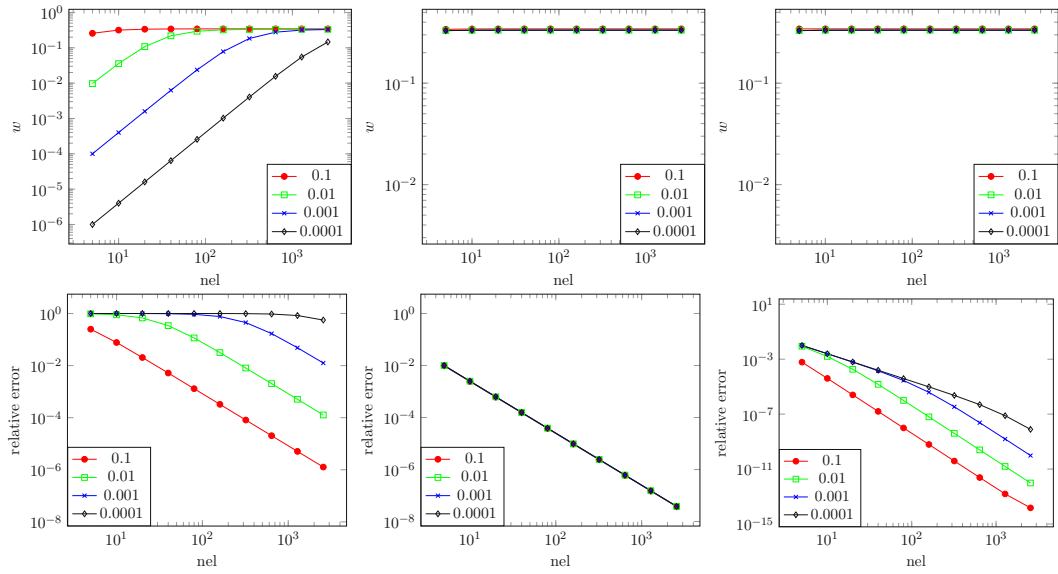
Figure 8.1.: Results for beam fixed on the left and shear force on the right boundary with $t = 0.1, \ldots, 0.0001$ and "do nothing" $k = 1$ (left), reduced integration $k = 1$ (middle), and "do nothing" $k = 2$ (right). Top: Vertical deflection w at right end point. Bottom: Relative error $|w - w_{\text{ex}}|/|w_{\text{ex}}|$ at right boundary.

the discretization intervals. For the enhanced assumed strain method the space for the displacements gets enriched with non-conforming elements of the form $\varepsilon_h \in E_h := \{\varepsilon \in L^2(\Omega) \,|\, \varepsilon \in \mathcal{P}^1(\mathcal{T}_h),\, \varepsilon(\xi_i) = 0, \xi_i$ the mid points of the intervals$\}$ and the shear term reads

$$\frac{1}{2t^2} \int_0^l (w_h' + \varepsilon_h - \beta_h)^2 \, dx,$$

leading to the same result as $\beta_h - \varepsilon_h = R\beta_h$.

If higher order elements are used, e.g., quadratic ones, the locking phenomenon vanishes too. For a numerical example we fix a beam $\Omega = [0, 1]$ on the left boundary and apply a shear force $f = t^3$ as external force on the right boundary. Note, that the cubic scaling with the thickness t is necessary as we are in the bending dominated case. Reference solutions are computed by using a fine grid in combination with a high polynomial order. As depicted in Figure 8.1 extreme locking occurs if lowest-order linear elements for displacements and rotations are used and the classical pre-asymptotic regimes can be observed. The reduced integration scheme leads to uniform convergence independently of the thickness t and also for quadratic elements the locking phenomenon is overcome.

Reissner–Mindlin plate: Next, we want to investigate the shear locking behavior for the Reissner–Mindlin plate (7.3.34) in two spatial dimensions $\Omega \subset \mathbb{R}^2$.

Following the same idea as for the Timoshenko beam we introduce the shear term $\gamma := t^{-2}(\nabla w - \beta)$ leading to the saddle point problem:

8.8 Problem. *Find $(w, \beta, \gamma) \in H_0^1(\Omega) \times [H_0^1(\Omega)]^2 \times [L^2(\Omega)]^2$ such that for all $(\delta w, \delta \beta, \delta \gamma) \in H_0^1(\Omega) \times [H_0^1(\Omega)]^2 \times [L^2(\Omega)]^2$*

$$\int_\Omega \boldsymbol{\epsilon}(\beta) : \boldsymbol{\epsilon}(\delta\beta)\, dx \quad + \int_\Omega (\nabla\delta w - \delta\beta) \cdot \gamma\, dx = \int_\Omega f\, \delta w\, dx \qquad (8.2.6a)$$

$$\int_\Omega (\nabla w - \beta) \cdot \delta\gamma\, dx - t^2 \int_\Omega \gamma \cdot \delta\gamma\, dx \qquad = 0. \qquad (8.2.6b)$$

One might try to prove stability using the L^2-norm of γ. This, however, turns out to fail. The reason is that in the limit case $t \to 0$ the L^2-regularity of γ is lost:

8.9 Problem (Kirchhoff plate via penalty). *Find $(w, \beta, \gamma) \in H_0^1(\Omega) \times [H_0^1(\Omega)]^2 \times H_0(\mathrm{curl}, \Omega)^*$ such that for all $(\delta w, \delta \beta, \delta \gamma) \in H_0^1(\Omega) \times [H_0^1(\Omega)]^2 \times H_0(\mathrm{curl}, \Omega)^*$*

$$\int_\Omega \boldsymbol{\epsilon}(\beta) : \boldsymbol{\epsilon}(\delta\beta)\, dx + \int_\Omega (\nabla\delta w - \delta\beta) \cdot \gamma\, dx = \int_\Omega f\, \delta w\, dx, \qquad (8.2.7a)$$

$$\int_\Omega (\nabla w - \beta) \cdot \delta\gamma\, dx \qquad\qquad = 0. \qquad (8.2.7b)$$

As the dual space of $H_0(\mathrm{curl})$ is $H^{-1}(\mathrm{div})$, see (3.1.16), stability of Problem 8.9 can be proven with the norms $\|w\|_{H^1}$, $\|\beta\|_{H^1}$, and $\|\gamma\|_{H^{-1}(\mathrm{div})}$, see e.g., [58]. With the help of the finite element dual space of $H_0(\mathrm{curl}, \Omega)^*$, see Section 5.3, we can also directly solve Problem 8.9 numerically.

Note that in Problem 8.9 γ is a Lagrange parameter, whereas in Problem 8.8 it has the physical meaning of a normalized shear stress. With the motivation of the limit problem, one can prove stability of Problem 8.8 with the norms $\|w\|_{H^1}$, $\|\beta\|_{H^1}$, and $\|\gamma\|_{H^{-1}(\mathrm{div})} + t\|\gamma\|_{L^2}$, where the constants are independent of the thickness parameter t. The proof is based on a Helmholtz-decomposition of $H^{-1}(\mathrm{div}) = \nabla H_0^1 \oplus \mathrm{Curl}(L^2/\mathbb{R})$ and $L^2 = \nabla H_0^1 \oplus \mathrm{Curl}(H^1/\mathbb{R})$ [64] leading to three decoupled problems, two Poisson and a Stokes problem with penalty. To be more precise, with $\gamma = \nabla r + \mathrm{Curl}(p)$ and $\delta\gamma = \nabla\delta r + \mathrm{Curl}(\delta p)$ one obtains

$$\int_\Omega \nabla r \cdot \nabla\delta w\, dx = \int_\Omega f\, \delta w\, dx \qquad\qquad \forall \delta w \in H_0^1(\Omega),$$

$$\int_\Omega \boldsymbol{\epsilon}(\beta) : \boldsymbol{\epsilon}(\delta\beta) - p\, \mathrm{curl}(\delta\beta)\, dx = \int_\Omega \nabla r \cdot \delta\beta\, dx \qquad\qquad \forall \delta\beta \in [H_0^1(\Omega)]^2,$$

$$-\int_\Omega \mathrm{curl}(\beta)\delta p + t^2 \mathrm{Curl}(p) \cdot \mathrm{Curl}(\delta p)\, dx = 0 \qquad\qquad \forall \delta p \in H^1(\Omega)/\mathbb{R},$$

$$\int_\Omega \nabla w \cdot \nabla\delta r\, dx = \int_\Omega \beta \cdot \nabla\delta r + t^2 f\, \delta r\, dx \quad \forall \delta r \in H_0^1(\Omega).$$

$$(8.2.8)$$

Using Stokes stable spaces we obtain that the problem is well-posed with constants independently of t. To mimic this procedure in the finite element setting a discrete Helmholtz-decomposition is needed. The following axioms of Brezzi, Bathe, and Fortin [62] are sufficient:

Let the spaces $U_h \subset H_0^1(\Omega)$, $V_h \subset [H_0^1(\Omega)]^2$, $Q_h \subset L^2(\Omega)/\mathbb{R}$, $\Gamma_h \subset H(\text{curl}, \Omega)$ and the reduction operator $R : V_h \to \Gamma_h$ have the following properties:

(P1) $\nabla U_h \subset \Gamma_h$,

(P2) $\text{curl}(\Gamma_h) \subset Q_h$,

(P3) The pairing (V_h, Q_h) fulfills the Stokes LBB condition: $\exists c \in \mathbb{R}^+$, $c \neq c(h)$, such that for all $p_h \in Q_h$

$$\sup_{\beta_h \in V_h} \frac{\int_\Omega \text{curl}(\beta_h)\, p_h\, dx}{\|\beta_h\|_{H^1}} \geq c \, \|p_h\|_{L^2},$$

(P4) With the L^2-projection onto Q_h there holds $\text{curl}(R\beta) = P_h\text{curl}(\beta)$ for all $\beta \in [H_0^1(\Omega)]^2$, i.e., the following diagram commutes

$$
\begin{array}{ccc}
[H_0^1(\Omega)]^2 & \xrightarrow{\ \text{curl}\ } & L^2(\Omega) \\
R \downarrow & & P_h \downarrow \\
\Gamma_h & \xrightarrow{\ \text{curl}\ } & Q_h
\end{array} \quad ,
$$

(P5) The sequence $U_h \xrightarrow{\ \nabla\ } \Gamma_h \xrightarrow{\ \text{curl}\ } Q_h$ is exact.

Then, with these finite element spaces and reduction operator R the discrete version of (8.2.8) is well-posed independent of t. The reduction operator R is defined via functionals as in Theorem 5.4, compare also (5.3.4).

Thus, it can be rigorously proven that a large class of MITC elements do not suffer from shear locking [65]:

8.10 Problem (MITC elements with reduction operator). *Let U_h, V_h, and a reduction operator R be given, such that there exists Q_h and Γ_h to fulfill axioms (P1)–(P5). Find $(w_h, \beta_h) \in U_h \times V_h$ such that for all $(\delta w_h, \delta \beta_h) \in U_h \times V_h$*

$$\int_\Omega \boldsymbol{\epsilon}(\beta_h) : \boldsymbol{\epsilon}(\delta\beta_h)\, dx + \frac{1}{t^2} \int_\Omega (\nabla w_h - R\beta_h) \cdot (\nabla \delta w_h - R\delta\beta_h)\, dx = \int_\Omega f\, \delta w_h\, dx. \quad (8.2.9)$$

Three families of stable combinations in the discrete setting were proposed in [65], see Figure 8.2.

In [21] the connection between MITC elements and the reduction operator R into the Nédélec space is discussed and an overview of other robust methods circumventing shear locking and stable elements is given and mathematically analyzed.

Nevertheless, we show how the tying point procedure and the reduction operator are related as we use this to reveal a relation between the proposed Regge interpolation and the MITC triangular shell procedure to alleviate membrane locking in Section 8.3.2. For
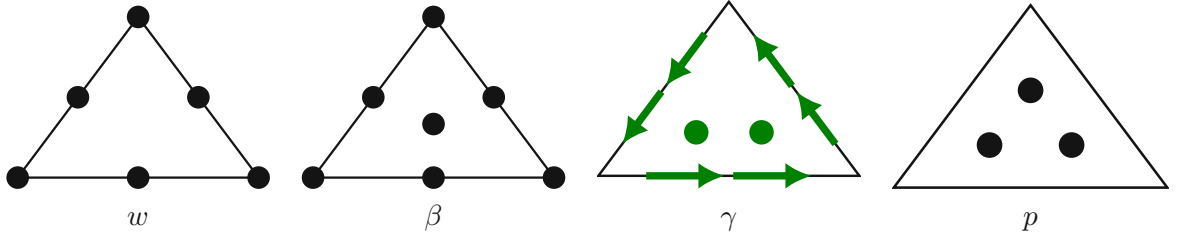
Figure 8.2.: MITC7 element: deflection w, rotation β, auxiliary shear γ, and auxiliary "pressure" p.
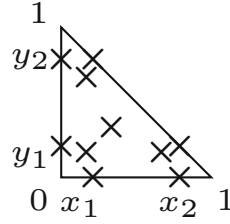

Figure 8.3.: Tying points for MITC7 element with $x_1 = y_1 = \frac{1}{2} - \frac{1}{2\sqrt{3}}$, $x_2 = y_2 = \frac{1}{2} + \frac{1}{2\sqrt{3}}$ and the inner points are placed at $M = (1/3, 1/3)$, $T_A = (1/6, 1/6)$, and $T_B = (2/3, 1/6)$, $T_C = (1/6, 2/3)$.

the MITC7 element [32] the reduction operator $\xi \mapsto R\xi$ is defined on each element T via the equations, compare also Section 5.3 and (5.3.4),

$$\int_E (\xi - R\xi)_t \, q_E \, ds = 0 \qquad \forall q_E \in \mathcal{P}^1(E), \tag{8.2.10a}$$

$$\int_T (\xi - R\xi) \cdot q_T \, dx = 0 \qquad \forall q_T \in [\mathcal{P}^0(T)]^2. \tag{8.2.10b}$$

On the other hand the shear strain $\tilde{\epsilon}$ is assumed to be of the following form

$$\begin{aligned}
\tilde{\epsilon}_x &= a_1 + b_1 x + c_1 y + y(dx + ey), \\
\tilde{\epsilon}_y &= a_2 + b_2 y + c_2 y - x(dx + ey),
\end{aligned} \tag{8.2.11}$$

and the coefficients are determined by forcing that the assumed strain $\tilde{\epsilon}$ coincides with the directly computed shear strain $\epsilon := \nabla w - \beta$ at so-called tying points depicted in Figure 8.3. More precisely, at the edges the conditions $\tilde{\epsilon}_x(x_1, 0) = \epsilon_x(x_1, 0)$, $\tilde{\epsilon}_x(x_2, 0) = \epsilon_x(x_2, 0)$, $\tilde{\epsilon}_y(0, y_1) = \epsilon_y(0, y_1)$, $\tilde{\epsilon}_y(0, y_2) = \epsilon_y(0, y_2)$, and, with $\epsilon_l := \frac{1}{\sqrt{2}} (\epsilon_y - \epsilon_x)$, $\tilde{\epsilon}_l(x_1, y_2) = \epsilon_l(x_1, y_2)$, $\tilde{\epsilon}_l(x_2, y_1) = \epsilon_l(x_2, y_1)$ are prescribed. This is equivalent to use a two-point Gauß quadrature formula for (8.2.10a). For the last two equations the mean value at the inner tying points is prescribed $\tilde{\epsilon}_x(M) = \frac{1}{3} (\epsilon_x(T_A) + \epsilon_x(T_B) + \epsilon_x(T_C))$ and analogically for $\tilde{\epsilon}_y$ and thus differ to (8.2.10b), as the constraint can be interpreted as under-integration of $\tilde{\epsilon}_x$ and $\tilde{\epsilon}_y$ by using the mid-point, whereas the given strain ϵ gets integrated with a rule exact for linear polynomials. Prescribing the mean values by using the mid-point rule for

both, however, is also possible.

As already discussed in Section 7.6.2 another possibility to obtain a robust finite element discretization is to directly use $H(\mathrm{curl})$-conforming Nédélec elements for the rotation field β instead of inserting a reduction operator R. To obtain a well-defined bending energy, the (symmetric part of the) gradient of $\beta \in H(\mathrm{curl})$ is not square-integrable, the moment tensor $\boldsymbol{\sigma}$ is additionally introduced [173]. The linked interpolation method [23] augments the deflection space by rotation degrees of freedom instead of reducing the rotation fields. As shown in [150] this method is connected to the MITC approach.

A different approach without using a Helmholtz decomposition is based on a splitting of the shearing term with $\frac{1}{t^2} = \frac{1}{h^2+t^2} + \frac{1}{t'^2}$, $t'^2 = t^2 \frac{h^2}{h^2+t^2}$, where h denotes the local mesh-size. The first part is added to the bending energy term yielding the saddle-point formulation:

8.11 Problem. *Find* $(w, \beta, \gamma) \in H_0^1(\Omega) \times [H_0^1(\Omega)]^2 \times [L^2(\Omega)]^2$ *such that for all* $(\delta w, \delta\beta, \delta\gamma) \in H_0^1(\Omega) \times [H_0^1(\Omega)]^2 \times [L^2(\Omega)]^2$

$$a_h\left((w,\beta),(\delta w, \delta\beta)\right) + \int_\Omega (\nabla\delta w - \delta\beta) \cdot \gamma \, dx = \int_\Omega f \cdot \delta w, \qquad (8.2.12a)$$

$$\int_\Omega (\nabla w - \beta) \cdot \delta\gamma \, dx - t'^2 \int_\Omega \gamma \cdot \delta\gamma \, dx \quad = 0. \qquad (8.2.12b)$$

As $a_h\left((w,\beta),(\delta w, \delta\beta)\right) := \int_\Omega \boldsymbol{\epsilon}(\beta_h) : \boldsymbol{\epsilon}(\delta\beta_h) + \frac{1}{h^2+t^2}(\nabla w - \beta)\cdot(\nabla\delta w - \delta\beta)\, dx$ is coercive on the whole space, stable finite elements can be constructed easier compared to the elements based on the discrete Helmholtz decomposition, see e.g., [74, 58, 21] for more details.

For a numerical example we consider a simply supported circle with radius $R = 5$ and parameters $\hat{E} = 10.92$, $\hat{\nu} = 0.3$, $\kappa = 5/6$, where a vertical force $f = 0.01$ is applied. Due to symmetry only one quarter of the circle is meshed and an exact solution is known [131]. As depicted in Figure 8.4 enormous locking occurs if no reduction operator for the rotations is considered, using linear elements for both unknowns. With the operator R, however, we obtain uniform convergence in the thickness parameter t. High-order methods may lead to less locking or even circumvent it [221].

8.12 Remark. *In contrast to the Timoshenko beam the term* $\nabla w - \beta$ *lies in the more regular space* $H(\mathrm{curl}, \Omega)$ *and not only in* $[L^2(\Omega)]^2$ *as* $\nabla H^1(\Omega) \subset H(\mathrm{curl}, \Omega)$. *Note, that in one dimension* $H(\mathrm{curl}, \Omega)$ *and* $L^2(\Omega)$ *coincide.*

8.3. Membrane locking and Regge interpolation

After the phenomenon of shear locking has been discussed and a variety of ideas to prevent locking have been presented we focus on curved shells, where membrane locking additionally appears in the bending dominated setting. In the following we consider Koiter shells, neglecting the shear energy and thus a priori circumventing shear locking, to focus on the
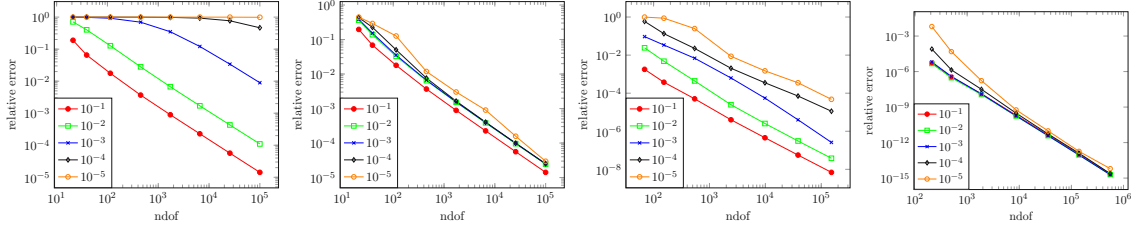
Figure 8.4.: Relative error $\|w - w_{\text{ex}}\|_{L^2}/\|w_{\text{ex}}\|_{L^2}$ for Reissner–Mindlin plate example with linear elements, reduction operator with linear elements, quadratic elements, and fourth order elements with thicknesses $t = 10^{-1}, \ldots, 10^{-5}$.

problem of membrane locking. We, however, emphasize that the results can directly be applied to Naghdi shells including shearing. If we assume the Kirchhoff–Love hypothesis (H5) the shell energy (7.3.38) can be written in operator notation

$$t\, E_{\text{mem}}(u) + t^3 E_{\text{bend}}(u) = f(u). \tag{8.3.1}$$

Dividing through t^3 and defining $\tilde{f} := t^{-3} f$ the rescaled right-hand side yields

$$\frac{1}{t^2} E_{\text{mem}}(u) + E_{\text{bend}}(u) = \tilde{f}(u). \tag{8.3.2}$$

If the new right-hand side is independent of the thickness parameter, i.e., $\tilde{f} = \mathcal{O}(1)$, we are in the bending dominated case (non-inhibited pure bending) and membrane locking may occur. For $t \to 0$ the first term of (8.3.2) can be interpreted as a penalty forcing $E_{\text{mem}}(u) = 0$ in the limit.

In the following we assume that the shell surface $\overline{\mathcal{S}}$ gets discretized by a triangulation $\mathcal{T}_h$ consisting of (curved) triangles and we follow [165].

8.3.1. Usage of Regge interpolant

Let the discrete displacements $u_h \in [U_h^k]^3$ live in the Lagrangian nodal finite element space (7.5.9). For the proposed method we insert the Regge interpolation operator into the Regge elements of polynomial order $k - 1$ into the membrane energy term

$$\int_{\overline{\mathcal{S}}} \|\mathcal{I}_{h,k-1}^{\mathcal{R}} \boldsymbol{E}_{\overline{\tau}}\|_{\boldsymbol{M}}^2 \, dx, \tag{8.3.3}$$

where $\mathcal{I}_{h,k}^{\mathcal{R}}$ is defined as (compare (5.2.40) and Section 5.3)

$$\int_E (\boldsymbol{E}_{\overline{\tau}} - \mathcal{I}_{h,k}^{\mathcal{R}} \boldsymbol{E}_{\overline{\tau}})_{\overline{\tau}_E \overline{\tau}_E}\, q \, d\lambda = 0 \qquad \text{for all } q \in \mathcal{P}^k(E), \tag{8.3.4a}$$

$$\int_T (\boldsymbol{E}_{\overline{\tau}} - \mathcal{I}_{h,k}^{\mathcal{R}} \boldsymbol{E}_{\overline{\tau}}) : \boldsymbol{Q} \, ds = 0 \qquad \text{for all } \boldsymbol{Q} \in [\mathcal{P}^{k-1}(T)]_{\text{sym}}^{2 \times 2}. \tag{8.3.4b}$$

Note that for the linearized membrane strain tensor $\boldsymbol{E}_{\overline{\tau}} \approx \frac{1}{2}(\boldsymbol{P}_{\overline{\tau}} \nabla_{\overline{\tau}} u_h + \nabla_{\overline{\tau}} u_h^\top \boldsymbol{P}_{\overline{\tau}})$ membrane locking also occurs and the Regge interpolation operator is used in the same way as in the nonlinear case.

Due to the tangential-continuity of the discrete Jacobian $\nabla_{\overline{\tau}} u_h$, the Green strain tensor $\boldsymbol{E}_{\overline{\tau}}$ is tangential-tangential continuous. Thus, it is mathematically equivalent to apply the projection operator $\mathcal{I}_{h,k-1}^{\mathcal{R}}$ only element-wise, which makes the method competitive – no additional global system has to be solved. Furthermore, beneficial properties of systems to be symmetric or positive definite are preserved. Therefore, only a small problem has to be solved on each element and the intrinsic tangential-tangential continuity is preserved comparable to the reduction operator for the Reissner–Mindlin plate from the previous section, where the tangential continuity is inherited.

We emphasize that (8.3.3) is equivalent to a three-field Hu–Washizu formulation by introducing the discontinuous Regge interpolant $\boldsymbol{E}_h \in \mathcal{R}_h^{k-1,\mathrm{dc}}$ and corresponding local shape functionals $\boldsymbol{Q}_h \in [\mathcal{R}_h^{k-1,\mathrm{dc}}]^*$ as additional unknowns. Note that the functionals (5.2.40) span the discrete topological dual space $[\mathcal{R}_h^{k-1,\mathrm{dc}}]^*$. The corresponding Lagrangian for the membrane energy reads

$$\mathcal{L}(u_h, \boldsymbol{E}_h, \boldsymbol{Q}_h) := \int_{\overline{\mathcal{S}}} \|\boldsymbol{E}_h\|_{\boldsymbol{M}}^2 \, dx + \langle \boldsymbol{E}_h - \boldsymbol{E}_{\overline{\tau}}, \boldsymbol{Q}_h \rangle_{\mathcal{T}_h}, \tag{8.3.5}$$

where, according to (5.2.40) and (8.3.4), with $\boldsymbol{Q}_h = (\boldsymbol{Q}_T, Q_E)$

$$\langle \boldsymbol{E}_h - \boldsymbol{E}_{\overline{\tau}}, \boldsymbol{Q}_h \rangle_{\mathcal{T}_h} := \sum_{T \in \mathcal{T}_h} \Big(\int_T (\boldsymbol{E}_h - \boldsymbol{E}_{\overline{\tau}}) : \boldsymbol{Q}_T \, dx + \sum_{E \in \partial T} \int_E (\boldsymbol{E}_h - \boldsymbol{E}_{\overline{\tau}})_{\overline{\tau}_E \overline{\tau}_E} : Q_E \, ds \Big) \tag{8.3.6}$$

and thus, $\boldsymbol{E}_h = \mathcal{I}_{h,k-1}^{\mathcal{R}} \boldsymbol{E}_{\overline{\tau}}$. In numerical experiments we observed that less Newton iterations are needed with (8.3.5) compared to the direct interpolation procedure (8.3.3), if the full nonlinear Green strain tensor $\boldsymbol{E}_{\overline{\tau}}$ is used.

8.3.2. Relation to MITC shell elements

Similar to shear locking where the MITC element procedure is highly related to the projection operator into $H(\mathrm{curl})$-conforming elements, called reduction operator R in Section 8.2, there exists a connection between the Regge interpolation (8.3.4) and the procedure used for triangular MITC shell elements.

Namely, the interpolation of a given strain $\boldsymbol{E}$ into the Regge finite element space $\mathcal{R}_h$ can also be performed by using tying points inspired by MITC elements. This entails the advantage to perform the interpolation without the need of implementing Regge shape functions and can thus be easily incorporated to existing finite element code. In the following we describe the procedure for second order displacements, corresponding first order Regge elements, and an isoparametrically quadratic curved geometry on the reference triangle. Further, we will consider the full nonlinear Green strain tensor $\boldsymbol{E} := \frac{1}{2}(\boldsymbol{P}_{\overline{\tau}} \nabla_{\overline{\tau}} u_h + \nabla_{\overline{\tau}} u_h^\top \boldsymbol{P}_{\overline{\tau}} + \nabla_{\overline{\tau}} u_h^\top \nabla_{\overline{\tau}} u_h)$ and stress that the procedure for the linearized strain tensor $\boldsymbol{E}^{\mathrm{lin}} = \frac{1}{2}(\boldsymbol{P}_{\overline{\tau}} \nabla_{\overline{\tau}} u_h + \nabla_{\overline{\tau}} u_h^\top \boldsymbol{P}_{\overline{\tau}})$ follows exactly the same lines. We begin by transforming the volume term of (8.3.6) to the reference triangle. Let Φ be the corresponding mapping, $T = \Phi(\hat{T})$, and $\boldsymbol{G} := \nabla_{\hat{x}} \Phi \in \mathbb{R}^{3 \times 2}$ the Jacobi matrix. Computing the first variation in direction $\delta \boldsymbol{Q}_h = (\delta \boldsymbol{Q}_T, \delta Q_E) \in [\mathcal{R}_h^{1,\mathrm{dc}}]^*$ yields with (5.3.7) for the surface (cf.
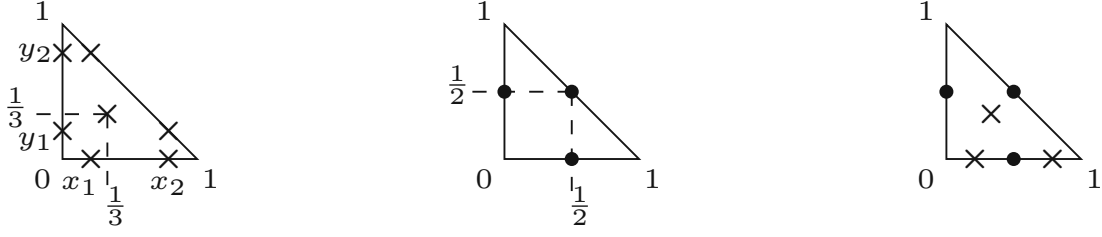
Figure 8.5.: Tying points ($\times$, left), integration points (circles, middle), and points for $\hat{\boldsymbol{E}}_{xx}$ component (right) with $x_1 = y_1 = \frac{1}{2} - \frac{1}{2\sqrt{3}}$ and $x_2 = y_2 = \frac{1}{2} + \frac{1}{2\sqrt{3}}$.

Remark 7.11), and $(\boldsymbol{P}_{\overline{\tau}} \nabla_{\overline{\tau}} u_h) \circ \Phi = \boldsymbol{P}_{\overline{\tau}} \circ \Phi \, \nabla_{\hat{x}} \hat{u}_h \boldsymbol{G}^{\dagger}$ that for all $\delta \hat{\boldsymbol{Q}}_T \in [\mathcal{P}^0(\hat{T})]^{2\times 2}_{\text{sym}}$

$$ 0 \overset{!}{=} \int_T (\boldsymbol{E}_h - \boldsymbol{E}) : \delta \boldsymbol{Q}_T \, dx = \int_{\hat{T}} (\hat{\boldsymbol{E}}_h - \boldsymbol{G}^{\top} \nabla_{\hat{x}} \hat{u}_h - \frac{1}{2} \nabla_{\hat{x}} \hat{u}_h^{\top} \nabla_{\hat{x}} \hat{u}_h) : \delta \hat{\boldsymbol{Q}}_T \, d\hat{x}. \qquad (8.3.7) $$

Here, we exploited the symmetry of $\delta \hat{\boldsymbol{Q}}_T$ and that $\boldsymbol{P}_{\overline{\tau}} \circ \Phi \, \boldsymbol{G} = \boldsymbol{G}$. For the boundary term we obtain analogously that for all $\delta \hat{Q}_E \in \mathcal{P}^1(\hat{E})$

$$ 0 \overset{!}{=} \int_E (\boldsymbol{E}_h - \boldsymbol{E})_{\overline{\tau}_E \overline{\tau}_E} \, \delta Q_E \, ds = \int_{\hat{E}} (\hat{\boldsymbol{E}}_h - \boldsymbol{G}^{\top} \nabla_{\hat{x}} \hat{u}_h - \frac{1}{2} \nabla_{\hat{x}} \hat{u}_h^{\top} \nabla_{\hat{x}} \hat{u}_h)_{\hat{t}\hat{t}} \, \delta \hat{Q}_E \, d\hat{s}. \qquad (8.3.8) $$

Note, that no inverse matrix appears after transformation to the reference element due to the dual transformations (5.3.7) entailing the advantage of using integration rules of reduced order to perform exact integration, if necessary.

In Figure 8.5 the used tying and integration points are depicted. The tangential-tangential components of the interpolated strain are assumed to be linear, e.g., $(\hat{\boldsymbol{E}}_h)_{xx} = a + bx + cy$. For integrating (8.3.8) we use the two point Gauß quadrature formula on the edges. Note that the integration is even exact as for second order displacements and for a quadratic curved geometry $\hat{\boldsymbol{E}} := \text{sym}(\boldsymbol{G}^{\top} \nabla_{\hat{x}} \hat{u}_h + \frac{1}{2} \nabla_{\hat{x}} \hat{u}_h^{\top} \nabla_{\hat{x}} \hat{u}_h)$ is quadratic and $\delta \hat{Q}_E$ is linear. The resulting two equations can be reformulated by prescribing the conditions $(\hat{\boldsymbol{E}}_h)_{xx}(x_1, 0) = \hat{\boldsymbol{E}}_{xx}(x_1, 0)$ and $(\hat{\boldsymbol{E}}_h)_{xx}(x_2, 0) = \hat{\boldsymbol{E}}_{xx}(x_2, 0)$ at the corresponding tying points. This ansatz is equivalent to the procedure used for the MITC6 triangular shell elements in [135] for edges.

The last equation for completely determining $(\hat{\boldsymbol{E}}_h)_{xx}$ is given by integrating (8.3.7) with a quadrature rule being exact for quadratic polynomials on the triangle: $(\hat{\boldsymbol{E}}_h)_{xx}(0.5, 0) + (\hat{\boldsymbol{E}}_h)_{xx}(0, 0.5) + (\hat{\boldsymbol{E}}_h)_{xx}(0.5, 0.5) = \hat{\boldsymbol{E}}_{xx}(0.5, 0) + \hat{\boldsymbol{E}}_{xx}(0, 0.5) + \hat{\boldsymbol{E}}_{xx}(0.5, 0.5)$. This corresponds to the tying point condition $(\hat{\boldsymbol{E}}_h)_{xx}(1/3, 1/3) = \frac{1}{3}(\hat{\boldsymbol{E}}_{xx}(0.5, 0) + \boldsymbol{E}_{xx}(0, 0.5) + \hat{\boldsymbol{E}}_{xx}(0.5, 0.5))$ as $(\hat{\boldsymbol{E}}_h)_{xx}$ is linear and $\delta \boldsymbol{Q}_T$ constant. We tried also the straight forward and simpler condition $(\hat{\boldsymbol{E}}_h)_{xx}(1/3, 1/3) = \hat{\boldsymbol{E}}_{xx}(1/3, 1/3)$, i.e., under-integration of the zero moment of $\hat{\boldsymbol{E}}_{xx}$ on the element by applying the mid-point rule. We observed in numerical experiments, however, that in the membrane dominated case this may lead to unstable behavior. It seems that due to the under-integration spurious zero energy modes get activated. In [135] different tying points for the three components of $\hat{\boldsymbol{E}}_h$ are chosen inside $\hat{T}$, and thus, the proposed method differs for the inner part.

The other two tangential-tangential components of $\hat{\boldsymbol{E}}_h$ are treated the same way, where the diagonal component is defined by $(\hat{\boldsymbol{E}}_h)_{ll} = \frac{1}{2}((\hat{\boldsymbol{E}}_h)_{xx} + (\hat{\boldsymbol{E}}_h)_{yy}) - (\hat{\boldsymbol{E}}_h)_{xy}$.

Consequently, we can interpret the interpolation procedure into the Regge finite element space as an MITC method of arbitrary order, where the tying points are chosen implicitly accordingly to the integration points for (8.3.7)–(8.3.8) or equivalently to the dofs of the Regge elements. The idea of choosing the tying points on the edges yields a tangential-tangential continuous assumed membrane strain, which has recently been investigated also for the quadrilateral MITC4+ shell element [137]. In this thesis, however, we only consider triangles for the Regge interpolation. Nevertheless, we emphasize that the five tying points chosen in [137] can be related to the five degrees of freedom of the lowest order quadrilateral Regge element, compare (5.2.46)–(5.2.47). First numerical experiments applying the proposed method for quadrilaterals were promising. Further investigation is topic of research, especially the question of possible requirement of special additional internal bubbles for the displacement field u as well as for the Regge elements.

8.3.3. Discussion

A rigorous mathematical proof that the proposed Regge interpolation method avoids membrane locking in the bending dominated case while staying stable in the membrane dominated regime has not been achieved yet, not even in the linear regime. The involved geometric quantities as the Weingarten tensor and the strong coupling between the membrane and bending (and possible shearing) energy makes a proof challenging. Therefore, we present a discussion based on more heuristic arguments instead, following [165].

Let u be the exact solution of the linear shell problem (7.3.40) in the bending dominated case such that the limit constraint $E_{\text{mem}}^{\text{lin}}(u) = 0$ is exactly fulfilled. Interpolating u into the Lagrangian finite element space $[U_h^k]^3$, $u_h := \mathcal{I}_{h,k}u$, where $\mathcal{I}_h$ denotes the nodal interpolation operator (5.3.4), does not guarantee in general that $E_{\text{mem}}^{\text{lin}}(u_h) = 0$ for the discrete displacements. I.e., the kernel of the membrane operator does not get preserved by the interpolation operator. As a result, pure bending modes might induce so-called artificial discrete parasitic membrane strains leading to unintended membrane energy. This effect gets amplified for small thickness parameters t and starts dominating the bending energy, the shell element is called to be too stiff and membrane locking occurs.

By applying the Regge interpolation operator, $\mathcal{I}_{h,k-1}^{\mathcal{R}} E_{\text{mem}}^{\text{lin}}(u_h)$, we are able to relax the discrete constraints. Reduced and selective integration schemes follow the same idea, using less Gauß integration points for the (components of the) membrane energy term, and are frequently used for quadrilateral elements. Placed inside the elements this corresponds to an L^2 rather than a Regge interpolation. If we compare the number of integration points, which can be interpreted as the number of constraints as each integration point induces an equation, we observe that on a single triangle T the number of constraints coincides, namely $3(k+1)(k+2)/2$. Note that in the context of variational interpolation (8.3.3), or equivalently three-field formulation (8.3.5), this number corresponds to the amount of dofs of the interpolation space $\mathcal{R}_h^k$.

Considering a triangulation $\mathcal{T}_h$, however, the number of constraints differs in the lowest order case significantly due to the different placements of the dofs. For Regge elements we

have one dof per edge, whereas in the reduced integration scheme three per element are used. Asymptotically there holds for a triangulation

$$\#T \approx 2\#V, \qquad \#E \approx 3\#V, \qquad \#E = \frac{3}{2}\#T, \tag{8.3.9}$$

where $\#T$, $\#E$, and $\#V$ denote the number of triangles, edges, and vertices, respectively. Therefore, there holds

$$\#E \approx 3\#V < 6\#V \approx 3\#T \tag{8.3.10}$$

and thus, using the Regge interpolation reduces the number of constraints asymptotically by a factor of two compared to the L^2-projection. Furthermore, on an infinite triangulation $\mathcal{T}_h$ there holds for the so-called constraint ratio (also denoted constraint count) [121]

$$r = \frac{\#\text{dofs}}{\#\text{constraints}} = \frac{3\#V}{\#E} \approx \frac{\#E}{\#E} = 1. \tag{8.3.11}$$

Here, the number of dofs are given by the three Lagrangian displacement fields at each vertex, involved in the membrane energy, and the number of constraints is the amount of dofs of the Regge space. For Lagrangian elements of polynomial order k and corresponding Regge elements of order $k-1$ the constraint ratio is thus given by

$$r = \frac{3(\#V + (k-1)\#E + \frac{(k-2)(k-1)}{2}\#T)}{k\#E + \frac{3(k-1)k}{2}\#T} = \frac{k^2\#E}{k^2\#E} = 1 \tag{8.3.12}$$

and therefore, the ratio is 1 for arbitrary order. In the continuous setting the constraint ratio is also 1 (three displacement fields and three equations forcing zero membrane energy in the limit $t \to 0$). As a result, (immense) locking ($r < 1$) is not expected. Further relaxation of the constraint would lead to $r > 1$ and thus, the constraints may be underrepresented and possibly spurious energy modes appear. Note that the concept of constraint ratio is not a rigorous mathematical proof whether locking is avoided or not. For a finite grid of a plate or non-closed surface there holds

$$3 + \#E = 3\#V - \#V_B = 2\#V + \#V_I, \tag{8.3.13}$$

where $\#V_B$ and $\#V_I$ are denoting the number of vertices on the boundary and in the inner domain, respectively. The discrepancy of three corresponds to the number of rigid-body motions in two dimensions: two translations and one rotation. Thus, for a given displacement field at the vertices one can find a unique value per edge describing the (tangential-tangential) distance (or stretch) between two vertices. This suits perfectly to the following exact sequence

$$
\begin{array}{ccccccc}
RB & \xrightarrow{\text{id}} & [C^\infty(\Omega)]^2 & \xrightarrow{\nabla_{\text{sym}}} & [C^\infty(\Omega)]^{2\times2}_{\text{sym}} & \xrightarrow{\text{curl}^\top\text{curl}} & C^\infty(\Omega) \\
& & \mathcal{I}_{h,k}\Big\downarrow & & \mathcal{I}^{\mathcal{R}}_{h,k-1}\Big\downarrow & & [\mathcal{I}_{h,k}]^*\Big\downarrow \\
RB & \xrightarrow{\text{id}} & [U_h^k]^2 & \xrightarrow{\nabla_{\text{sym}}} & \mathcal{R}_h^{k-1} & \xrightarrow{\text{curl}^\top\text{curl}} & [U_h^k]^*
\end{array}, \tag{8.3.14}
$$

where $RB := \{Ax + b \,|\, A \in \mathbb{R}^{2\times2},\, A^\top = -A,\, b \in \mathbb{R}^2\}$ denotes the set of linearized rigid body motions, $[\mathcal{I}_{h,k}]^*$ is defined by the relation $\langle[\mathcal{I}_{h,k}]^*u, v_h\rangle_{\mathcal{D}'} = \langle u, v_h\rangle_{L^2}$ for all $u \in C^\infty(\Omega)$ and $v_h \in U_h^k$, and $[U_h^k]^*$ is the topological dual space of U_h^k spanned by the corresponding functionals, cf. Section 5.3.

In [85, 113] the authors used this sequence, also called *Kröner complex*, in three dimensions as a part of a larger complex and proved in the lowest order case that it is commuting and exact. For a nonlinear complex one has to replace the symmetric gradient by the Green strain tensor and $RB = \{Ax + b \,|\, A \in SO(2),\, b \in \mathbb{R}^2\}$, where $SO(2)$ denotes the set of all orthogonal 2×2 matrices with determinant one. The incompatibility operator $\mathrm{curl}^\top\mathrm{curl}$ is the linearization of the *Riemann curvature tensor*, see e.g., [88]. An extension of (8.3.14) onto the surface is not straight forward. With sequence (7.5.7) there holds e.g., $\mathrm{curl}_\tau^\top\mathrm{curl}_\tau(\mathrm{sym}(\nabla_\tau\cdot)) = 0$, but the linearized membrane strains are given by the covariant derivative $\mathrm{sym}(\nabla_\tau^{\mathrm{cov}}) = \mathrm{sym}(\boldsymbol{P}_\tau\nabla_\tau\cdot)$ and pure bending modes are also included in the kernel of $\mathrm{sym}(\nabla_\tau^{\mathrm{cov}})$. The extension of the incompatibility operator to the surface can be achieved by seeing it as part of the Saint–Venant compatibility equations on surfaces [89].

If the full nonlinear membrane energy term is considered in (7.3.38), the Green strain operator $\boldsymbol{E}_\tau : [\mathcal{P}^k(\mathcal{T}_h)]^d \to [\mathcal{P}^{2k-2}(\mathcal{T}_h)]^{d\times d}_{\mathrm{sym}}$ doubles the polynomial degree asymptotically, with the exception of lowest-order $k = 1$. This can lead to even worse discrete kernel conservation. Due to the Regge interpolant, however, the Green strain tensor gets projected back to polynomial degree $k - 1$ and again the number of constraints are significantly reduced.

In the lowest order case $k = 1$ for the displacements, membrane locking is not observed as long as an isoparametric mapping for the shell geometry is considered, i.e., affine elements are used. Curving the geometry by a higher polynomial degree as the displacement field leads to immense membrane locking. However, using the lowest-order Regge interpolation $\mathcal{I}_{h,0}^\mathcal{R}$ reduces this locking phenomena too.

As already discussed above, the Regge interpolation procedure is connected to the MITC triangular shell elements, if the tying points are chosen accordingly. Therefore a new finite element context and thus more structure is given by explicitly describing the involved interpolation space. In Section 8.2 an identification of the MITC plate tying points as interpolation of the shear strain into the $H(\mathrm{curl})$-conforming Nédélec element space has been discussed. This relation has been successfully exploited to prove rigorously that the MITC (plate) elements are free of shear locking [65] independent of the thickness parameter t. Therefore, the usage of Regge elements might be a step towards a better understanding of membrane locking and maybe will build an ingredient for a rigorous mathematical proof.

8.4. Numerical examples

We conclude the thesis by presenting several benchmarks to demonstrate the excellent performance of the proposed Regge interpolation method, which are taken from [165].

To avoid a priori possible shear locking effects we use the Koiter shell model presented in Section 7.7. For the benchmarks we use second order finite elements for the displacements u and the geometry is mapped isoparametrically. When using the presented tying point
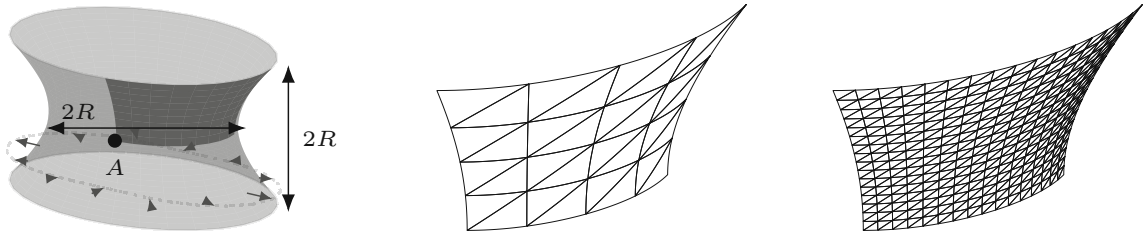
Figure 8.6.: Geometry and meshes with 4×4 and 16×16 grids for axisymmetric hyperboloid with free ends benchmark.

procedure the effort of the proposed method is comparable with that of (the membrane part of) the MITC6 shell elements. Further, we use the MITC6 membrane procedure as comparison.

The forces are chosen such that the deformations stay in the linear regime. Thus, the differences between the linearized and full nonlinear membrane energy is negligible. Further, the forces are scaled appropriately with the thickness parameter t (t^3 in the bending dominated and t in the membrane dominated regime) such that the deformations stay in the same magnitude. The reference values are computed by using fourth order finite elements for the displacement on the finest mesh and the relative error of the quantities of interest is computed by `|result - reference|/|reference|`.

8.4.1. Axisymmetric hyperboloid with free ends

An axisymmetric hyperboloid described by the equation

$$x^2 + y^2 = R^2 + z^2, \quad z \in [-R, R] \tag{8.4.1}$$

with free boundaries is loaded by a force, see [72, 135, 137]. Due to symmetries we consider only one eighth of the geometry and symmetry boundary conditions are prescribed, compare Figure 8.6 for the geometry and meshes. The material and geometric parameters are given by $R = 1$, $\hat{E} = 2.85 \times 10^4$, $\hat{\nu} = 0.3$, $t \in \{0.1, 0.01, 0.001, 0.0001\}$, $P = \frac{t^3}{\sqrt{x^2+y^2}} \cos(2\zeta) \, (x, \, y, \, 0)^\top$.

The radial deflection at point A is listed in Tables 8.1–8.2 and the relative error in Figure 8.7. Therein the classical locking behavior can be observed, if the membrane term is left untreated, as the pre-asymptotic range increases rapidly for smaller thicknesses. The MITC procedure improves this unsatisfactory behavior and also decreases the initial error for coarse meshes. Using Regge interpolation avoids the pre-asymptotic behavior further. We emphasize that for $t = 0.0001$ with 8 elements the difference with a factor of 10^5 is immensely between "do nothing" and Regge interpolation (2×10^{-10} vs. 1.92×10^{-5} with the reference value 1.89×10^{-5}).

8.4.2. Uniform bending of cylindrical shell

We apply a moment force M to a cylindrical shell, which is fixed at the top and free on the other boundaries [139]. The material and geometric parameters are $R = 0.1$, $b = 0.025$, $\hat{E} = 2 \times 10^5$, $\hat{\nu} = 0$, $t \in \{0.1, 0.01, 0.001, 0.0001\}$, $M_0 = (t/R)^3$, see also Figure 8.8.

<div align="center">

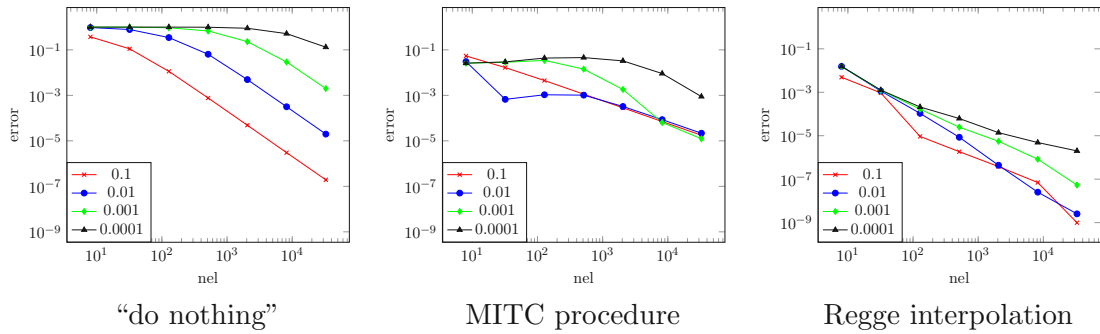"do nothing"   MITC procedure   Regge interpolation

</div>

Figure 8.7.: Relative error with respect to number of elements for axisymmetric hyperboloid with free ends with "do nothing", MITC procedure, and Regge interpolation.

nel \ t	0.1	0.01	0.001	0.0001
8	-1.40971	-0.08393	-0.00216	-0.00002
32	-1.99954	-0.41024	-0.01227	-0.00013
128	-2.22354	-1.23888	-0.11740	-0.00182
512	-2.24731	-1.77470	-0.61248	-0.02537
2048	-2.24893	-1.88687	-1.45795	-0.20875
8192	-2.24903	-1.89560	-1.83745	-0.91489
32768	-2.24904	-1.89616	-1.88895	-1.64433

Table 8.1.: Results for axisymmetric hyperboloid with free ends $\times 10^5$ with "do nothing" and 2×2, 4×4, 8×8, ..., 128×128 triangular grids.

nel \ t	0.1	0.01	0.001	0.0001
8	-2.23800	-1.92570	-1.92213	-1.92209
32	-2.24693	-1.89837	-1.89502	-1.89498
128	-2.24902	-1.89641	-1.89303	-1.89299
512	-2.24904	-1.89622	-1.89276	-1.89271
2048	-2.24904	-1.89620	-1.89270	-1.89262
8192	-2.24904	-1.89620	-1.89271	-1.89259
32768	-2.24904	-1.89620	-1.89271	-1.89259

Table 8.2.: Results for axisymmetric hyperboloid with free ends $\times 10^5$ with Regge interpolation and 2×2, 4×4, 8×8, ..., 128×128 triangular grids.
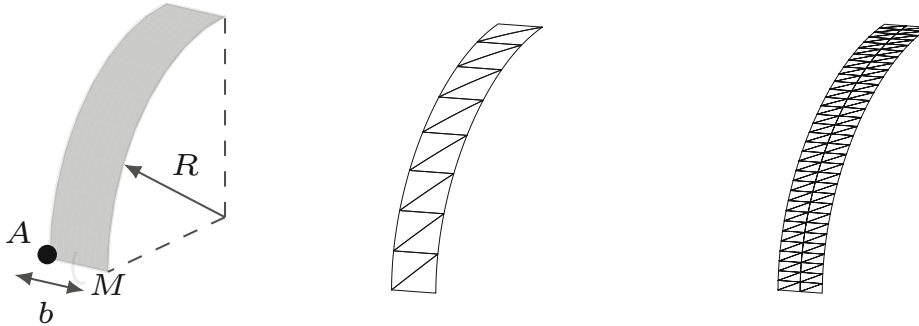
Figure 8.8.: Geometry and meshes with 8×1 and 32×2 grid for uniform bending of cylindrical shell benchmark.

nel \ t	0.1	0.01	0.001	0.0001
8	6.00078	5.20275	2.43791	2.23652
16	6.00142	5.95961	4.44983	2.89530
32	6.00029	5.99792	5.88843	4.62872
128	6.00011	5.99971	5.96252	5.18277
384	6.00010	6.00007	5.99700	5.80409
1024	6.00010	6.00010	5.99987	5.98020
2560	6.00010	6.00010	6.00008	5.99852

Table 8.3.: Results for uniform bending of cylindrical shell $\times 10^4$ with "do nothing" and 4×1, 8×1, 16×1, 32×2, 64×3, 128×4, and 256×5 triangular grids.

The deflection orthogonal to the radial direction is computed at point A. The results can be found in Tables 8.3–8.4 and Figure 8.9. In this benchmark the method without any interpolation does not produce a strong pre-asymptotic regime for small thicknesses. However, the initial relative error increases and the error curves are shifted parallel. In contrast, the initial errors with the Regge interpolation are independent of the thickness and show a uniform convergence behavior. Furthermore, the MITC procedure delivers exactly the same results in this example as the proposed Regge interpolation.

As the Poisson ratio $\hat{\nu} = 0$ the membrane energy density $\|\boldsymbol{E}_{\mathrm{mem}}\|_{\boldsymbol{M}}^2$ of the exact solution hast to be exactly zero. The numerical result for $t = 0.0001$ and a 32×2 grid depicted in Figure 8.10 shows significant oscillations in the membrane energy density with a magnitude of about 1×10^{-7} for the "do nothing" method. For the Regge interpolation on the other hand the density of the interpolated strain $\|\mathcal{I}_{h,1}^{\mathcal{R}} \boldsymbol{E}_{\mathrm{mem}}\|_{\boldsymbol{M}}^2$ is constant and with 4.5×10^{-14} nearly exact zero.
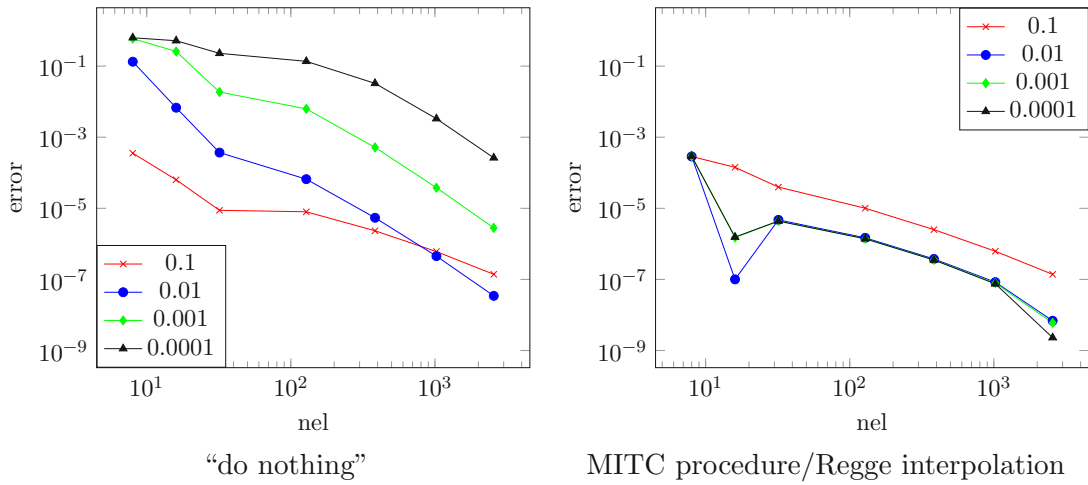
"do nothing" MITC procedure/Regge interpolation

Figure 8.9.: Relative error with respect to number of elements for uniform bending of cylindrical shell with "do nothing" and MITC procedure/Regge interpolation.

nel \ t	0.1	0.01	0.001	0.0001
8	6.00051	6.00050	6.00050	6.00050
16	6.00013	6.00013	6.00013	6.00013
32	6.00010	6.00010	6.00010	6.00010
128	6.00010	6.00010	6.00010	6.00010
384	6.00010	6.00010	6.00010	6.00010
1024	6.00010	6.00010	6.00010	6.00010
2560	6.00010	6.00010	6.00010	6.00010

Table 8.4.: Results for uniform bending of cylindrical shell $\times 10^4$ with Regge interpolation and 4×1, 8×1, 16×1, 32×2, 64×3, 128×4, and 256×5 triangular grids.
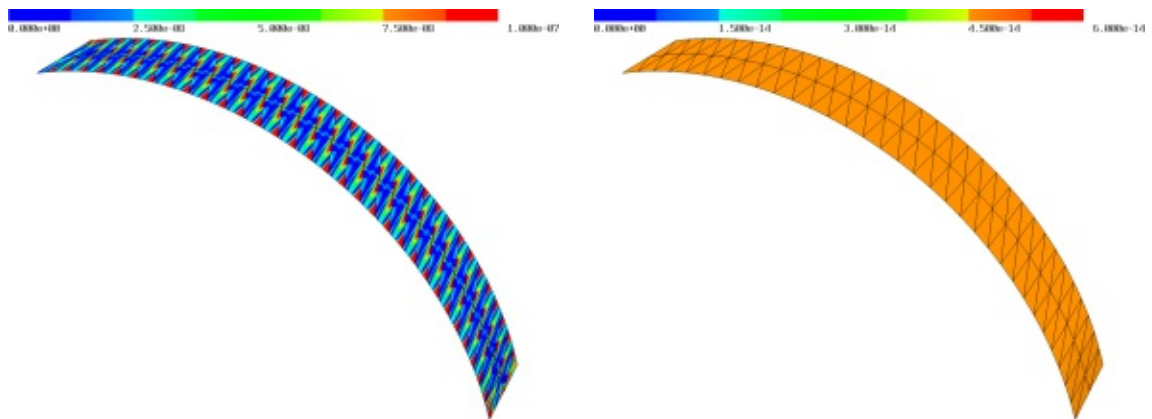

Figure 8.10.: Membrane energy density of uniform bending of cylindrical shell with "do nothing" and Regge interpolation for $t = 0.0001$ and 32×2 grid.
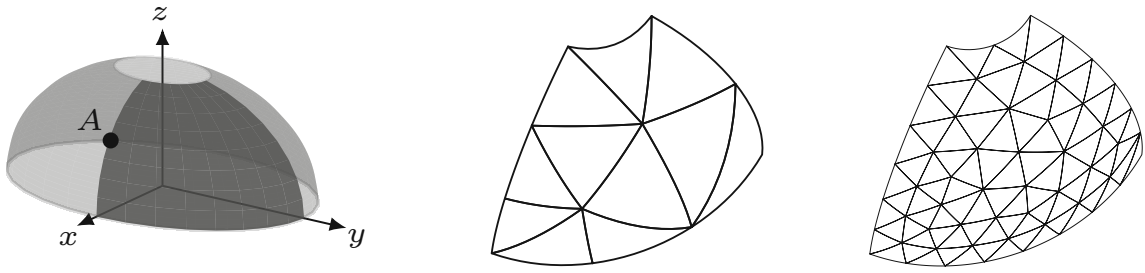
Figure 8.11.: Geometry and unstructured meshes with 11 and 84 elements for open hemisphere with clamped ends benchmark.

nel \ t	0.1	0.01	0.001	0.0001
11	1.40550	1.41500	1.41510	1.41510
20	1.17835	1.14513	1.14461	1.14460
84	1.13244	1.12607	1.12551	1.12551
342	1.12707	1.12036	1.12034	1.12034
1368	1.12762	1.11990	1.11917	1.11919
5420	1.12765	1.12028	1.11895	1.11899
21482	1.12765	1.12031	1.11917	1.11897

Table 8.5.: Results for open hemisphere with clamped ends $\times 10^5$ with "do nothing".

8.4.3. Open hemisphere with clamped ends

As a final example we consider an 18° open hemisphere with clamped top and bottom edges [72], which falls in the membrane dominated case. Only one fourth of the hemisphere is considered due to symmetry with appropriate boundary conditions, see Figure 8.11. The material and geometric parameters are given by $R = 10$, $\hat{E} = 6.825 \times 10^7$, $\hat{\nu} = 0.3$, and $t \in \{0.1, 0.01, 0.001, 0.0001\}$. The volume force density is $P = \frac{t}{10}\cos(2\zeta)\overline{\nu}$, where ζ denotes the angle between the x and y component.

The deflection in x-direction at point A is listed in Table 8.5 and 8.6. In Figure 8.12 the relative error is shown. As expected the "do nothing" method does not suffer from membrane locking in the case of inhibited pure bending. Using the Regge interpolation

nel \ t	0.1	0.01	0.001	0.0001
11	1.31230	1.31583	1.31587	1.31587
20	1.20520	1.20922	1.20927	1.20927
84	1.12825	1.13285	1.13302	1.13303
342	1.12726	1.12282	1.12369	1.12370
1368	1.12762	1.12028	1.12045	1.12054
5420	1.12765	1.12030	1.11942	1.11964
21482	1.12765	1.12031	1.11923	1.11926

Table 8.6.: Results for open hemisphere with clamped ends $\times 10^5$ with Regge interpolation.
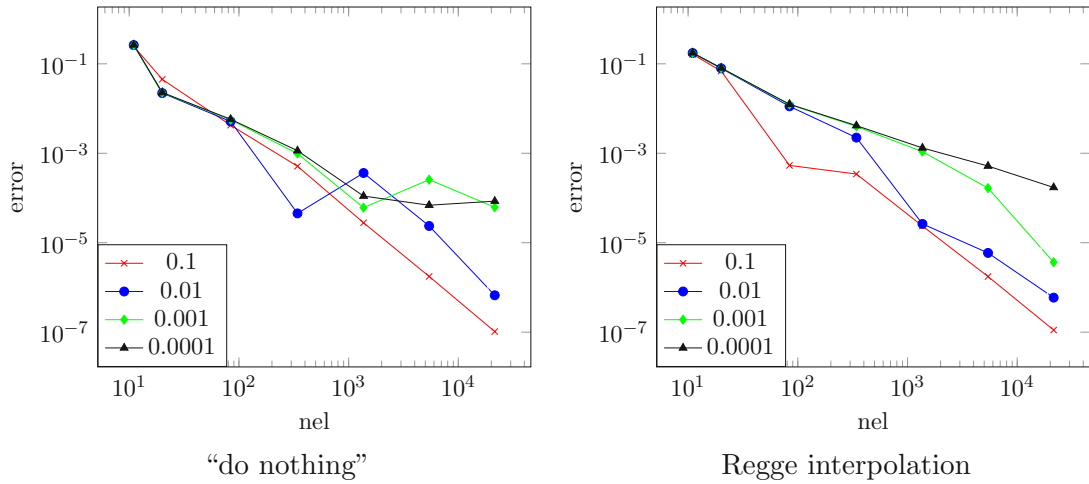
"do nothing"　　　　　　　　　Regge interpolation

Figure 8.12.: Relative error with respect to number of elements for open hemisphere with clamped ends with "do nothing" and Regge interpolation.

operator only a minimal deterioration in the convergence rates for smaller thicknesses can be observed. However, this effect is nearly negligible. Interestingly, also in this membrane dominated example the usage of the interpolation operator yields better results if a coarse mesh is used.

A. Curvilinear coordinates

Let $\vec{g}^i$, $i = 1, 2, 3$, be a (contravariant) basis of $\mathbb{R}^3$ and $\vec{g}_i$ the corresponding dual (covariant) basis defined by the relation

$$\vec{g}^i \cdot \vec{g}_j = \delta_j^i, \qquad i, j = 1, 2, 3,$$

where δ_j^i denotes the Kronecker delta. Then a vector $\vec{a} \in \mathbb{R}^3$ is given in co- and contravariant components by

$$\vec{a} = a_i \vec{g}^i = a^i \vec{g}_i, \qquad a_i = \vec{a} \cdot \vec{g}_i, \quad a^i = \vec{a} \cdot \vec{g}^i,$$

where we used the *Einstein summation convention* $a_i \vec{g}^i = \sum_{i=1}^{3} a_i \vec{g}^i$ with the convention that Latin indices range from one to three and Greek indices from one to two. A matrix $\boldsymbol{A}$ is given in co-, contravariant, and mixed components by

$$\boldsymbol{A} = A_{ij} \vec{g}^i \otimes \vec{g}^j = A^{ij} \vec{g}_i \otimes \vec{g}_j = A_i^{\cdot j} \vec{g}^i \otimes \vec{g}_j$$

with the (dyadic) tensor product $\otimes$. The scalar and Frobenius scalar product is defined by

$$\vec{a} \cdot \vec{b} = a_i b^i, \qquad\qquad\qquad \boldsymbol{A} : \boldsymbol{B} = A_{ij} B^{ij}.$$

The metric tensor $\boldsymbol{g}$ is given by

$$g_{ij} = \vec{g}_i \cdot \vec{g}_j, \qquad g^{ij} = \vec{g}^i \cdot \vec{g}^j, \qquad g_j^{\cdot i} = g_{\cdot j}^i = \delta_j^i,$$

which is used to transform coordinates from co- to contravariant components and vice-versa (also called raise/lower indices)

$$a^i = g^{ij} a_j, \qquad\qquad\qquad a_i = g_{ij} a^j,$$

where a_i and a^i are the co- and contravariant components of the vector $\vec{a}$. If $\vec{g}_i$ are orthonormal there holds $g_{ij} = g^{ij} = \delta_{ij}$.

Let $\Omega \subset \mathbb{R}^3$ be open and $\Phi : \Omega \to \mathbb{R}^3$ smooth and injective. The curvilinear coordinates induced by the mapping Φ are defined by

$$\vec{g}_i := \frac{\partial \Phi(\xi^1, \xi^2, \xi^3)}{\partial \xi^i}, \qquad i = 1, 2, 3,$$

and $\vec{g}_i$ are linearly independent at each point. Let $\vec{u}$ be a vector given in the curvilinear basis. Then, with the notation $\vec{u}_{,i} := \frac{\partial \vec{u}}{\partial \xi^i}$, the (covariant-covariant) components of $\nabla \vec{u}$ are given by

$$u_{j\|i} := u_{j,i} - \bar{\Gamma}_{ji}^k u_k, \qquad\qquad \nabla \vec{u} = u_{j\|i} \, \vec{g}^j \otimes \vec{g}^i,$$

where $\bar{\Gamma}_{ji}^k$ denotes the 3D Christoffel symbol

$$\bar{\Gamma}_{ji}^k := \vec{g}_{j,i} \cdot \vec{g}^k. \tag{A.0.1}$$

B. Computation of variations

Variations of geometric vectors: As preparation we use the following identity in three dimensions for the variation of the cofactor matrix

$$\text{cof}(\boldsymbol{A})^\top = \frac{1}{2}\left(\text{tr}(\boldsymbol{A})^2 - \text{tr}(\boldsymbol{A}^2)\right)\boldsymbol{I} - \text{tr}(\boldsymbol{A})\boldsymbol{A} + \boldsymbol{A}^2,$$

yielding

$$\partial_u(\text{cof}(\boldsymbol{F}_{\overline{\tau}})\overline{\nu})(\delta u) = \left(\text{tr}(\boldsymbol{F}_{\overline{\tau}})\text{tr}(\nabla_{\overline{\tau}}\delta u) - 2\boldsymbol{F}_{\overline{\tau}}^\top : \nabla_{\overline{\tau}}\delta u\right)\overline{\nu} - \text{tr}(\nabla_{\overline{\tau}}\delta u)\boldsymbol{F}_{\overline{\tau}}^\top\overline{\nu}$$
$$- \text{tr}(\boldsymbol{F}_{\overline{\tau}})\nabla_{\overline{\tau}}\delta u^\top\overline{\nu} + \boldsymbol{F}_{\overline{\tau}}^\top\nabla_{\overline{\tau}}\delta u^\top\overline{\nu} + \nabla_{\overline{\tau}}\delta u^\top\boldsymbol{F}_{\overline{\tau}}^\top\overline{\nu}. \tag{B.0.1}$$

The second variation is straight forward as the cofactor matrix is quadratic in 3D

$$\partial_u^2(\text{cof}(\boldsymbol{F}_{\overline{\tau}})\overline{\nu})(\delta u, \Delta u) = \left(\text{tr}(\nabla_{\overline{\tau}}\Delta u)\text{tr}(\nabla_{\overline{\tau}}\delta u) - 2\nabla_{\overline{\tau}}\Delta u^\top : \nabla_{\overline{\tau}}\delta u\right)\overline{\nu} - \text{tr}(\nabla_{\overline{\tau}}\delta u)\nabla_{\overline{\tau}}\Delta u^\top\overline{\nu}$$
$$- \text{tr}(\nabla_{\overline{\tau}}\Delta u)\nabla_{\overline{\tau}}\delta u^\top\overline{\nu} + (\nabla_{\overline{\tau}}\Delta u^\top\nabla_{\overline{\tau}}\delta u^\top + \nabla_{\overline{\tau}}\delta u^\top\nabla_{\overline{\tau}}\Delta u^\top)\overline{\nu}.$$

With the tensor cross product $\times$ defined in [55] the cofactor matrix reads $\text{cof}(\boldsymbol{A}) = \frac{1}{2}\boldsymbol{A} \times \boldsymbol{A}$ and with linearity and symmetry a more compact notation of the derivatives is achieved: $\partial_u(\text{cof}(\boldsymbol{F}_{\overline{\tau}})\overline{\nu})(\delta u) = (\boldsymbol{F}_{\overline{\tau}} \times \nabla_{\overline{\tau}}\delta u)\overline{\nu}$, $\partial_u^2(\text{cof}(\boldsymbol{F}_{\overline{\tau}})\overline{\nu})(\delta u, \Delta u) = (\nabla_{\overline{\tau}}\Delta u \times \nabla_{\overline{\tau}}\delta u)\overline{\nu}$.

Now, we start with the variations of the normalized tangential vector

$$\partial_u(\tau \circ \phi)(\delta u) = \partial_u\left(\frac{\boldsymbol{F}_{\overline{\tau}}\overline{\tau}}{\|\boldsymbol{F}_{\overline{\tau}}\overline{\tau}\|}\right)(\delta u) = \frac{\nabla_{\overline{\tau}}\delta u\overline{\tau}}{\|\boldsymbol{F}_{\overline{\tau}}\overline{\tau}\|} - \frac{\boldsymbol{F}_{\overline{\tau}}\overline{\tau}}{\|\boldsymbol{F}_{\overline{\tau}}\overline{\tau}\|^3}\langle\boldsymbol{F}_{\overline{\tau}}\overline{\tau}, \nabla_{\overline{\tau}}\delta u\overline{\tau}\rangle = \boldsymbol{P}_{\tau_E}^\perp\frac{\nabla_{\overline{\tau}}\delta u\overline{\tau}}{\|\boldsymbol{F}_{\overline{\tau}}\overline{\tau}\|}$$

and

$$\partial_u^2(\tau \circ \phi)(\delta u, \Delta u) = -\frac{\nabla_{\overline{\tau}}\delta u\overline{\tau}}{\|\boldsymbol{F}_{\overline{\tau}}\overline{\tau}\|^3}\langle\boldsymbol{F}_{\overline{\tau}}\overline{\tau}, \nabla_{\overline{\tau}}\Delta u\overline{\tau}\rangle - \frac{\nabla_{\overline{\tau}}\Delta u\overline{\tau}}{\|\boldsymbol{F}_{\overline{\tau}}\overline{\tau}\|^3}\langle\boldsymbol{F}_{\overline{\tau}}\overline{\tau}, \nabla_{\overline{\tau}}\delta u\overline{\tau}\rangle$$
$$+ 3\frac{\boldsymbol{F}_{\overline{\tau}}\overline{\tau}}{\|\boldsymbol{F}_{\overline{\tau}}\overline{\tau}\|^5}\langle\boldsymbol{F}_{\overline{\tau}}\overline{\tau}, \nabla_{\overline{\tau}}\delta u\overline{\tau}\rangle\langle\boldsymbol{F}_{\overline{\tau}}\overline{\tau}, \nabla_{\overline{\tau}}\Delta u\overline{\tau}\rangle - \frac{\boldsymbol{F}_{\overline{\tau}}\overline{\tau}}{\|\boldsymbol{F}_{\overline{\tau}}\overline{\tau}\|^3}\langle\nabla_{\overline{\tau}}\Delta u\overline{\tau}, \nabla_{\overline{\tau}}\delta u\overline{\tau}\rangle.$$

For the outer normal vector we have analogically

$$\partial_u(\nu \circ \phi)(\delta u) = \boldsymbol{P}_\nu^\perp\frac{\partial_u(\text{cof}(\boldsymbol{F}_{\overline{\tau}})\overline{\nu})(\delta u)}{\|\text{cof}(\boldsymbol{F}_{\overline{\tau}})\overline{\nu}\|}$$

with

$$\boldsymbol{P}_\nu^\perp v = v - (\nu \circ \phi \cdot v)\nu \circ \phi$$

and the second variation follows the same lines as for the tangential vector. The variations of the element normal vector follows now immediately as $\mu \circ \phi = \nu \circ \phi \times \tau \circ \phi$

$$
\begin{aligned}
\partial_u(\mu \circ \phi)(\delta u) = \partial_u(\nu \times \tau) &= \boldsymbol{P}_\nu^\perp \frac{\partial_u(\mathrm{cof}(\boldsymbol{F}_{\overline{\tau}})\overline{\nu})(\delta u)}{\|\mathrm{cof}(\boldsymbol{F}_{\overline{\tau}})\overline{\nu}\|} \times \tau \circ \phi + \nu \circ \phi \times \boldsymbol{P}_{\tau_E}^\perp \frac{\nabla_{\overline{\tau}} \delta u \overline{\tau}}{\|\boldsymbol{F}_{\overline{\tau}} \overline{\tau}\|} \\
&= \frac{\partial_u(\mathrm{cof}(\boldsymbol{F}_{\overline{\tau}})\overline{\nu})(\delta u)}{\|\mathrm{cof}(\boldsymbol{F}_{\overline{\tau}})\overline{\nu}\|} \times \tau \circ \phi - \mu \circ \phi \frac{\langle \nu \circ \phi, \partial_u(\mathrm{cof}(\boldsymbol{F}_{\overline{\tau}})\overline{\nu})(\delta u)\rangle}{\|\mathrm{cof}(\boldsymbol{F}_{\overline{\tau}})\overline{\nu}\|} \\
&\quad + \nu \circ \phi \times \frac{\nabla_{\overline{\tau}} \delta u \overline{\tau}}{\|\boldsymbol{F}_{\overline{\tau}} \overline{\tau}\|} - \mu \circ \phi \frac{\langle \tau \circ \phi, \nabla_{\overline{\tau}} \delta u \overline{\tau}\rangle}{\|\boldsymbol{F}_{\overline{\tau}} \overline{\tau}\|}.
\end{aligned}
$$

The second variation is a simple but lengthy calculation and thus not stated here.

First variations: We compute the first variations of (7.7.13). For a more compact notation we neglect the ϕ dependency and write e.g., τ instead of $\tau \circ \phi$. Further we write $\{\nu\}$ instead of $\{\nu\}^n$ – note that $\{\nu\}$ does not depend on u:

$$
\partial_u\left(\frac{t}{2}\|\boldsymbol{E}_{\overline{\tau}}\|_{\boldsymbol{M}}^2\right)(\delta u) = 2t\langle \boldsymbol{M}\boldsymbol{E}_{\overline{\tau}}, \boldsymbol{F}_{\overline{\tau}}^\top \nabla_{\overline{\tau}} \delta u\rangle,
$$

$$
\partial_{\boldsymbol{\sigma}}\left(\frac{6}{t^3}\|\boldsymbol{\sigma}\|_{\boldsymbol{M}^{-1}}^2\right)(\delta\boldsymbol{\sigma}) = \frac{12}{t^3}\langle \boldsymbol{M}^{-1}\boldsymbol{\sigma}, \delta\boldsymbol{\sigma}\rangle,
$$

$$
\partial_u\left((\nabla_{\overline{\tau}}^2 u_i\nu_i + (1 - \overline{\nu}\cdot\nu)\nabla_{\overline{\tau}}\overline{\nu}) : \boldsymbol{\sigma}\right)(\delta u) = (\nabla_{\overline{\tau}}^2 \delta u_i\nu_i + \nabla_{\overline{\tau}}^2 u_i\partial_u\nu_i(\delta u) - \overline{\nu}\cdot\partial_u\nu(\delta u)\nabla_{\overline{\tau}}\overline{\nu}) : \boldsymbol{\sigma},
$$

$$
\partial_{\boldsymbol{\sigma}}\left((\nabla_{\overline{\tau}}^2 u_i\nu_i + (1 - \overline{\nu}\cdot\nu)\nabla_{\overline{\tau}}\overline{\nu}) : \boldsymbol{\sigma}\right)(\delta\boldsymbol{\sigma}) = (\nabla_{\overline{\tau}}^2 u_i\nu_i + (1 - \overline{\nu}\cdot\nu)\nabla_{\overline{\tau}}\overline{\nu}) : \delta\boldsymbol{\sigma},
$$

$$
\partial_u\left(\sphericalangle(P_{\tau_E}^\perp(\{\nu\}), \mu)\right)(\delta u) =
$$

$$
-\frac{1}{\sqrt{1 - (P_{\tau_E}^\perp(\{\nu\})\cdot\mu)^2}}\left(\frac{\{\nu\}\cdot\partial_u\mu(\delta u)}{\|\{\nu\} - \{\nu\}\cdot\tau\tau\|} + \frac{\{\nu\}\cdot\mu}{\|\{\nu\} - \{\nu\}\cdot\tau\tau\|^3}(\{\nu\}\cdot\partial_u\tau(\delta u))(\{\nu\}\cdot\tau)\right).
$$

Second variations: The second variations, especially the boundary jump term, are quite lengthy, but manageable:

$$\partial_u^2(\frac{t}{2}\|\boldsymbol{E}_{\overline{\tau}}\|_{\boldsymbol{M}}^2)(\delta u, \Delta u) = 4t\langle \boldsymbol{M}\,\mathrm{sym}(\boldsymbol{F}_{\overline{\tau}}\nabla_{\overline{\tau}}\Delta u), \boldsymbol{F}_{\overline{\tau}}\nabla_{\overline{\tau}}\delta u\rangle + 2t\langle \boldsymbol{M}\boldsymbol{E}_{\overline{\tau}}, \nabla_{\overline{\tau}}\Delta u^{\top}\nabla_{\overline{\tau}}\delta u\rangle,$$

$$\partial_{\boldsymbol{\sigma}}^2(\frac{6}{t^3}\|\boldsymbol{\sigma}\|_{\boldsymbol{M}^{-1}}^2)(\delta\boldsymbol{\sigma}, \Delta\boldsymbol{\sigma}) = \frac{12}{t^3}\langle \boldsymbol{M}^{-1}\Delta\boldsymbol{\sigma}, \delta\boldsymbol{\sigma}\rangle,$$

$$\partial_u^2((\nabla_{\overline{\tau}}^2 u_i\nu_i + (1 - \overline{\nu}\cdot\nu)\nabla_{\overline{\tau}}\overline{\nu}) : \boldsymbol{\sigma})(\delta u, \Delta u) = (\nabla_{\overline{\tau}}^2\delta u_i\partial_u\nu_i(\Delta u) + \nabla_{\overline{\tau}}^2\Delta u_i\partial_u\nu_i(\delta u)$$
$$+ \nabla_{\overline{\tau}}^2 u_i\partial_u^2\nu_i(\delta u, \Delta u) - \overline{\nu}\cdot\partial_u^2\nu(\delta u, \Delta u)\nabla_{\overline{\tau}}\overline{\nu}) : \boldsymbol{\sigma}$$

$$\partial_{\boldsymbol{\sigma}}\partial_u((\nabla_{\overline{\tau}}^2 u_i\nu_i + (1 - \overline{\nu}\cdot\nu)\nabla_{\overline{\tau}}\overline{\nu}) : \boldsymbol{\sigma})(\delta u, \Delta\boldsymbol{\sigma}) = \Big(\nabla_{\overline{\tau}}^2\delta u_i\nu_i + \nabla_{\overline{\tau}}^2 u_i\partial_u\nu_i(\delta u)$$
$$- \overline{\nu}\cdot\partial_u\nu(\delta u)\nabla_{\overline{\tau}}\overline{\nu}\Big) : \Delta\boldsymbol{\sigma},$$

$$\partial_u^2(\sphericalangle(P_{\tau_E}^{\perp}(\{\nu\}), \mu))(\delta u, \Delta u) = -\frac{1}{\sqrt{1 - (P_{\tau_E}^{\perp}(\{\nu\})\cdot\mu)^2}^3}(P_{\tau_E}^{\perp}(\{\nu\})\cdot\mu)\times$$

$$\Big(\frac{\{\nu\}\cdot\mu}{\|\{\nu\} - \{\nu\}\cdot\tau\tau\|^3}(\{\nu\}\cdot\partial_u\tau(\Delta u))(\{\nu\}\cdot\tau) + \frac{\{\nu\}\cdot\partial_u\mu(\Delta u)}{\|\{\nu\} - (\{\nu\}\cdot\tau)\tau\|}\Big)\Big(\frac{\{\nu\}\cdot\partial_u\mu(\delta u)}{\|\{\nu\} - (\{\nu\}\cdot\tau)\tau\|}$$

$$+ \frac{\{\nu\}\cdot\mu}{\|\{\nu\} - (\{\nu\}\cdot\tau)\tau\|^3}(\{\nu\}\cdot\partial_u\tau(\delta u))(\{\nu\}\cdot\tau)\Big) - \frac{1}{\sqrt{1 - (P_{\tau_E}^{\perp}(\{\nu\})\cdot\mu)^2}}\times$$

$$\Big(\frac{\{\nu\}\cdot\partial_u^2\mu(\delta u, \Delta u)}{\|\{\nu\} - \{\nu\}\cdot\tau\tau\|} + \frac{\{\nu\}\cdot\partial_u\mu(\delta u)}{\|\{\nu\} - \{\nu\}\cdot\tau\tau\|^3}(\{\nu\}\cdot\partial_u\tau(\Delta u))(\{\nu\}\cdot\tau) + \Big[\frac{\{\nu\}\cdot\partial_u\mu(\Delta u)}{\|\{\nu\} - \{\nu\}\cdot\tau\tau\|^3}$$

$$+ 3\frac{\{\nu\}\cdot\mu}{\|\{\nu\} - \{\nu\}\cdot\tau\tau\|^5}(\{\nu\}\cdot\partial_u\tau(\Delta u))(\{\nu\}\cdot\tau)\Big](\{\nu\}\cdot\partial_u\tau(\delta u))(\{\nu\}\cdot\tau) + \frac{\{\nu\}\cdot\mu}{\|\{\nu\} - \{\nu\}\cdot\tau\tau\|^3}\times$$

$$\big[(\{\nu\}\cdot\partial_u^2\tau(\delta u, \Delta u))(\{\nu\}\cdot\tau) + (\{\nu\}\cdot\partial_u\tau(\delta u))(\{\nu\}\cdot\partial_u\tau(\Delta u))\big]\Big).$$

Projection update in every Newton iteration: If we average the normal vector after every Newton iteration there holds $\{\nu\}\cdot\tau = 0$ and thus

$$\partial_u(\sphericalangle(P_{\tau_E}^{\perp}(\{\nu\}), \mu))(\delta u) = -\frac{1}{\sqrt{1 - (\{\nu\}\cdot\mu)^2}}\{\nu\}\cdot\partial_u\mu(\delta u)$$

and

$$\partial_u^2(\sphericalangle(P_{\tau_E}^{\perp}(\{\nu\}), \mu))(\delta u, \Delta u) = -\frac{1}{\sqrt{1 - (\{\nu\}\cdot\mu)^2}^3}(\{\nu\}\cdot\mu)(\{\nu\}\cdot\partial_u\mu(\Delta u))(\{\nu\}\cdot\partial_u\mu(\delta u))$$

$$- \frac{1}{\sqrt{1 - (\{\nu\}\cdot\mu)^2}}\Big(\{\nu\}\cdot\partial_u^2\mu(\delta u, \Delta u) + (\{\nu\}\cdot\mu)(\{\nu\}\cdot\partial_u\tau(\delta u))(\{\nu\}\cdot\partial_u\tau(\Delta u))\Big).$$

Bibliography

[1] M. Abramowitz. *Handbook of Mathematical Functions, With Formulas, Graphs, and Mathematical Tables.* Dover Publications, Inc., New York, NY, USA, 1974.

[2] R. A. Adams and J. J. Fournier. *Sobolev spaces.* Academic Press, 2 edition, 2003.

[3] S. Adams and B. Cockburn. A mixed finite element method for elasticity in three dimensions. *Journal of Scientific Computing*, 25(3):515–521, 2004.

[4] S. M. Alessandrini, D. N. Arnold, R. S. Falk, and A. L. Madureira. Derivation and justification of plate models by variational methods. In M. Fortin, editor, *Plates and Shells (Quebec 1996)*, volume 21, pages 1–20. AMS Providence RI, 1999.

[5] G. E. Andrews, R. Askey, and R. Roy. *Special functions.* Encyclopedia of Mathematics and its Applications. Cambridge University Press, 1999.

[6] A. Angoshtari, M. F. Shojaei, and A. Yavari. Compatible-strain mixed finite element methods for 2D compressible nonlinear elasticity. *Computer Methods in Applied Mechanics and Engineering*, 313:596–631, 2017.

[7] A. Angoshtari and A. Yavari. Hilbert complexes of nonlinear elasticity. *Zeitschrift für angewandte Mathematik und Physik*, 67(6):143, 2016.

[8] D. N. Arnold. Discretization by finite elements of a model parameter dependent problem. *Numerische Mathematik*, 37(3):405–421, 1981.

[9] D. N. Arnold, G. Awanou, and R. Winther. Finite elements for symmetric tensors in three dimensions. *Mathematics of Computation*, 77(263):1229–1251, 2008.

[10] D. N. Arnold and F. Brezzi. Mixed and nonconforming finite element methods : implementation, postprocessing and error estimates. *ESAIM: M2AN*, 19(1):7–32, 1985.

[11] D. N. Arnold and F. Brezzi. Locking-free finite element methods for shells. *Mathematics of Computation of the American Mathematical Society*, 66(217):1–14, 1997.

[12] D. N. Arnold, F. Brezzi, B. Cockburn, and L. D. Marini. Unified analysis of discontinuous Galerkin methods for elliptic problems. *SIAM Journal on Numerical Analysis*, 39(5):1749–1779, 2002.

[13] D. N. Arnold, F. Brezzi, and J. Douglas. PEERS: a new mixed finite element for plane elasticity. *Japan Journal of Applied Mathematics*, 1(2):347, 1984.

[14] D. N. Arnold, J. Douglas, and C. P. Gupta. A family of higher order mixed finite element methods for plane elasticity. *Numerische Mathematik*, 45(1):1–22, 1984.

[15] D. N. Arnold, R. Falk, and R. Winther. Mixed finite element methods for linear elasticity with weakly imposed symmetry. *Mathematics of Computation*, 76(260):1699–1723, 2007.

[16] D. N. Arnold, R. Falk, and R. Winther. Finite element exterior calculus: from Hodge theory to numerical stability. *Bulletin of the American Mathematical Society*, 47(2):281–354, 2010.

[17] D. N. Arnold and R. S. Falk. Asymptotic analysis of the boundary layer for the Reissner–Mindlin plate model. *SIAM Journal on Mathematical Analysis*, 27(2):486–514, 1996.

[18] D. N. Arnold, R. S. Falk, and R. Winther. Finite element exterior calculus, homological techniques, and applications. *Acta numerica*, 15:1–155, 2006.

[19] D. N. Arnold and S. W. Walker. The Hellan–Herrmann–Johnson method with curved elements. *SIAM Journal on Numerical Analysis*, 58(5):2829–2855, 2020.

[20] D. N. Arnold and R. Winther. Mixed finite elements for elasticity. *Numerische Mathematik*, 92(3):401–419, 2002.

[21] F. Auricchio, L. B. da Veiga, F. Brezzi, and C. Lovadina. *Mixed Finite Element Methods*, pages 1–53. American Cancer Society, 2017.

[22] F. Auricchio, L. B. Da Veiga, C. Lovadina, A. Reali, R. L. Taylor, and P. Wriggers. Approximation of incompressible large deformation elastic problems: some unresolved issues. *Computational Mechanics*, 52(5):1153–1167, 2013.

[23] F. Auricchio and C. Lovadina. Analysis of kinematic linked interpolation methods for Reissner–Mindlin plate problems. *Computer Methods in Applied Mechanics and Engineering*, 190(18):2465–2482, 2001.

[24] I. Babuška. The finite element method with Lagrangian multipliers. *Numerische Mathematik*, 20(3):179–192, 1973.

[25] I. Babuška, J. Osborn, and J. Pitkäranta. Analysis of mixed methods using mesh dependent norms. *Mathematics of Computation*, 35(152):1039–1062, 1980.

[26] I. Babuška and J. Pitkäranta. The plate paradox for hard and soft simple support. *SIAM Journal on Mathematical Analysis*, 21(3):551–576, 1990.

[27] I. Babuška and M. Suri. Locking effects in the finite element approximation of elasticity problems. *Numerische Mathematik*, 62(1):439–463, 1992.

[28] I. Babuška and M. Suri. On locking and robustness in the finite element method. *SIAM Journal on Numerical Analysis*, 29(5):1261–1293, 1992.

[29] J. M. Ball. Convexity conditions and existence theorems in nonlinear elasticity. *Archive for Rational Mechanics and Analysis*, 63(4):337–403, 1976.

[30] K.-J. Bathe. *Finite element procedures*. Pearson Education, Inc, Watertown, MA, 2 edition, 2014.

[31] K.-J. Bathe and F. Brezzi. A simplified analysis of two plate bending elements – the MITC4 and MITC9 elements. In G. N. Pande and J. Middleton, editors, *Numerical Techniques for Engineering Analysis and Design*, pages 407–417, Dordrecht, 1987. Springer Netherlands.

[32] K.-J. Bathe, F. Brezzi, and S. W. Cho. The MITC7 and MITC9 plate bending elements. *Computers & Structures*, 32(3):797–814, 1989.

[33] K.-J. Bathe, D. Chapelle, and P.-S. Lee. A shell problem 'highly sensitive' to thickness changes. *International Journal for Numerical Methods in Engineering*, 57(8):1039–1052, 2003.

[34] K.-J. Bathe and E. N. Dvorkin. A four-node plate bending element based on Mindlin/Reissner plate theory and a mixed interpolation. *International Journal for Numerical Methods in Engineering*, 21(2):367–383, 1985.

[35] K.-J. Bathe and E. N. Dvorkin. A formulation of general shell elements–the use of mixed interpolation of tensorial components. *International Journal for Numerical Methods in Engineering*, 22(3):697–722, 1986.

[36] K.-J. Bathe, A. Iosilevich, and D. Chapelle. An evaluation of the MITC shell elements. *Computers & Structures*, 75(1):1–30, 2000.

[37] K.-J. Bathe, A. Iosilevich, and D. Chapelle. An inf-sup test for shell finite elements. *Computers & Structures*, 75(5):439–456, 2000.

[38] J.-L. Batoz, K.-J. Bathe, and L.-W. Ho. A study of three-node triangular plate bending elements. *International Journal for Numerical Methods in Engineering*, 15(12):1771–1812, 1980.

[39] J.-L. Batoz and I. Katili. On a simple triangular Reissner/Mindlin plate element based on incompatible modes and discrete constraints. *International Journal for Numerical Methods in Engineering*, 35(8):1603–1632, 1992.

[40] J. L. Batoz and P. Lardeur. A discrete shear triangular nine D.O.F. element for the analysis of thick to very thin plates. *International Journal for Numerical Methods in Engineering*, 28(3):533–560, 1989.

[41] J. L. Batoz, C. L. Zheng, and F. Hammadi. Formulation and evaluation of new triangular, quadrilateral, pentagonal and hexagonal discrete Kirchhoff plate/shell elements. *International Journal for Numerical Methods in Engineering*, 52(5-6):615–630, 2001.

[42] U. Bauer, K. Polthier, and M. Wardetzky. Uniform convergence of discrete curvatures from nets of curvature lines. *Discrete & Computational Geometry*, 43(4):798–823, 2010.

[43] H. R. Bayat, J. Krämer, L. Wunderlich, S. Wulfinghoff, S. Reese, B. Wohlmuth, and C. Wieners. Numerical evaluation of discontinuous and nonconforming finite element methods in nonlinear solid mechanics. *Computational Mechanics*, 62(6):1413–1427, 2018.

[44] S. Beuchler and J. Schöberl. New shape functions for triangular p-FEM using integrated Jacobi polynomials. *Numerische Mathematik*, 103(3):339–366, 2006.

[45] S. Bieber, B. Oesterle, E. Ramm, and M. Bischoff. A variational method to avoid locking–independent of the discretization scheme. *International Journal for Numerical Methods in Engineering*, 114(8):801–827, 2018.

[46] M. Bischoff. *Theorie und Numerik einer dreidimensionalen Schalenformulierung.* PhD thesis, University of Stuttgart, 1999.

[47] M. Bischoff and E. Ramm. Shear deformable shell elements for large strains and rotations. *International Journal for Numerical Methods in Engineering*, 40(23):4427–4449, 1997.

[48] M. Bischoff, E. Ramm, and D. Braess. A class of equivalent enhanced assumed strain and hybrid stress finite elements. *Computational Mechanics*, 22(6):443–449, 1999.

[49] M. Bischoff, E. Ramm, and J. Irslinger. *Models and Finite Elements for Thin-Walled Structures*, pages 1–86. American Cancer Society, 2017.

[50] K.-U. Bletzinger, M. Bischoff, and E. Ramm. A unified approach for shear-locking-free triangular and rectangular shell finite elements. *Computers & Structures*, 75(3):321–334, 2000.

[51] H. Blum and R. Rannacher. On the boundary value problem of the biharmonic operator on domains with angular corners. *Mathematical Methods in the Applied Sciences*, 2(4):556–581, 1980.

[52] H. Blum and R. Rannacher. On mixed finite element methods in plate bending analysis. *Computational Mechanics*, 6(3):221–236, 1990.

[53] D. Boffi, F. Brezzi, and M. Fortin. *Mixed finite element methods and applications*, volume 44. Springer-Verlag Berlin Heidelberg, Berlin, Heidelberg, 1 edition, 2013.

[54] J. Bonet, A. J. Gil, and R. Ortigosa. A computational framework for polyconvex large strain elasticity. *Computer Methods in Applied Mechanics and Engineering*, 283:1061–1094, 2015.

[55] J. Bonet, A. J. Gil, and R. Ortigosa. On a tensor cross product based formulation of large strain solid mechanics. *International Journal of Solids and Structures*, 84:49–63, 2016.

[56] J. Bonet, A. J. Gil, and R. D. Wood. *Nonlinear Solid Mechanics for Finite Element Analysis: Statics.* Cambridge University Press, 2016.

[57] D. Braess. Enhanced assumed strain elements and locking in membrane problems. *Computer Methods in Applied Mechanics and Engineering*, 165(1):155–174, 1998.

[58] D. Braess. *Finite Elemente - Theorie, schnelle Löser und Anwendungen in der Elastizitätstheorie.* Springer-Verlag, Berlin Heidelberg, 5 edition, 2013.

[59] D. Braess, A. Pechstein, and J. Schöberl. An equilibration based a posteriori error estimate for the biharmonic equation and two finite element methods. *IMA Journal of Numerical Analysis*, 40(2):951–975, 2019.

[60] D. Braess, S. Sauter, and C. Schwab. On the justification of plate models. *Journal of Elasticity*, 103(1):53–71, 2011.

[61] F. Brezzi. On the existence, uniqueness and approximation of saddle-point problems arising from Lagrangian multipliers. *R.A.I.R.O. Analyse Numérique*, 8(R2):129–151, 1974.

[62] F. Brezzi, K.-J. Bathe, and M. Fortin. Mixed-interpolated elements for Reissner–Mindlin plates. *International Journal for Numerical Methods in Engineering*, 28(8):1787–1801, 1989.

[63] F. Brezzi, J. Douglas, and L. D. Marini. Two families of mixed finite elements for second order elliptic problems. *Numerische Mathematik*, 47(2):217–235, 1985.

[64] F. Brezzi and M. Fortin. Numerical approximation of Mindlin-Reissner plates. *Mathematics of computation*, 47(175):151–158, 1986.

[65] F. Brezzi, M. Fortin, and R. Stenberg. Error analysis of mixed-interpolated elements for Reissner-Mindlin plates. *Mathematical Models and Methods in Applied Sciences*, 1(2):125–151, 1991.

[66] F. Brezzi, L. Marini, A. Quarteroni, and P. Raviart. On an equilibrium finite element method for plate bending problems. *CALCOLO*, 17(3):271–291, 1980.

[67] F. Brezzi and P. Raviart. Mixed finite element methods for 4th order elliptic equations. In J. J. H. Miller, editor, *Numerical Analysis III: Proceedings of the Royal Irish Academy Conferenceon Numerical Analysis*, pages 33–56, London, 1977. Academic Press Chichester.

[68] M. Brunet and F. Sabourin. Analysis of a rotation-free 4-node shell element. *International Journal for Numerical Methods in Engineering*, 66(9):1483–1510, 2006.

[69] E. Campello, P. Pimenta, and P. Wriggers. A triangular finite shell element based on a fully nonlinear shell formulation. *Computational Mechanics*, 31(6):505–518, 2003.

[70] C. Carstensen and G. Dolzmann. An a priori error estimate for finite element discretizations in nonlinear elasticity for polyconvex materials under small loads. *Numerische Mathematik*, 97(1):67–80, 2004.

[71] D. Chapelle and K. Bathe. Fundamental considerations for the finite element analysis of shell structures. *Computers & Structures*, 66(1):19–36, 1998.

[72] D. Chapelle and K.-J. Bathe. *The finite element analysis of shells - fundamentals.* Springer-Verlag, Berlin Heidelberg, 2 edition, 2011.

[73] D. Chapelle, D. Oliveira, and M. Bucalem. MITC elements for a classical shell model. *Computers & Structures*, 81(8):523–533, 2003. K.J Bathe 60th Anniversary Issue.

[74] D. Chapelle and R. Stenberg. An optimal low-order locking-free finite element method for Reissner–Mindlin plates. *Mathematical Models and Methods in Applied Sciences*, 8(3):407–430, 1998.

[75] D. Chapelle and R. Stenberg. Stabilized finite element formulations for shells in a bending dominated state. *SIAM Journal on Numerical Analysis*, 36(1):32–73, 1998.

[76] D. Chapelle and R. Stenberg. Locking-free mixed stabilized finite element methods for bending-dominated shells. volume 21, pages 81–94, 1999.

[77] J. Cheeger, W. Müller, and R. Schrader. On the curvature of piecewise flat spaces. *Communications in Mathematical Physics*, 92(3):405–454, 1984.

[78] J. Cheeger, W. Müller, and R. Schrader. Kinematic and tube formulas for piecewise linear spaces. *Indiana University Mathematics Journal*, 35(4):737–754, 1986.

[79] L. Chen, J. Hu, and X. Huang. Multigrid methods for Hellan–Herrmann–Johnson mixed method of Kirchhoff plate bending problems. *Journal of Scientific Computing*, 76(2):673–696, 2018.

[80] L. Chen and X. Huang. Finite elements for divdiv-conforming symmetric tensors. *arXiv preprint 2005.01271*, 2020.

[81] L. Chen and X. Huang. Finite elements for divdiv-conforming symmetric tensors in three dimensions. *arXiv preprint 2007.12399*, 2020.

[82] D. Chenais and J.-C. Paumier. On the locking phenomenon for a class of elliptic problems. *Numerische Mathematik*, 67(4):427–440, 1994.

[83] D. Choi, F. Palma, E. Sanchez-Palencia, and M. Vilarino. Membrane locking in the finite element computation of very thin elastic shells. *ESAIM: Mathematical Modelling and Numerical Analysis*, 32(2):131–152, 1998.

[84] S. H. Christiansen. A characterization of second-order differential operators on finite element spaces. *Mathematical Models and Methods in Applied Sciences*, 14(12):1881–1892, 2004.

[85] S. H. Christiansen. On the linearization of Regge calculus. *Numerische Mathematik*, 119(4):613–640, 2011.

[86] P. G. Ciarlet. *The Finite Element Method for Elliptic Problems.* North-Holland Publishing Co., Amsterdam, New York,Oxford, 1978.

[87] P. G. Ciarlet. *Mathematical Elasticity. Vol. I: Three-Dimensional Elasticity*, volume 20. North-Holland, Amsterdam, 1988.

[88] P. G. Ciarlet. An introduction to differential geometry with applications to elasticity. *Journal of Elasticity*, 78-79(1):1–215, 2005.

[89] P. G. Ciarlet, L. Gratie, and C. Mardare. Intrinsic methods in elasticity: a mathematical survey. *Discrete & Continuous Dynamical Systems - A*, 23(1&2):133–164, 2009.

[90] B. Cockburn, J. Gopalakrishnan, and R. Lazarov. Unified hybridization of discontinuous Galerkin, mixed, and continuous Galerkin methods for second order elliptic problems. *SIAM Journal on Numerical Analysis*, 47(2):1319–1365, 2009.

[91] M. I. Comodi. The Hellan–Herrmann–Johnson method: Some new error estimates and postprocessing. *Mathematics of Computation*, 52(185):17–29, 1989.

[92] E. Cosserat and F. Cosserat. Théorie des corps déformables. *Nature*, 81(67), 1909.

[93] M. C. Delfour and J.-P. Zolésio. *Shapes and geometries: metrics, analysis, differential calculus, and optimization*. SIAM, Philadelphia, 2 edition, 2011.

[94] L. Demkowicz. Projection-based interpolation. *ICES Report*, 4(3):1–22, 2004.

[95] M. Dubiner. Spectral methods on triangles and other domains. *Journal of Scientific Computing*, 6(4):345–390, 1991.

[96] G. Duvant and J. L. Lions. *Inequalities in Mechanics and Physics*, volume 219 of *Grundlehren der mathematischen Wissenschaften*. Springer-Verlag, Berlin Heidelberg, 1 edition, 1976.

[97] G. Dziuk and C. M. Elliott. Finite element methods for surface PDEs. *Acta Numerica*, 22:289–396, 2013.

[98] R. Echter, B. Oesterle, and M. Bischoff. A hierarchic family of isogeometric shell finite elements. *Computer Methods in Applied Mechanics and Engineering*, 254:170–180, 2013.

[99] G. Engel, K. Garikipati, T. J. R. Hughes, M. Larson, L. Mazzei, and R. Taylor. Continuous/discontinuous finite element approximations of fourth-order elliptic problems in structural and continuum mechanics with applications to thin beams and plates, and strain gradient elasticity. *Computer Methods in Applied Mechanics and Engineering*, 191(34):3669–3750, 2002.

[100] C. Felippa and B. Haugen. A unified formulation of small-strain corotational finite elements: I. Theory. *Computer Methods in Applied Mechanics and Engineering*, 194(21):2285–2335, 2005. Computational Methods for Shells.

[101] C. A. Felippa. A study of optimal membrane triangles with drilling freedoms. *Computer Methods in Applied Mechanics and Engineering*, 192(16):2125–2168, 2003.

[102] F. G. Flores and E. Oñate. A rotation-free shell triangle for the analysis of kinked and branching shells. *International Journal for Numerical Methods in Engineering*, 69(7):1521–1551, 2007.

[103] P. J. Flory. Thermodynamic relations for high elastic materials. *Trans. Faraday Soc.*, 57:829–838, 1961.

[104] G. Fu, C. Lehrenfeld, A. Linke, and T. Streckenbach. Locking free and gradient robust H(div)-conforming HDG methods for linear elasticity. *arXiv preprint 2001.08610*, 2020.

[105] M. Gärdsback and G. Tibert. A comparison of rotation-free triangular shell elements for unstructured meshes. *Computer Methods in Applied Mechanics and Engineering*, 196(49):5001–5015, 2007.

[106] K. Gerdes, A. Matache, and C. Schwab. Analysis of membrane locking in hp FEM for a cylindrical shell. *ZAMM - Journal of Applied Mathematics and Mechanics / Zeitschrift für Angewandte Mathematik und Mechanik*, 78(10):663–686, 1998.

[107] Y. Gingold, A. Secord, J. Y. Han, E. Grinspun, and D. Zorin. A discrete model for inelastic deformation of thin shells. Technical report, Courant Institute of Mathematical Sciences, New York University, 2004.

[108] J. Gopalakrishnan, P. L. Lederer, and J. Schöberl. A mass conserving mixed stress formulation for the Stokes equations. *IMA Journal of Numerical Analysis*, 40(3):1838–1874, 2019.

[109] E. Grinspun, Y. Gingold, J. Reisman, and D. Zorin. Computing discrete shape operators on general meshes. *Computer Graphics Forum*, 25(3):547–556, 2006.

[110] H. Hakula, Y. Leino, and J. Pitkäranta. Scale resolution, locking, and high-order finite element modelling of shells. *Computer Methods in Applied Mechanics and Engineering*, 133(3):157–182, 1996.

[111] P. Hansbo and M. G. Larson. Continuous/discontinuous finite element modelling of Kirchhoff plate structures in R3 using tangential differential calculus. *Computational Mechanics*, 60(4):693–702, 2017.

[112] P. Hansbo, M. G. Larson, and F. Larsson. Tangential differential calculus and the finite element modeling of a large deformation elastic membrane problem. *Computational Mechanics*, 56(1):87–95, 2015.

[113] P. Hauret and F. Hecht. A discrete differential sequence for elasticity based upon continuous displacements. *SIAM Journal on Scientific Computing*, 35(1):B291–B314, 2013.

[114] K. Hellan. Analysis of elastic plates in flexure by a simplified finite element method. *Acta Polytechnica Scandinavica, Civil Engineering Series*, 46, 1967.

[115] E. Hellinger. Die allgemeinen Ansätze der Mechanik der Kontinua. In F. Klein and C. Müller, editors, *Mechanik*, pages 601–694, Wiesbaden, 1907. Vieweg+Teubner Verlag.

[116] L. R. Herrmann. Finite element bending analysis for plates. *Journal of the Engineering Mechanics Division*, 93(5):13–26, 1967.

[117] G. Holzapfel. *Nonlinear Solid Mechanics. A Continuum Approach for Engineering.* John Wiley & Sons, LTD, Chichester, 2000.

[118] P. Hood and C. Taylor. Numerical solution of the Navier-Stokes equations using the finite element technique. *Computers & Fluids*, 1(1):73–100, 1973.

[119] H. C. Huang and E. Hinton. A new nine node degenerated shell element with enhanced membrane and shear interpolation. *International Journal for Numerical Methods in Engineering*, 22(1):73–92, 1986.

[120] J. Huang, X. Huang, and Y. Xu. Convergence of an adaptive mixed finite element method for Kirchhoff plate bending problems. *SIAM Journal on Numerical Analysis*, 49(2):574–607, 2011.

[121] T. J. R. Hughes. *The finite element method: linear static and dynamic finite element analysis.* Dover Publications Inc., Mineola, New York., 2000.

[122] T. J. R. Hughes, J. Cottrell, and Y. Bazilevs. Isogeometric analysis: CAD, finite elements, NURBS, exact geometry and mesh refinement. *Computer Methods in Applied Mechanics and Engineering*, 194(39):4135–4195, 2005.

[123] T. J. R. Hughes and T. E. Tezduyar. Finite elements based upon Mindlin plate theory with particular reference to the four-node bilinear isoparametric element. *Journal of Applied Mechanics*, 48(3):587–596, 1981.

[124] A. Ibrahimbegović. Stress resultant geometrically nonlinear shell theory with drilling rotations–Part I. A consistent formulation. *Computer Methods in Applied Mechanics and Engineering*, 118(3):265–284, 1994.

[125] J. Jang and P. M. Pinsky. An assumed covariant strain based 9-node shell element. *International Journal for Numerical Methods in Engineering*, 24(12):2389–2411, 1987.

[126] H.-M. Jeon, Y. Lee, P.-S. Lee, and K.-J. Bathe. The MITC3+ shell element in geometric nonlinear analysis. *Computers & Structures*, 146:91–104, 2015.

[127] C. Johnson. On the convergence of a mixed finite element method for plate bending moments. *Numerische Mathematik*, 21(1):43–62, 1973.

[128] E. Karabelas, G. Haase, G. Plank, and C. M. Augustin. Versatile stabilized finite element formulations for nearly and fully incompressible solid mechanics. *Computational mechanics*, 65(1):193–215, 2020.

[129] E. P. Kasper and R. L. Taylor. A mixed-enhanced strain method: Part I: Geometrically linear problems. *Computers & Structures*, 75(3):237–250, 2000.

[130] E. P. Kasper and R. L. Taylor. A mixed-enhanced strain method: Part II: Geometrically nonlinear problems. *Computers & Structures*, 75(3):251–260, 2000.

[131] I. Katili. A new discrete Kirchhoff-Mindlin element based on Mindlin-Reissner plate theory and assumed shear strain fields–Part I: An extended DKT element for thick-plate bending analysis. *International Journal for Numerical Methods in Engineering*, 36(11):1859–1883, 1993.

[132] I. Katili, J.-L. Batoz, I. J. Maknun, A. Hamdouni, and O. Millet. The development of DKMQ plate bending element for thick to thin shell analysis based on the Naghdi/Reissner/Mindlin shell theory. *Finite Elements in Analysis and Design*, 100:12–27, 2015.

[133] P. Khosravi, R. Ganesan, and R. Sedaghati. An efficient facet shell element for corotational nonlinear analysis of thin and moderately thick laminated composite structures. *Computers & Structures*, 86(9):850–858, 2008. Composites.

[134] J. Kiendl, K.-U. Bletzinger, J. Linhard, and R. Wüchner. Isogeometric shell analysis with Kirchhoff–Love elements. *Computer Methods in Applied Mechanics and Engineering*, 198(49):3902–3914, 2009.

[135] D.-N. Kim and K.-J. Bathe. A triangular six-node shell element. *Computers & Structures*, 87(23):1451–1460, 2009.

[136] G. Kirchhoff. Über das Gleichgewicht und die Bewegung einer elastischen Scheibe. *Journal für die reine und angewandte Mathematik*, 40:51–88, 1850.

[137] Y. Ko, P.-S. Lee, and K.-J. Bathe. A new MITC4+ shell element. *Computers & Structures*, 182:404–418, 2017.

[138] W. Koiter. A consistent first approximation in the general theory of thin elastic shells. In W. Koiter, editor, *The theory of thin elastic shells*, pages 12–33. North-Holland, Amsterdam, 1960.

[139] F. Koschnick, M. Bischoff, N. Camprubí, and K.-U. Bletzinger. The discrete strain gap method and membrane locking. *Computer Methods in Applied Mechanics and Engineering*, 194(21):2444–2463, 2005.

[140] R. Kupferman and J. P. Solomon. A Riemannian approach to reduced plate, shell, and rod theories. *Journal of Functional Analysis*, 266(5):2989–3039, 2014.

[141] O. A. Ladyzhenskaya. *The mathematical theory of viscous incompressible flow*, volume 2. Gordon and Breach New York, New York, 1969.

[142] P. Le Tallec. Numerical methods for nonlinear three-dimensional elasticity. volume 3 of *Handbook of Numerical Analysis*, pages 465–622. Elsevier, 1994.

[143] P. L. Lederer. *A Mass Conserving Mixed Stress Formulation For Incompressible Flows.* PhD thesis, TU Wien, 2019.

[144] P. L. Lederer, C. Lehrenfeld, and J. Schöberl. Divergence-free tangential finite element methods for incompressible flows on surfaces. *International Journal for Numerical Methods in Engineering*, 121(11):2503–2533, 2020.

[145] C. Lehrenfeld. Hybrid discontinuous Galerkin methods for solving incompressible flow problems. Master's thesis, Rheinisch-Westfälischen Technischen Hochschule Aachen, 2010.

[146] M. Lenoir. Optimal isoparametric finite elements and error estimates for domains involving curved boundaries. *SIAM Journal on Numerical Analysis*, 23(3):562–580, 1986.

[147] L. Li. *Regge Finite Elements with Applications in Solid Mechanics and Relativity.* PhD thesis, University of Minnesota, 2018.

[148] C. Lovadina. A low-order nonconforming finite element for Reissner–Mindlin plates. *SIAM Journal on Numerical Analysis*, 42(6):2688–2705, 2005.

[149] A. E. H. Love. XVI. The small free vibrations and deformation of a thin elastic shell. *Philosophical Transactions of the Royal Society of London. (A.)*, 179:491–546, 1888.

[150] M. Lyly. On the connection between some linear triangular Reissner-Mindlin plate bending elements. *Numerische Mathematik*, 85(1):77–107, 2000.

[151] R. H. Macneal. Derivation of element stiffness matrices by assumed strain distributions. *Nuclear Engineering and Design*, 70(1):3–12, 1982.

[152] R. H. Macneal and R. L. Harder. A proposed standard set of problems to test finite element accuracy. *Finite Elements in Analysis and Design*, 1(1):3–20, 1985.

[153] D. S. Malkus and T. J. R. Hughes. Mixed finite element methods – Reduced and selective integration techniques: A unification of concepts. *Computer Methods in Applied Mechanics and Engineering*, 15(1):63–81, 1978.

[154] J. E. Marsden and T. J. R. Hughes. *Mathematical foundations of elasticity.* Dover Publication, Inc, New York, 1994.

[155] M. Meindlhumer and A. Pechstein. 3D mixed finite elements for curved, flat piezoelectric structures. *International Journal of Smart and Nano Materials*, 10(4):249–267, 2019.

[156] R. Mindlin. Influence of rotatory inertia and shear on flexural motions of isotropic, elastic plates. *Journal of Applied Mechanics*, 18:31–38, 1951.

[157] P. Monk. *Finite element methods for Maxwell's equations.* Numerical Mathematics and Scientific Computation. Oxford University Press, New York, 2003.

[158] D. Morgenstern. Herleitung der Plattentheorie aus der dreidimensionalen Elastizitäts-theorie. *Archive for Rational Mechanics and Analysis*, 4(1):145–152, 1959.

[159] L. S. D. Morley. The constant-moment plate-bending element. *Journal of Strain Analysis*, 6(1):20–24, 1971.

[160] P. Naghdi. The theory of shells. In S. Flügge, editor, *Handbuch der Physik*, volume VI/2. Springer-Verlag, Berlin and New York, 1972.

[161] J. C. Nédélec. Mixed finite elements in R3. *Numerische Mathematik*, 35(3):315–341, 1980.

[162] J. C. Nédélec. A new family of mixed finite elements in R3. *Numerische Mathematik*, 50(1):57–81, 1986.

[163] M. Neunteufel, A. S. Pechstein, and J. Schöberl. Three-field mixed finite element methods for nonlinear elasticity. *arXiv preprint 2009.03928*, 2020.

[164] M. Neunteufel and J. Schöberl. The Hellan–Herrmann–Johnson method for nonlinear shells. *Computers & Structures*, 225:106109, 2019.

[165] M. Neunteufel and J. Schöberl. Avoiding membrane locking with Regge interpolation. *Computer Methods in Applied Mechanics and Engineering*, 373:113524, 2021.

[166] E. Oñate and F. Zárate. Rotation-free triangular plate and shell elements. *International Journal for Numerical Methods in Engineering*, 47(1-3):557–603, 2000.

[167] B. Oesterle, R. Sachse, E. Ramm, and M. Bischoff. Hierarchic isogeometric large rotation shell elements including linearized transverse shear parametrization. *Computer Methods in Applied Mechanics and Engineering*, 321:383–405, 2017.

[168] R. Ogden. *Non-linear Elastic Deformations*. Dover Civil and Mechanical Engineering. Dover Publications, 1997.

[169] E. Oñate, F. Zarate, and F. Flores. A simple triangular element for thick and thin plate and shell analysis. *International Journal for Numerical Methods in Engineering*, 37(15):2569–2582, 1994.

[170] K. C. Park and G. M. Stanley. A curved C0 shell element based on assumed natural-coordinate strains. *Journal of Applied Mechanics*, 53(2):278–290, 1986.

[171] A. Pechstein and J. Schöberl. Tangential-displacement and normal-normal-stress continuous mixed finite elements for elasticity. *Math. Models Methods Appl. Sci.*, 21(8):1761–1782, 2011.

[172] A. Pechstein and J. Schöberl. Anisotropic mixed finite elements for elasticity. *International Journal for Numerical Methods in Engineering*, 90(2):196–217, 2012.

[173] A. Pechstein and J. Schöberl. The TDNNS method for Reissner–Mindlin plates. *Numerische Mathematik*, 137(3):713–740, 2017.

[174] A. Pechstein and J. Schöberl. An analysis of the TDNNS method using natural norms. *Numerische Mathematik*, 139(1):93–120, 2018.

[175] A. S. Pechstein. Large deformation mixed finite elements for smart structures. *Mechanics of Advanced Materials and Structures*, 0(0):1–11, 2019.

[176] R. Pfefferkorn and P. Betsch. Extension of the enhanced assumed strain method based on the structure of polyconvex strain-energy functions. *International Journal for Numerical Methods in Engineering*, 121(8):1695–1737, 2020.

[177] W. Pietraszkiewicz and V. Konopińska. Junctions in shell structures: A review. *Thin-Walled Structures*, 95:310–334, 2015.

[178] J. Pitkäranta. The problem of membrane locking in finite element analysis of cylindrical shells. *Numerische Mathematik*, 61(1):523–542, 1992.

[179] J. Pitkäranta, A.-M. Matache, and C. Schwab. Fourier mode analysis of layers in shallow shell deformations. *Computer Methods in Applied Mechanics and Engineering*, 190(22):2943–2975, 2001.

[180] G. Prange. *Das Extremum der Formänderungsarbeit: Habilitationsschrift Technische Hochschule Hannover 1916.* Edited by K. Knothe , Lehrstuhl für Geschichte der Naturwissenschaften, LMU München, 1999.

[181] A. Quaglino. A framework for creating low-order shell elements free of membrane locking. *International Journal for Numerical Methods in Engineering*, 108(1):55–75, 2016.

[182] K. Rafetseder and W. Zulehner. A decomposition result for Kirchhoff plate bending problems and a new discretization approach. *SIAM Journal on Numerical Analysis*, 56(3):1961–1986, 2018.

[183] K. Rafetseder and W. Zulehner. A new mixed approach to Kirchhoff–Love shells. *Computer Methods in Applied Mechanics and Engineering*, 346:440–455, 2019.

[184] P.-A. Raviart and J.-M. Thomas. A mixed finite element method for 2-nd order elliptic problems. In *Mathematical Aspects of Finite Element Methods*, volume 66, pages 292–315. Springer, 1977.

[185] B. Reddy and J. Simo. Stability and convergence of a class of enhanced strain methods. *SIAM Journal on Numerical Analysis*, 32(6):1705–1728, 1995.

[186] S. Reese. On the equivalent of mixed element formulations and the concept of reduced integration in large deformation problems. *International Journal of Nonlinear Sciences and Numerical Simulation*, 3(1):1–34, 2002.

[187] S. Reese. A large deformation solid-shell concept based on reduced integration with hourglass stabilization. *International Journal for Numerical Methods in Engineering*, 69(8):1671–1716, 2007.

[188] S. Reese, H. Bayat, and S. Wulfinghoff. On an equivalence between a discontinuous Galerkin method and reduced integration with hourglass stabilization for finite elasticity. *Computer Methods in Applied Mechanics and Engineering*, 325:175–197, 2017.

[189] S. Reese, P. Wriggers, and B. Reddy. A new locking-free brick element technique for large deformation problems in elasticity. *Computers & Structures*, 75(3):291–304, 2000.

[190] T. Regge. General relativity without coordinates. *Il Nuovo Cimento (1955-1965)*, 19(3):558–571, 1961.

[191] E. Reissner. The effect of transverse shear deformation on the bending of elastic plates. *Journal of Applied Mechanics*, 67:A69–A77, 1945.

[192] E. Reissner. On a variational theorem in elasticity. *Journal of Mathematics and Physics*, 29(1-4):90–95, 1950.

[193] E. Reissner. On the foundations of the theory of elastic shells. In H. Görtler, editor, *Applied Mechanics*, pages 20–30, Berlin, Heidelberg, 1966. Springer Berlin Heidelberg.

[194] A. Reusken. Stream function formulation of surface Stokes equations. *IMA Journal of Numerical Analysis*, 40(1):109–139, 2018.

[195] R. S. Rivlin and J. L. Ericksen. Stress-deformation relations for isotropic materials. *Journal of Rational Mechanics and Analysis*, 4:323–425, 1955.

[196] J. Schöberl. NETGEN an advancing front 2D/3D-mesh generator based on abstract rules. *Computing and Visualization in Science*, 1(1):41–52, 1997.

[197] J. Schöberl. C++ 11 implementation of finite elements in NGSolve. *Institute for Analysis and Scientific Computing, Vienna University of Technology*, 2014.

[198] J. Schöberl and S. Zaglmayr. High order Nédélec elements with local complete sequence properties. *COMPEL - The international journal for computation and mathematics in electrical and electronic engineering*, 24(2):374–384, 2005.

[199] D. Schöllhammer and T. Fries. Reissner–Mindlin shell theory based on tangential differential calculus. *Computer Methods in Applied Mechanics and Engineering*, 352:172–188, 2019.

[200] D. Schöllhammer and T.-P. Fries. Kirchhoff–Love shell theory based on tangential differential calculus. *Computational Mechanics*, 64(1):113–131, 2019.

[201] J. Schröder, P. Wriggers, and D. Balzani. A new mixed finite element based on different approximations of the minors of deformation tensors. *Computer Methods in Applied Mechanics and Engineering*, 200(49):3583–3600, 2011.

[202] C. Schwab. *p-and hp-finite element methods: Theory and applications in solid and fluid mechanics.* Clarendon Press, Oxford, 1998.

[203] M. F. Shojaei and A. Yavari. Compatible-strain mixed finite element methods for incompressible nonlinear elasticity. *Journal of Computational Physics*, 361:247–279, 2018.

[204] M. F. Shojaei and A. Yavari. Compatible-strain mixed finite element methods for 3D compressible and incompressible nonlinear elasticity. *Computer Methods in Applied Mechanics and Engineering*, 357:112610, 2019.

[205] J. Simo, F. Armero, and R. Taylor. Improved versions of assumed enhanced strain tri-linear elements for 3D finite deformation problems. *Computer Methods in Applied Mechanics and Engineering*, 110(3):359–386, 1993.

[206] J. Simo and D. Fox. On a stress resultant geometrically exact shell model. Part I: Formulation and optimal parametrization. *Computer Methods in Applied Mechanics and Engineering*, 72(3):267–304, 1989.

[207] J. Simo, D. Fox, and M. Rifai. On a stress resultant geometrically exact shell model. Part II: The linear theory; computational aspects. *Computer Methods in Applied Mechanics and Engineering*, 73(1):53–92, 1989.

[208] J. Simo, R. Taylor, and K. Pister. Variational and projection methods for the volume constraint in finite deformation elasto-plasticity. *Computer Methods in Applied Mechanics and Engineering*, 51(1):177–208, 1985.

[209] J. C. Simo and F. Armero. Geometrically non-linear enhanced strain mixed methods and the method of incompatible modes. *International Journal for Numerical Methods in Engineering*, 33(7):1413–1449, 1992.

[210] J. C. Simo and M. S. Rifai. A class of mixed assumed strain methods and the method of incompatible modes. *International Journal for Numerical Methods in Engineering*, 29(8):1595–1638, 1990.

[211] A. Sinwel. *A new family of mixed finite elements for elasticity*. PhD thesis, Johannes Kepler Universität Linz, 2009.

[212] J. Solomon, E. Vouga, M. Wardetzky, and E. Grinspun. Flexible developable surfaces. *Computer Graphics Forum*, 31(5):1567–1576, 2012.

[213] M. Spivak. *A comprehensive introduction to differential geometry*, volume 1. Publish or Perish, Inc., Houston, Texas, 3 edition, 1999.

[214] J. Steiner. Über parallele Flächen. *Monatsber. Preuss. Akad. Wiss*, 2:114–118, 1840.

[215] R. Stenberg. A family of mixed finite elements for the elasticity problem. *Numerische Mathematik*, 53(5):513–538, 1988.

[216] R. Stenberg. Postprocessing schemes for some mixed finite elements. *ESAIM: M2AN*, 25(1):151–167, 1991.

[217] H. Stolarski and T. Belytschko. Membrane locking and reduced integration for curved elements. *Journal of Applied Mechanics*, 49(1):172–176, 1982.

[218] H. Stolarski and T. Belytschko. Shear and membrane locking in curved C0 elements. *Computer Methods in Applied Mechanics and Engineering*, 41(3):279–296, 1983.

[219] H. Stolarski and T. Belytschko. Limitation principles for mixed finite elements based on the Hu-Washizu variational formulation. *Computer Methods in Applied Mechanics and Engineering*, 60(2):195–216, 1987.

[220] M. Suri. Analytical and computational assessment of locking in the hp finite element method. *Computer Methods in Applied Mechanics and Engineering*, 133(3):347–371, 1996.

[221] M. Suri, I. Babuška, and C. Schwab. Locking effects in the finite element approximation of plate models. *Mathematics of Computation*, 64(210):461–482, 1995.

[222] K. Y. Sze, X. H. Liu, and S. H. Lo. Popular benchmark problems for geometric nonlinear analysis of shells. *Finite Elements in Analysis and Design*, 40(11):1551–1569, 2004.

[223] S. Terrana, N. Nguyen, J. Bonet, and J. Peraire. A hybridizable discontinuous Galerkin method for both thin and 3D nonlinear elastic structures. *Computer Methods in Applied Mechanics and Engineering*, 352:561–585, 2019.

[224] A. Tessler and T. J. R. Hughes. A three-node Mindlin plate element with improved transverse shear. *Computer Methods in Applied Mechanics and Engineering*, 50(1):71–101, 1985.

[225] S. P. Timoshenko and S. Woinowsky-Krieger. *Theory of plates and shells*. Engineering Mechanics series. McGraw-Hill, New York, 2 edition, 1959.

[226] F. van Keulen and J. Booij. Refined consistent formulation of a curved triangular finite rotation shell element. *International Journal for Numerical Methods in Engineering*, 39(16):2803–2820, 1996.

[227] N. Viebahn, P. M. Pimenta, and J. Schröder. A simple triangular finite element for nonlinear thin shells: statics, dynamics and anisotropy. *Computational Mechanics*, 59(2):281–297, 2017.

[228] V. Štembera and J. Füssl. DKMQ24 shell element with improved membrane behaviour. *Finite Elements in Analysis and Design*, 175:103341, 2020.

[229] S. Walker. The Kirchhoff plate equation on surfaces: The surface Hellan–Herrman–Johnson method. 2020.

[230] K. Washizu. *Variational methods in elasticity and plasticity*, volume 3. Pergamon press Oxford, 1975.

[231] C. Weischedel. *A discrete geometric view on shear-deformable shell models.* PhD thesis, Georg-August-Universität Göttingen, 2012.

[232] C. Weischedel, A. Tuganov, T. Hermansson, J. Linn, and M. Wardetzky. Construction of discrete shell models by geometric finite differences. Technical Report 220, Fraunhofer (ITWM), 2012.

[233] H. Whitney. *Geometric integration theory.* Princeton University Press, Princeton, N. J, 1957.

[234] R. M. Williams and P. A. Tuckey. Regge calculus: a brief review and bibliography. *Classical and Quantum Gravity*, 9(5):1409–1422, 1992.

[235] K. Wisniewski. *Finite rotation shells. Basic equations and finite elements for Reissner kinematics.* Springer, Netherlands, 1 edition, 2010.

[236] P. Wriggers. *Nonlinear finite element methods.* Springer Science & Business Media, Heidelberg, 1 edition, 2008.

[237] S. Wulfinghoff, H. R. Bayat, A. Alipour, and S. Reese. A low-order locking-free hybrid discontinuous Galerkin element formulation for large deformations. *Computer Methods in Applied Mechanics and Engineering*, 323:353–372, 2017.

[238] H. T. Y. Yang, S. Saigal, A. Masud, and R. K. Kapania. A survey of recent shell finite elements. *International Journal for Numerical Methods in Engineering*, 47(1-3):101–127, 2000.

[239] S. Zaglmayr. *High Order Finite Element Methods for Electromagnetic Field Computation.* PhD thesis, Johannes Kepler Universität Linz, 2006.

[240] O. Zienkiewicz and R. Taylor. *The Finite Element Method. Vol. 1: The Basis.* Butterworth-Heinemann, Oxford, 5 edition, 2000.

[241] O. C. Zienkiewicz, R. L. Taylor, and J. M. Too. Reduced integration technique in general analysis of plates and shells. *International Journal for Numerical Methods in Engineering*, 3(2):275–290, 1971.

[242] O. C. Zienkiewicz and J. Z. Zhu. A simple error estimator and adaptive procedure for practical engineering analysis. *International Journal for Numerical Methods in Engineering*, 24(2):337–357, 1987.

Curriculum Vitae

Persönliche Daten

Name	**Michael Neunteufel**
Geburtsdatum	01.03.1994
Geburtsort	Wien
Nationalität	Österreich
Email	`michael.neunteufel@tuwien.ac.at`

Ausbildung

seit 01/2020	Universitätsassistent am Institut für Analysis und Scientific Computing, TU Wien, Österreich
11/2017–12/2019	Projektassistent am Institut für Analysis und Scientific Computing, TU Wien, Österreich
10/2016–10/2017	Masterstudium Technische Mathematik, TU Wien, Österreich
10/2013–10/2016	Bachelorstudium Technische Mathematik, TU Wien, Österreich
06/2012	Matura, Schulen der Dominikanerinnen, Wien, Österreich

Wissenschaftliche Publikationen

- A. Chejanovsky, M. Neunteufel, I. Münch, J. Schöberl and P. Neff, *A hybrid H1xH(curl) finite element formulation for a planar relaxed micromorphic continuum*, (arXiv:2009.13397)

- M. Neunteufel, A. Pechstein and J. Schöberl, *Three-field mixed finite element methods for nonlinear elasticity*, (arXiv:2009.03928)

- D. Melching, M. Neunteufel, J. Schöberl and U. Stefanelli, *A finite-strain model for incomplete damage in elastoplastic materials*, Computer Methods in Applied Mechanics and Engineering, 374 (2021), 113571

- M. Neunteufel and J. Schöberl, *Avoiding Membrane Locking with Regge Interpolation*, Computer Methods in Applied Mechanics and Engineering, 373 (2021), 113524

- M. Neunteufel and J. Schöberl, *Fluid-structure interaction with H(div)-conforming finite elements*, Computers & Structures, 243 (2021), 106402

- P. Gangl, K. Sturm, M. Neunteufel and J. Schöberl, *Fully and Semi-Automated Shape Differentiation in NGSolve*, Structural and Multidisciplinary Optimization, (2020)

- M. Neunteufel and J. Schöberl, *The Hellan–Herrmann–Johnson Method for Nonlinear Shells*, Computers & Structures, 225 (2019), 106109

Wien, am 11. Februar 2021

Michael Neunteufel